SAPIENZA
UNIVERSITÀ DI ROMA

DIPARTIMENTO DI INGEGNERIA DELL'INFORMAZIONE,
ELETTRONICA E TELECOMUNICAZIONI

DOTTORATO DI RICERCA IN
TELERILEVAMENTO
XXV CICLO

---

PhD Thesis

# Dynamics and Distributions of Minor Species in the Martian Atmosphere by PFS/MEX Data

Candidate:
**Giuseppe SINDONI**
matricola 1171228

Tutor:
Chiar.mo Prof. **Roberto SEU**

Co-Tutor:
Dott. **Davide GRASSI**

ANNO ACCADEMICO 2011/2012

# Contents

# Introduction

In the history of Mars exploration its atmosphere and planetary climatology aroused particular interest. The pressure, temperature, wind speed, the optical depth of the aerosols and their physical characteristics, and the abundance of gases in the atmosphere are the principal quantities on which the attention is focused on. All these amounts may vary with time and place, and, regarding to the abundances of atmospheric gases, we must also take into account the photochemical processes which normally occur in the atmosphere of Mars.

In the study of the minor gases abundance in the Martian $CO_2$-rich atmosphere, which constitutes about 95% of it, water vapor became especially important, both because it is the most variable trace gas, and because it is involved in several processes characterizing the planetary atmosphere. In fact, the water vapor photolysis controls the Mars atmosphere photochemistry, producing odd hydrogen species, such as H, OH, $HO_2$ and $H_2O_2$. The latest mean global models of Mars photochemistry were calculated by Nair et al. (1994) [155] and by Krasnopolsky (1995) [118].

The carbon monoxide (CO), produced by the $CO_2$ photodissociation, is closely related to water vapor not only by photochemical causes, such as the $CO_2$ catalyzed recombination ($CO + OH \rightarrow CO_2 + H$), but also by dynamical effects. The water vapor is a condensable species, while the carbon monoxide is a non condensable one, so they respond differently to atmospheric processes.

The first observations of Mars atmosphere composition were made using ground-based instruments in the first ‘60 [193]. About the seasonal evolution of water vapor, the first data set was provided by the Echelle-Coudé scanner at McDonald Observatory during the period between 1972 and 1974 [31] and later by the MAWD spectrometer on board the Viking 1 lander using the 1.38 $\mu$m absorption band. The main result obtained from this experiment was the coverage of the complete seasonal cycle on Mars, showing a variability of water vapor abundance from a few up to about 100 pr.$\mu$m (precipitable microns). These results suggested a water vapor exchange between the atmosphere and the superficial reserves, as permanent and seasonal polar caps and regolith, and a clear transport from north to south caused by the global circulation [113].

At the end of the ’80s and in the ’90s data acquired by new spacecrafts were available. The ISM spectrometer on board the *Phobos 2* measured a mean column density of 9±3 pr.$\mu$m in the south and of 12±3 pr.$\mu$m in the north [176]. Another instrument on Phobos 2, AUGUSTE, provided an independent measurement of 10 pr.$\mu$m of water with an abundance of 150 ppm up to an altitude of 12 km decreasing down to 3 ppm at 40 km [117]. All these observations were made around Ls[1] = 10°. In 1997 the photocamera on board the lander *Pathfinder* photometrically measured a column density of 6±4 pr.$\mu$m in the "Ares Vallis" region at Ls = 150° and a water vapor confinement in the boundary layer (1-3 km upon the surface) [202].

In the period between 1999 and August 2004 the "Thermal Emission Spectrometer" (TES) on board the *Mars Global Surveyor* acquired spectra covering the spectral band 20-45 $\mu$m. These data cover more than three Martian years always at 14:00 local time [186]. A reanalysis of TES acquired spectra has lowered the water vapor results by 30% [189]. The whole seasonal coverage includes three summers of the northern hemisphere and shows a maximum water vapor column density from 55 pr.$\mu$m to 80 pr.$\mu$m varying in the three different years. Recently, Smith et al. [190] published also the water vapor results obtained from MRO/CRISM data.

At the same time, water vapor was studied using Earth-based instruments in the 0.82 $\mu$m band. The large dataset thus obtained by Sprague et al. [196] allowed a comparison of two Martian years during the northern summer and showed a variation up to a factor 3 between the two years. Although the general trend of the seasonal cycle was reproduced quite well, they detected only 36.4 pr$\mu$m at 71.2° N during Ls = 100°, ie during the sublimation of the permanent north polar cap. The maximum detected amount of water was about 40-45 pr$\mu$m at latitudes around 60-80° N before and after the summer solstice [194].

Since January 2004 Europe has been contributing to the Mars exploration with *Mars Express*. Water vapor in the atmosphere has been studied by the three spectrometers on board: Encrenaz et al. [67] and Melchiorri at al. [145] published $H_2O$ measurements by the OMEGA spectrometer, which covers the 2.6 $\mu$m band, Fedorova et al. published results on the 1.38 $\mu$m band using the SPICAM intrument [76] and, finally, Fouchet et al. [86] analyzed the water vapor absorption band around 25 $\mu$m with the LW of PFS, while Tschimmel et al. [204] and Sindoni et al. [183] studied the water vapor trend using the 2.6 $\mu$m band covered by the SW of PFS. The last work [183] has been carried out in the context of this thesis.

Although water vapor and a few atmospheric species involved in Mars photochemistry, such as $O_3$ [73, 74], $H_2O_2$ [69] and the $O_2$ [21, 124], were observed and studied with a close examination, we do not know much about the carbon monoxide. Regarding the CO study in the Mars atmosphere, Krasnopolsky [124] published a paper in which the CO mixing ratio variations are shown as observed from Earth with the IRTF/CSHELL instrument using the 1.57 $\mu$m band spectroscopy. Another paper was published by Encrenaz et al. [68] about the study of the CO concentration variations over Hellas region as observed

---

[1] The Martian seasons are usually dated in terms of *Aerocentric Longitude* (Ls), which describes the position of Mars in its orbit around the Sun. Ls = 0° is defined as the vernal equinox in the northern hemisphere (autumn equinox in the southern hemisphere), with Ls = 90°, 180° and 270°, corresponding respectively to the summer solstice, autumnal equinox and the winter solstice for the northern hemisphere.

by OMEGA instrument on board the Mars Express, but the first description of the seasonal dependence of the carbon monoxide mixing ratio over a wide latitude range was given by Smith et al. [190] from CRISM data. Recently two papers on the CO observations from PFS-MEX data were also published: the first is a study of the 4.7 $\mu$m band by Billebaud et al. [38], but in this case the data set was rather limited, followed by the wide study about the geographical and seasonal CO distribution by Sindoni et al. [183] obtained analyzing the 2.36 $\mu$m band. Also in this case the last work [183] has been carried out in the context of this thesis.

The study of carbon monoxide is of primary importance for the so-called "stability problem" of the Mars atmosphere. In fact the $CO_2$ dissociation in CO and O by photolysis should destroy the whole atmosphere in 6000 years. Then, the CO is recombined forming again $CO_2$ thanks to the catalysis of $H_2O$ photolysis products. The lack of many simultaneous measurements of water vapor and carbon monoxide makes their comparison an issue of great interest for the understanding of photochemical and dynamical processes involved in the Mars planetary atmosphere. So, the aim of this work is to investigate these two atmospheric species and their connections.

The study of the water vapor and carbon monoxide distributions is very important because they can be used as tracer for many dynamical processes in the Martian atmosphere. One of the most interesting process is the presence of "planetary waves": in the Mars atmosphere the interaction between strong winds and the zonally varying topography excites quasi-stationary waves, which take the form of planetary waves [105]. The stationary waves can influence the stability of the atmosphere and play a significant role in the heat transport from the equator to the pole [28]. Banfield et al. [27] were able to isolate the $s = 1$ and $s = 2$ stationary waves using TES data, while Wilson [212] shows the stationary wave pattern in TES data at Ls = 120°–140° and Hinson et al. [104] identified both stationary waves and thermal tides in radio occultations from MGS for Ls = 75° and 66° N latitude. Finally, Hinson et al. [105] observed stationary planetary waves in the Southern Hemisphere of Mars using two independent instruments (TES and RS) on board the Mars Global Surveyor (MGS) during midwinter (Ls = 134°–160°). These complex dynamical processes can force the zonal/regional circulation and possibly affect the local distribution of minor species in the atmosphere. Therefore, by studying the influence of planetary waves on longitudinal gaseous distribution and thermal profiles we can also get indirect information about their vertical distribution. Infact, although the geographical and seasonal distribution of water vapor and carbon monoxide in the Martian atmosphere was widely studied, we have only indirect information about their vertical distribution. The reason for this lack in the knowledge of minor species vertical distribution lies in the absence of a stable algorithm able to retrieve the gaseous concentrations by limb measurements. The difficulty in modelling the radiative transfer for limb geometries is caused by the multiple scattering treatment, which becomes very important in the infrared range when the atmosphere contains dust and/or water ice aerosols particles (the typical case of Mars). One simple solution is to adapt a multiple scattering algorithm developed for nadir or pseudo-nadir measurements with the use of the Curtis-Godson approximation. This approximation replaces an inhomogeneous path with a homogeneous one by using average values for the various band-model parameters. The Curtis-Godson approximation is very accurate for paths where the temperature and concentration gradients are not particularly steep. This solution, obviously, introduces uncertainties that can be important when simulating limb acquisitions of the Martian atmosphere. Therefore, the best solution is to develop a new algorithm able to take into account the multiple scattering by aerosols particles using a radiative transfer code for optically spherically-symmetric parametrically-defined atmosphere. This is the case of the "Monte-Carlo"-based codes, which calculate the spectral monochromatic intensity by a statistical modeling.

In this thesis we will study the variability of water vapor and carbon monoxide in the atmosphere of Mars from data by the PFS (*Planetary Fourier Spectrometer*) instrument on board Mars Express. It is developed in seven chapters. In the first chapter we will provide an overview of the planet Mars, whereas in the second one we will focus on the planetary atmosphere, with particular attention to the photochemistry and stability problem. In the third chapter we will describe in detail the Mars Express mission, reviewing some instruments on board and ending with the accurate description of the PFS instrument. In the fourth chapter we will describe the data analysis method developed specifically for the concentrations retrieval of atmospheric water vapor and carbon monoxide by nadir and pseudo-nadir ("slant") PFS measurements. In chapter five we will report experimental results thus obtained about the seasonal and geographical mapping of water vapor and carbon monoxide, their variability and correlations/anticorrelations. In the sixth chapter we will use the water vapor and carbon monoxide retrieval method, together with thermal profiles retrieved by PFS, to investigate important atmospheric dynamical processes, as the planetary waves, and thus to get indirect suggestions about their vertical distribution. Finally, in chapter seven, we will describe the first attempt to develop a stable retrieval algorithm for the retrieval of minor atmospheric species by limb measurements, based on the statistical Monte-Carlo modeling, with particular attention on the scattering treatment.

# Chapter 1

# Mars

Mars, the fourth planet of our Solar System, takes its name from the Roman god of the war because of its reddish color, evident to the naked eye and more visible with a telescope. Its apparent magnitude reaches -2.9 [211], a brightness lower only than the one of Venus, of the Moon, of the Sun, and in most cases even than the one of Jupiter. It has many features in common with the Earth. Although its diameter is only slightly more than half of the Earth one, its structure is typical of a differentiated planet: a central metallic core is surrounded by a mantle, which is in turn covered by a crust. A very thin atmosphere contains clouds of water ice and dust, while the considerable inclination of the rotation axis on the plane of the orbit around the sun causes a marked alternation of seasons. A wide variety of geological formations and giant volcanoes are evidence of an intense internal activity now extinct. The reddish color of the soil indicates the oxidation of the surface rocks, where we can find evidence of the role of water in the mineralogical evolution of Mars. Nevertheless, we do not know yet if the water existed in liquid form, or as it is

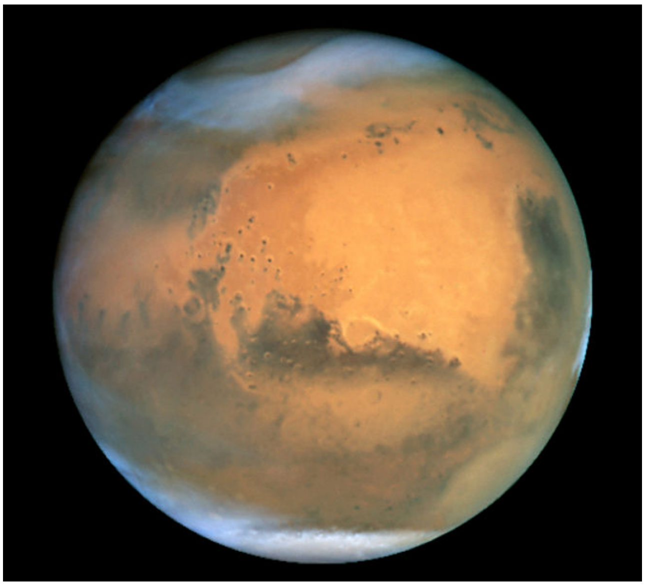

Figure 1.1: Mars as observed by the Hubble Space Telescope.

today, it was only solid (as ice) or as vapor. A clue that would lead to believe that liquid water has flowed on the Martian surface is the presence of vast dry gorges (*canyons*). But, to allow the existence of liquid water, the total pressure of water vapor should have been more than 6.1 mbar, value that is considerably higher than the current value.

Since Mars is more massive than the Moon and Mercury, it kept for a long time high temperature, which gave rise to a considerable geological activity and led to an intense volcanism. Finally, the introduction of large quantities of water and carbon dioxide in the atmosphere occured. This, in turn, has raised the surface temperature because of the greenhouse effect. Generally, it is conceivable that the thermodynamic conditions (pressure and temperature) allowed the existence of water in all the three phases. One possible consequence is that Mars could have been a site of biochemical evolution.

The internal energy of the planet decreases with time, since the radioactive decay generates heat, which is gradually dissipated. Today, Mars is probably geologically quiescent, while the Earth, more massive, is still very active. From the standpoint of comparative planetology, Mars is unique since it allows us to track the complete evolutionary history of an active planet. Moreover, it is also close enough to be accessible for space exploration, and for this reason many missions have already been undertaken and others will be undertaken in the future.

Mars currently hosts three working spacecraft: Mars Odyssey, Mars Express and Mars Reconnaissance Orbiter, while on the surface there are two Mars Exploration Rovers (Spirit and Opportunity), the Phoenix lander, the Mars Science Laboratory (Curiosity), and other landers and rovers that have been completed or failed their mission. Geological evidence gathered by this and previous missions confirms the hypothesis of a past large-scale coverage of water on Mars, while observations also indicate that small geyser-like streams of water were present during the past decade [1].

Mars has two moons, Phobos and Deimos, which are small and irregularly shaped, a characteristic that would suggest their origin as captured asteroids.

In this Chapter we will introduce the planet Mars and all its general characteristics leaving the atmosphere to be discussed in greater details in next Chapter.

## 1.1 Mars Observation by Spacecraft

The first map of Mars, taken from astronomical observations, dates back to the 17th century. However, unlike the case of the Moon, which is a thousand times closer, the red planet was known very little even at the dawn of the space age.

In the 1960s, Americans and Soviets took turns, with MARS and MARINER probes, to photograph the surface, to analyze the atmosphere, and to measure some of general physical properties. The first 21 photographs transmitted by Mariner 4 in 1965 revealed a body marked by impact craters, just like the Moon: Mars appeared as a geologically dead planet, and the Mariner 6 and

7 missions confirmed this hypothesis. The Mariner 9 probe, which orbited around the planet in 1971-2, transmitted the first complete set of photographs of the surface (about 7300 photos), giving an almost full coverage, with a resolution better than 5 km. Due to its orbit, it was even possible to obtain a resolution of a few hundreds of meters on a surface portion. These photographs, sent in digital form, were the bases of the first detailed geological maps of Mars. Mariner 9 revealed a wide range of geological structures, particularly giant volcanoes and canyons. However, none of the observed canyons is one of the famous *Schiaparelli's canals* that earlier astronomers thought to have seen on Mars.

The next step in the exploration of Mars was reached with the spectacular American VIKING program, which consisted of two spacecrafts, each of them with a landing probe (a *lander*), able to collect and analyze samples in situ, and with a *orbiter*, designed to observe the planet from low orbit and transmit to Earth all the data obtained, including those from the landers. The first landing took place on July 20th, 1976 in the region of Chryse Planitia (27.2° north latitude, 47.97° longitude). The second probe landed on the following September 3rd, in a region called Utopia Planitia (47.7° north latitude, 225.7° longitude), which is located 6500 km far from the first. The observations made by the orbiters provided more than 50000 photographs of the surface, with a resolution ranging from 10 to 150 m depending on the particular observed area [2].

Since the end of the Viking program, in November of 1982, space exploration of Mars has experienced a moment of stasis. After the Soviet PHOBOS mission in 1989, and despite the unfortunate failure of NASA MARS OBSERVER MISSION in 1993, exploring the red planet has been moving towards a more systematic study of the planet. In fact, in 1996, NASA launched the MARS GLOBAL SURVEYOR[3]. The mission was a complete success, ending its primary mapping mission in early 2001. The contact with the spacecraft was lost in November 2006 during the third extension of its program, spending exactly 10 operational years in the space. Only a month after the launch of the Surveyor, NASA launched the MARS PATHFINDER, which carried a robotic rover, *Sojourner*, which landed on Mars in Ares Vallis. That mission was successful, and received much publicity, partially due to a many images the probe sent to Earth.

In 2001 NASA launched the MARS ODYSSEY orbiter, which is still in orbit and its mission ending date has been extended until 2010, being the longest-working spacecraft ever sent to Mars. The *Gamma Ray Spectrometer* on board the Odyssey measured significant amounts of hydrogen on the Martian surface. It was suggested that this hydrogen may have been contained in large deposits of water ice [44].

In 2003, ESA launched the MARS EXPRESS spacecraft, consisting of the *Mars Express Orbiter* and the lander *Beagle 2*. The latter failed during its landing phase and was declared lost in February 2004 [206]. In early 2004 the team of the *Planetary Fourier Spectrometer* (PFS) announced the detection of methane in the Martian atmosphere [83]. Finally, the ESA announced in

June 2006, the discovery of auroras on Mars [36].

Figure 1.2: Image representing the Mars Express Orbiter with the Beagle 2 lander.

In 2003 too, NASA had launched the MARS EXPLORATION ROVERS named *Spirit* (MER-A) and *Opportunity* (MER-B). Both missions had landed successfully in January 2004 and had completed their goals. Among the most significant scientific results, there was the conclusive evidence that liquid water has existed for some time in the past in both landing sites. Occasional dust storms cleaned the solar panels of both rovers, thus increasing their life span [4].

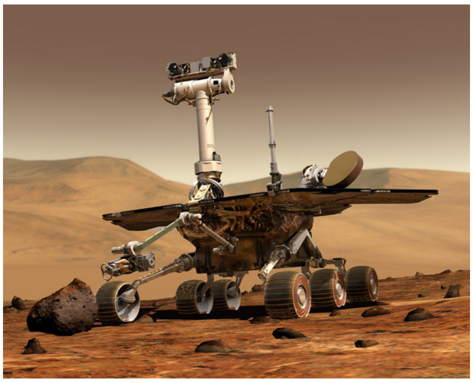

Figure 1.3: Image representing the Spirit rover (MER-A).

On August 12, 2005 NASA RECONNAISSANCE ORBITER was launched toward the planet and arrived in orbit on the 10th of March 2006 to conduct a scientific observation for two years. The orbiter task was to map the Martian surface and climate to find suitable landing sites for future missions. It also contains an improved telecommunications link, with more banda width than the combination of the previous missions. The Mars Reconnaissance Orbiter captured the first image of a series of active avalanches near the north pole on March 3rd, 2008 [5].

The most recent mission on Mars is the NASA PHOENIX lander, which was launched on 4 August 2007 and arrived on the northern polar region of Mars on May 25, 2008 [6]. The lander has a 2.5 m robotic arm able to dig up to a meter deep in the Martian soil. The lander has a microscopic camera with a

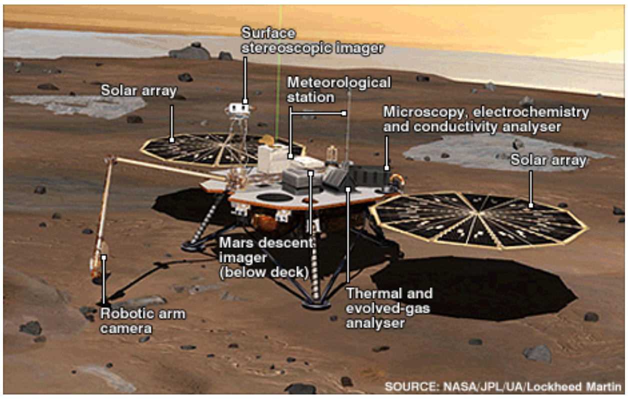

SOURCE: NASA/JPL/UA/Lockheed Martin

Figure 1.4: Image of the Phoenix lander.

resolution capable of resolving objects with dimensions of a hundredth of the human hair thickness, as to identify the composition of the soil in its landing site. By this instrument the presence of water ice has been confirmed on June 20, 2008 [7].

On the 25th of February 2007, the Rosetta spacecraft performed a "fly by" on Mars for a gravity assist on its ten-year journey towards the comet 67P Churyumov-Gerasimenko. The closest approach to the planet occurred at a height of 250 km. The success of this step in the vicinity of Mars allowed to verify the correct operation of the instruments on board the vehicle, as well as their results allowed comparisons between simultaneous observations acquired by the Mars Express orbiter. Similarly, the Dawn satellite performed a "fly by" on Mars in February 2009 in its path toward the investigation of Vesta and Ceres.

The Phoenix lander is followed by the Mars Science Laboratory (named *Curiosity*), launched on the 26th of November 2011 and successfully landed in Gale Crater on the 6th of August 2012. It is a larger and faster (90 m/h) version of the Mars Exploration Rovers. The overall objectives include investigating Mars' habitability, studying its climate and geology, and collecting data for a manned mission to Mars. Among its experiments it includes a samples laser analyzer, which is able to deduce the composition of rocks from a distance of 13 m [8].

The samples return mission from the satellite Phobos, the so-called Phobos-Grunt, born by a collaboration between Russia and China, launched on the 8th of November 2011, failed because of a malfunction of the propulsion system of the carrier due to a wrong orientation, which prevented the solar panels to receive the light needed to power electronic systems on board.

Regarding the future missions, ExoMars (Exobiology on Mars), which is currently under development by the European Space Agency (ESA) with collaboration by the Russian Federal Space Agency (Roscosmos), is a robotic mission to Mars in search for possible biosignatures of Martian life, past or present. The program includes several spacecraft elements to be sent to Mars on two launches. An orbiter and a static lander are planned for 2016, and a Russian lander to deliver the rover is planned for 2018. The ExoMars rover will be able to dig 2 m down in the soil looking for organic molecules[9].

MetNet is an atmospheric science mission to Mars, initiated and defined by the Finnish Meteorological Institute. The mission includes sending several tens of MetNet landers on the Martian surface. The objective is to establish a widespread surface observation network on Mars to investigate the planet's atmospheric structure, physics and meteorology. A precursory mission consisting of one lander is scheduled for launch in the launch window starting from 2014. Other launches are planned in extended time windows up to 2022.

## 1.2 Orbital Characteristics, General Physical Properties and Internal Structure

The main features of Mars are summarized in table 1.1.

| | |
|---|---|
| Heliocentric Distance | 1.52 U.A. = 227 940 000 Km |
| Revolution Period | 1.8808 anni = 686.98 giorni |
| Obliquity[1] | 25° 11’ |
| Orbital Eccentricity | 0.093 |
| Orbital Inclination to the Ecliptic Plane | 1° 51’ |
| Mean Orbital Speed | 24.14 Km/sec |
| Mass | $6.42\cdot10^{23}$ Kg |
| Mean Radius | $(3389.508\pm0.003)$ Km |
| Mean Equatorial Radius | $(3396.200\pm0.160)$ Km |
| North Polar Radius | $(3376.189\pm0.050)$ Km |
| South Polar Radius | $(3382.580\pm0.050)$ Km |
| Mean Density | 3940 Kg/m$^3$ |
| Ellipticity | 0.0052 |
| Equatorial Surface Gravity | 3.72 m/sec$^2$ |
| Escape Velocity | 5000 m/sec |
| Minimum Surface Temperature | 150 K |
| Maximum Surface Temperature | 310 K |
| Rotation Period | 24h 37m 22s |
| Mean Albedo | 0.25 |
| Maximum Visual Magnitude | -2.01 |
| Number of Satellites | 2 |

Table 1.1: Main orbital, physical and geodetic parameters of Mars.

[1] The *Obliquity* is defined as the inclination of the axis of rotation with respect to the orbital plane.

We can note that Mars has a much smaller average density than the Earth one. Although we have to take into account the different degrees of internal compression, this probably indicates a lower iron content in Mars: about 25%, compared to 33% of the Earth. This lower overall content is, however, accompanied by a higher concentration in the outer layers (the crust and the mantle). This could lead to think that there is no metal core, but we have to take into account the value of the total moment of inertia, which is estimated to be 0,365, expressed in terms of the ratio $C/(M \cdot R^2)$, where $C$ is the moment of inertia on the axis of rotation, $M$ is the mass, and $R$ is the mean radius. This value is typical for a body with a high concentration of the central mass. The problem can be approached in another way, as the Soviet probe Mars 3 and Mars 5 measured a very weak magnetic field: their magnetometers found a field of about 60 nanoTesla near the equator (at an altitude of 1500 km). This should correspond to a dipole moment of $2.4 \times 10^{22}$gauss/cm$^3$, about 1/4000 of the Earth value. Therefore, we expect that the liquid iron core of Mars, if it exists, is very small, or because of its dynamic properties prevents any significant dynamo effect. This does not exclude, however, the presence of a solid iron core.

Although Mars has not a significant intrinsic magnetic field, observations show that parts of the planet crust have been magnetized and that alternating polarity reversals of its dipolar field occurred. This paleomagnetism of magnetically susceptible minerals has properties very similar to those represented by the alternating bands found on Earth ocean floors. A theory, published in 1999 and revised in October 2005 (with the help of the Mars Global Surveyor, fig. 1.5), suggests that these bands demonstrate plate tectonics on Mars 4 billion years ago, before the mechanism of planetary dynamo fail to operate, and that this caused the disappearance of the intrinsic magnetic field [90].

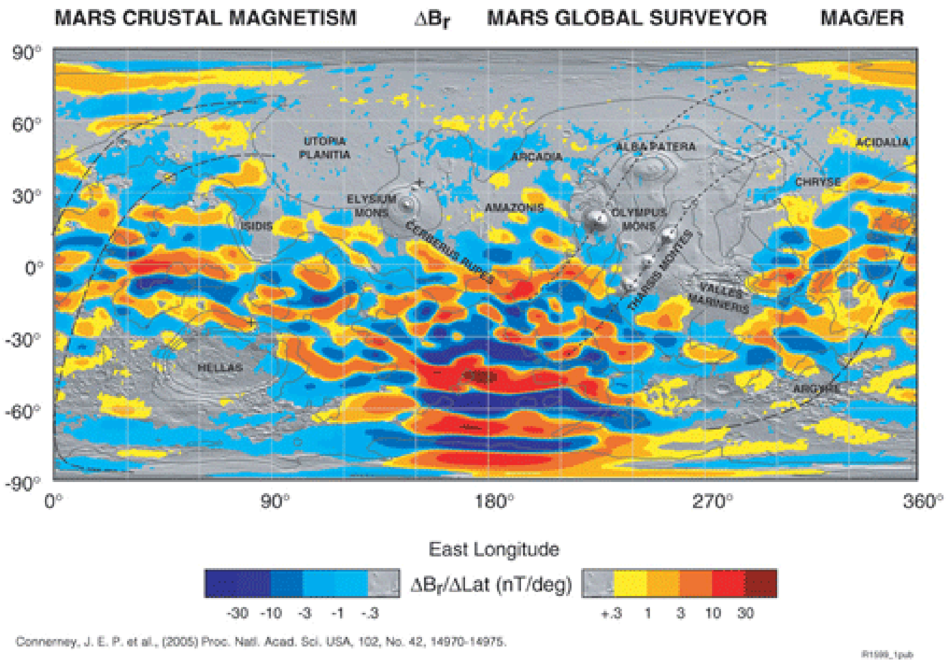

Connerney, J. E. P. et al., (2005) Proc. Natl. Acad. Sci. USA, 102, No. 42, 14970-14975.

Figure 1.5: Map of Mars, where colors represent the strength and direction of the field generated by the magnetization of the crust, obtained from the analysis of data acquired by the Mars Global Surveyor.

Although at the moment we have information provided only by few measurements made in order to identify unambiguously the internal structure of

Mars, it is generally believed that the planet is covered by a crust, which consists primarily of hydrated silicates. Its thickness, although it is not the same all over the planet, is about 50 km, with a maximum of 125 km. A mantle below, thick a few hundred kilometers, undoubtedly contains olivine, a magnesium iron silicate having the general formula $(Mg,Fe)_2SiO_4$, and iron oxide FeO. The thickness of this mantle would avoid any type of tectonic activity as observed on the Earth. Finally, the central core (about 1480 km in radius) consists of a mixture of iron and ferrous sulfide FeS (about 14-17%). This ferrous sulfide is partially fluid and is enriched with a double concentration of lighter elements if compared to the core of the Earth [114].

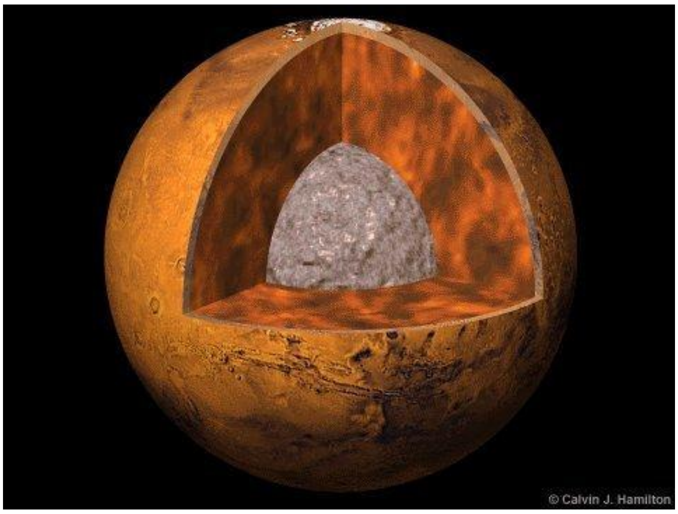

Figure 1.6: Model of the possible core structure of Mars.

Mars is not a perfect sphere: its flattening is greater than the Earth one. The north polar radius is 20 km less than the mean equatorial radius. Hence, we find that the relationship between this difference and the mean equatorial radius is equal to 1:192, compared with the same ratio of 1:298 for the Earth. Furthermore, the differences in altitude are much more pronounced, and show a strong north-south asymmetry.

In the southern hemisphere, below the level of the average area of the planet there are two extended and deep basins, Argyre Planitia and Hellas Planitia. The bottom of Hellas, at about -9 km, is the lowest point on Mars. These basins were probably produced, such as the large lunar basins, by the impact of large asteroids about 4 billion years ago. In general terms, the southern hemisphere contains ancient lands, which are covered by craters, and its average altitude is low.

In the north, on the other hand, there are very high areas, including Tharsis Ridge, where the elevation of the crust (about 6 km) is at its maximum. It is on this plateau, three giant volcanoes of Mars were found, all lined up and having similar height. Not far from here stands the Olympus Mons (Fig. 1.7), more than 25 km high, and 700 km in diameter. It is probably the biggest volcano in the Solar System. In agreement with the method of dating through the study of the craters, the lifting of the Tharsis plateau occurred between 4.1 and 3.3

billion years ago. The volcanic complex does not appear, however, until about 3 - 2.5 billion years ago. The huge size of volcanoes indicates the presence of a lithosphere thick enough to carry them. This can be explained as follows: in the absence of plate tectonics (commonly accepted hypothesis), the volcanoes were on magma areas and as a result the accumulated lava has increased the size of these structeres until the local sources of magma remained. It seems that this volcanism lasted until recent time, i.e. until a couple of hundreds of millions of years ago. The activity of smaller volcanoes (all placed in the northern hemisphere), on the other hand, would have ceased a long time before in the history of the planet. However, perhaps it should not be ruled out the possibility of some, albeit limited, residual phenomena of volcanism today.

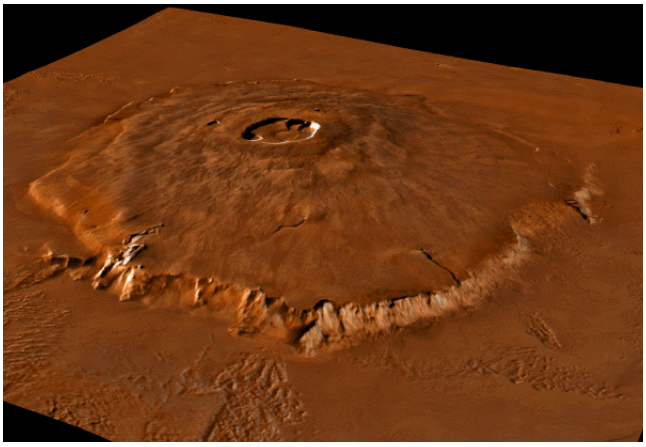

Figure 1.7: 3D Image of the Olympus Mons as seen from the north-east side.

Mars has a gigantic network of canyons, placed around Valles Marineris, a canyon cutting across one entire hemisphere of Mars, with a length of 5000 km, depth of up to 7 km, and an average width of 200 km. It originates in the west side of the Tharsis Ridge and extends eastward, lieing approximately on the equator. The photographs clearly show these canyons as the result of river-like erosion, which implies that liquid water must have been able to flow on the surface. It has been suggested, in particular by Masson [141], a model based on the observation of the geological surface. This suggests that the initial growth of the planet was followed by a deep outgassing, which produced a dense and hot atmosphere, particularly rich in water vapor. As soon as the surface cooled, this water condensed, causing rain and an intense erosion. Later the water seeped into the soil, and once it reached the freezing point, there was the gradual growth of the thickness of the permafrost. The final melting of these masses of ice, probably triggered by volcanic activity, produced severe flooding, which dug the network of canyons we can observe.

Apart from the geological formations on a large scale (impact craters, volcanoes and canyons) a whole set of morphologically complex structures on Mars can be seen: faults, landslides and valleys. Therefore the tectonic activity has taken place on Mars, but this was different from the tectonic plates found on Earth: none of the associated geological formations (mountainous regions, in particular) are observed on Mars, and there are not two types of crust (oceanic and continental).

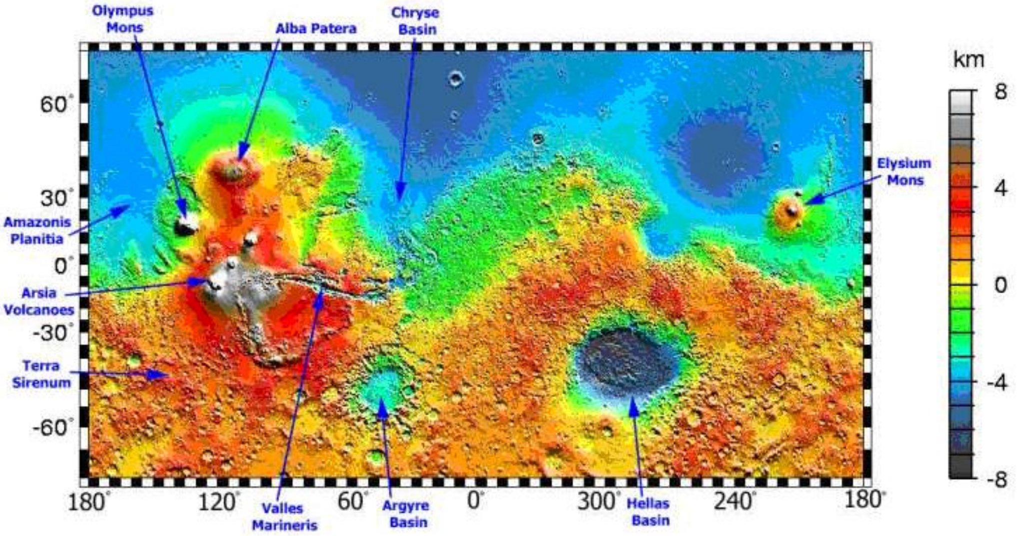

Figure 1.8: Topographic map of Mars, compiled in the summer of 1999 from data acquired by the Mars Orbiter Laser Altimeter (MOLA) on board the NASA's Mars Mars Global Surveyor (MGS).

Large regions of sand dunes, especially near the north polar cap, are visible. They are the direct result of the violent winds that sweep the surface. These are also responsible for the constant wind erosion taking place on Mars. This, in particular, is the process which destroys the impact craters with diameters below about one hundred meters. The redistribution of the particles also produces layered deposits ("laminated area"), particularly in the polar caps. These deposits act as tracers for the accumulation of the ice cap, and thus they can be used as chronometers for the Martian paleoclimatology.

Studies of the impact craters density on the Martian surface allow us to identify three broad periods in the geological time scale: as the oldest surfaces have more craters, so the youngest ones have a smaller amount of them [45]. The eras are named after the places they refer to. The precise positioning of these time periods is not known because there are many competing models that describe the fall rate of meteors on Mars, so the dates given here are approximate. The approximation used for this classification of Martian eras is based on the assumption of a temporal and spatial uniformity of the fall rate of meteorites forming impact craters. From the oldest to the youngest, the time periods are:

- **Noachian Period** (so called by *Noachis Terra*): Formation of the oldest extant surfaces of Mars, between 4.6 and 3.5 billion years ago. Surfaces of the Noachian age are marked by many large impact craters. It is thought that the Tharsis plateau was formed during this period, accompanied by large floods of liquid water towards the end of the period.

- **Hesperian Period** (so called by *Hesperia Planum*): from 3.5 to 1.8 billion years ago. This era is marked by the formation of extensive lava plains.

- **Amazonian Period** (so called by *Amazonis Planitia*): from 1.8 billion years ago to date. Regions formed in this era have few meteorite impact craters but they are very diversified. The Olympus Mons formed during this period along with lava flows elsewhere on Mars.

Recently it has been proposed a different timeline based on the correlation between the mineralogy and the geology of the planet. This proposal emerged from recent observations by the OMEGA instrument (*Visible and Infrared Mineralogical Mapping Spectrometer*) on board the Mars Express orbiter. The proposed timeline divides planet history into three eras [210, 37]:

- **Phyllocian Period** (so called by the phyllosilicates minerals rich of clay which characterize the era): it extends from the formation of the planet to about 4 billion years ago. The formation of phyllosilicates requires the presence of an alkaline environment rich in water. It is therefore believed that the deposits dating from this period are the best candidates for finding evidence of past life on the planet.

- **Theiikian Period** (so called, in greek, by the sulfide minerals formed at that time): from 4 billion to 3500 million years ago. This was a period of volcanic activity. Also lava and various gases, particularly sulfur dioxide, which, combining with the water created an acidic and sulphurous environment, were released.

- **Siderikian Period**: from 3500 million years ago until today. With the end of volcanism and the absence of liquid water, the most remarkable geological process was the oxidation of iron-rich rocks by atmospheric peroxides, leading to red iron oxides that give the planet its familiar color.

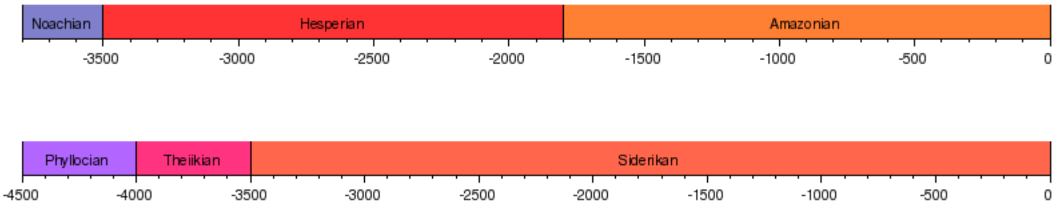

Figure 1.9: Timeline from impact craters (top) and mineralogical timeline (below) for the planet Mars.

## 1.3 The Composition of the Martian Soil

Part of the surface is covered by water (about 15%) and carbon dioxide (about 85%) in the form of ice. The polar ice caps may extend up to latitude 60° in winter. In spring, they partially sublimate recondensing at the other pole. Under the Martian regime of pressure, the condensation temperatures of water and carbon dioxide are respectively about 190 K and 150 K. Because of this, there are permanent water ice caps (mostly in the north than the south), while the carbon dioxide evaporates almost completely, condensing alternatively on either a cap or the other. Furthermore, the water condensation in winter, mainly at high latitudes, forms an ice surface. This covers only a part of the surface, because the precipitation of the entire amount of atmospheric water would correspond to a layer of only about one hundred mm [10]. The south polar cap (Planum Southern) differs from the north polar cap (Planum Boreum, fig. 1.10) as it appears to contain at least some permanent deposits of $CO_2$, which are changing with time scales order of years [11]. It was recently confirmed that the complete (seasonal + permanent) south polar cap is a 3 km thick slab of about 80% of water ice, whereas MEX/MARSIS measured a residual cap thickness of 14 m [152]. NASA scientists calculated that the volume of water ice in the south polar cap, if melted, would be sufficient to cover the entire surface of the planet to a depth of 11 meters [12]. The extent of water ice at the surface and the size of ice grains were monitored as a function of time for the northern polar cap by the MEX/OMEGA instrument[126]. Bright, small-grained frost, which initially covered a large fraction of the polar cap, waned in favor of large-grained ice. In outlying regions, dominated by large grained ice, the albedo increased over the period (Ls = 93°-127°). Moreover, the spectral features observed by OMEGA on the dark longitudinal dunes of Olympia Planitia can be unambiguously attributed to calcium-rich sulfates, most likely gypsum. These observations reveal that water alteration played a major role in the formation of the mineral constituents of the northern circumpolar lands [127].

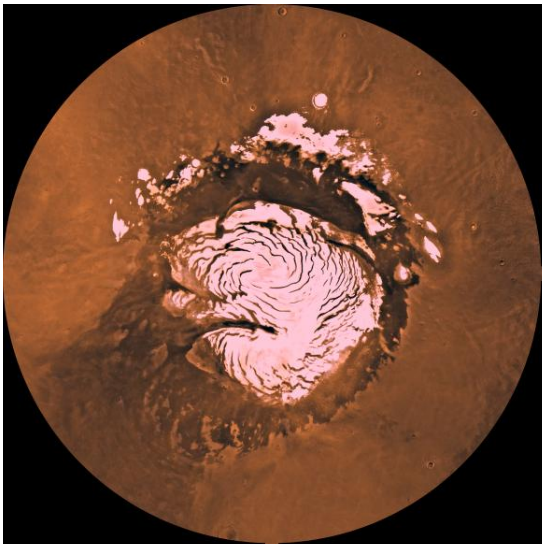

Figure 1.10: Mars north polar cap (Planum Boreum) photographed by the Viking orbiter.

Moreover, the temperature beneath the surface, at latitudes greater than about 60°, would allow the ice to remain like this throughout the year. In that case, these subsurface layers would form the equivalent of Earth *permafrost* layers [116]. Their explanation has theoretical basis: although the thermodynamic conditions currently prevent the existence of water in liquid form, it is probable that a different situation occurred in the past, when the internal activity released large amounts of water vapor in the atmosphere. The presence of grooves appears to indicate there was water flowing on the surface of the planet; further it would have penetrated into the ground and would form thick masses of underground ice. Another explanation is given by the observations: some impact craters are surrounded, not by spokes structures as those found when the impact takes place on rock or on dust, but by structures typical of an impact on a fluid. These characteristics have been interpreted as the result produced by a frozen, or even liquid, substrate: under the permafrost, porous rocks would contain large amounts of liquid water. So some areas of the Martian surface may form a several kilometers thick "hydrolithosphere".

Using the Gamma-Ray Spectrometer on board the Mars Odyssey, Boynton et al. [43] have identified two regions near the poles that are enriched in hydrogen, which indicate the presence of a subsurface layer enriched in hydrogen overlain by a hydrogen-poor layer. The thickness of the upper layer decreases with decreasing distance to the pole, ranging from a column density of about 150 grams per square centimeter at -42° latitude to about 40 grams per square centimeter at -77°.

Radar detection of subsurface ice on Mars has been widely debated even because the dielectric signature of ice, as deduced from the dielectric constant, can be confused with dry-silicate-rich materials. However, recent results by the MEX/MARSIS and MRO/SHARAD instruments provided important indications about the Martian permafrost [41]. The attenuation coefficient calculated from SHARAD data over the Deuteronilus Mensae region and Amazonis Planitia suggest that the two regions have different bulk compositions, with the former being ice-rich sediments and the latter being nonconsolidated volcanic deposits [41].

As well as for water, we assume the existence of traps also for the carbon dioxide. Even though it is the major component of air, the absolute abundance of $CO_2$ is very low if compared, for example, with the Venus one. In the past it was suggested the existence of a cycle, such as the one present on the Earth, where a significant fraction of carbon dioxide in gaseous form is trapped in surface rocks (as carbonates), after its liquefaction. On Mars, the first successful identification of a strong infrared spectral signature from surficial carbonate minerals of local scale ($< 10$ km$^2$) was made by the MRO-CRISM team [62]. Their spectral modeling identified a key deposit in Nili Fossae dominated by a single mineral phase that was spatially associated with olivine outcrops. Moreover, carbonates mixed with the martian soil materials were observed by PFS [163]. The materials that best reproduce the detected feature are Mg-rich carbonates (huntite [$CaMg_3(CO_3)_4$] and/or magnesite [$MgCO_3$]). The presence of carbonates is demonstrated in both bright and dark martian regions and the widespread distribution of carbonates supports scenarios that suggest carbonate formation occurred not by precipitation in a water-rich environment but by weathering processes.

Finally, the explanation of the low amount of $CO_2$ in the atmosphere of Mars can be found in a past gas escape from the planet, which reduced the atmospheric pressure, or even in a significant condensation occurred in the past on the permanent south polar cap, where still $CO_2$ would be in the form of not sublimable ice. If the water is now mostly locked in permafrost and $CO_2$ in the permanent south polar cap, we must determine where the Nitrogen is: or in N-rich rocks, or as bark in the permafrost water ice. Under Martian conditions, however, an efficient mechanism of trapping has to be discovered yet. It is possible that nitrogen escaped from the planet and it is also possible that the process of escaping affected all the volatile species, including $H_2$ O and $CO_2$.

The composition of the grains of "dust" on the surface of Mars was obtained for the first time by the mission Mariner 9, thanks to a Michelson interferometer (IRIS), which analyzed the Martian atmosphere. It obtained the infrared spectrum between 5 and 50 $\mu$m, with a spectral resolution of 2 $cm^{-1}$. From these measurements we found evidence of an intense absorption centered at about 1000 $cm^{-1}$, which was attributed to the presence of particles raised into the atmosphere during the dust storm of 1971-2. Therefore, attempts were made to reproduce the same effect with terrestrial minerals and it was found that the best result corresponded to a mixture of basalts and montmorillonite, a clay formed by a water induced alteration of silicates.

Although related to their individual points on the surface, the experiments carried aboard each Viking Lander led to important results. They analyzed samples by their X-ray emission, which is typical of the chemical composition. The soil is very similar in both sites of Viking 1 and 2, although these are very far apart. But anyway, we cannot conclude from this information that there is a considerable uniformity in the composition of Martian soil, because the two sites were chosen specifically for their similarities.

Figure 1.11: Picture of the Martian surface taken by the Viking 1 lander.

The main discovery is the importance of $SiO_2$ (45±5%) and $Fe_2O_3$ (19±3%). It is also important the high concentration of sulfur, which was unexpected: it is about one hundred times the concentration of sulfur in the Earth crust. On the other hand, the potassium is rare: it has been established an upper limit of 0.25%, about five times less if compared to its concentration in the Earth crust. Finally, we note that the density of the dust is $1.1 \pm 0.15$ g/cm$^3$, which indicates that its porosity is about 60%.

It is possible to build a mineralogical model of the dust using all these data. Its composition was compared with about one hundred of minerals and with many possible mixtures. The best fits are those obtained by mixing different kinds of clay, with montmorillonite $Si_2Al_4O_{10}(OH)_2 \cdot nH_2O$ as a base, mixed with nontronite (where part of Al is replaced by $Fe^{+++}$) and saponite (where Al is replaced by Mg).

The analyzes performed by the X spectrometer aboard the Pathfinder have only partially confirmed this suggestion. In fact, according to these data the abundances of magnesium and aluminium would be higher, while the abundances of iron, chlorine and sulfur seem to be lower. The rocks analyzed were similar to andesites, terrestrial materials derived from the fractionation of basalt in intrusive conditions. This discovery, therefore, has partially brought into question the nature of the mafic surface.

In June 2008, the Phoenix lander acquired data showing that the polar soil is slightly alkaline and contains vital nutrients as magnesium, sodium, potassium and chloride, all elements necessary for the growth of living organisms [13]. Moreover, in August 2008, the Phoenix lander conducted simple chemistry experiments, mixing water brought from Earth with the Martian soil to obtain its pH, and found traces of perchlorate salts. Their presence, if confirmed, would seem to make the soil more exotic (non-endemic) than believed before [46]. There are, however, necessary further tests to eliminate the possibility that the detection of perchlorates has been influenced by terrestrial sources which may have been transported by the probe, both in those samples and in the instrument [14].

The presence of clays on the surface of Mars can be explained in two ways: first, one can assume that the silicates are altered by the water, particularly in the form of vapor, that is, by the Martian atmosphere, and the reaction is accelerated by solar ultraviolet radiation. Similarly, one can assume we are dealing with the results of volcanic activity, which took place under a thick layer of ice. We know that a volcanic eruption under a glacier, causing a violent reaction between the iron-rich magma and the underground ice, can produce these kinds of minerals, as shown by the palagonite in Iceland.

The "ISM" instrument on board the Soviet spacecraft Phobos 2 obtained spectral images in the near infrared (0.8-3.2 $\mu$m) of selected areas of the Martian surface. Despite the premature end of the mission, the main geological units were mapped, most of them with a resolution of about 20 Km. The brightest regions, having an albedo higher of 30%, are covered with a homogeneous composition of reddish soil. It consists mainly of hydrated silicates: hematite is the most likely constituent. The darkest areas are dominated by Mg-Fe-rich minerals, mainly calcium clinopyroxenes, such as augite. This clearly indicates that the basaltic volcanism remained the dominant surface process. This is the case, for example, of the material located within the canyons, which is rich in these silicates, with a low water content. This contrasts with the bright plateaux, which are dominated by highly hydrated iron oxides. A clear mineralogical stratigraphy within the canyons is consistent with the deposition of sediments in an environment characterized by water floods.

Spectra provided by the NASA THEMIS probe showed the possibility of the existence of the olivine mineral on Mars by the study of the infrared radiation emitted by the planet. This mineral is found all over the planet, but the maximum abundance is in Nili Fossae, a region of estimated formation during the Noachian period. Another area in which the olivine is present in large quantities is the Ganges Chasma, a depression on the east side of Valles Marineris [139]. The discovery is interesting because the mineral, which is associated with volcanic activity, is much influenced by the effect of water, and so its presence and distribution, obtained by satellite measurements, might give us some information about the history of water on Mars.

Olivine and high-calcium pyroxene-rich regions are found also in deposits that span the age range of geologic units by the MEX/OMEGA instrument [154].

## 1.4 The Search for Organic Material

Scientists have long speculated about the possibility of life on Mars because of the proximity and similarity of the Earth planet, but in spite of the knowledge we have acquired until now, there are very different opinions. So, if life exists now on Mars, or existed in the past, remains an open question.

### 1.4.1 The Viking Experiments

On the contrary of observations made before the space missions, Mariner 9 proved the existence of surface formations that can be interpreted as the result of a water flow. Nothing more was needed to give a new impetus to theories predicting the organic evolution could have produced biological systems. Then, at the Viking program was given a primary objective: to find evidence of chemical evolution, or organic activity, even if fossil, on the surface of Mars. First, the detection of nitrogen in the atmosphere was considered as an indication that conditions were suitable for biological evolution. Each of the two landers had an arm, capable of collecting samples and place them in an experimental chamber, where they were analyzed and subjected to specific tests. The experiments were of two types: chemical and biological.

The chemical experiment lied in the analysis of soil by gas chromatography followed by mass spectrometry. The aim was to reveal complex organic compounds, considering only the carbon-based chemistry. The result was more than disappointing: it was not found any fragment of proteins or nucleic acids, and even hydrocarbons. This seems to indicate that the organic compounds, such as those originated from the fall of carbonaceous chondrites, for example, are rapidly destroyed by solar radiation.

The biological experiment was able not only to reveal organic matter, but to determine if there was metabolic activity in the sample. Seven experiments, including those performed in the dark, gave a positive result: some carbon was fixed by the samples, without the help of photosynthesis. The fixed quantities were infinitesimal, and this could explain why the chemical experiments did not reveal anything.

The other two experiments, known as the Gas Exchange and Labelled Release experiments, involved reactions of Martian soil with a nutrient medium based on water. They then required that the samples were placed in a pressurized and heated chamber, where the water could remain liquid. Immediately after the solution was introduced, were revealed large amounts of carbon dioxide and oxygen, but these decreased gradually with time. The explanation was soon evident: it was not a biological but a chemical reaction that was freeing carbon dioxide trapped in the soil, as well as for oxygen, which had been formed by the decomposition of peroxides by means of water vapor in the presence of iron compounds.

The Labelled Release experiment produced reactions between samples and simple organic compounds, in particular formic acid, where the carbon was radioactive ($^{14}$C). As found in the Gas Exchange experiment, the carbon dioxide was released at the start of the experiment. However, this production of $^{14}CO_2$ can be explained by the theory that the Martian soil contains peroxides: these react with formic acid, releasing carbon dioxide and water.

Similar experiments were carried out by the intruments aboard the following landers and rovers (Pathfinder, MER, Phoenix and Curiosity). By the light of all these experiments, it does not seem to be evidence of life on Mars, but this may also depend on the landing sites, which for safety reasons, were chosen in order to avoid hills and canyons. Therefore, it is not possible, at present, to put claims about the existence of biological activity on Mars without any ambiguity.

### 1.4.2 Meteorites

NASA has a catalog of at least 57 meteorites coming from Mars [15], which are very valuable because they are the only available physical samples of Mars. Speculation has grown just when the results of studies have shown that at least three of them may possess evidence of possible past life on the planet. Although the scientific evidence is reliable, its interpretation varies.

During the past decades eight criteria have been established for the recognition of past life in terrestrial geological samples. These criteria are [208]:

1. Compatibility of the sample geological context with past life.
2. Compatibility of the age and stratigraphic position of the sample with possible life.

3. Evidences of cell morphology in the sample.

4. Evidences of colonies in the sample.

5. Evidences of biomaterials that exhibit chemical or mineral imbalance.

6. Evidences of stable isotopes configurations unique in biology.

7. Presence of organic biomarkers.

8. If the sample characteristics are indigenous.

To generally confirm the past life in a geological sample, the criteria previously described should be all positive, or nearly all.

Among the most interesting findings of meteorites for the study of Mars, there is the meteorite ALH84001 (1.93 kg) [16] (Fig. 1.12), found in Antarctica in December 1984 by ANSMET project members. The sample was ejected from Mars about 17 million years ago and spent 11 thousand years in Antarctic glaciers. The analysis of its composition made by NASA revealed a kind of magnetite that on Earth is associated only with certain microorganisms [208]. Subsequently, in August 2002, another team of NASA published a study indicating that 25% of the magnetite in ALH84001 appears as small crystals of uniform size, which on Earth are associated only with biological activity, and that the rest the material appears to be normal inorganic magnetite. The extraction technique did not allow the verification of the chain structure typical of this kind of magnetite. The meteorite shows an indication of a secondary mineralization of water at low temperature and presents evidence of pre-terrestrial aqueous alteration. Has also been identified the presence of polycyclic aromatic hydrocarbons (PAH).

Some structures resembling the mineralized casts of terrestrial bacteria and their appendages ("fibrils") of ALH84001 have been found (Fig. 1.12). The size and shape of these objects is consistent with the fossilized terrestrial nanobacteria, but even the existence of nanobacteria is controversial.

In 1998, a team of NASA Johnson Space Center obtained a small sample of the Nakhla meteorite, fallen on Earth on June 28, 1911 in the town of Nakhla (Alexandria, Egypt) [26, 17], for its analysis. The researchers found stages of pre-terrestrial aqueous alteration and objects [174] having size and shape consistent with the fossilized terrestrial nanobacteria, which has been mentioned previously. The gas chromatographic analysis (GC) and mass spectrometry (MS) studied the high molecular weight of its polycyclic aromatic hydrocarbons in 2008, and NASA scientists concluded that about 75% of organic matter in Nakhla may not be associated with recent terrestrial contamination [149, 209].

This caused a growing interest in the meteorite, so that in 2006 NASA asked to obtain a larger sample from the London Natural History Museum, which preserves the meteorite. On this second sample a large dendritic carbon content was observed. When results and findings were published in 2006, independent researchers hypothesized that those carbon deposits were of biological origin.

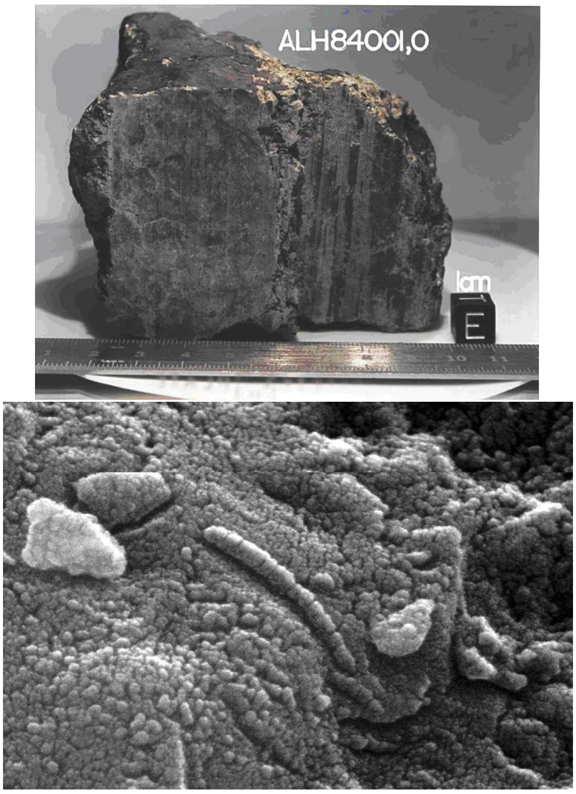

Figure 1.12: Photos of the meteorite ALH84001 (left) and micro-organisms found by NASA on it (right).

However, it must be emphasized the fact that the carbon is the fourth most abundant element in the universe, and moreover its finding into interesting structures cannot be considered an evidence of biological origin [209].

The Shergotty meteorite, a Martian meteorite of 4 kg, fell on Earth in Shergotty (India) on the 25th of August 1865 and it was almost immediately recovered by eyewitnesses. This meteorite is relatively young: it is estimated that it was formed on Mars only 165 million years ago by volcanic origin. It is composed primarily by pyroxene and probably it has undergone aqueous alteration for many centuries. Some interior features suggest that it is a remnant of a biofilm and that they are associated with micro-bacterial communities [208]. Even today scientists are carrying out analyzes of this meteorite in search of magnetites preserving indications of alteration phases.

## 1.5 Phobos and Deimos

Mars has two moons: Phobos and Deimos. They are both small objects and do not possess spherical shape, but they are approximately ellipsoidal, measuring 27x21x19 km and 15x12x11 km respectively for Phobos and Deimos. Discovered in August 1877 by Asaph Hall, their exploration mainly dates back to the American Mariner and Viking missions. Thanks to the latest we have high-resolution images of the two satellites, which reaches a few meters to

Phobos. Thanks to the Soviet mission Phobos (1989), infrared spectra of the surface with a spatial resolution of a couple of km were recorded, giving general information about the mineralogical composition of the satellite surface.

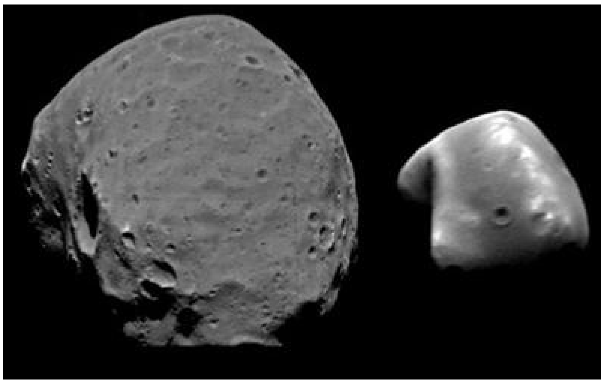

Figure 1.13: The Martian satellites: Phobos (left) and Deimos (right).

The orbits of Phobos and Deimos are circular, lie on the equatorial plane of Mars, and are directed. Their radii are 9354 and 23490 km, corresponding to orbital periods of 7 h 39 m and 30 h 18 m, respectively.

The tidal effects acting between Mars and its satellites have two main consequences:

1. The satellites are stabilized in *synchronous rotation*, ie, their rotation periods are equal to the orbital period around Mars: Phobos and Deimos always show the same face to Mars and their major axis point toward its center;
2. The equatorial "swellings" of Mars have a different symmetry axis with respect to the Mars-satellite axis. This is partially due to the high viscosity of the interior of Mars, and partly due to the fact that the Martian rotation period of 24 h 37 m is different from the satellites one. As a result, the gravitational force exerted on them is not strictly radial. In the case of Phobos, which orbits faster than Mars rotates (it rises on the west and sets on the east), the tidal component is equivalent to the braking force, and this inexorably causes the shortening of the Phobos orbit. In a couple of millions of years Phobos will crash into Mars. Deimos, on the other hand, makes less than a revolution in a rotation of Mars, and this produces a slow, but gradual increase in the radius of its orbit, similar to the effect that occurs in the Earth-Moon system.

The average density of the satellites is about 2 g/cm$^3$. It is therefore different from the Mars one, and probably reflects a difference in the overall composition. This also appears in the surface composition: Phobos and Deimos have a very low albedo (about 5%), lower even than the darker lunar surface albedo. They appear to be dominated by the presence of opaque and carbon rich minerals, similar to the matrix found in carbonaceous chondrites, the most primitive meteorites.

There is general agreement on the theory that Phobos and Deimos should have had different origins respect to the Mars one: they would not have been formed from the growth in orbit of material similar to that which gave life to Mars. They would be objects from the family of asteroids (more precisely, C-type asteroids, which are numerous in the outer main belt and among Apollo-Amor objects) that were finally captured by Mars.

The surfaces of both Phobos and Deimos are covered by *regoliths* and they are characterized by meteorite impact craters. Their density allows us to date the satellites back to more than three billion years. But there are several differences between the two satellites. The thickness of the regolith is distinctly larger (more than 200 m) on Phobos then on Deimos. Phobos has two large craters, *Stickney*, 10 kilometers in diameter, and *Hall*, 6 km in diameter. The diameter of Stickney is more than a third of the entire satellite. The effects of the impact responsible for this crater can be seen in a series of grooves, long many hundreds of meters and occasionally twenty meters deep, which cover a large part of the surface. Deimos shows contrasts in the albedo on small-scale and rock blocks not observed on Phobos.

A IR spectral image, taken by the ISM instrument, from a distance of 200 km gave some indications about the Phobos mineralogy. This covers part of the satellite at a resolution of 700 m. The surface is dark and very dry, and, mineralogically, is highly homogeneous. The bottom of a crater shown in the image reveals a different composition with an increased value of pyroxene. This is a strong indication that, despite its small size, this object has undergone some degree of internal metamorphism in the past.

Recently, PFS/MEX and TES/MGS observations of Phobos in the thermal infrared [91] showed several spectral features that can be used to investigate the composition of the surface. Results show that the majority of the spectra are consistent with the presence of phyllosilicates, particularly in the area northeast of Stickney. The PFS and TES analyzed spectra are also consistent with the presence of tectosilicates, especially feldspars/feldspathoids, in an other region of Phobos. Comparison of the TES and PFS data to the meteorites shows that no class of chondritic meteorites provides significant agreement with the spectral features observed. The lack of consistency of the PFS and TES spectra to analogs of ultraprimitive materials (organic residues) suggests that an origin via capture of a transneptunian object is not supported by these observations, although it cannot be completely ruled out [91].

Finally, the origin and evolution of these satellites, their degree of internal differentiation, and the presence of carbon compounds and water are some of the scientific issues to be still resolved.

# Chapter 2

# The Martian Atmosphere

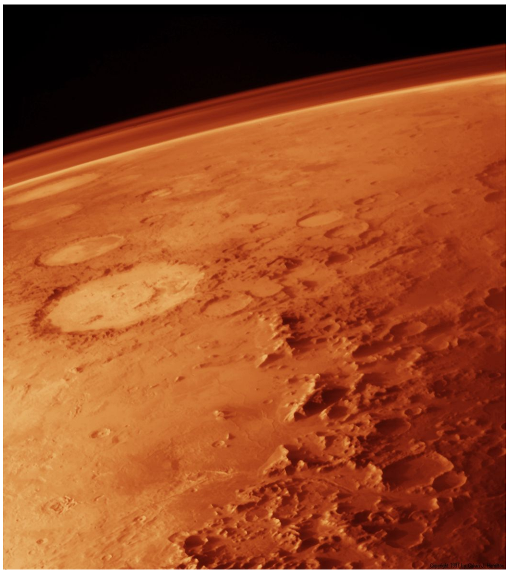

Figure 2.1: Picture of the Martian atmosphere taken by the Viking orbiter in low orbit.

The past decade has experienced a huge increase in the amount of data received from Mars. The success of many missions to the planet, including Pathfinder, Mars Global Surveyor (MGS), Mars Odyssey, Mars Express, Mars Exploration Rovers (MERS), and Mars Reconnaisance Orbiter (MRO), which followed the previous missions Mariner 9 and Viking, allowed to examine the surface and atmosphere of Mars with unprecedented details. Although there is still a lot to understand, it is possible with data we have now, to draw a reasonable framework of the present climate of Mars.

The main interesting quantities in the characterization of the Martian current atmosphere are the pressure, atmospheric temperatures, the wind speed, the optical depth of aerosols and their physical characteristics, and the abundances of the gases that constitute the atmosphere. All these quantities vary with time and place. Furthermore, with regard to the abundances of atmospheric gases, we must also take into account the influence of photochemical processes which normally occur in the Martian atmosphere. The goal of the observations, from satellite and Earth, is to quantify the spatial, diurnal, seasonal, and interannual variations. Once the current atmospheric state has been characterized, the data can be used together with models for understanding the physical processes that control the climate on Mars, such as the mechanisms for dust storms, the role of clouds, and the interactions between the local and global phenomena, between the surface and atmosphere.

This Chapter describes the general charateristics and summarizes the current state of the Martian atmosphere below 60 km, as observed by the spacecraft mentioned above. Moreover, the atmospheric photochemistry on Mars involves many minor species gases and may alter their concentrations in certain conditions. Therefore, since the aim of this work is to study the distribution of water vapor and carbon monoxide, and they are strictly bound by photochemical reactions which guarantee the stability of the atmosphere, then we will describe the currently accepted photochemical model of the Martian atmosphere (nominal model), together with the contribution of observations, which strive for verifying this model.

## 2.1 General Characteristics

Mars lost its magnetosphere about 4 billion years ago, allowing the solar wind to interact with the Martian ionosphere and keeping the atmosphere thinner than it was in the past only because of the escape of molecules from the outer layers. Both Mars Global Surveyor and Mars Express have detected these atmospheric ionized particles into the space in the wake of Mars [168, 133].

Before the space age, estimates of the atmospheric pressure on Mars, based on the sunlight diffusion, gave values close to 100 millibars. Carbon Dioxide ($CO_2$), which was revealed spectroscopically from Earth, appeared to be a minor component. The Mariner 6, 7, 9 missions determined the total pressure by means of the radio waves occultation as they passed behind the planet, and discovered that the atmosphere consists of almost pure carbon dioxide. Today we know that it is more than 95% of the atmosphere and the mean pressure on the surface is about 6 millibars. The main constituents of the lower atmosphere are summarized in Table 2.1.

The abundance of water may seem very low. This is the result of very low temperatures found on the surface of the planet. In the phase diagram of water, the triple point is located at $T = 273$ K and $P = 4.6$ mm Hg (6.1 millibars). Under Martian conditions, therefore, liquid water can not be found if the partial pressure of $H_2O$ is less than 4.6 mmHg. Currently, the maximum partial pressures of water does not reach the value of 0.5 mmHg: then, water can only exist as vapor or as ice, based on the temperature.

Because of the low content of $O_2$, a very small (about 0.04 ppm) amount of ozone $O_3$ is present. So the Martian atmosphere is highly transparent to the solar ultraviolet radiation. A direct consequence is the presence of a significant atmospheric photochemistry. The most abundant components, $CO_2$ and $H_2O$, are partially dissociated into $CO + O + OH$ and H respectively. The molecular oxygen is generated mainly by the recombination of individual atoms of oxygen.

| **Gas** | **Volume Abundance** |
|---|---|
| $CO_2$ | 95.32 % |
| $N_2$ | 2.7 % |
| Ar | 1.6 % |
| $O_2$ | 0.13 % |
| CO | 0.07 % |
| $H_2O$ | 0.03 % (a) |
| Ne | 2.5 ppm |
| Kr | 0.3 ppm |
| Xe | 0.08 ppm |
| $O_3$ | 0.04÷0.2 ppm (a) |

Table 2.1: Composition of the lower Martian atmosphere [160].
(a) Mean value, because it strongly varies with seasons and latitudes.

Since abundances of CO and $O_2$ actually observed are low, the mechanism that creates $CO_2$ from the CO should be very effective in Martian conditions. It has been suggested that OH radicals play a role in this reaction, assuming the existence of a vertical transport mechanism capable of ensuring a rapid mixing, as the distribution profiles of $CO_2$ and of the $H_2O$ are probably different. Furthermore, in the study of atmospheric photochemistry we must take into account the presence and distribution of aerosols, which play an important role in the mixing phase whereby these chemical reactions can take place.

As we mentioned previously, although the carbon dioxide is the main atmospheric component, it can be found also in the form of carbonates in the rocks of the surface. The same could be said for the other atmospheric gases such as nitrogen and water. In fact we already discussed the possible presence of a layer of subsurface permafrost. However, we must also consider the possibility that part of water vapor escaped from the atmosphere going into the space, as happened to Venus.

Concerning the noble gases, helium is not gravitationally held and, apart from the argon, the others are present only in small quantities: Ne (2.5 ppm), Kr (2.5 ppm) and Xe (0.08 ppm). Their elemental and isotopic abundances are important tracers of the Martian atmosphere evolution, and of the whole planet.

Variations of the surface temperature are considerable, considering the low mass of the atmosphere and the absence of heat "reserve", which instead are provided by the oceans on Earth: the temperature may vary more than 50°C between day and night at the sites of Viking 1 and 2. Generally, the climate of Mars is cold: the temperature can droop up to -120°C at the south pole during winter, and rise up to about 0°C only near the equator during summer, while, because of the strong greenhouse effect, due to dust, during the large global dust storms, the atmospheric temperature may rise even up to 40°-50° C.

The Martian atmosphere undergoes large changes in climate over a year, which are strongly dependent on latitude. In fact, the dynamic properties of

Mars are significant because of the large obliquity of its rotation axis (25.1°) and of the large eccentricity (0.0934). As a consequence, the Martian year (which lasts 669 Martian days, or 687 Terrestrial days) is divided by very marked seasons, and these do not have equal length, because of Kepler's Third Law. In the northern hemisphere, spring, summer, autumn and winter, respectively, last 194, 178, 143 and 154 Martian days. The highest temperature is reached during the southern hemisphere summer, because then the distance from the Sun is minimal. On the other hand, this season is shorter than the northern hemisphere one, where it lasts 24 Martian days more.

Studies conducted by J. Lasker and his colleagues on the behavior of the orbital motion of Mars reveal that its obliquity is still subject to a chaotic regime and varies from 0° to 60° on a couple of million years. The present value of 25.1 ° is neither primordial nor stable. Obviously, these changes result in climate dramatic changes.

The dynamic properties of Mars are correlated with significant temperature and pressure variations, causing precipitation of ices (water and carbon dioxide snow) or their vaporization. Clouds, which are formed differently during the seasons, are the direct effects of these processes. Frozen fog formations cover the polar caps during the winter, while during the summer the formation of clouds is rather confined in reliefs (like the top of volcanoes). Clouds of water ice were photographed by the Opportunity rover in 2004 [18]. The atmospheric pressure can vary up to 30% in a year, because of condensation and sublimation of $CO_2$ in the south polar region. Strong winds sweep the surface with measured velocities of hundreds Km/h (with maxima up about 400 km/h) and develop cyclones and anticyclones (high and low pressure systems, respectively). Storms raise large amounts of dust in the atmosphere, carrying them up to altitudes of about 50 km. In turn, this dust affects the Martian meteorology by increasing the atmospheric opacity. Precipitations of water and carbon dioxide, in addition, occur with the dust settling, a phenomenon mostly notable on the polar caps.

The minor compounds of the Martian atmosphere are shown in Table 2.2.

| **Gas** | **Retrieval Spectral Band ($cm^{-1}$)** | **Concentration (upper limit in ppmv)** |
|---|---|---|
| $C_2H_2$ | 729 | 0.002 |
| $C_2H_4$ | 1443 | 0.5 |
| $C_2H_6$ | 821 | 0.4 |
| $CH_4$ | 1306 | 0.02 |
| $N_2O$ | 1258 | 0.1 |
| $NO_2$ | 1621 | 0.01 |
| $NH_3$ | 968 | 0.005 |
| $PH_3$ | 1122 | 0.1 |
| $SO_2$ | 1362 | 0.1 |
| OCS | 859 | 0.01 |

Table 2.2: Minor compounds of the Martian atmosphere [136].

The PFS/MEX team revealed the presence of methane in the Martian atmosphere with a concentration of about 10 volume ppb [83, 19]. Since methane is an unstable gas, because it is destroyed by the ultraviolet radiation, it typically remains in the Martian atmosphere for about 340 years [35]. Therefore, its presence would indicate a recent or current gas source on the planet. Volcanic activity, cometary impacts, and the presence of methanogenic bacterial life forms could be possible sources. It was recently pointed out that methane can also be produced by a non-biological process called "serpentinization[1]", which involves water, carbon dioxide, and the olivine mineral, very common on Mars [180].

## 2.2 Surface Pressure

The surface pressure provides a direct indication of the integrated air mass on the atmospheric column. It was measured in situ using the sensors on board the Viking [201] and Pathfinder landers [179], and by the abundance retrieval of the $CO_2$ column by orbital measurements. Thanks to their accuracy, frequent sampling, and longevity, the data collected from the pressure sensors aboard the two Viking landers provide the most complete picture of the surface pressure variation at a given place, allowing the study of variations on time scales ranging from hours to years.

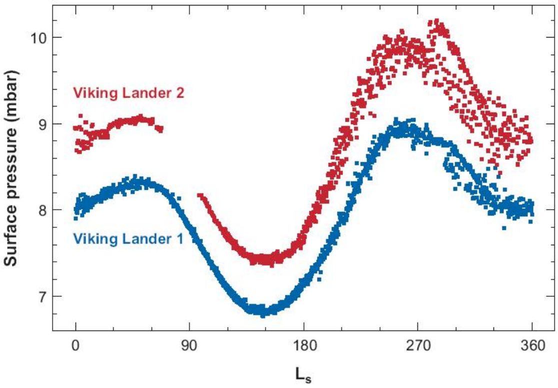

Figure 2.2: Daily averages of surface pressure recorded by the two Viking landers.

The figure 2.2 shows the daily averaged surface pressure recorded by the two Viking landers. The offset between the two curves is due to the altimetry difference between the two sites (approximately 1.2 km). In the course of a Martian year, the surface pressure varies up about 30%, decreasing when the $CO_2$ condensation on the seasonal ice cap at the winter pole, and increasing when the $CO_2$ sublimates from the same pole during summer. The variations

---

[1] Hydrothermal process in which magnesium-rich silicate minerals are converted to or replaced by "serpentine minerals". There are many serpentinization reactions. The reaction that produces methane from the olivine can be written (in a balanced form) as: $18Mg_2SiO_4+6Fe_2SiO_4+26H_2O+CO_2 \rightarrow 12Mg_3Si_2O_5(OH)_4+4Fe_3O_4+CH_4$.

overposed on the annual cycle are the result of progressive atmospheric waves, similar to the passage of storm systems on Earth [131]. These waves are most prominent in autumn and winter. The diurnal and semidiurnal thermal tides cause additional variations in the surface pressure over timescales of a day or less. It was observed the amplitude of the tides increases significantly during the great dust storms [216].

The $CO_2$ absorption band in the near infrared, centered at 2.0 $\mu$m, as well as many other minor bands, is suitable for the retrieval of the $CO_2$ column abundance, and it is covered by the Mars Express OMEGA and PFS instruments [192, 96] and the MRO CRISM instrument [190] spectral ranges. Since the 95% of the Martian atmosphere is composed by $CO_2$, the column abundance of this atmospheric component can be used as a reasonable indicator of atmospheric pressure.

OMEGA reflectances in the $CO_2$ absorption band at 2 $\mu$m were used to retrieve a hydrostatic estimation of surface pressure with a precision sufficient to draw maps of this field and thus analyze meteorological events in the Martian atmosphere [192]. Their observed three main phenomena in the resulting OMEGA surface pressure maps: horizontal pressure gradients, atmospheric oscillations, and pressure perturbations in the vicinity of topographical obstacles [192].

## 2.3 Atmospheric Temperature

The atmospheric temperature is one of the fundamental quantities because it describes the state of the atmosphere, and it has been studied using a considerable number of different observational techniques.

### 2.3.1 Thermal Infrared Profile

The most widely used technique to retrieve the atmospheric temperature is the analysis of the $CO_2$ thermal infrared band at 15 microns. The variation in the known optical depth as a function of the frequency for the band is used to probe atmospheric temperatures at different levels. This approach to derive profiles of atmospheric temperature has been used on the thermal infrared spectra acquired by the following instruments: IRIS Mariner 9 [58], MGS Thermal Emission Spectrometer (TES) [59], Mars Express Planetary Fourier Spectrometer (PFS) [96], and MRO Mars Climate Sounder (MCS). The typical vertical range of sensitivity spreads from the surface to approximately 40-50 km with a nadir view, and up to 65-90 km with limb observations. The typical vertical resolution is approximately half "scale height" of pressure (about 5 km [57]).

The advantage in obtaining the infrared thermal profile is related to the possibility of acquiring spectra systematically on a global scale by an orbiting spacecraft. Currently, the PFS/MEX instrument provided the best single data set available: so far it has already provided, with excellent spectral resolution, an almost global coverage of atmospheric temperatures for more than six Martian years (since January 2004). Another important data set is provided by the TES instrument [186], but its coverage is restricted to only two different local times (about 2:00 am and about 2:00 pm) on daily basis for almost three Martian years (from March 1999 to August 2004).

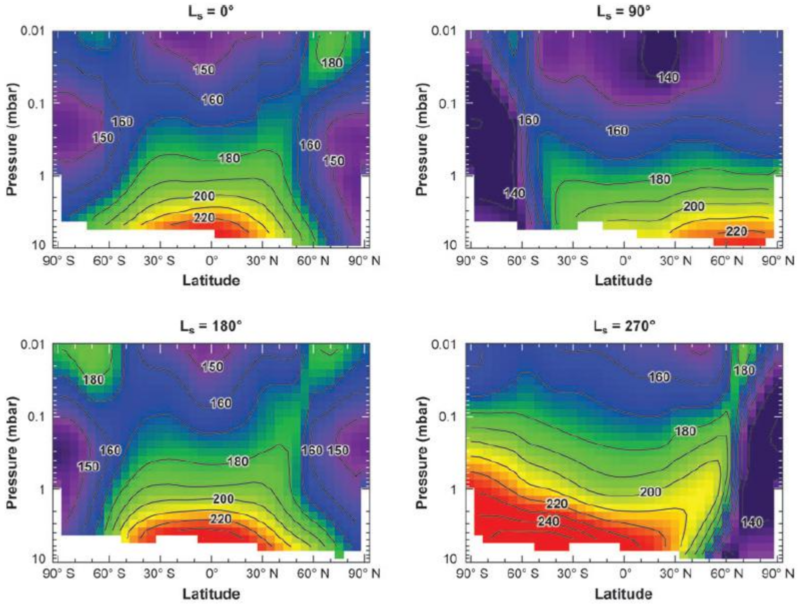

Figure 2.3: Daily temperature averages (acquired approximately at 2:00 pm in local time) as a function of latitude and pressure (or height above the surface) as observed by TES for four different seasons. The upper limit of 0.01 mbar corresponds approximately to a height of 65 km above the surface.

In Figure 2.3, temperatures are generally far from the radiative equilibrium, a fact which indicates a strong modification of the thermal structure because of the effect of dynamic processes. Under the conditions present at the solstice (Ls = 90° and 270°), the strong solar heating occurs at the summer pole, and near the surface temperatures reach their peak. In the summer hemisphere, temperatures increase toward the pole in all the layers. In the winter hemisphere, there is a very strong temperature gradient with latitude between the adiabatically heated local maxima caused by motions to the lower atmosphere and by the very cold temperatures of the polar night. The latitudinal position of this polar front has a characteristic inclination and this causes a temperature inversion at altitudes below the level corresponding to 1 mbar in mid-latitudes regions, where the cold polar air is carried toward the equator near the surface. Because of the strong eccentricity of the Mars orbit around the Sun, the duration of the perihelion (Ls = 252 °) near the winter solstice of the northern hemisphere (Ls = 270 °) causes a latitudinal temperature gradient significantly greater in the north than in the south. This also leads to generally warmer temperatures during the summer in the southern hemisphere than in the northern hemisphere.

The thermal structure during the two equinox periods (Ls = 0 ° and 180 °)

is similar in both cases and it is almost symmetric about the equator: warmer temperatures are close to the surface at the equator, and in each hemisphere, they decrease toward the pole at an altitude lower than about 0.3 mbar (30 km). Above this pressure level (up to at least 0.01 mbar), there is a minimum temperature at the equator and a maximum temperature at the middle-high latitudes in each hemisphere.

Daily and on a global scale monitoring of atmospheric temperatures, made possible by the asynchronous observations of TES, shows a variety of waves, which play an important role in the horizontal and vertical transport of heat, of the moment, and of atmospheric constituents such as aerosols and water vapor [28, 29]. In addition, the observed temperature variations can be caused by planetary wave, solar thermal tides, and by the interaction of the atmosphere with the topography of Mars.

### 2.3.2 Occultation Observations

The radio occultation experiments work by monitoring the signal sent from a spacecraft when it passes behind a planet as seen from Earth. In both input and output points, the signal passes through the atmosphere, which causes a slight refraction of the beam, thus producing a Doppler shift in the observed frequency. This information can be used to determine the refractive index of the atmosphere as function of the height, which can be converted to temperature since we know the atmospheric composition and we assume the hydrostatic equilibrium.

MGS [103] and MEX/MaRS [165] performed radio occultations of Mars. Their temperature profiles cover a vertical range going from the surface to about 45 km, with a vertical resolution of approximately 500 m. Since radio occultations technique provides data with a better vertical resolution than data obtained using the thermal infrared spectra, it is especially useful for probing the temperature near the surface and to resolve the vertical structure of waves. The disadvantage of the thermal profiles obtained by radio occultations is their relatively poor spatial and temporal coverage, which is limited to times and places where the orbital geometry allows the spacecraft occultation.

The Figure 2.4 shows the temperature profiles derived from MGS radio occultations. In the afternoon (red profiles), the temperatures are closely in agreement with the TES results if convoluted with the vertical resolution of infrared thermal profiles [106]. During the night (blue and violet profiles), the upper vertical resolution of temperature profiles obtained by radio occultations allows the characterization of an inversion layer near the surface, which does not appear in the TES profiles. A couple of radio occultation profiles show large amplitude waves (violet profile), which can be caused by the presence of water ice clouds [107].

The stellar occultation, where a satellite sees a star disappear and reappear behind the limb of Mars, has been used to derive the temperatures in the middle atmosphere (50-130 km) using UV observations made by the SPICAM instrument on board Mars Express [172]. They showed that accurate

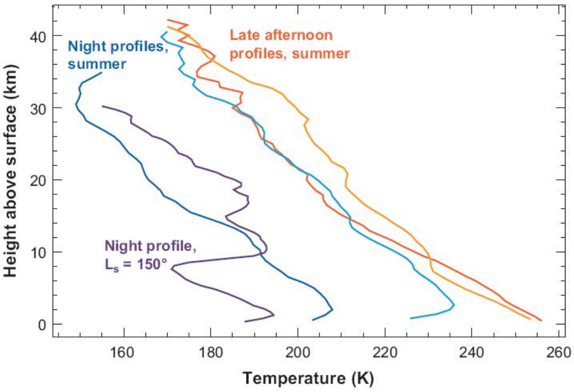

Figure 2.4: Temperature profiles as a function of height above the surface as derived from MGS radio occultation data. The temperatures in the late afternoon are shown for the southern mid-latitudes in summer. The temperatures at night are also shown for the mid-latitudes during the summer. The night profile shows big waves when it is close to the Tharsis volcanoes for Ls = 150°.

temperature profiles can be obtained below 110 km from the vertical profiles of density. Below 50 km, profiles are very uncertain due to the preponderance of aerosol extinction [172].

### 2.3.3 Profiles by Landers and Boundary Layer

Seven different spacecrafts landed successfully on Mars. Each of them carried accelerometers able to measure the air resistance during their descent through the atmosphere. These measurements, known the aerodynamic properties of the spacecraft, allow to obtain the density, and thus the temperature as a function of the height. The five profiles acquired by the Viking 1 and 2 [181], Pathfinder [135], and MERS Spirit and Opportunity [214] landers show large amplitude oscillations growing with height (except for Spirit), which are typical of the vertically propagating waves.

The observations of atmospheric temperatures by orbit provide a helpful perspective on large-scale thermal structure, but even the radio occultation observations do not have sufficient vertical resolution to characterize the details of the so-called "planetary buondary layer" (PBL) near to the surface. The PBL is important because it is a portion of the atmosphere that interacts directly with the surface, undergoing influences due to effects such as friction and surface heating. The temperatures of the PBL were measured directly using thermocouples mounted on the Viking landers [102] and Pathfinder [179], and they were derived by thermal infrared spectra acquired by the MER Mini-TES instrument [187, 191].

Both the thermocouple measures and the temperatures obtained using thermal infrared spectra show a significant diurnal structure (Fig. 2.5). The atmosphere is cold and stably stratified before dawn. Just after this, it is established a superadiabatic vertical temperature gradient in the first 100 m of

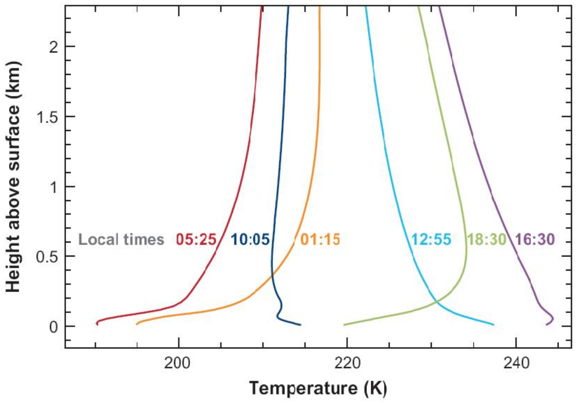

Figure 2.5: Atmospheric temperatures as a function of height above the surface for different times of day derived from the observations made by Mini-TES instrument aboard the MER Spirit rover.

atmosphere until mid-morning. This establishes a regime of turbulent convection for all this lowest layer, with fluctuations in temperature from 15 to 20 K recorded in the first meter above the surface and up to 5 K in the first 100 m on time scales of 30-60 s. The turbulent convection continues until late afternoon (about 16:30), when the surface becomes colder than the atmosphere close to it, the convection ends, and the temperature gradient near the surface is reversed. The reversal grows during the night, reaching a depth of at least 1 km before reversing again in the morning.

## 2.4 Water Vapor and Other Trace Gases

Although few abundance retrievals of water vapor were made using data acquired by the first missions, as the IRIS instrument aboard Mariner 9 [58], the first definitive description of latitude and seasonal trend of water vapor was derived by the MARS ATMOSPHERIC WATER DETECTORS (MAWD) onboard the Viking orbiter [113]. These data showed an average global and annual column abundance of about 10 precipitable microns of water vapor, with higher values on the northern hemisphere during summer, reaching a maximum of about 75 precipitable microns[2] near the north pole for Ls = 120°. The MAWS experiment observed the absorption bands of water vapor in the near infrared at a wavelength of approximately 1.4 microns. Scattering by areosols (dust and ice) is important to these wavelengths and it must be carefully taken into account to obtain valid abundances values for the water vapor [75]. Observations of the water vapor abundance by the first spacecraft were also provided by Phobos [176] and Pathfinder [202].

One of the best descriptions of the spatial and seasonal trend of water vapor is provided by the thermal infrared spectra acquired by TES [185], although it was necessary to correct the obtained values by about 30%, when compared

---

[2] The *precipitable micron* is a unit of column number density equal to $3.34 \cdot 10^{18}$ cm$^{-2}$.

with those obtained with PFS, which also has a higher spectral resolution. The rotational bands of the water vapor observed by TES at a wavelength of approximately 30 $\mu$m are much less affected by aerosols than those in the near infrared, and the long (almost three Martian years) and systematic coverage of TES allows the analysis of variations on interannual time scale. The retrievals of the column abundance of water vapor show a seasonal dependence similar to the one obtained from the data of MAWD, but with a generally little lower abundance, and the addition of a relative maximum of water vapor in the southern hemisphere near the pole during summer, probably hidden by the large dust storms during MAWD observations. The summer season peak in the water vapor column abundance is twice as high in the north than in the south.

The column abundance of water vapor annually averaged as observed by TES is shown in Figure 2.6. There is an apparent anticorrelation with the topography. The depressed areas, such as the Hellas Basin (45°S, 290°W) and almost the entire northern hemisphere, have higher abundance because there is more atmosphere over these areas. The latitudes band between about 10°S and 40°N has a relatively high average because water vapor is held there during a year, while further north and south there are significant portions of the year with very little water vapor content. There is also a significant positive correlation between the abundance of water vapor and the albedo surface: brightest areas have a greater quantity of water vapor. There is a negative correlation with the thermal inertia, which indicates that the properties of the surface, as the grains size, contribute to the water vapor distribution.

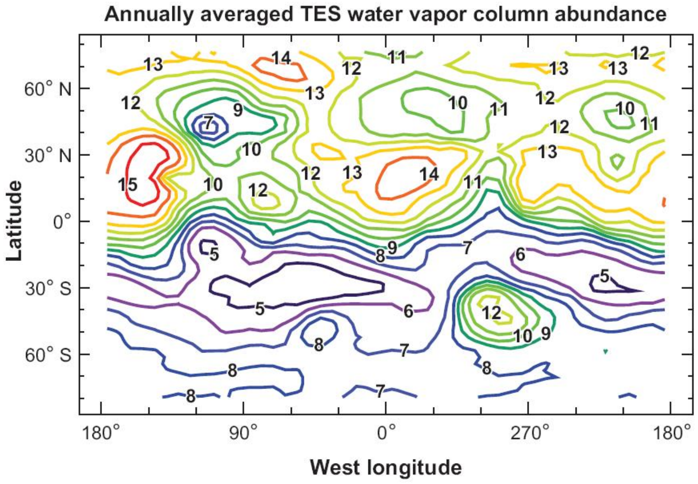

Figure 2.6: Map showing the spatial distribution of the water vapor column abundance annually averaged (in precipitable microns) as observed by TES.

The seasonal asymmetry in the condensation height allows the water vapor transport by means of the "Hadley Cells" through the equator from south to north during the perihelion season [50]. It results in a more uniform latitudinal distribution of the water vapor during the perihelion season, and a steep latitudinal gradient in the water vapor content during the aphelion, with the formation of a cloud band of water ice at low latitudes, where the water vapor condenses.

The water vapor continues to be an issue of great interest in the observations from the current satellite. Mars Express has three instruments able to retrieve the abundance of water vapor. As TES, the PFS instrument on board Mars Express observed water vapor in the thermal infrared [86] and also in the near infrared [204, 183], whereas the OMEGA [145] and the SPICAM [76] instruments observed it in the near infrared. On board MRO, both CRISM (near infrared) and MCS (thermal infrared) are currently monitoring the water vapor. Also the MER Mini-TES instrument can retrieve the integrated column of water vapor from the surface [187]. All these instruments measured the water vapor annual cycle. The maximum value of $H_2O$ abundance they observed is about 60 pr.$\mu$m over the sublimating northern polar cap, whereas the mean annual and global abundance is around 9.5 pr.$\mu$m. Moreover, two local maxima was observed in the geographical water vapor distribution around the Tharsis and Arabia Terra regions.

Most of the work characterizing the trace gas was made using Earth-based telescopes because the spectral resolution of these instruments is typically much larger than the one of instruments carried by spacecraft [65]. However, the satellite observations have also been used for the characterization of this type of gases. The mass spectrometer on board the Viking measured the amount of nitrogen and argon, and identified the krypton, xenon, and neon [161]. In 1977 Maguire [136] used the spectra acquired by the IRIS Mariner 9 instrument to put constraints on some trace species.

The gases (apart from water vapor) most commonly studied by spacecraft observations have been the carbon monoxide (CO), ozone ($O_3$) and methane ($CH_4$). Carbon monoxide has absorption bands in the near infrared, which were used by a multitude of instruments including Phobos ISM [176], Mars Express PFS [38, 183] and OMEGA [68], and MRO CRISM [190] to study its abundance. The retrievals show an abundance of about 700 ppm, with seasonal and geographical variations. Ozone has been observed by UV wavelengths by the Mars Express SPICAM [167], and MRO MARCI instruments. These measurements found that ozone presents large seasonal and spatial variations and they are anticorrelate with the water vapor abundance. The MRO CRISM observations in the near-infrared of the $O_2$ singlet delta have been used as tracer for ozone, as the $O_2$ singlet delta is an excited state of oxygen, which is produced by photodissociation of ozone.

Recently, the detection of methane in the atmosphere of Mars has generated great interest because of the possibility of its biological origin. Ground-based observations [123, 153] indicate an abundance of about 10 ppb evenly distributed, which would be inexplicable in view of the life time (about 300-600 years) of methane on Mars. Using Mars Express PFS instrument, thanks to its good spectral resolution and signal to noise ratio suitable for detecting a signal so weak, Formisano et al. [83] reported evidence of a 0-30 ppb spatial variability in the detection of methane. Then, Geminale et al. [88] observed an increase of methane over the north polar cap during local summer, which cannot be explained by global circulation. This strongly suggests that there could be a methane reservoir associated with the polar cap. Clearly, this is a key issue in the space exploration and this will be very important for future spacecraft with instrumentation specifically designed to measure the methane abundance.

The work of this thesis will improve our knowledge about annual cycle of the water vapor and carbon monoxide and their spatial distribution in the Martian atmosphere. Since the CO is a non condensable gas, its behaviour is common to all the non condensable gasses and therefore it can be used as a tracer for the distribution of other species by means of the atmospheric dynamics.

## 2.5 Annual[3] Variability of Martian Atmospheric Parameters

An overview of the latitudinal and seasonal variation of temperature at 0.5 mbar (about 25 km in altitude), the optical depth of aerosols (dust and water ice), and the abundance of water vapor as observed by MGS TES is shown in Figure 2.7. Here almost three Martian years of observations are shown, since March 1999 to August 2004. The current Martian climate has a distinct and generally repetitive dependence by season, latitude, and longitude. In particular, the perihelion season (Ls = 180° - 360°) is relatively warm, dusty, and free of water ice clouds. On the contrary, the aphelion season (Ls = 0° - 180°) is relatively cold, cloudy, and dust free. The water vapor abundance is greater near the equator in both hemispheres during the summer. The perihelion season shows a high degree of variability in the interannual atmospheric temperature and in the dust optical depth, primarily associated with the nature of interannual events such as the global dust storms. The aphelion season shows a relatively small interannual variability in temperature and aerosols optical depth. The figure 2.8 shows the globally averaged daily temperatures at a pressure level of 0.5 mbar depending on the season (Ls) as observed by the Viking IRTM, MGS TES, and Mars Odyssey THEMIS instruments. The globally averaged temperatures follow a well-defined seasonal cycle. The annual minimum is close to Ls = 40°, so before the aphelion (Ls = 71°), at a temperature of approximately 165 K (at 0.5 mbar). Temperatures are usually very repetitive during all the aphelion season, with temperature differences from year to year within the measurements uncertainties. The perihelion season shows large differences in temperature from year to year. These differences, associated with the intermittent events of global dust storms, may be of 20 K or more. Excluding the effects of large dust storms, atmospheric temperatures globally averaged (at 0.5 mbar) have a peak of approximately 200 K at about

---

[3] When making comparisons between observations taken at different years, it is useful to use the numbering system of the “Martian Year” according to the calendar proposed by R. Todd Clancy [53]: Martian Year 1 (MY1) begins (at a time such that Ls=0) on April 11th, 1955.

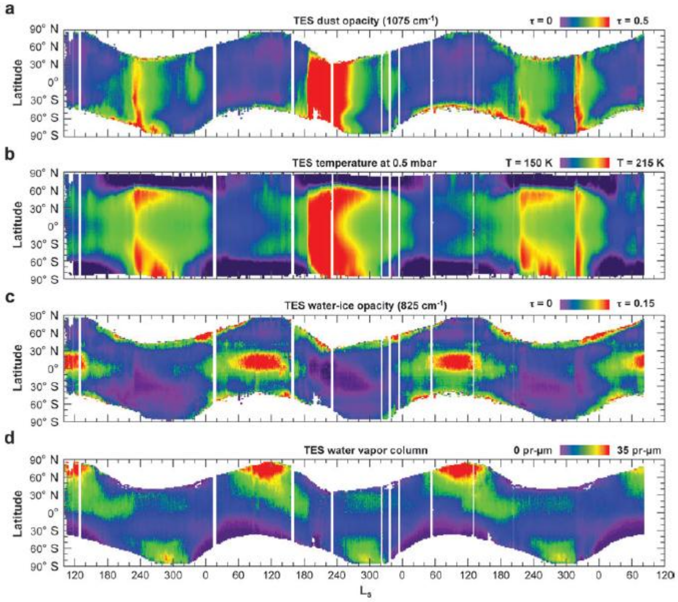

Figure 2.7: Overview of the atmospheric daytime observations of TES showing the seasonal and latitudinal variation of (a) dust optical depth (at a wavelength of 9 $\mu$m), (b) atmospheric temperatures (K) at 0.5 mbar (about 25 km), (c) water ice optical depth (at a wavelength of 12 $\mu$m), and (d) of water vapor column abundance (in precipitable microns). The data lacks (vertical white stripes) were caused by spacecraft anomalies and solar conjunctions.

Ls = 260°, giving a peak to peak annual interval of approximately 35 K.

The presence of the largest dust storms seems to be periodic, in fact in Figure 2.7 a certain seasonal and positional preference can be noticed, and it is also observed a tendency to have a global dust storm every two Martian years during the southern summer. The dust optical depth appears to have a background of approximately 0.15 at 9 $\mu$m during the perihelion season. Overlapped to this background level there is a series of dust storms, which vary strongly in intensity and duration. Periods near Ls = 225° and 315° appear to be particularly favorable for the formation of dust storms on regional scale [132]. After Ls = 0°, the dust optical depth gradually decreases until the minimum level of 0.05 for Ls = 135°, after which the global optical depth of the dust begins to increase again. The aphelion season shows a much less interannual variability, and no dust storm on regional or global scale.

The water ice optical depth at low latitudes is quite anticorrelated with the dust optical depth, with maximum values in the aphelion season around Ls = 110° and low values during the perihelion season. The tropical cloud belt formed during the aphelion season (Fig. 2.7) is repetitive from year to year, with clouds forming over the same regions with approximately the same optical depth. At high latitudes, the clouds form over the winter polar regions with similar structures every year.

The greatest interannual variation in the water vapor is in the southern hemisphere during the summer, and it can be influenced by the variability in

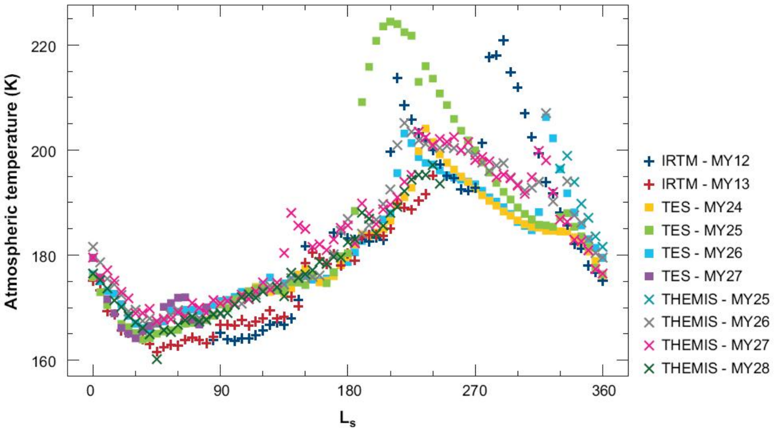

Figure 2.8: Globally averaged values of atmospheric temperatures at about 25 km, as observed by the Viking IRTM, MGS TES, and Mars Odyssey THEMIS instruments.

temperatures caused by dust storms. Although the almost complete lack of a maximum in the southern summer observed by the MAWD instrument on board the Viking orbiter [113] is probably due to the fact that water vapor was masked by two dust storms that have surrounded the planet [185, 75], variations from year to year up to about 20% appear to be real.

## 2.6 Photochemistry and Stability of the Martian Atmosphere

The annual cycle of sublimation-condensation in the polar regions produces an increase and a decrease in the total atmospheric pressure on planetary scale. The study of photochemistry of the Martian atmosphere is the study of the photochemistry of a $CO_2$ atmosphere with varying amounts of $H_2O$ added under varying conditions of pressure, temperature and sunlight. The photochemistry of this system $CO_2/H_2O/N_2$ produces carbon monoxide (CO), molecular oxygen ($O_2$), Ozone ($O_3$), and nitrogen oxides ($NO_x$).

Below the photochemical model currently accepted will be described in more detail and then, the problem of stability of the Martian atmosphere will be treated.

### 2.6.1 Atmospheric Photochemistry

On Mars, the photodissociation of $CO_2$ takes place on the entire height of the atmosphere. The relatively high pressure of $CO_2$ implies that the photoabsorption by this species takes place from the surface to the ionosphere, which lies above 100 km. Thus, it is important to include the contribution of the ionosphere, even if we are treating the lower atmosphere.

The chemical reactions that produce and destroy the various neutral constituents in the Martian atmosphere are shown in Table 2.3, and the main reactions are shown in figure 2.9. The absorption of the solar photons for

| | Reactions | Rate Constants[b] |
|---|---|---|
| R1 | $H_2O + h\nu \rightarrow OH + H$ | |
| R2 | $CO_2 + h\nu \rightarrow CO + O$ | |
| R3 | $CO + O + M \rightarrow CO_2 + M$ | $9.8 \times 10^{-33} \exp(-2180/T)$ |
| R4 | $H + O_2 + M \rightarrow HO_2 + M$ | $5.7 \times 10^{-32} (T/300)^{-1.6}$ |
| R5 | $HO_2 + HO_2 \rightarrow H_2O_2 + O_2$ | $2.3 \times 10^{-13} \exp(600/T)$ |
| R6 | $O + HO_2 \rightarrow OH + O_2$ | $2.9 \times 10^{-11} \exp(200/T)$ |
| R7 | $H_2O_2 + h\nu \rightarrow OH$ | |
| R8 | $HO_2 + h\nu \rightarrow OH + O$ | |
| R9 | $CO + OH \rightarrow CO_2 + H$ | $4.35 \times 10^{-14} (T/298)^{1.35} \times \exp(365/T)$ |
| R10 | $H + HO_2 \rightarrow 2OH$ | $7.2 \times 10^{-11}$ |
| R11 | $H + HO_2 \rightarrow H_2 + O_2$ | $5.6 \times 10^{-12}$ |
| R12 | $H + HO_2 \rightarrow H_2O + O$ | $2.4 \times 10^{-12}$ |
| R13 | $H + O_3 \rightarrow OH + O_2$ | $1.4 \times 10^{-10} \exp(-470/T)$ |
| R14 | $O + OH \rightarrow O_2 + H$ | $2.2 \times 10^{-11} \exp(120/T)$ |
| R15 | $O + O + M \rightarrow O_2 + M$ | $5.21 \times 10^{-35} \exp(900/T)$ |
| R16 | $O + O_2 + M \rightarrow O_3 + M$ | $6.0 \times 10^{-34} (T/300)^{-2.3}$ |
| R17 | $OH + HO_2 \rightarrow H_2O + O_2$ | $4.8 \times 10^{-11} \exp(250/T)$ |
| R18 | $H_2O_2 + OH \rightarrow HO_2 + H_2O$ | $2.9 \times 10^{-12} \exp(-160/T)$ |
| R19 | $O_3 + h\nu \rightarrow O_2 + O(^1D)$ | |
| R20 | $O_3 + h\nu \rightarrow O_2 + O(^3P)$ | |
| R21 | $O_2 + h\nu \rightarrow 2O$ | |
| R22 | $O(^1D) + H_2O \rightarrow 2OH$ | $2.2 \times 10^{-10}$ |
| R23 | $O(^1D) + CO_2 \rightarrow O + CO_2$ | $7.4 \times 10^{-11} \exp(120/T)$ |
| R24 | $O(^1D) + H_2 \rightarrow OH + H$ | $10^{-10}$ |

Table 2.3: Chemical reactions in the neutral atmosphere of Mars important for the problem of atmospheric stability.

[b] The units for the specific speed of the reaction (rate constant) are $cm^3 s^{-1}$ for two-bodies reactions and $cm^6 s^{-1}$ for three-bodies reactions.

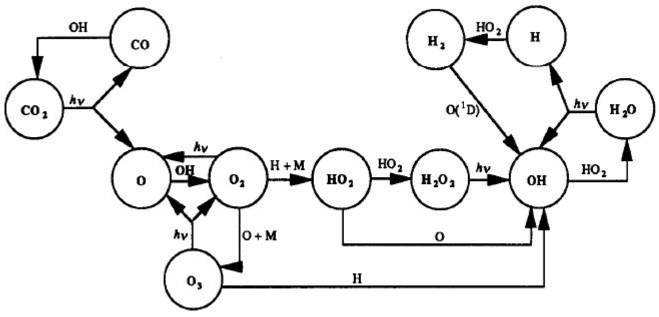

Figure 2.9: Schematic representation of the significant chemical reactions in the neutral atmosphere of Mars.

wavelengths below 220 nm is caused primarily by the $CO_2$, leading to the formation of CO and O (R2 in Table. 2.3). The reverse reaction (R3) is spin-forbidden, so its rate is extremely slow. The main mechanism of CO loss is a reaction with the hydroxyl radical, OH, which regenerates the $CO_2$ (R9). Although the abundance of OH is fundamentally linked to water vapor, its main source is the reaction of $HO_2$ with atoms of O (R6), which produces nearly two-thirds of the column abundance of OH, while the remaining third is produced by photolysis of hydrogen peroxide, $H_2O_2$ (R7). The $H_2O_2$ is produced in the reaction of $HO_2$ with itself (R5), while the same $HO_2$ results from the reaction of H with $O_2$ (R4). The H atoms are generated by $H_2O$ photolysis

(R1) below 190 nm. Furthermore, it is important to note that the direct production of OH from the $H_2O$ photolysis or in the reaction of $O(^1D)$ with $H_2$ (R22) or with $H_2O$ (R24) is negligible. The other significant process of OH production is the reaction of ozone with H atoms (R13). A schematic representation of the relative contribution to the production rate of OH is shown in Figure 2.10. The total production rate integrated on the altitude for a nominal model is $1.2\times10^{12}$cm$^{-2}$s$^{-1}$ [24]. This model assumes globally, seasonally and daily averaged parameters, for the solar flux (considering the mean solar activity) and for the water vapor (10 pr$\mu$m or 150 ppm on the surface), a surface temperature of 210 K, dust optical depth of 0.4 (UV), and a turbulent diffusion coefficient of $10^6$ cm$^2$s$^{-1}$ up to 40 km and increasing to $10^6$ cm$^2$s$^{-1}$ at 125 km. The altitude-integrated photolysis rate for the $CO_2$ in this model is $0.77\times10^{12}$ cm$^{-2}$s$^{-1}$ [24].

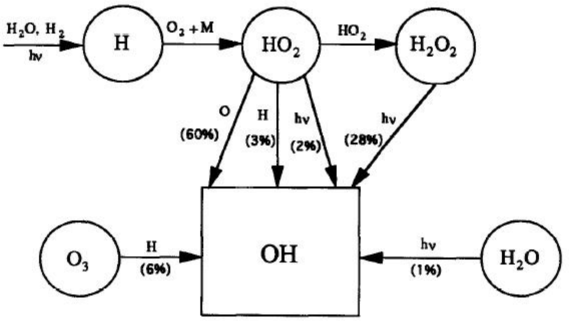

Figure 2.10: Sources of OH production along with their relative contributions in the atmosphere of Mars.

Once produced by the $CO_2$ photolysis, oxygen atoms recombine to produce molecules of $O_2$ (R15),

$$\begin{array}{c} 2CO_2 + h\nu \rightarrow 2CO + 2O \\ 2O + CO_2 \rightarrow O_2 + CO_2 \\ \hline 2CO_2 + h\nu \rightarrow 2CO + O_2 \end{array}$$

These reactions, therefore, imply that CO and $O_2$ are in the ratio 2 to 1, but measured data give a ratio of 0.54 to 1 in the composition. The mixing ratios of CO and $O_2$ are quite variable in the atmosphere of Mars, and their photochemical lifetimes (about 6-8 years for each) are long. As shown above, the abundances of CO and $O_2$ are controlled by odd hydrogen, in particular by OH, and then by $H_2O$, which is very variable. The reason why the observed $CO/O_2$ ratio is not 2:1 can be explained by the fact that the recombination reaction $CO + OH \rightarrow CO_2 + H$ causes a decrease in the CO abundance, but leaves unchanged the $O_2$ one.

More than 4/5 of the atomic oxygen production comes from $CO_2$ photolysis, while the remaining amount is the result of the photolysis of newly formed $O_2$ (R21) with $HO_2$ (R8). The loss of oxygen atoms is due to the recombination reaction (R15) and the reaction with $HO_2$ that form OH (R6). The molecular oxygen is formed directly or by recombination of oxygen atoms (R15), or through the catalysis of odd hydrogen, as shown below:

$$H + O_2 + M \rightarrow HO_2 + M$$
$$O + HO_2 \rightarrow O_2 + OH$$
$$O + OH \rightarrow O_2 + H$$

---

$$O + O \rightarrow O_2$$

And also,

$$O_3 + H \rightarrow OH + O_2$$
$$O + OH \rightarrow H + O_2$$

---

$$O + O_3 \rightarrow 2O_2$$

The indirect recombination of odd oxygen shown above justifies all the $O_2$ production rate below about 60 km: hence the catalysis of hydrogen plays a crucial role in the $O_2$ formation. The column production rate of $O_2$ for the nominal model is $2\times10^{11}$ $cm^{-2}s^{-1}$. The loss of $O_2$ is due to the ultraviolet photolysis (R21), as well as the loss of the even oxygen species, $HO_2$ and $H_2O_2$. This last indirect photolysis accounts for about 70% of the $O_2$ loss rate in the nominal model. The $O_2$ photochemical life time in the atmosphere of Mars is 8 years, which is much greater than the average time of mixing (about 10 days) in the lower atmosphere. It is therefore expected that the $O_2$ remains well mixed throughout the atmosphere.

The $O_2$ reaction with O produces $O_3$ (R16), as in the Earth's atmosphere. The primary mechanism for the loss of ozone is the ultraviolet photolysis during daylight hours (R19, R20) and the reaction with the atomic hydrogen (R13). The latter is the dominant loss mechanism for $O_3$ during the night. The distribution of odd oxygen abundance can be written as

$$[O_3] \,/\, [O] = k_{16}\,[O_2]\,[CO_2] \,/\, (J_{O_3} + k_{13}\,[H])$$

where the specific reaction speeds of the$k_{16}$ and $k_{13}$ are those for the R16 and R13 reactions (production and loss of ozone), and $J_{O_3}$ is the $O_3$ photolysis rate. The second term in the denominator is negligible in the nominal model.

The relation written above reveals that the dominant form of odd oxygen is the $O_3$ below 25-30 km, and the O above it. The peak in odd oxygen is located approximately at an altitude of 50 km in the nominal model. The

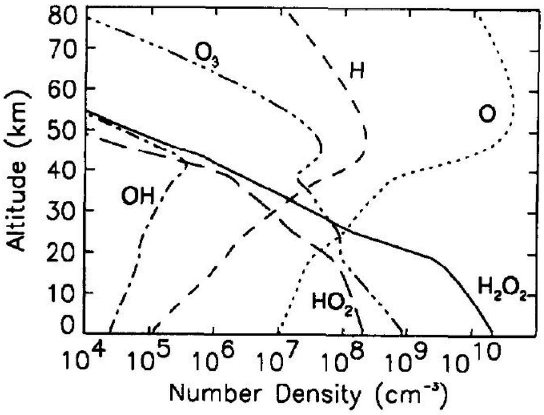

Figure 2.11: Distribution of photochemical constituents in the atmosphere of Mars (based on nominal model).

odd hydrogen, hydrogen peroxide and odd oxygen (O and $O_3$) distributions, calculated for the nominal model are shown in Figure 2.11.

The abundance of ozone in the atmosphere of Mars shows a significant seasonal variation as it was revealed by satellite observations of the Mariner 9. A maximum of 57 $\mu$m-atm [4] was measured at mid-latitudes during the northern hemisphere winter, while the value drops to less than 3 $\mu$m-atm on the north polar cap region. Minor amounts of ozone are found in the summer. The solar occultation experiments of Phobos made during the northern spring equinox near the equator revealed an amount of ozone at or below 2 $\mu$m-atm when data were extrapolated down to the surface [40], and even smaller amounts ($10^{-2}$ $\mu$m-atm) were measured by observations of the Hubble Space Telescope (HST) on the north polar cap during the spring equinox [49]. Moreover, vertical profiles of ozone have been obtained by SPICAM/MEX for one Martian year [128]: the ozone abundance increases during northern spring at mid and low latitudes from Ls=0° to Ls=100° reaching a maximum value of $6 - 9 \cdot 10^9$ $cm^{-3}$ at Ls=40°, whereas it is not detected after Ls=130°. Also the OMEGA instrument on board of MEX provided indirect information about the ozone abundance by studying the $O_2$ dayglow emission at 1.27 $\mu$m [21].

These observations show an anticorrelation between the amount of ozone and the abundance of water vapor. Larger values of ozone are found in winter, when the abundance of water vapor drops to its minimum value, and smaller values of ozone are recorded in the summer period, when the abundance of water reaches its peak. This anticorrelation between $O_3$ and $H_2O$ vapor is expected since the reactions of odd oxygen (O and $O_3$) with H and $HO_x$ (R6, R13, R14) are the dominant mechanism of ozone loss because O and $O_3$ are interchangeable during the day.

The production and loss of hydrogen is controlled both by photochemistry and by the escape of atmospheric gases. The molecular hydrogen is produced in the lower atmosphere by a reaction between hydrogen atoms and the $H_2O$

---

[4] 1 $\mu$m-atm = $2.687 \times 10^{15}$molecules$\cdot$cm$^{-2}$.

(R11) at a rate of $3\times10^9$cm$^{-2}$s$^{-1}$ in the nominal model. The upward $H_2$ flow is $5\times10^8$cm$^{-2}$s$^{-1}$ from the lower atmosphere to the ionosphere. Once in the ionosphere, $H_2$ undergoes the dissociation caused by the ultraviolet photons and by the following reactions:

$$CO_2 + h\nu \rightarrow CO_2^+ + e$$
$$H_2 + CO_2^+ \rightarrow CO_2H^+ + H$$
$$CO_2H^+ + e \rightarrow CO_2 + H$$

---

$$H_2 + h\nu \rightarrow 2H$$

In the middle atmosphere, the $H_2$ removal takes place by means of its reaction with O($^1$D), producing a small amount of OH and H (R24). The $H_2$ net mixing ratio for the nominal model is $5\times10^{-5}$. The $H_2$ life time compared with a photochemical loss in the lower atmosphere ($>$ 30 years) is long, while the vertical mixing time is of the order of 10 days (for a *turbulent diffusion coefficient* K = $10^6$cm$^2$s$^{-1}$). This allows these species to remain relatively well mixed in the Martian atmosphere. The loss from the higher atmosphere occurs at a critical level in the escape of atomic hydrogen, while the direct escape of $H_2$ is small. The $H_2$ mixing ratio and the escape rate of H atom may be moderately influenced by the following nitrogen reaction:

$$NO + HO_2 \rightarrow NO_2 + OH \qquad k = 3.7 \times 10^{-12}\exp(240/T)\ cm^3s^{-1}.$$

### 2.6.2 Atmospheric Stability

The Martian atmosphere is stable despite the photochemical loss. This is particularly striking in the case of the main atmospheric constituent, the $CO_2$, where the photolysis rate is of the order of $10^{12}$cm$^{-2}$s$^{-1}$, as already mentioned previously. This means that the whole atmosphere of Mars should be separated into its products CO and $O_2$ in about 6000 years [25], i.e. a relatively small period. Moreover, current concentrations of CO and $O_2$ (about 0.1%) should be increased significantly in 3-6 years. We know that, except for regular seasonal changes (about 30%), the $CO_2$ concentration in the Martian atmosphere is constant, and the concentrations of CO and $O_2$ did not continue to grow if compared to their current levels in the atmosphere. The $CO_2$ recycling by the reaction of CO with O (R3) is spin-forbidden. The apparent success of previous attempts to explain the $CO_2$ recycling [144, 164] by the reaction between CO and OH (R9), was fortuitous because these models assumed incorrect values both for the turbulent mixing coefficient in the middle atmosphere and for the water vapor amount. Moreover, they assumed wrong absorption cross sections and chemical kinetic data for the $CO_2$. With absorption cross section data of $CO_2$ available in 1972 (at the time of development of these models), and using the correct values for the turbulent mixing coefficient in the middle atmosphere ($10^6$ $cm^2s^{-1}$) and for the average water vapor amount (150 ppm), the ratio between the $CO_2$ reformation rate and the $CO_2$ loss rate by photolysis resulted to be about 0.15 and 0.3, respectively for McElroy and Donahue's model (1972) [144], and for Parkinson and Hunten's model (1972) [164]. In other words, the $CO_2$ loss exceeds its recycling rate of factors 3 and 6, respectively. However, improvements on the absorption cross section data of $CO_2$, which were found to be dependent on temperature, show that, at the low temperature of the Martian surface and at the atmosphere bottom, the absorption cross section of $CO_2$ is 2-3 times smaller than the value available at the time these models were calculated. This means that the loss rate should be reduced if the new $CO_2$ absorption cross sections are used. Furthermore, it was discovered that the new reaction specific speed for the recycling reaction R9, $CO + OH \rightarrow CO_2 + H$ is greater than the value used in the models of 1972 by about a factor 2-3. Therefore, the use of the new reaction rate constant should result in an increased recycling rate for the $CO_2$. The new data on the relevant cross sections and on the reactions rate constant result in an increase in the $CO_2$ reformation rate so that it should tend to have a stability parameter close to 1. A detailed photochemical model developed by Atreya and Gu (1994) [24] shows, however, that the laboratory data available on the reactions kinetics, on the cross sections and on atmospheric parameters give a substantial excess (about 40%) of the production rate if compared to the loss rate of $CO_2$. Although we have achieved a significant improvement over previous models in which the discrepancy between the average production and loss rate was of factors ranging from 3 to 6, we should still seek some physical mechanism that can reconcile this difference. Furthermore, it should be noted that all these models are "one-dimensional", while other parameters should be taken into account, such as temporal one, latitude and longitude, and changes of atmospheric water vapor amount, the turbulent mixing, the dust opacity and temperatures, as well as the atmospheric dynamics.

The model, developed in 1995 [25], has been validated by performing calculations which take into account the actual variations of relevant atmospheric parameters during a Martian day. These calculations show that the production and loss rate are almost balanced to each other when averaged over a period of 24 hours. This illustrative calculation was performed for the site of the Viking 1 lander, taking into account the actual diurnal variation of the three most important parameters: amount of water vapor, surface and atmospheric temperature, and solar zenith angle. The $H_2O$ vapor varies from 1 pr$\mu$m at dawn to 10 pr$\mu$m at noon even if it changes very little at sunset [72]. The surface temperature varies from dawn to noon of about 45 K [182]. The critical parameter in the stability problem is the OH density and its dramatic variability from day to night, because its photochemical lifetime is less than 1 second, while the lifetime of the other critic constituent, the CO , is so long (about 8 years) that we expect its density has not a diurnal variation. The figure 2.12 shows the distribution of OH density over a period of 24 hours in the Martian atmosphere. The value at midnight of [OH] is dramatically reduced below 40

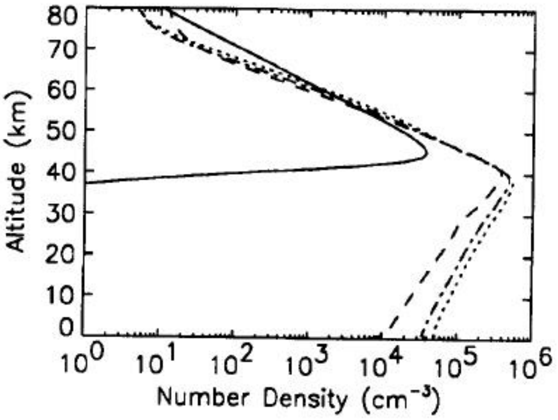

Figure 2.12: OH concentration [OH] in the atmosphere of Mars for midnight (solid line), for the 6 am (broken line), for the 8 am (point-to-tract) and noon (dotted line). The shown calculations refers to the summer at 20°N.

km because of the important reduction in the density of atomic oxygen in this region at night, which prevents the formation of OH (R6). A further decrease of OH takes place because of the absence of $H_2O_2$ photolysis (R7). Although the recycling rate of the resulting $CO_2$ (R9) should be dramatically reduced during the night, this happens for the loss by photolysis.

The ratio of these production and loss rates, integrated for the altitudes, results to be 0.98, when computing a simple average of the values corresponding to a period of 24 hours. However, this simplified illustration represents only a single day on Mars, so it does not take into account the actual latitudinal and seasonal variations of the relevant atmospheric parameters. Indeed, we recall that the globally averaged model provides a 40% discrepancy between the $CO_2$ production and loss rates, so it would be necessary some mechanism to be included in this model that can reduce the OH production or allow additional CO loss, since the mechanism for the $CO_2$ recycling (R9) depends on the CO and OH abundances. Atreya and Blamont (1990) [23] suggested that heterogeneous processes on the aerosols (dust and ice) surfaces in the Martian atmosphere could produce a reduction in the abundances of CO, O, $O_2$, OH, $H_2O$, $H_2O_2$ or of other species involved in the $CO_2$ recycling.

### 2.6.3 Experimental Contribution to Photochemicals Models

During the years elapsed since the publication of the models described in the previous section, there was a significant progress in experimental data on the photochemistry of the Martian atmosphere. The five years of observations of temperature profiles, water vapor abundance, and dust and ice aerosol opacity using the TES instrument aboard the Mars Global Surveyor (MGS) (section 2.5) provide detailed data for photochemical modeling at various latitudes and seasons. The ozone abundances have been observed in various conditions using both ultraviolet spectroscopy of the Hubble Space Telescope (HST) [52] and infrared spectroscopy of ground-based instruments [73, 71]. The $O_2(^1\Delta)$ dayglow observations at 1.27 $\mu$m using the CSHELL spectrograph at NASA Infrared Telescope Facility (IRTF) were carried out by Krasnopolsky and Bjoraker (2000) [120], Novak et al. (2000) [157], and Krasnopolsky (2006) [124], to monitor the Mars photochemistry. These observations are currently the most detailed database for changes in the photochemistry of Mars. In addition, the ESA Mars Express orbiter is observing ozone, 1.27 $\mu$m dayglow, $H_2O$, CO, dust and ice aerosols, and temperature profiles in the atmosphere.

Another advance in the photochemical modeling of Mars is related to the coupling of photochemistry with general circulation models (GCMs). This was done by Lefevre et al. (2004) [129], who calculated the three-dimensional variations of ozone. The GCMs models are the best tools for the modeling of atmospheric dynamics, thermal structure, and aerosols and water vapor distributions: the GCM photochemical models take into account all these effects on the photochemistry.

Observations of changes in the photochemistry of Mars with the season, latitude, and local time are among the main objectives in the study of the Martian atmosphere.

#### 2.6.3.1 $O_2$ Dayglow Observations

The $O_2$ dayglow at 1.27 $\mu$m is excited by the photolysis of ozone, and the $O_2(^1\Delta)$ molecules so formed, either emit photons at 1.27 $\mu$m or are de-excited in collisions with $CO_2$.

Clancy and Nair (1996) [51] calculated the seasonal behavior of Mars photochemistry at low and middle latitudes. They claimed that the atmosphere is cool and dust free at the aphelion and hot and dusty at perihelion. This changes significantly the water vapor condensation level and strongly influences the water photolysis, and thus the production of odd hydrogen. Water and, therefore, odd hydrogen are absent above the level of condensation, and this allows the ozone formation. The calculated column abundance of ozone varies by a factor of 3 at low latitudes, while its variation also reaches a factor of about 10 above 20 km.

Krasnopolsky (1997) [119] found that the best way to observe ozone at high altitudes is measuring the $O_2$ dayglow at 1.27 $\mu$m using CSHELL. The dayglow is destroyed by collisions with $CO_2$ below 15-20 km and therefore it reflects the ozone at high altitudes, which is the most sensitive tracer of Mars photochemistry at low and middle latitudes.

The latitudinal variations of the dayglow intensity for several Martian seasons are shown in figure 2.13 . The vertical axis intensity varies from 0.4 MR[5] at 40°N for Ls = 247° to 17 MR at 65°S for Ls = 173°. The data in figure refer to the central part of the day: the dayglow appears to be maximum at 12:30, and the variations in intensity from 9:00 to 15:00 are typically of about 20%.

The Martian atmosphere is optically thin at the wavelengths responsible for

---

[5] 1 MR (MegaRayleigh) is the emission of $10^{12}$ photons per $cm^2 s$ in $4\pi$ steradians.

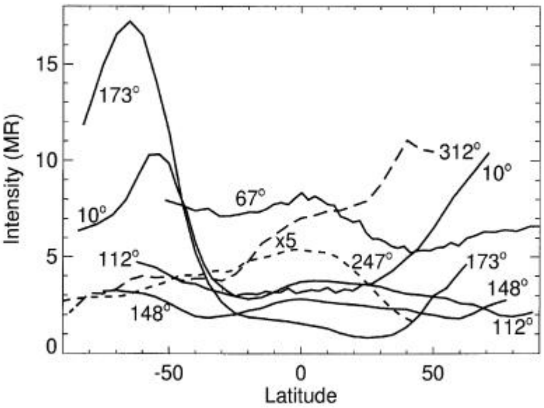

Figure 2.13: Latitudinal variation of $O_2$ dayglow at 1.27 $\mu$m observed for several seasons by the CSHELL instrument [124]. The dayglow intensities at Ls = 247° and Ls = 312° are scaled by a factor of 5.

the ozone photodissociation. Thus, the diurnal variations of the $O_2$ dayglow reflect the changes in the ozone abundances and of its vertical profiles, while the photodissociation rate remains constant.

The $O_2$ dayglow intensities, shown in figure 2.13, can be combined to build a map of the latitudinal and seasonal dayglow variations (Figure [fig: 2.14 ). This map reflects the response of the Martian photochemistry to latitudinal and seasonal variations of temperature profiles, water vapor abundance, aerosols opacity, and to the dynamic processes in the atmosphere. Thus, this map can be used to predict the intensity of the dayglow for various observing conditions and it is also a test for the modeling of Mars photochemistry and its variations.

A recent model of Martian photochemistry variations [119] is based on data by MGS/TES about temperature, water vapor abundance and aerosols opacities. In general, this model (Fig. 2.14) results to be in good agreement with observational data of the $O_2$ dayglow and of the peroxides abundances.

The 1.27 $\mu$m dayglow was also observed by the IR spectrometer SPICAM on board the Mars Express orbiter [76](Fig. 2.15). SPICAM observations provide a regular monitoring of the $O_2$ dayglow, and a better coverage at higher latitudes, which are typically not seen by telescopes on Earth. The IRTF/CSHELL observations have been made with an average frequency of one per year and with a spatial resolution significantly lower than the one of the spacecraft. Obviously SPICAM observations are not influenced by the telluric absorption, which restricts observations to periods with Earth's high geocentric speeds. The IRFT/CSHELL advantages are the highest spectral resolution (by a factor of about 18) and the highest signal to noise ratio (about 300 for the observations of 2005-2006). IRTF/CSHELL observations may be better for the weak $O_2$ dayglow typical of low latitudes, especially near the Mars perihelion. Moreover, these observations are not tied to a certain local time, as in the case of Mars Express data.

In Fedorova et al. (2006) [76] we find a detailed comparison between SPICAM results and observations reported in Krasnopolsky (2003) [121], showing

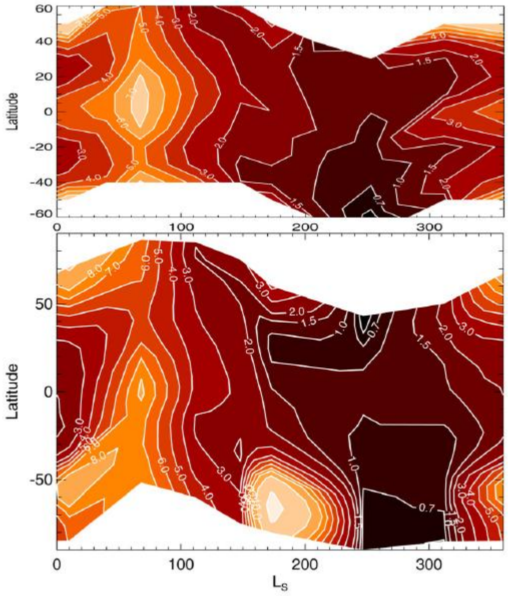

Figure 2.14: Map of seasonal-latitudinal variations of the $O_2$ dayglow at 1.27 $\mu$m (in MR). In the lower panel is shown the map retrieved by the observations, while in the upper panel there are the results of photochemical model [119] in the range of latitudes covered by the water vapor observations by MGS/TES [186].

a generally reasonable agreement (Fig. 2.16), which was also recently found by studying data by the PFS/MEX instrument [89].

#### 2.6.3.2 CO Observations

CO is the fundamental product of the $CO_2$ photolysis. It reacts very slowly with O, $O_2$ and $O_3$, so its mixing ratio should be 0.08, as expected from modeling in a $CO_2$ atmosphere and with $H_2O$ absence [155], but the observed values are lower by two orders of magnitude: this is the stability problem of the Martian atmosphere, solved years ago using a very effective catalysis of the $H_2O$ photolysis products (Section. 2.6.2). This catalysis is so efficient that, taking it into account, the model expected that CO abundances are, this time, smaller than the observed average value $8\times10^{-4}$ by a factor of 5, and still the problem of stability remains partly unsolved.

The CO production rate is just equal to the flux of solar photons with $\lambda < 200$ nm, which dissociate the $CO_2$. This annual global average flow is equal to $9\times10^{11}$cm$^{-2}$s$^{-1}$, with a CO column abundance of $1.8\times10^{20}$cm$^{-2}$ for a mixing ratio of $8\times10^{-4}$: this information is translated into an average life time of about 6-8 years for CO. This lifetime is much longer than the Martian day, and then CO variations with local time are not expected. The time of vertical mixing is

$$\frac{H^2}{K} \approx 2 \text{ weeks}$$

in the lower atmosphere, where $H$ is the scale height and $K \approx 10^6$cm$^2$s$^{-1}$ is

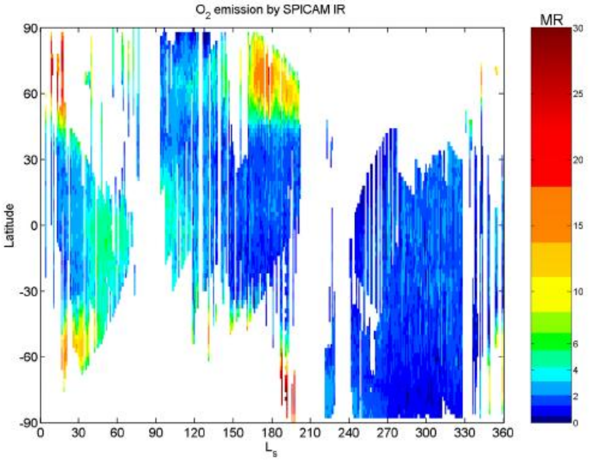

Figure 2.15: Seasonal distribution map of the $O_2$ emission observed by SPICAM since Ls = 330° (January 2004) to Ls = 327 ° (November 2005) [76].

the turbulent diffusion coefficient [125]. So the CO mixing ratio should be constant until about an altitude of 40 km.

From spectroscopy of the CO band at 2.35 $\mu$m by the Phobos orbiter data [176], the CO mixing ratios resulted to be lower over large Martian volcanoes at a height of about 20 km from the flat areas by a factor of 5-8, a fact that is completely inconsistent with the photochemistry predictions. Hünten (1993) [111] showed that small changes in the continuous level of CO spectral band could remove the variation of the CO mixing ratio with altitude in the Phobos observations.

Krasnopolsky [122] observed an increase in the CO mixing ratio by a factor of about 1.5 from the equator to 50°S. The observations were made during the south winter at Ls = 112°, and the increase was explained by the $CO_2$ condensation in the winter polar cap. $CO_2$ condensation and sublimation result in an enrichment and depletion of long-lived non-condensable gases ($N_2$, Ar, $O_2$, CO, $H_2$) on the polar caps and neighboring regions. The value and the extent of this effect are directly related to the atmospheric dynamics and polar processes, and they could be simulated by general circulation models (GCMs). This effect was observed for Ar using the gamma ray spectrometer on board the Mars Odyssey orbiter [195].

Krasnopolsky presented in [124] the study on CO mixing ratio variations as observed by the IRTF/CSHELL instrument. The figure 2.17 shows the CO mixing ratio as a function of the altitude from the surface for observations made on 8 December 2003, averaged in intervals of 1 km altitude. In the range of altitude ranging from -4.5 to 8.5 km are not observed significant changes. The variations in the CO mixing ratio with the latitude for four seasons are shown in figure 2.18. For Ls = 112° there is a more or less constant mixing ratio in the northern hemisphere and it is growing from the equator to the south polar cap. In fact, the condensation rate is maximum near Ls≈100°, and atmospheric dynamics ensure that the CO amount reaches its maximum with a certain delay (Ls ≈ 112°). A similar situation occurs for the northern winter,

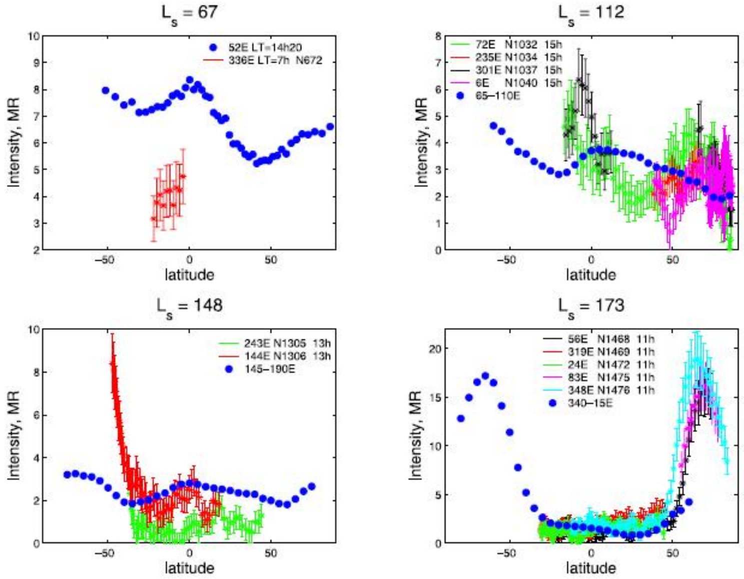

Figure 2.16: Comparison of $O_2$ emission profiles between SPICAM observations and ground-based observations for four seasonal points [76]. The circles represent observations from Earth, the asterisks with error bars represent SPICAM data for different longitudes, and N is the number of the orbit. The ground-based measurements for Ls = 112°, 148° and 173° were averaged for the local time range going from 11:00 to 14:00.

Ls = 312°. However, the northern winter corresponds to a Mars position close to the perihelion, and therefore it is not as cold as the southern winter. Thus, the $CO_2$ condensation rate and the CO increase are significantly weaker than in the previous case. The southern cap begins to sublime for Ls = 173°. The southern mixing made the abundance flat up to 45°S for a month after the end of the condensation. The other features are similar to those for Ls = 112°. The explanation of the CO behavior for Ls = 10° requires very complex dynamics.

Although the CO distribution for four seasons is generally insufficient to create a map of the latitudinal and seasonal variations, Krasnopolsky [124] presented a preliminary version of it, shown in Figure 2.19.

Since the aim of this thesis work is the study of water vapor and carbon monoxide distributions and their relations, and they are strictly bound each other by the photochemistry of the Martian atmosphere, we will improve the knowledge of the atmospheric scenario, which is needed to guarantee the stability of the atmosphere itself.

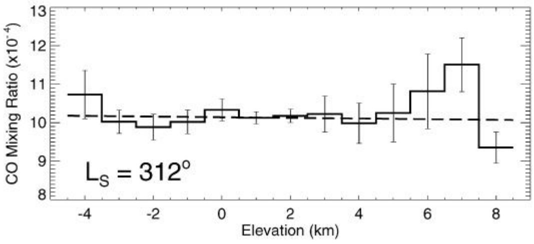

Figure 2.17: Evolution of the CO mixing ratio (corrected for the latitudinal dependence) as a function of the altitude from the surface for observations made on December 8, 2003 with the IRTF/CSHELL instrument [124]. The dashed line represents the data linear fit.

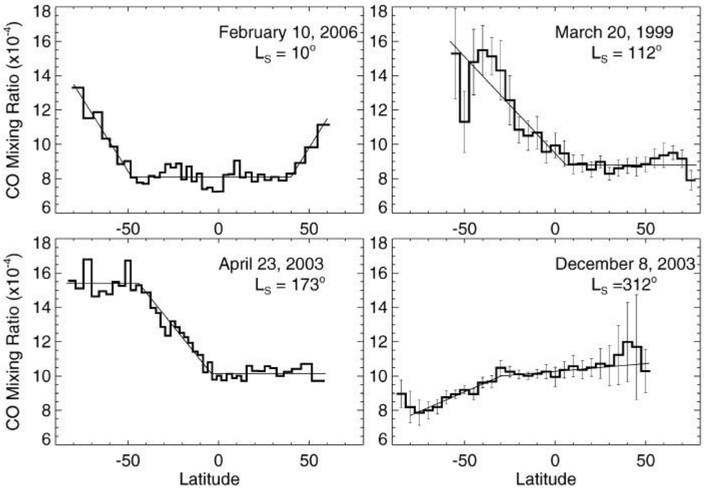

Figure 2.18: Latitudinal variations of the CO mixing ratio for four seasons [124]. The observational data are approximated by broken lines.

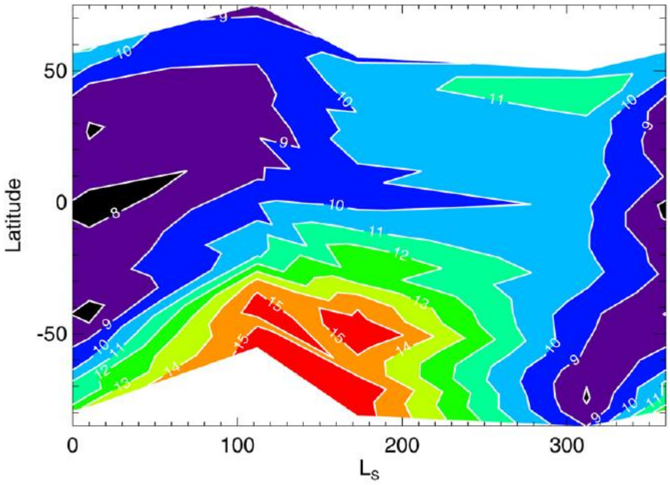

Figure 2.19: Seasonal and latitudinal variations map of the CO mixing ratio (in $10^{-4}$)[124].

# Chapter 3

# Mars Express (MEX) and the Planetary Fourier Spectrometer (PFS)

MARS EXPRESS (MEX) is a space exploration mission conducted by the European Space Agency (ESA). The Mars Express mission is exploring the planet Mars, and it is the first planetary mission undertaken by ESA. The word “Express” in the mission name refers to the speed and efficiency with which the spacecraft was designed and built. However, “Express” also describes the relatively short interplanetary journey of the spacecraft, as a result of its launch when the orbits of Earth and Mars allowed that the path was the shorter of the last 60000 years.

Mars Express consists of two parts: the *Mars Express Orbiter* and *Beagle 2*, a lander designed to perform geochemical and exobiological research. Although the lander failed during landing on the Martian surface, losing its contact, the orbiter successfully performs scientific measurements since the beginning of 2004 as, in particular, collection of images (*imaging*) and high-resolution mineralogical mapping of surface, radar sounding of subsurface structure beneath the permafrost, precise determination of the atmospheric circulation and composition, and study of the interaction between the atmosphere and the interplanetary medium.

Some of the instruments aboard the orbiter reuse the design developed for the failed Russian mission of 1996, MARS 96, as many instruments and funding came from European countries. The basic design of Mars Express is based on the ESA ROSETTA mission, on which a considerable sum was spent for its development. The same design was also used for the VENUS EXPRESS mission in order to increase reliability and reduce costs and development time.

Thanks to the valuable scientific return and to the highly flexible mission profile, ESA has granted to Mars Express four straight mission extensions till (at least) December 2014.

In this Chapter we will provide a general overview of the Mars Express mission and then we will describe in details the Planetary Fourier Spectrometer (PFS) [84] and the calibration procedure for its spectra [92, 93].

## 3.1 The Mission

The spacecraft was launched on June 2, 2003 at 23:45 local time (17:45 UTC) from the "Baikonur Cosmodrome" in Kazakhstan, using a Soyuz-Fregat rocket. The Mars Express and the booster rocket were initially placed in a parking orbit at 200 km altitude around the Earth, then the Fregat was rekindled at 19:14 UTC to enter the satellite into a transfer orbit to Mars. The Fregat and Mars Express separated at approximately 19:17 UTC. After the solar panels were deployed and was made the trajectory correction maneuver on June 4 to allow the reaching of Mars through the interplanetary space.

Once the initial phase finished, for the next five months took place the "interplanetary cruise" phase, which lasted until about a month before the Mars capture maneuvers and involved trajectory correction maneuvers and the payload calibration. The latter remained mostly switched off during the cruise phase, with the exception of some intermediate controls. Although this step is called "cruising", it was very difficult: in fact, there were "Star Tracker" (identification of star positions to adjust the satellite direction and position) problems: a power problem of electrical system, extra maneuvers, and on October 28 the spacecraft was hit by one of the largest solar flares ever recorded.

The Beagle 2 lander was released on December 19 at 8:31 UTC toward the surface. The lander entered the Martian atmosphere on the morning of Dec. 25. The landing was scheduled for about 02:45 UTC on December 25. However, after having repeatedly tried to contact the lander by Mars Express and NASA Mars Odyssey orbiters, it was declared lost on February 6th 2004 by the "Beagle 2 Management Board".

Mars Express arrived at Mars after a 400 million km journey, and after two course corrections in September and December, 2003. The Mars Express, on December 20 briefly rekindled the thrusters to place itself in the orbital position around the planet. Then, its main engine was turned on and it went into a highly elliptical (250 km × 150000 km) initial capture orbit with an inclination of 25 ° on December 25 at 03:00 UTC.

The first calculation of the orbital insertion data showed that the orbiter reached its first goal. The orbit was later adapted by other main engines starting up to reach the desired quasi-polar orbit (inclination of 86 °) of 259 km × 11560 km with a period of 7.5 hours. After 100 days, the orbit apocentre was lowered to 10107 km, while the pericentre was increased to 298 km for an orbital period of 6.7 hours.

Since May 4, 2005 until June 17, 2005 the gradual deployment of the antennas of the MARSIS (*Mars Advanced Radar for Subsurface and Ionosphere Sounding*) instrument was made. This phase was quite critical and so complex as to require cooperation between different agencies, including ESA, NASA, and public universities. The phase of nominal science observations began on January 7, 2004 for all instruments, except for MARSIS which became operating on July 2005.

Operations of the mission management are conducted by a multinational group of ESA "Operations Centre" engineers in Darmstadt. The group began its preparations for the mission about 3 or 4 years before the effective date of the launch.

The "Mission Control Team" consists of the Flight Control Team, Flight Dynamics Team, Ground Operations Managers, Software Support and Ground Facilities Engineers. All of these groups are located at ESOC, together with other external groups, such as Project and Industry Support groups, which designed and built the spacecraft.

Since its orbit insertion, Mars Express is gradually taking its original scientific objectives. Normally, the satellite points Mars while acquires scientific data and then sends them to Earth when it is in a position where he can point it, although some instruments such as Radio Science, or MARSIS can be managed operatively only when the vehicle points to the Earth.

## 3.2 Structure and Subsystems of the Mars Express Orbiter

### 3.2.1 Structure

The Mars Express Orbiter is a cubic shape spacecraft with two wings made of solar panels extending from two opposite sides. Its mass at launch was 1123 kg and includes a main frame with a payload (113 kg), the lander (60 kg) and 457 kg of propellant. The main body has dimensions 1.5 m × 1.8 m × 1.4 m, with an aluminum structure covered in turn by an aluminum layer. The solar panels are about 12 m tip-tip. The two long dipole antennas extend from opposite sides perpendicular to the solar panels as part of the radar sounder [70].

### 3.2.2 Propulsion

The Soyuz/Fregat launcher supplied most of the thrust needed to reach Mars. The Fregat final stage was expelled once the probe had no problems on the way to Mars. The propulsion means on board the vehicle were used for the probe insertion into the Mars orbit and for the following orbital corrections [70].

The spacecraft body is built around the main propulsion system, which consists of a 400 N main bipropellant engine. The two propellant 267 liters tanks have a total capacity of 595 kg. Approximately 370 kg were needed for the nominal mission. Pressurized helium contained in a 35 liters tank is used to push the fuel into the engine. Trajectory corrections were made using a set of eight 10 N thrusters, each placed at each corner of the vehicle structure. The satellite configuration has been optimized for a Soyuz/Fregat, and it was almost completely compatible with the Delta II launch vehicle.

### 3.2.3 Power Supply

The power supply of the satellite is provided by the solar panels, which contain 11.42 square meters of silicon cells. A power of 660 W was originally planned, but a defective connection has reduced the available power of 30%, i.e. up to 460 W. This energy loss should not have a significant impact on the scientific return of the mission. Energy is stored in three lithium-ion batteries with a total capacity of 64.8 Ah to be used during the eclipse. The power is completely adjusted to 28 V.

### 3.2.4 Avionics

The attitude control (3-axis stabilization) is achieved using two units of 3-axis inertial measurement, a set of two stellar cameras and two sun sensors, gyroscopes, accelerometers, and four 12 N·m·s reaction rotors. The pointing accuracy is 0.04° with respect to the inertial reference system and 0.8 ° to the Mars orbit. Three systems on board Mars Express help to maintain a very precise pointing accuracy, which is essential to allow the satellite to communicate with Earth.

### 3.2.5 Communications Subsystem

The communication subsystem is composed of three antennas: a parabolic antenna with high gain of 1.7 m in diameter and two omni-directional antennas. The first provides the connections (remote control in uplink and telemetry in downlink) in both the X-band (7.1 GHz) and in S-band (2.1 GHz) and it is used during the nominal science phase around Mars. The low gain antennas were used during the launch and in the first operations on Mars and may be used in case of necessity in the orbital phase around Mars.

Two UHF antennas have been mounted on the upper part for communication with Beagle 2.

### 3.2.6 Earth Stations

Although communications with Earth were originally scheduled to be made with the ESA Ground Station (35 meters antenna) located in New Norcia (Australia), the mission profile, aimed to a progressively improving of flexibility in the scientific return, has led to use the ESA ESTRACK Ground Station in Cebreros Station which is located in Madrid (Spain).

Moreover, further agreements with the NASA Deep Space Network have made possible the use of American stations in the planning of the nominal mission, thus increasing the complexity, but with a clear positive impact in the scientific return.

This cooperation between different agencies has been made possible thanks to the adoption by both agencies of Space Communications Standards set out in the Consultative Committee for Space Data Systems (CCSDS).

### 3.2.7 Thermal Control

The thermal control is maintained through the use of radiators, "multi-layer" insulation, and controlled active heaters. The satellite should provide an optimal environment for the instruments and equipment on board. Two instruments, PFS and OMEGA, have infrared detectors and they need to be kept at very low temperatures (about 212 K for PFS and about 180 K for OMEGA), as well as the sensors on the camera (HRSC). But the rest of instruments and equipment on board work optimally at room temperature (10 - 20°C).

The satellite is covered by a coating of gold Kapton (multi-layer thermal cover), which maintains a temperature of 10 - 20°C inside the vehicle. The instruments that operate at low temperatures are thermally insulated to be kept cool from this relatively high temperature, and emit the excess heat in space using the appropriate radiators [70].

### 3.2.8 Control Unit and Data Storage

The vehicle uses two control and data management units with a 12 GigaBits solid state memory [70] for storing data and the information management during the transmission phase. The onboard computer controls all aspects concerning the satellite operation including instruments power on and off, the evaluation of its orientation, and the whole management.

### 3.2.9 The Lander

The objectives of the Beagle 2 lander were to characterize the geology, mineralogy, and geochemistry of the landing site, the physical properties of the atmosphere and of the surface layers, collect data on Martian meteorology and climatology, and look for possible evidence of life. However, the landing attempt was unsuccessful and the lander was declared lost (section 3.1). A court of inquiry about Beagle 2 identified four possible causes for the lander failure, including the insufficient strength of the airbags and problems with parts of the landing system, but was unable to reach any definitive conclusion.

## 3.3 Mars Express Instruments

The scientific objectives of Mars Express are to obtain a high-resolution (10 m resolution) global photographic map, the mineralogical mapping (100 m) and the mapping of atmospheric composition, to study the subsurface structure, the global atmospheric circulation, and the interaction between the atmosphere and surface, and between the atmosphere and the interplanetary medium.

The Mars Express Payload is composed by the following instruments:

- **Analyzer of Space Plasmas and Energetic Atoms (ASPERA)**: It studies the interaction between the upper atmosphere and the solar wind. Its mass is 7.9 kg [47].

- **High Resolution Stereo Camera (HRSC)**: It produces color images with a resolution ranging up to 2 m. Its mass is 20.4 kg [47].
- **Mars Radio Science Experiment (MaRS)**: It uses radio signals to study the atmosphere, gravity and density of the solar corona during the solar conjunctions. It uses the communication subsystem.
- **Sub-Surface Sounding Radar Altimeter (MARSIS)**: A radar altimeter used to estimate the sub-soil composition in search of ice and liquid water. This instrument includes two antennas of 20 m and has a mass of 13.7 kg [47].
- **Mars Express Lander Communications (MELACOM)**: It allows to Mars Express to act as a communications transit station for landers on the Martian surface. It has been tested with the Mars Exploration Rovers, and was used to support the landing of NASA Phoenix mission.
- **Visible and Infrared Mineralogical Mapping Spectrometer (OMEGA)**: It determines the mineralogical composition of the surface with a resolution of up to 100 m [37]. This instrument is a spatial dispersion spectrometer [47].
- **Planetary Fourier Spectrometer (PFS)**: It observes atmospheric temperature and pressure, as well as it can study the composition of the atmosphere. This instrument is a Fourier transform interferometer and has a mass of 30.8 kg [47].
- **Ultraviolet and Infrared Atmospheric Spectrometer (SPICAM)**: It evaluates the elemental composition of the atmosphere by spectral analysis. This instrument is a spatial dispersion spectrometer in the UV and IR ranges and has a mass of 4.7 kg [47].
- **VMC**: A small camera to monitor the lander ejection.

Table 3.1 summarizes the instruments on-board Mars Express with the corresponding *Principal Investigators* (PI) and origin institutions.

| Name | P. I. | Institution |
|---|---|---|
| ASPERA | R. Lundin | Swedish Institute of Space Physics |
| Beagle 2 | C. Pillinger | Open University, Milton Keynes, Uk |
| HRSC | G. Neukum | DLR, Institut fur Planetenerkundung, Berlin, Germany |
| MaRS | M. Patzold | University of Koln, Germany |
| MARSIS | G. Picardi | Università di Roma “Tor Vergata”, Italia |
| OMEGA | J-P. Bibring | Institut d’Astrophysique Spatiale, Orsay, France |
| PFS | V. Formisano | Istituto di Fisica dello Spazio Interplanetario, Roma, Italia |
| SPICAM | J-L. Bertaux | Service d’Aèronomie, Verrières-le-Buisson, France |

Table 3.1: Mars Epress Instruments, Principal Investigators and origin institution.

Below we will briefly describe some instruments aboard the Mars Express orbiter. The PFS will be described in more detail in section 3.4.

### 3.3.1 MaRS: Mars Radio Science Experiment

The Mars Radio Science Experiment (MaRS) has the ability to probe the Martian atmosphere and ionosphere during the occultation with the Earth. During the occultation events, the MEX satellite disappears behind the planetary disk of Mars as seen from Earth, with the result that both the uplink and downlink radio signals pass through the ionosphere and atmosphere from the surface up to a maximum altitude of about 1500 km [165].

The main scientific objectives can be summarized as:

- Probing the neutral atmosphere of Mars to retrieve density, pressure and temperature vertical profiles as a function of the altitude with a vertical spatial resolution better than 500 meters;
- Probing the ionosphere to retrieve the ionospheric electron density profiles and provide a description of the Martian ionosphere through its diurnal and seasonal variations depending only on the solar wind conditions;
- Determining the dielectric and diffusive properties of Martian surface in specific target areas by means of a bistatic radar experiment;
- Determining the gravity anomalies for the investigation of the structure and evolution of the Martian crust and lithosphere, together with the observations of HRSC as basis for the three-dimensional topography;
- Probing the solar corona during the superior conjunction of the planet Mars with the Sun.

For these studies the Telemetry, Tracking and Command (TTC) sub-systems for the radio link between the orbiter and the Earth have been used. The simultaneous and coherent dual-frequency signals, one in the X-band (8.4 GHz) and the other in the S-band (2.3 GHz) through the High Gain Antenna (HGA), allow the separation of contributions by the simple Doppler shift and by the dispersion effects of the medium caused by the satellite motion relative to Earth and by the propagation of signals through the dispersive medium, respectively.

The MaRS study depends on the observation of the phase, amplitude, polarization and propagation times of radio signals transmitted from the satellite and received by the antennas of the receiving station on Earth. Radio signals are affected by the medium through which the signal propagates (atmosphere, ionosphere, interplanetary medium, solar corona), by the gravitational influence of the planet on the spacecraft and finally by the performance of the various systems involved in both the satellite and Earth.

### 3.3.2 MARSIS: Sub-Surface Sounding Radar Altimeter

The MARSIS instrument (Sub-Surface Sounding Radar Altimeter) is a low frequency radar which transmits pulses and receives the corresponding echoes. MARSIS is used for the radar sounding of the ionosphere as well as the subsurface. Its main scientific objectives can be summarized as:

- Mapping the water distribution in the upper part of the crust down to a depth of 3 - 5 km;
- To examine the sub-surface geology;
- To characterize the topography of the planet;
- To examine the ionosphere, to understand its characteristics and its interactions with the solar wind [48].

The MARSIS instrument is composed by

- a subsystem having a primary dipole antenna, which is 40 m long, for the transmission and reception of electromagnetic pulses and a secondary unipolar antenna, measuring 7 m, for the exclusion of parasite echo coming from the surface;
- a radio frequency subsystem which contains both the transmitter and the two digital receivers, one for the dipole antenna and the other for the unipolar one;
- an electronic digital subsystem which includes a signal generator, a control and a processing data units.

The MARSIS operates both in passive (receiving only) and in active mode. The passive mode carries out in-situ measurements of electron density by the thermal emission at the electronic plasma frequency. In the active mode, MARSIS transmits a pulse MARSIS at a certain frequency and then it measures the radar echo reflection intensity as a function of the signal delay.

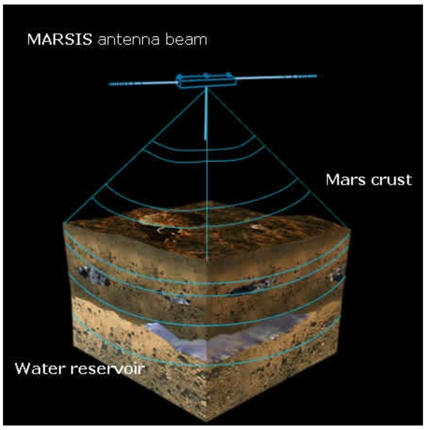

Figure 3.1: Representation describing the the MARSIS instrument operation and the possible detection of underground water reserves.

The transmission and reception cycle is repeated at a fixed rate under the control of the system called "Pulse Repetition Frequency". Of the five bandwidths (Fig. 3.2) the first is only for the ionosphere sounding, while the other four are for the sounding of both the ionosphere and the subsurface. The

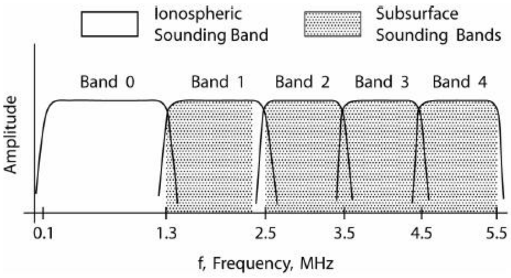

Figure 3.2: The five bands of MARSIS receiver. The first is only for the ionosphere sounding, while the other four are for the sounding of both the ionosphere and the subsurface.

active mode performs the ionosphere sounding in the orbiter passages at an altitude below 1200 km, both during the day and the night. The sinusoidal pulses, having a nominal duration of 91.4 $\mu$s, are sent in 160 frequencies, which cover the range from 100 kHz to 5.5 MHz [169]. The pulse is transmitted every 7.85 ms by the dipole antenna and the intensity of each echo return is detected in a frequency band of 10.9 kHz digitally constructed and centered on the frequency of the transmitted pulse. The echo delay is determined by sampling the signal intensity in 80 temporal cells equally spaced, extending from 0 to 73.1 ms after the transmitted pulse. The total frequencies range, 5400 kHz, is divided into 495 small intervals of 10.9 kHz for each one. Among these 495 frequency values, only 160 are chosen having a fractional frequency difference equal between them on a quasi-logarithmic scale. Some of these 160 frequency values have been replaced by nearby frequency values because the high level of interference caused by the satellite electronics at certain frequencies. A full scan of all 160 frequencies employs 1.257 s, and the entire basic cycle is repeated every 7.54 s.

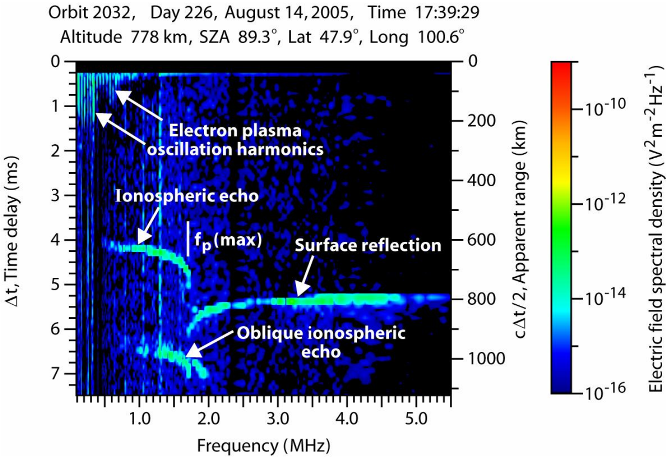

Figure 3.3: Example of a typical ionogram retrieved by MARSIS data, in which it is possible to clearly recognize the vertical and oblique ionospheric echoes, as well as the reflection from the surface.

It is important to investigate the ionosphere of Mars both because we know relatively little about it and because it has a strong influence on the surface and subsurface exploration. Since the electronic plasma frequency is given by $f_p = 8980\sqrt{n_e}$, where $n_e$ is the number density electronics in $\text{cm}^{-3}$, the sounding is possible because radio waves at a certain frequency $f$ are reflected by the ionosphere if $f = f_p$. The reflection occurs because the free space cannot propagate electromagnetic waves through an ionized gas at frequencies below the electronic plasma frequency [97]: when the wave frequency is equal to $f_p$, the vertically incident radio waves on the horizontally stratified ionosphere are reflected back towards the satellite. The transmission through the ionosphere is possible only at frequencies higher than the maximum frequency of inospheric electronic plasma. Even at frequencies higher than the maximum $f_p$ the ionosphere still has an effect on the radar signal because the refractive index deviates from the value that it would have in the free space ($n = 1$) [169, 97]: this effect is called "dispersion".

The MARSIS ionospheric radar soundings showed that the ionosphere of Mars is in good agreement with the expectations of the photo-equilibrium theory (Chapman, 1931) for the origin of planetary ionosphere. The data also revealed a number of not expected features, including echoes which recur with electron cyclotron period, large variations in the absorption apparently caused by energetic solar events, oblique echoes caused by ionospheric structures associated with magnetic fields of the Martian crust, widespread echoes apparently caused by diffusion by ionospheric irregularities, and ionospheric holes. Since the subsurface sounding must be carried out at frequencies much higher than the maximum electronic plasma frequency in the ionosphere and under conditions of low ionospheric absorption, has been demonstrated that these measures are very useful for planning subsurface sounding operations. The echoes of electronic cyclotron also provide a new method to measure the strength of the local magnetic field, since Mars Express does not have a magnetometer.

### 3.3.3 OMEGA: Visible and Infrared Mineralogical Mapping Spectrometer

OMEGA, born by the international collaboration between France, Italy and Russia, is an imaging spectrometer in the visible and near infrared, which operates in the spectral range 0.35 - 5.2 $\mu$m. This instrument is designed to provide the mineralogical and molecular composition of the surface and of atmosphere of Mars. OMEGA has two channels, one for the visible radiation (0.35 - 1.0 $\mu$m) and the other one for the IR radiation (1.0 - 5.2 $\mu$m). Both channels include:

- a telescope;
- a spectrometer;
- a device for focusing the light on a CCD (charge coupled device), in the case of the visible channel, and on two InSb arrays, in the case of the IR channel.

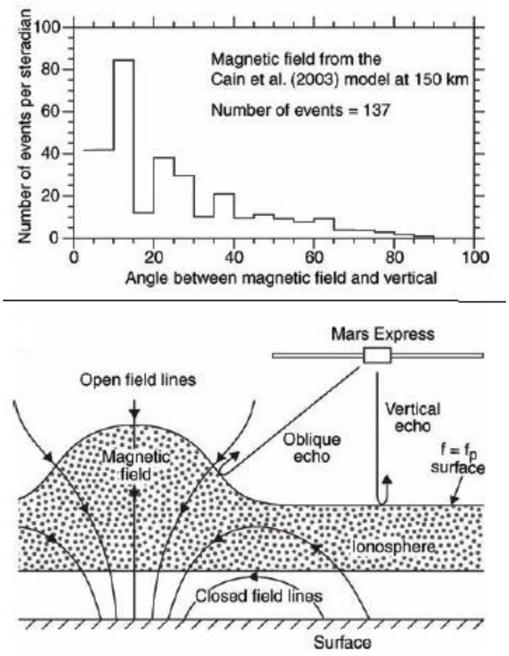

Figure 3.4: Top: Events distribution of oblique echo as a function of the angle between the magnetic field and the vertical axis as measured by MARSIS [98]. Bottom: Representation of the ionospheric density structures that are responsible for oblique ionospheric echoes.

The visible channel uses a 384 x 288 pixels CCD that, in the predefined operational modes, are coupled in 3 × 3 or 3 × 2, giving a spectral resolution of 7 nm and 4 nm, respectively. The total field of view is 8.8°. The IR channel is divided into two subchannels operating in the wavelength range 1.0-2.7 $\mu$m and 2.6-5.2 $\mu$m, with a spectral resolution of 13 and 20 nm, respectively. The detectors are constituted by 128 InSb in series detectors, each cooled to 70K by a dedicated cryogenic cooling system, while the two spectrometers are cooled to 190K by a passive radiator. The instrument weighs 29 kg (Fig. 3.5).

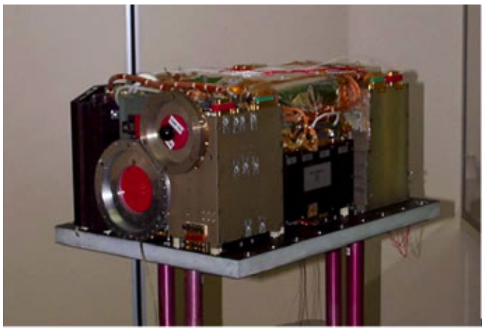

Figure 3.5: The OMEGA instrument in the laboratory. We can see two entrance windows for the visible and the IR channels.

With the progress of the Mars Express orbiter in its orbit, OMEGA builds gradually the planet map into squares, which correspond to pixels, with sides ranging from 4 km to 300 m on the surface. One of the main goals of this instrument is to generate a map of the entire surface with a resolution of 1 to 4 km and of the selected sites (2 - 5% of the Martian surface) with a resolution of 300 m. The OMEGA high spatial resolution had never been achieved before: this feature and its spectral range make possible to identify specific minerals on Mars more accurately than any other instrument aboard a previous spacecraft.

OMEGA maps silicates, the surface iron content, the oxidation level of the iron, the hydration of rocks and clay minerals and the abundances of the non-silicates, such as carbonates and nitrates. The knowledge of this composition is necessary for an understanding of many issues about Mars. Our understanding of the tectonic history of the planet, for example, becomes increasingly profound thanks to more accurate knowledge of the location and composition of igneous rocks. The climatic history and the current climate of the planet are studied through accurate measurements of the content of water and carbon dioxide in the ice caps, because these quantities vary with the season. In addition, OMEGA studies indirectly carbon dioxide from the calcium carbonate measurements, in fact it is created when water containing dissolved carbon dioxide reacts with calcium. Therefore, the discovery of sedimentary rocks consisting of carbonates on Mars would be strong evidence of the fact that the planet housed for a long time liquid water on the surface, with the possibility to support the existence of simple living organisms. The major objective of OMEGA lies in mapping the bands intensity at 3.6 $\mu$m and 3.9 $\mu$m (calcium carbonate), and at 3 $\mu$m (water) on the Martian surface.

### 3.3.4 SPICAM: Ultraviolet and Infrared Atmospheric Spectrometer

SPICAM is a UV-IR small instrument originally designed for the Mars 96 mission, and used, after the application of some changes, for the Mars Express mission: its aim is the study of the Martian atmosphere.

A UV spectrometer (118 - 320 nm, with spectral resolution of 1.5 nm) works in three different operational modes: in the first mode, *nadir pointing*, the instrument points directly Mars and the sensor detects the sunlight that has passed through the atmosphere after being been reflected from the planet surface; in the second mode, *solar-stellar occultation*, the instruments points a star, or the Sun, and directly measures the radiation absorbed by the atmosphere; in the third mode, *limb pointing*, the instrument points the atmosphere without the presence of a star in the background, thereby it measures the radiation emitted or scattered by the atmosphere. Thus, it is able to study the ozone and its coupling with $H_2O$, aerosols, vertical structures of atmospheric temperatures and also the ionosphere.

The telescope of the SPICAM UV channel is a single axis parabolic mirror, and in its focus there is a slit, which acts both to define the *Field of View* (FOV) and as the spectrometer entry slit. This instrument uses a toroidal holographic grating, with the dispersion direction perpendicular to the slit. Thus, each point of the slit has its spectrum perpendicular to it, the photocathode of an image intensifier with a cathode of CSTE (sensitive to UV radiation, but not to the visible one), an electrons photomultiplier plate, and a phosphorus output screen. The image is transferred from the screen by optical fiber coupled to a Thomson CCD (384 × 288 pixels). The 288 rows of the CCD are oriented along the spectral direction, and each line records the spectrum of an entry point of the slit, with 384 spectral elements. The telescope focal length is such that a pixel of the CCD covers a FOV of 0.01 × 0.01°.

A IR spectrometer (1.0 - 1.7 $\mu$m, with 0.5 - 1.2 nm resolution) makes only nadir observations and it is dedicated to the study of $H_2O$, $CO_2$, CO, aerosols vertical profiles, and to the exploration of carbon compounds during solar occultation. A simple processing units provides the interface of these sensors with the satellite.

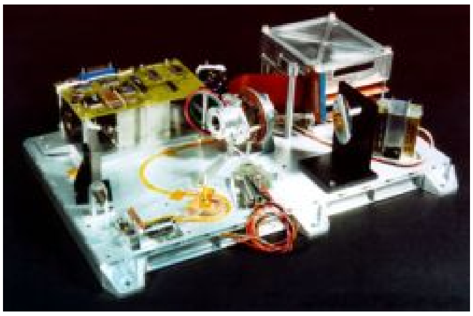

Figure 3.6: A SPICAM model used in pre-launch tests.

In the nadir orientation, the SPICAM UV is essentially an ozone detector, by measuring the stronger $O_3$ absorption band at 250 nm in the spectrum of solar light diffused back from the surface. In the stellar occultation mode the UV sensor measures $CO_2$, temperature, $O_3$, clouds and aerosols vertical profiles.

Temperature and density profiles obtained with SPICAM help in the development of meteorological and dynamical atmospheric models, from the surface to 160 km in the atmosphere: this will be essential for future missions, which could use the atmospheric friction to gradually bring a spacecraft to a desired orbit (*aerobraking*), or on the surface (*aerocapture*).

The UV observations of the upper atmosphere allow the study of the ionosphere through the CO, $CO^+$, and $CO_2^+$ emissions, and their direct interaction with solar wind. This instrument also allows a better understanding of the escape mechanisms and to estimate their magnitude, crucial for the study of the Martian atmosphere evolution.

The main scientific aims of SPICAM IR sensor are to map the whole $H_2O$, $CO_2$, CO, HDO, aerosols, atmospheric density, and temperature vertical structure by solar occultation. The high spectral resolution of the IR spectrometer allows the study and research of carbon compounds in the Martian atmosphere.

## 3.4 Planetary Fourier Spectrometer (PFS)

The Planetary Fourier Spectrometer (PFS) [84] was built the first time for the Russian Mars 96 mission. This instrument is a double pendulum Fourier transform interferometer, with capabilities similar to the IRIS Mariner 9 experiment in the thermal infrared wavelengths (250 - 170 $cm^{-1}$ or 5.5 - 45 $\mu$m), but with an additional channel for small wavelengths (SW), which covers the spectral range from 1700 to 8200 $cm^{-1}$ (1.2 -5.7 $\mu$m). The spectral resolution is the same over the entire spectral range and it is equal to 1.3 $cm^{-1}$.

The PFS aboard Mars Express is the result of the collaboration of several groups from different countries: Italy, Russia, Poland, Germany, France and Spain. The flight hardware has been produced in Italy (main electronics, which controls the experiment, the interferometer block with the electronic control and the GSE with the satellite simulator), and in Poland (the power supply and pointing systems). Russia and Germany have produced some flight parts, whereas flight software was produced in Italy. Although the project was taken by the previous Russian Mars 96 mission, the implementation of a strong revision had the effect of decreasing the original mass from 42 kg to 30.8 kg for MEX.

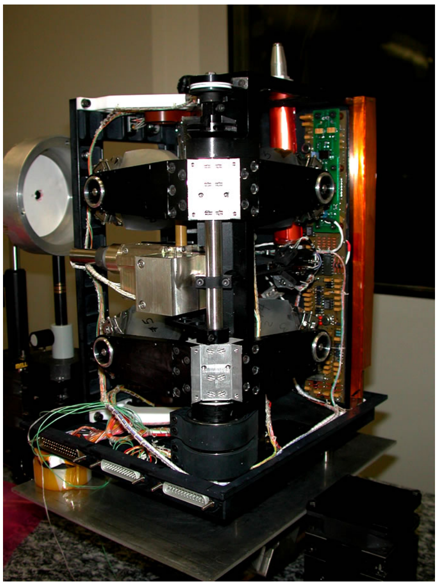

Figure 3.7: Photos of the PFS instrument in the laboratory.

This instrument has been designed with the aim of solving the $CO_2$ band inversion problem at 15 $\mu$m to obtain the vertical profile of the atmospheric temperature without any assumption about the pressure and temperature on the ground, and to retrieve the dust content of the atmosphere. Another very important goal is to obtain a complete global coverage of the planet Mars in every season to study the seasonal variations in global circulation. The high spectral resolution in the SW channel (resolving power greater than 5500) allows to study the mixing ratio of trace gases in the atmosphere of Mars. Furthermore, when the atmospheric transmissivity allows it, we can study the mineralogical composition of the soil, and in particular the hydrated minerals and ice caps [159, 162].

In this section we will focus on the PFS description, on the operations in space, on the problems encountered and on the two channels calibration.

### 3.4.1 Instruments Description

PFS is a double pendulum interferometer working in two wavelengths ranges (1.2 - 5.7 and 5.5 - 45 $\mu$m). The radiation to be analyzed is divided into two beams by a dichroic mirror. The two intervals correspond to two planes, one above the other, in which the two interferometers are placed, so that the same motor can move simultaneously the two pendulums and so the two channels are simultaneously and independently sampled. The pendulum motion is controlled accurately by means of a reference channel generated with a laser diode, which uses the same optics used by Mars radiation. The same laser diode also generates the sampling signal for the analog-digital converter (A/D), measuring a difference in optical path length of 608.4 nm.

| PFS Parameters | SW Channel | LW Channel |
|---|---|---|
| Spectral Range | 1.2-5.5 $\mu$m (1700-8200 cm$^{-1}$) | 5.5-45 $\mu$m (250-1700 cm$^{-1}$) |
| Spectral Resolution | 1.3 cm$^{-1}$ | 1.3 cm$^{-1}$ |
| FOV | 1.6° | 2.8° |
| Detector Type | Photoconductor | Pyroelectric |
| Detector Material | PbSe | $LiTaO_3$ |
| Temperature | 210 K | 290 K |
| Beamspitter | $CaF_2$ | CsI |
| Max. optic. path differ | ±5 mm | ±5 mm |
| Time for motion | 5 s | 5 s |
| Samplings number | 16384 | 4096 |
| Sampling step | 608 nm | 608 nm (over sampled ) |
| Dynamical range | $2^{15}$ | $2^{15}$ |
| Spectral points | 8192 | 2048 |

Table 3.2: Detailed parameters of the PFS instrument for the two channels (SW and LW).

The PFS is divided into four parts, called modules, connected by cables to various interfaces. The interferometer, with its optical and electronic systems, is the main part of the experiment and is called “O Module”. The pointing device, which allows to collect the radiation from Mars or from on-board calibration sources, is the “S Module”. The digital electronics, including the 32 Mbit mass memory and a device for the FFT calculation in real time, constitute the “E Module”. The power supply unit, together with the two DC / DC converters, a generator of reference voltage for the 16-bit Analog-to-Digital converters and a second group of redundant power supply, is the “P Module”.

#### 3.4.1.1 PFS optical scheme

The optical scheme of PFS is shown in Figure 3.8. The incident IR beam arrives (from a pointing mirror) on the input filter which separates the radiation in two beams and directs each of them in the appropriate channel (SW and LW) of the interferometer. The pointing mirror ("scanner") in front of the interferometer allows the FOV (*Field Of View*) to be pointed along or laterally respect to the projection of the flight path on the Martian surface, and also directs the FOV to the black body internal source and toward the deep space for in-flight calibration.

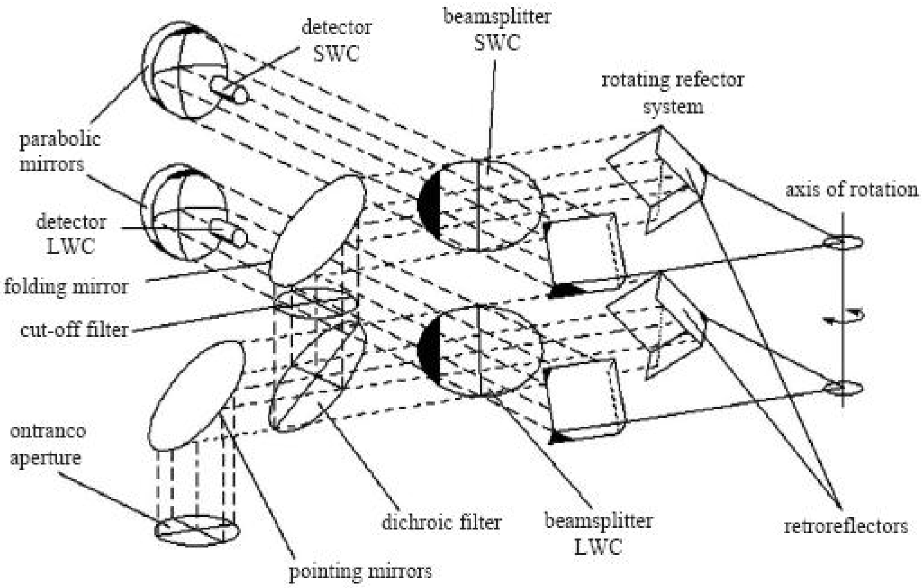

Figure 3.8: PFS optical scheme.

Each PFS channel is equipped with a pair of retroreflectors attached through bearings to an axis which is rotated by the torque generator, forming a double pendulum. The same axis and the guide mechanism are used for both channels, which are placed one upon another. The difference in the optical path is generated by the angular movement of the retroreflectors [108]. This design provides a more robust instrument than the classical Michelson interferometer.

The detectors are placed at the center of parabolic mirrors. The optical path is changed by rotating the double pendulum shaft along its axis. In this way, the optical path difference is four times greater than the displacement of a single cubic mirror (retroreflector) since the two mirrors move at the same time. The dichroic mirror has the task of dividing the radiation in the two spectral ranges: it reflects all wavelengths smaller than 5.5 $\mu$m and transmits the higher ones. The filter that defines the bandwidth and eliminates the radiation having a wavelength smaller than 1.2 $\mu$m is constituted by a silicon window, having a cutoff at 1.24 $\mu$m and placed in the optical entrance of the SW channel; this filter is tilted by 1.5° to prevent the radiation from the source which is partially reflected on the detector.

The double pendulum axis rotates by means of a brushless motor (two for redundancy) which has no mechanical friction. Thus, the double pendulum support is sustained by two ball bearings, which are characterized by very low friction, while it was added an additional friction to stabilize the speed of the pendulum.

If we set the zero optical path difference at the center of the mirror displacement, we can acquire interferograms called "double sided". A double sided interferogram has many advantages, including the lower sensitivity to phase errors. A bilateral operation is taken to reduce the cycle time of each measurement, but it is recommended a separate calibration for each direction to keep the predetermined radiometric accuracy.

A laser diode (InGaAsP at 1.216 $\mu$m) acts as a spectral reference and its detector is a infrared photodiode with maximum responsivity at about 1.2 $\mu$m. The beam of the reference channel is processed as the input signal so that the optical path of the reference signal is exactly coincident with that of the signal to be studied. In addition, each channel has its own reference beam and the different length of the double pendulum arms is completely compensated. The beam path of the reference channel is just outside the Mars radiation beam. Since the beam splitter of the LW channel is not transparent at the corresponding laser diode wavelength used as reference, it has been included a small special window during its manufacture so as to produce a negligible attenuation of the laser beams through the beam splitter itself. The outgoing beams of the two unused reference channels terminate in optical traps [170].

#### 3.4.1.2 PFS-O Electronics

The most important block in the O-module electronics is the speed controller. The interferogram zero-crossing of a monochromatic source with a very stable wavelength can be used to sample the interferogram of the source that should be studied. In the ideal case the interferogram of a monochromatic source should be a pure sine wave, but this is not possible because its interferogram is limited in time. In general, smaller is the reference source wavelength, greater is the accuracy of the sampling.

PFS uses a laser diode emitting at 1216 $\mu$m as the reference source because this type of device has a limited availability, and to simplify the optical design. Since the wavelength of a laser diode depends on its temperature and power, it must take special care in controlling them. The speed of the double pendulum is such that a radiation is generated at a frequency of 2 kHz for the SW channel: thus a pulses train with a frequency of 4 kHz comes out from the SW reference channel electronics. The thermal control is very important for an infrared interferometer and for this reason PFS uses eight points for reading the temperatures and for heating the structure.

During launch and during the orbit insertion and orbital corrections maneuvers it has been used a locking system of the double pendulum. The procedure for locking and unlocking takes a minimum of 10 min but it may be repeated hundreds of times since it uses a paraffinic actuator.

The SW channel detector is a photoconductor capable of working at low temperatures down to 200 K: its cooling is obtained passively by means of a radiator and its support is partially isolated from the rest of the interferometer. For the LW channel has been used a pyroelectric detector capable of working without degradation in performance even at room temperature.

#### 3.4.1.3 Operational Modes

The PFS experiment has three operational modes:

- *Science Mode*: used during the observing sessions;
- *Sleep Mode*: the interferometer and the pointing mirror are switched off, while the digital electronics keep data, receive remote controls, and perform other activities;
- *Autotest Mode*: making a series of special measures to control the motion stability, the optical alignment, and other special features.

### 3.4.2 Thermal Control

PFS must meet many contradictory requirements, as, in particular, what concerns the SW channel detector, which needs to be cooled to 200-210 K, while the rest of the experiment operates at 285 K. The temperature of the laser diode needs to be stable within 0.1° to ensure that the motion is free from problems caused by laser non-monochromaticity. The LW channel detector needs to be thermally stable, to measure a variable planetary surface temperature, because PFS works as a differential instrument.

The temperature of the laser diode is very well controlled and stable, so that it is guaranteed a good stable motion of the double pendulum. Similarly, the detector temperature of the LW channel is well controlled. On the other hand, the detector temperature the SW channel is well cooled thanks to the radiator provided by the satellite.

### 3.4.3 Mechanical Control

PFS has three mechanical devices, whose performance is essential for the functioning of the experiment:

- Locking-release system: a paraffin actuator used to lock the pendulum during the launch of the spacecraft and during the other possible violent maneuvers;
- Pointing mirror: it has eight possible positions: five around the Nadir (0, ± 12.5°, ± 25°), one to deep space (+85°), and the other two to the internal calibration blackbody and lamp;
- Double pendulum: it has only one motor for the two channels, plus a spare motor.

The motor speed, which must be as constant as possible, is controlled by a system that uses the interferogram of the laser diode signal to generate a feedback to keep it. The interferogram of the laser diode radiation is a sine wave whose zero crossings are used to sample the interferogram of Martian radiation, and at the same time, to control the pendulum speed. In the operational mode called "Autotest", it is measured the time between successive zero crossings as a test for the quality of the motion speed. Incorrect laser diode temperatures may occasionally generate a non-monochromatic signal, which generates a non-uniform motion, and this problem can be revealed by the Autotest mode. Also the external vibrations can generate a non-uniform motion, and these can always be detected in the Autotest procedure (Fig. 3.9).

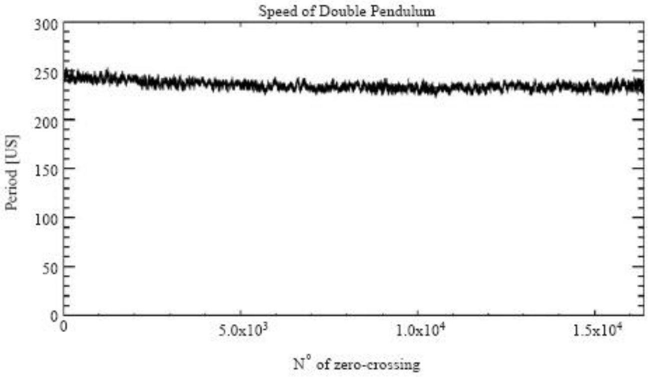

Figure 3.9: Example of Autotest measures acquired in the laboratory.

The time difference measured between the zero crossings determines the speed: for the nominal speed, the interval between zero crossings should be close to 250 $\mu$s (2000 Hz). On board MEX and in space, speed measurements by the Autotest procedure gave a clear indication of the presence of mechanical vibrations. In particular, the disturbance frequencies were identified in the spectrum of the laser diode radiation as a central peak at 595 Hz, with two secondary peaks at 545 and 655 Hz. The effect of these disturbances is to increase the noise in measurements in special narrow bands of wave numbers equivalent to those of the mechanical vibration.

These frequencies depend on the speed used for the pendulum, so changing it, it is possible to move the narrow-band with increased noise in different parts of the radiation spectrum. After a long study, the speed of the pendulum was increased by 25% to reach the best compromise between noise in the LW and SW channels. In practice, the compromise shifts the disturbances to a wave numbers range of lower scientific importance.

### 3.4.4 In Flight Activity

During the observation session on a Mars orbit (pericentre passage) PFS initially performs the calibration measurements, pointing the scanner sequentially toward deep space and the calibration sources. Then, PFS acquires a predetermined number of measurements with the scanner pointing nadir. Finally, the calibration sequence is repeated. The Autotest is performed before the first and after the second calibration sequence. Each measurement has a header that contains all the necessary preparation information.

#### 3.4.4.1 Data Transmission Modes

The data transmission mode defines the type of scientific data PFS must select and store in the mass memory to be sent to Earth. The transmission modes 1-14 are obtained with PFS functioning as operational science mode, while only the transmission mode 0 is obtained when PFS is operating in the Autotest mode.

For each transmission mode of scientific data, PFS acquires both LW and SW interferograms, and if the spectra are required, it makes a fast Fourier transform (FFT) of the interferograms. Finally, according to the data transmission mode, PFS produces the required data. The instruments can transmit both full interferograms or only their central part, however, providing a reduced spectral resolution.

### 3.4.5 Calibration of the LW Channel

The detector of the LW channel works at room temperature $T_0$ and it is sensitive to the temperature difference between the emitting source ($T_s$) and the temperature of the detector itself. The amplitude of the measured signal is therefore dependent on $\Delta T = |T_0 - T_s|$, giving great importance to the thermal control of the detector during the calibration measurements.

The amplitude $S(\nu)$ of the LWC spectrum is proportional to the difference between the radiance coming from the source to be studied $I(\nu)$ and the instrument emission $I_0(\nu)$:

$$|S(\nu)| = R(\nu)\, |I(\nu) - I_0(\nu)| \tag{3.1}$$

The proportionality factor $R(\nu)$ is the instrument *responsivity.* The instrument emission $I_0(\nu)$ depends essentially on its temperature. If the instrument thermal conditions are stable, i.e., if $I_0(\nu)$ remains constant during different observations, we can obtain the responsivity directly from equation 3.1 simply observing a reference blackbody with two different temperatures and thus eliminating the emission of the instrument itself $I_0(\nu)$. Unfortunately, in this case the instrument is not composed by a single block at the same temperature, but by two parts: the detector and the optical bench. The detector temperature was not stable in the laboratory measurements, while the interferometer temperature is not usually stable in space.

In order to achieve the best interaction model, several approaches have been tried and the results are different if developed by ground or in space measurements [92]. In particular, the calibration procedure has been studied in three different cases:

1. By laboratory measurements using two external black body sources and one internal to the instrument. The two external sources are the *IFSI*

*black body* with a certified emissivity of 0.970±0.005 in the range 8-15 and 3-5 $\mu$m, and the *IKI black body*, developed in Russia, but available in IFSI, and having an emissivity of 1.0±0.1 estimated by laboratory measurements in Lecce.

2. From measurements acquired during the space phase called Near Earth Verification (NEV).

3. From measurements acquired in orbit around Mars.

The detailed structure of the responsivity curve (Fig. 3.10) is determined primarily by the properties of the beam splitters coatings, by the characteristic transmission of the input window and by the spectral response of the detector.

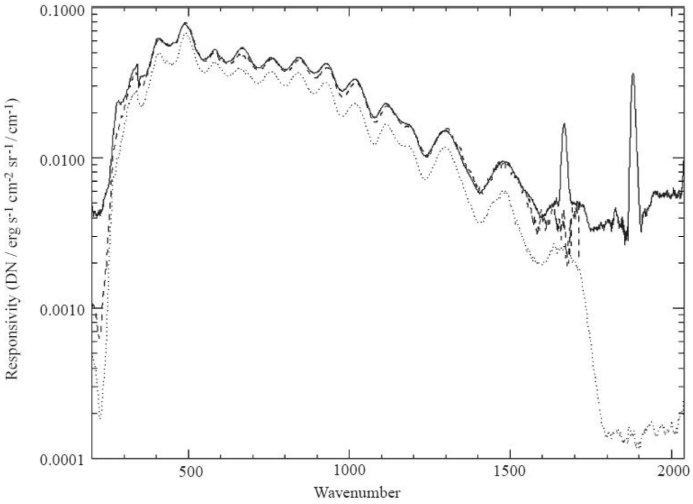

Figure 3.10: Comparison between the responsivity measured in space (continuous line), the responsivity measured in the laboratory with the IFSI black body (dotted line) and the one with the IKI black body (dashed line) [92].

Once obtained the responsivity curve, and therefore the radiance, we can calculate the NER (Noise Equivalent Radiance), which represents the radiance that a source must have in order to produce a signal equal to that generated by the instrumental noise, or in other words, the minimum detectable signal. For a fixed source and for many measurements, the radiance as seen from the PFS can be expressed as

$$b_{i,T}(\nu) = \frac{S_{i,T}(\nu)}{R(\nu)}, \tag{3.2}$$

where $S_{i,T}(\nu)$ is the i-th spectrum of the measurement session with a blackbody at the $T$ temperature and $R(\nu)$ is the responsivity previously calculated.

Using all the spectra for various temperatures, the NER is given by

$$NER(\nu) = \sqrt{\frac{\sum_T \sum_i \left[b_{i,T}(\nu) - \bar{b}_T(\nu)\right]^2}{n}}, \tag{3.3}$$

where$\bar{b}_T(\nu)$ is the average radiance per temperature and $n$ is the total number of spectra. The NER of PFS in the laboratory officially adopted is taken from measurements made in a thermal-vacuum chamber pointing the internal black body, and it is shown in Figure 3.11.

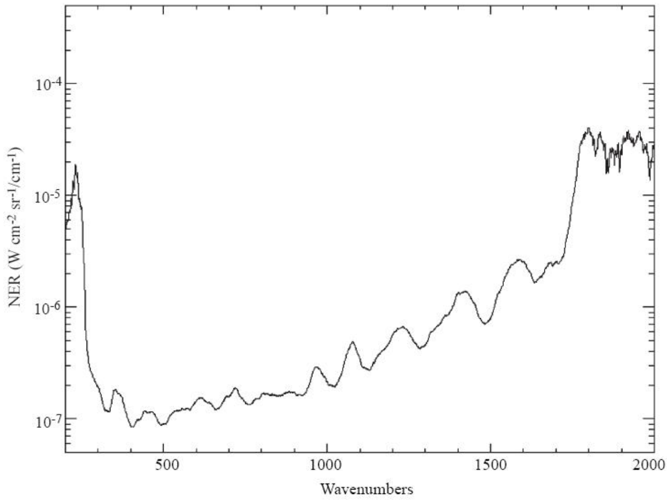

Figure 3.11: NER obtained from internal black body measurements in a thermal-vacuum chamber.

As previously mentioned (par. 3.4.3) it was necessary to increase the double pendulum speed by the 25%, so the calibration procedure was repeated for this new parameter. A different speed implies a different band-pass filter applied to the signal, then the spectral shape of the same source has become a little different, as well as the positions of the peaks induced by mechanical vibration are also different. From this study it was possible to note that the responsivity and the NER calculated at different speeds of the double pendulum have small differences: in particular the responsivity curve calculated at 2500 Hz is slightly higher before 500 cm$^{-1}$ and lower after 500 cm$^{-1}$.

On Mars, using the calibration procedures developed by both ground measurements and during NEV, results were affected by problems: in fact, the small oscillations due to optical modulation of the signal, having maximum amplitude when the instrument points deep space, and minimum when Mars has the same temperature of the instrument (287 K), have not been completely eliminated, thus introducing unwanted structures in the spectrum. In this case the equation 3.1 can be rewritten as

$$|S(\nu)| = R(\nu)I(\nu) - R^0 I^0(\nu), \tag{3.4}$$

i.e., the PFS responsivity of deep space observations must be considered different from the responsivity of Mars observations. On the other hand, the second term is the spectrum measured by observing the deep space. This term is not constant since it depends on the interferometer temperature, and it undergoes changes during the transit around the pericentre. Fortunately, we have deep space measurements just before and just after this transit, so we can interpolate the deep space spectrum at the temperatures measured for each acquisition. The equation 3.4 provides the Mars radiance if you use the correct responsivity. Sometimes, also the laser diode temperature is not constant, then we must resample $R$ at the corrected wave numbers taking into account the laser diode temperature.

Finally, in this way, we obtain the thermal calibrated radiance emitted by Mars. A typical single calibrated spectrum of Mars is shown in Figure3.12: it is evident the very deep $CO_2$ band at 15 $\mu$m, as well as a dust wide band between 850 and 1200 cm$^{-1}$.

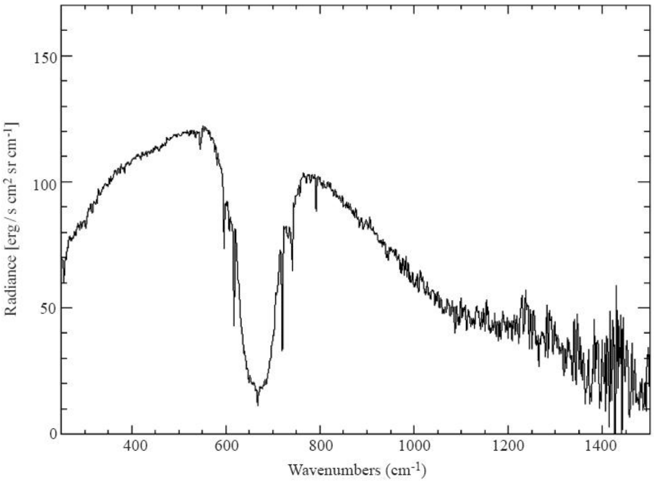

Figure 3.12: Typical calibrated spectrum of the PFS LW channel of a Mars measurement.

### 3.4.6 Calibration of the SW Channel

The SW channel detector is a semiconductor device, working at the cooled temperature of $T_0$ = 200-220 K. Since the same detector covers a wide spectral range, the SW channel is capable to measure two different regimes: thermal radiation and reflected solar radiation. This implies two different behaviors for the interaction of the system detector-instrument-source: in the thermal regime there is an interaction similar to the one studied for the LW channel (par. 3.12), while in the solar radiation range this interaction is negligible. The solar radiation in the range 1.2-4 $\mu$m, if expressed in terms of *brightness temperature*[1], should give very high temperatures, certainly higher than the detector temperature ($T_d$ = 210 K), and than the instrument one ($T_i$ = 283

---

[1] The *brightness temperature* characterizes the *brightness* (or *specific intensity*) at a certain frequency and it is defined as the temperature of the black body having the same brightness at that frequency.

K). In the thermal radiation range of the SW channel, PFS is sensitive to the temperature difference between the emitting source ($T_s$) and the temperature of the detector, so the amplitude of the signal depends from $\Delta T = |T_0 - T_s|$. This means that the thermal conditions of the instrument are very important: in the laboratory it has not been possible to stabilize the detector temperature at 200-220 K, as required, while in space, although not stably, these temperatures are well achieved.

As in the case of the LW channel also as regards the SW channel the calibration procedure has been studied in three different cases (par. 3.12): on ground laboratory, in NEV and on Mars. The calibration on the ground has been carried out using four calibration sources, two of which are the same used for the LW channel, and the others are: a "sphere integrator", which provides a radiance spectrum from 4000 to 8200 cm$^{-1}$, and a "mercury lamp", which provides a series of Hg lines, with the strongest at 6537.74 cm$^{-1}$. Moreover, also the internal black body interior and the internal calibration lamp were used as calibration sources.

The laser diodes used by PFS are, as already mentioned several times, temperature sensitive. This aspect is very important because during a measurement session, if the thermal conditions are not constant, the sampling step changes from one measurement to another. The used laser diode has also the tendency to have temperature ranges in which the wavelength is constant, and temperature ranges in which the laser is not monochromatic, and the double pendulum motion becomes disrupted, producing some "spiky" interferograms. The two laser diodes of PFS were calibrated in wavelength as a function of temperature using the mercury lamp (in laboratory) and some very narrow and well known (Martian) $CO_2$ lines together with the PFS monochromatic transfer function.

The monochromatic transfer function of a spectrometer is a very important function which must be measured because it introduces spurious structures in the measurements, so we must also study it to verify the validity of the apodization function adopted to eliminate the fictitious negative lobes on the sides of each spectral line. The transfer function of PFS was measured by pointing a monochromatic source (the mercury lamp) for a long time. The temperature of the laser diode, and thus the wavelength, changed with time, while maintaining fixed the source, and then producing a relative displacement between the source and the sampling point. The final result is a sinc-type function, while the instrument seems to have a (not apodized) spectral resolution of 1.3 cm$^{-1}$ (Fig. 3.13). The sinc function shows asymmetrical side lobes called *"ringing"*[2], important when studying individual lines in a spectrum. This effect is much smaller with the apodization (Fig. 3.13).

The calibration of SW channel on Mars can be divided into two parts: one related with the spectral range $\nu < 3900$ cm$^{-1}$ (thermal region) and the other related with the spectral range $\nu \geq 3900$ (solar region). The thermal

---

[2] When an interferogram ends at a finite length (real case), the monochromatic spectral lines have finite width and are accompanied by a series of side lobes, called *ringing*. The monochromatic spectral lines are modulated by a sinc function.

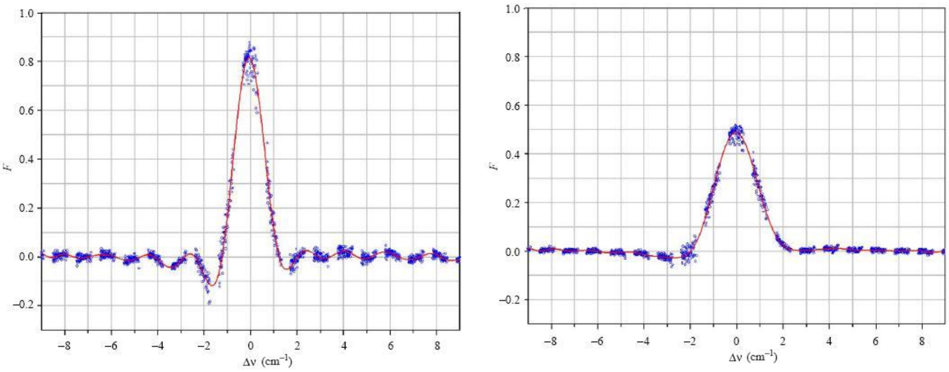

Figure 3.13: PFS not apodized (left) and apodized (right) monochromatic transfer function measured with a mercury lamp, where $F$ represents the line intensity.

responsivity in the thermal region can be obtained in the same way as the channel LW one (par. 3.4.5):

$$S(\nu) = R(\nu)I(\nu) - S_0(\nu), \tag{3.5}$$

where $S(\nu)$ is the spectrum amplitude of the PFS SW channel when pointing to a certain source, $I(\nu)$ is the radiance of the source, $S_0(\nu)$ is the emission of the instrument and $R(\nu)$ is the responsivity to be calculated. It is possible to use the internal blackbody as calibration source and deep space measurements to estimate the emission spectrum $S_0(\nu)$: the latter depends on the temperature of the interferometer, which is not constant during the transit to the pericentre. So, even this time, as in the case of the LW channel (par. 3.4.5) we interpolate the deep space spectrum in accordance with the interferometer temperature, having its measurements available before and after the transit to the pericentre.

From the two in-flight calibration sessions, we can calculate two responsivity curves by the equation 3.5 and then we can average them. However, since the SW channel responsivity depends on the detector temperature, if this is not stable we must interpolate the responsivity itself in agreement with the actual detector temperature during the acquisition of each spectrum of Mars.

Since during the in-flight calibration sessions only 10-20 internal blackbody and deep space spectra are acquired, the responsivity curve calculated by the equation3.5 is very noisy above about 2600 $\mathrm{cm}^{-1}$. In order to solve this problem we use the calibration measurements obtained during the NEV activity (more than 200 spectra) and a comparison with the Infrared Space Observatory (ISO) SWS observation of Mars made in July-August 1997 [85].

From studies made in the laboratory it has been demonstrated that the responsivity of the SW detector increases linearly with the temperature [93], so the spectrum of the internal calibration lamp, with the SW detector cooled to 212 K, is only 1-2 times higher than the signal with the detector at room temperature, despite the predictions of saturation. The reason can be found in a loss of optical alignment due, possibly, to the stress undergone by the PFS during the launch phase.

The responsivity of the SW channel on Mars in the solar spectral region is given by:

$$R^{212K}_{Mars}(\nu) = R^{293K}_{Lab}(\nu)K(\nu)V^{2500}_{2000}(\nu),$$

where $R^{293K}_{Lab}(\nu)$ is the responsivity obtained in the laboratory, $K(\nu)$ is the effective increase in the SW channel responsivity when it passes from laboratory conditions to the ones in space, and $V^{2500}_{2000}(\nu)$ is the function that takes into account the spectral changes introduced by the different speed used in the space (2500 Hz) and in the laboratory (2000 Hz).

Combining the thermal and solar ranges responsivities we obtain the entire responsivity of PFS SW channel, and then from this it is possible to draw the NER (Fig. 3.14).

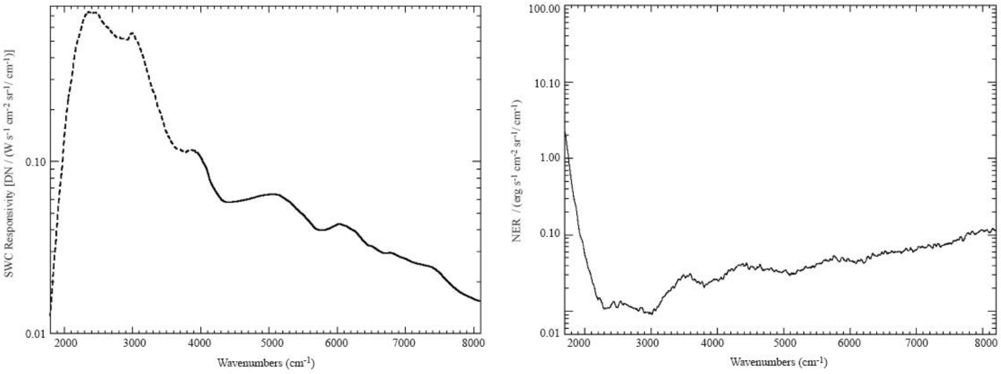

Figure 3.14: Left: Total responsivity of the SW channel in operating conditions in space, obtained by combining the responsitivies calculated for the thermal (dashed line) and solar (continuous line) ranges. Right: The NER of the SW channel in operating conditions in space. It is 10-20 times lower than the NER at room temperature.

Finally, in this way, we obtain the calibrated radiance emitted by Mars. A typical average Mars spectrum (1680 measurements) calibrated is shown in Figure 3.15: we can clearly identify a number of absorption bands due to CO, $CO_2$ and water vapor present in the Martian atmosphere. The Planck function for $T = 275.5$ K (average temperature of the PFS averaged spectra, taken from the LWC channel spectra) reproduces very well the thermal part of the observations.

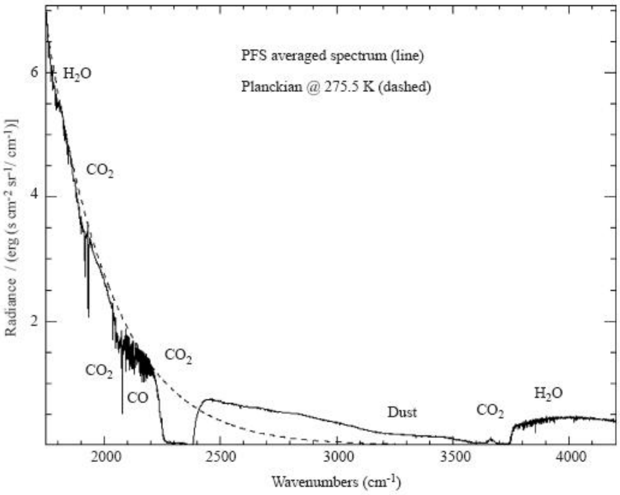

Figure 3.15: Calibrated PFS average spectrum in the range 1750-4200 cm$^{-1}$ in which there are shown the main absorption bands. The dashed line represents the Planck function for a blackbody at a temperature of 275.5 K, and it reproduces the thermal part of the spectrum.

# Chapter 4

# PFS Data Analysis

The study of data acquired by the PFS instrument, with the aim of retrieving the concentrations of water vapor and carbon monoxide in the atmosphere of Mars, requires the development of an analysis method suitable for this purpose.

Although there are several $H_2O$ and CO absorption bands in the spectral range covered by PFS, we used the 2.6 $\mu$m (3845 $cm^{-1}$) band for the water vapour and the 2.36 $\mu$m (4235 $cm^{-1}$) band for the CO analysis, because these ranges are less affected by instrumental problems compared with the other ones, and are out of the thermal range limit, avoiding in this way calibration problems due to thermal inversions in the PFS/SWC spectrum (Fig. 4.1).

This chapter describes the analysis method developed for the study of the $H_2O$ and CO concentrations in the atmosphere of Mars [183].

## 4.1 Data

Apodized spectra were used for this work because of their noise reduction and the decrease of the "overshooting" effect in the red wing that is typical for the PFS instrumental function. The spectral response function of the instrument has a FWHM[1] of 2.04 cm-1 with Hamming apodization and a sampling step of 1.05 cm-1. The loss of spectral resolution caused by the use of apodized spectra is not a problem, because the abundance analysis is done on absorption bands and not on single lines.

Regarding the in-flight performance, there are three causes for instrumental uncertainties that have to be taken into account: problems with radiometric calibrations, random noise due to the detector and AD converter and the influence of spacecraft vibrations [93]. The apparent partial loss of the optical alignment during the launch makes the absolute radiative calibration a difficult task, because it causes a modulation in the spectrum that must be corrected.

These instrumental uncertainties may alter the effective depth of the absorption lines, leading to errors in the estimations of gas abundance. In order

---

[1] The "Full Width at Half Maximum" (FWHM) is an expression of the extent of a function, given by the difference between the two extreme values of the independent variable at which the dependent variable is equal to half of its maximum value. In spectroscopy it expresses the spectral resolution.

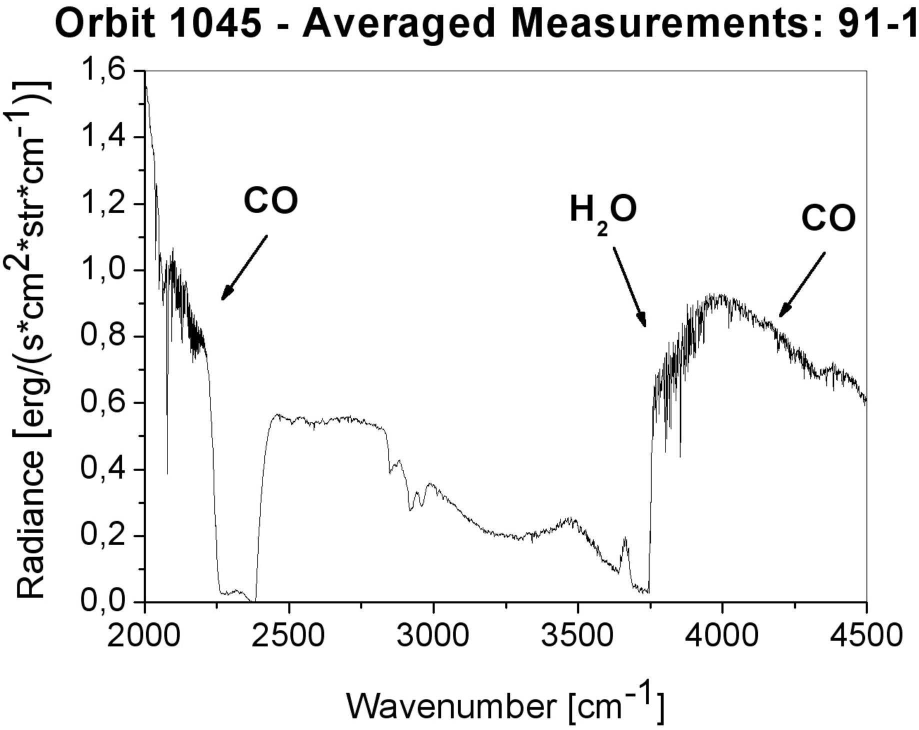

Figure 4.1: Portion of a typical mean apodized spectrum acquired by the PFS SW channel in the spectral range 2000-4400 cm$^{-1}$. We can clearly recognize the $H_2O$ (3846 cm$^{-1}$) and CO (2150 cm$^{-1}$ and 4235 cm$^{-1}$) absorption bands.

to reduce the noise and thus to improve the signal-to-noise ratio (S/N), we used average spectra and, to be independent on the absolute calibration, we analyzed the relative band depths. As inferred by Comolli and Saggin [56] and confirmed by Giuranna et al. [94] the spacecraft vibrations affect only the level of the continuum leaving unaltered the relative depth of the atmospheric absorption lines.

## 4.2 Analysis Procedure

In order to retrieve the $H_2O$ and CO concentration in the Mars atmosphere, we developed an analysis algorithm. The procedure carried out can be articulated in several points:

1. Reading of the averaged spectrum and its geometry data;

2. Wavelength grid correction;

3. Extraction of a vertical temperature and pressure profile from the Mars Climate Database (MCD, version 4.2 [80]);

4. Creation of synthetic spectrum by a line-by-line calculation of monochromatic opacities for $CO_2$, $H_2O$ (considering the saturation level of water, as defined in Section 4.2.2) and CO on the basis of MCD input. The obtained transmittance spectrum is multiplied with the solar spectrum and convolved with the PFS instrumental function;

5. Ratio of the averaged PFS spectrum and of the synthetic spectrum by their own specific defined continuum (normalization);

6. Finding the $H_2O$ and CO mixing ratio in a fitting loop using a $\chi^2$ minimization;

7. A posteriori CO values correction.

Moreover, we consider dust and ice aerosols particles, assumed to have an exponential vertical distribution. The properties of dust as a function of wavenumber are those proposed by Ockert-Bell et al. [158], whereas for water ice we used infrared refractive indices published by Hansen [101]. The grain size distribution used for the aerosols is that described in the model by Clancy et al. [54].

In this section we will describe all these points in detail.

### 4.2.1 Wavelength Grid Correction

The wavelength sampling in the averaged measured spectra can be lightly shifted because of the small temporal variations in the laser diode temperature and in the pendulum motion. Then, it is necessary to follow a correction procedure for the spectrum grid. The correction is done for each individual spectrum using a reference synthetic spectrum, which contains 300 ppm of $H_2O$ and 800 ppm of CO: in this way the exact wavelength of each absorption line is well defined. The procedure consists in the choice of three minima, representing the position in wavelength of three strong absorption lines in the spectral range where the absorption band of interest is contained, both for the observed and synthetic spectra. The correction factor for the wavelength grid is the mean value of the ratio between the wn (wavenumber) positions in the measured spectrum ($wnm$) and the corresponding ones in the synthetic spectrum ($wns$), i.e.

$$corr = \frac{\sum_{i=1}^{3} \frac{wnm_i}{wns_i}}{3}. \tag{4.1}$$

Averaging the three values is necessary because the correction factor can sometimes be slightly different over the whole spectral range considered. Therefore, in order to obtain the corrected spectrum it is sufficient to divide the old wavelength grid by the correction factor and then to interpolate the spectrum on the new grid (Fig. 4.2). The correction factor ranges from 1.00000 to 1.00046, with a mean value of 1,000180.00008 and a peak value of the histogram distribution of 1.00015±0.00015.

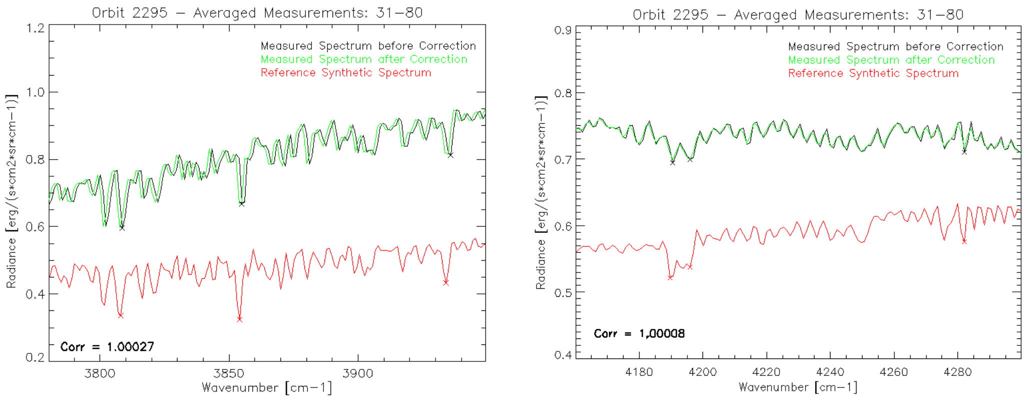

Figure 4.2: Typical examples of the correction procedure for the wave number spectral ranges containing the $H_2O$ (left) and the CO (right) bands in which we have highlighted the points chosen for this purpose.

### 4.2.2 Vertical Atmospheric Profiles

Before the computation of synthetic spectra, geometry data (Latitude, Longitude, Ls, Local Time and Altimetry) of the individual mean spectrum are used as input for the MCD Global Circulation Model (GCM) [80], which provides the vertical temperature and pressure profiles. We divided the atmosphere in 65 layers and the vertical resolution of our model decreases with altitude, going from about 400 m close to the surface, to 7 km at 115 km.

Alternatively, the vertical temperature and pressure profile can be obtained from PFS/LWC measurements using the approach by Grassi et al. [96].

Consequently the temperature profile determines the saturation pressure $p_s$ over ice (given in [Pa]) of the water vapour, according to the formula by Marti and Mauersberger [140] for the temperature $T$:

$$\log p_s = -\frac{2663.5 \pm 0.8}{T} + (12.537 \pm 0.011) \qquad (4.2)$$

Typical temperature and pressure vertical profiles provided by the MCD model are shown in Figure 4.3.

### 4.2.3 The Synthetic Spectrum

The atmospheric modelling was performed using the approach of Ignatiev et al. [112], thus considering the multiple scattering and the LTE (*Local Thermodynamic Equilibrium*[2]) conditions. Synthetic spectra are calculated line-by-line using the absorption coefficients extracted from precalculated gaseous opacities for the temperature and pressure profile of interest. The spectral lines are extracted from the molecular spectroscopic database HITRAN 2004 [178].

---

[2] We have a *Local Thermodynamic Equilibrium* condition when the intensive parameters (which do not depend on the system size or the amount of material in the system, as the temperature) are varying in space and time, but they are varying so slowly that, for any point, one can assume thermodynamic equilibrium in some neighborhood about that point.

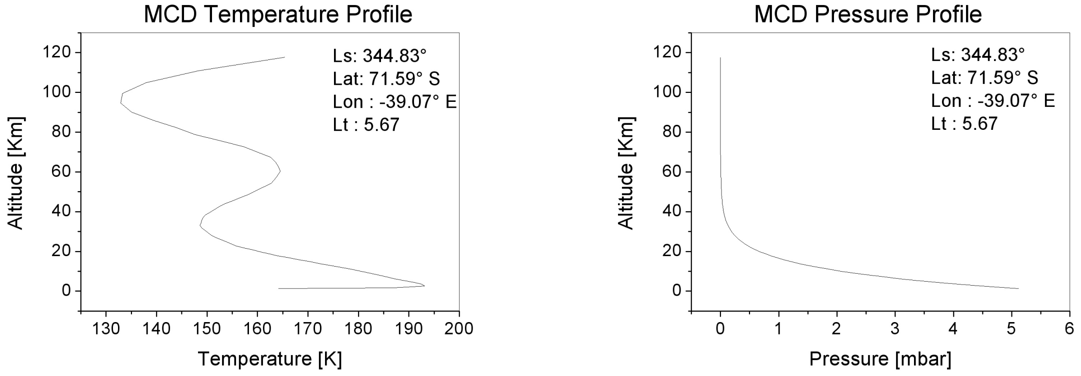

Figure 4.3: Typical temperature and pressure vertical profiles provided by the MCD model.

Like other databases, it contains, in particular, the following spectroscopic information for each line included:

- $\nu_0$: central line position (the subscript "0" indicates "normal conditions", ie at temperature $T_0$= 296 K, and pressure $p_0$= 1 atm = 101325 Pa);
- $S(T_0)$ : line intensity;
- $\alpha_{air}(P_0, T_0)$ : line half-width due to the air-broadening;
- $\alpha_{self}(P_0, T_0)$ : line half-width due to the self-broadening;
- $E''$ : lower state energy of the transition;
- $m$ : temperature dependence index of the Lorentz half-width.

Moreover, the FORTRAN codes of HITRAN include a subroutine for calculating the statistical sum $Q(T)$[3]. From these information we can calculate the gaseous absorption properties [178]. The absorption cross-section per molecule [cm$^2$] in a spectral line, considering a Voight line-shape[4], is given by the formula

$$\sigma_\nu = \frac{Sa}{\pi^{3/2}\beta}\int_{-\infty}^{\infty}\frac{e^{-t^2}}{a^2+(x-t)^2}dt, \tag{4.3}$$

with $a = \alpha/\beta$ and $x = (\nu - \nu_0)/\beta$, where $S$ is the line intensity, $\nu_0$ is the line center, $\alpha$ is the Lorentz half-width, $\beta$ is the Doppler half-width, which is defined as

$$\beta = \frac{\nu_0}{c}\sqrt{\frac{2RT}{M}}, \tag{4.4}$$

---

[3] The statistical sum (or partition function) is a function used in the statistical equilibrium physics and it is equal to a normalization constant in the density expression of a *Gibbs' canonical ensemble.*

[4] The Voight profile of a spectral line combines the Lorentz and Doppler effects in the functional form $f(\nu) = A\int_{-\infty}^{\infty}\frac{\gamma e^{-t^2}}{[(\nu_0-\nu)-t]^2+\gamma^2}dt$, where $A$ is a normalization constant and $\gamma$ is a parameter related to the width of the profile function.

where $R$ is the universal gas constant, $T$ is the temperature, and $M$ is the gas molecular weight expressed in [g/mole]. The integral over $t$ can be calculated using special procedures, described for example in [110] or in [142].

If we know the Lorentz half-width $\alpha(p_0, T_0)$ at pressure $p_0$ and temperature $T_0$, it can be calculated also for other pressures and temperatures by means of the formula:

$$\alpha(p, T) = \alpha(p_0, T_0)\frac{p}{p_0}\left(\frac{T_0}{T}\right)^m, \tag{4.5}$$

where $m$ is a particular parameter for each individual line. When the collisional cross-section is not dependent on temperature, the theory gives $m = 0.5$, but in practice $m$ is slightly different. Moreover, we have to keep in mind that since this database was created for the Earth's atmosphere, the correction for an atmosphere dominated by $CO_2$ (Mars case) is done using a broadening parameter varying between 0.9 and 1.9 from line to line [87]. In our case the broadening factor is set to 1.3, as done by Fedorova et al. [112].

However, we have to notice that the formula given by [177] for the half-width of the Lorentz line includes both the air and the self broadening:

$$\alpha(p, T) = \left(\alpha_{air}(p_0, T_0)\,(p - p_s) + \alpha_{self}(P_0, T_0)p_s\right)\frac{1}{p_0}\left(\frac{T_0}{T}\right)^m. \tag{4.6}$$

However, the validity of the formula 4.6 is not evident, indeed summing the opacity rather than the half-widths seems more reasonable, and for minor gases it might give only a very small correction to the spectra. For this reason, in our code we used the formula 4.5.

The line intensity for any temperature (for the HITRAN database) is defined as follows:

$$S(T) = S(T_0)\frac{Q(T_0)}{Q(T)}\exp\left\{-c_2E''\left(\frac{1}{T} - \frac{1}{T_0}\right)\right\}\frac{1 - \exp\left(-c_2\nu_0/T\right)}{1 - \exp\left(-c_2\nu_0/T_0\right)}, \tag{4.7}$$

where $c_2 = hc/k_b$, $S(T_0)$ is the line intensity at temperature $T_0$, $E''$ is the lower state energy of the transition, $Q(T)$ is the complete statistical sum (rotational + vibrational).

The total opacity produced by all the lines is equal to the sum of the opacities of individual lines:

$$\sigma_\nu = \sum_i \sigma_{\nu i} \tag{4.8}$$

The absorption coefficient for unitary path length for a hypothetical mixing ratio of 100% is equal to

$$k^1_\nu = \sigma_\nu n, \tag{4.9}$$

where $n = p/(k_bT)$. The optical depth $\tau_\nu$ is the integral of $k^1_\nu$ times the mixing ratio $q(l)$ along the vertical axis or the line of sight, depending on the considered particular situation:

$$\tau_\nu = \int k^1_\nu(l)q(l)dl. \tag{4.10}$$

The transmittance is simply defined as the exponent of the optical depth along the line of sight:

$$t_\nu = e^{-\frac{\tau_\nu}{\cos\theta}}. \tag{4.11}$$

In the solar region, we often deal with the total transmittance of the atmosphere from space to the surface and on the contrary:

$$t_\nu = e^{-\tau_\nu\left(\frac{1}{\cos\theta_0}+\frac{1}{\cos\theta}\right)}, \tag{4.12}$$

where $\tau_\nu$ is the total optical depth in the nadir direction, $\theta_0$ is the solar zenith angle, and $\theta$ is the zenith angle of the line of sight.

In the thermal region, the radiance $I_\nu$ is the integral of the Plank function over the transmittance from the bottom up to the top of the atmosphere, plus the emission of the surface

$$I_\nu = \varepsilon_\nu B_\nu(T_s)e^{-\frac{\tau_{max}}{\cos\theta}} + \int_0^{\tau_s} B_\nu(T(\tau_\nu))e^{-\frac{\tau_\nu}{\cos\theta}} d\left(\frac{\tau_\nu}{\cos\theta}\right) = \varepsilon_\nu B_\nu(T_s)\cdot t_{\nu s} + \int_{t_{min}}^{1} B_\nu(T(t_\nu))dt_\nu. \tag{4.13}$$

In the near infrared, which is dominated by solar radiation, the radiance is simply given by the solar radiation flux of $F_\nu^0$ out of the atmosphere (divided by $\pi$) multiplied by the total transmission of the atmosphere, taking into account the surface albedo $A_\nu$:

$$I_\nu = \frac{F_\nu^0 \cos\theta_0}{\pi} \cdot A_\nu \cdot e^{-t_\nu\left(\frac{1}{\cos\theta_0}+\frac{1}{\cos\theta}\right)}. \tag{4.14}$$

The high-resolution solar spectrum, used in our case, is the one provided by Fiorenza and Formisano [78] and it is shown in Figure 4.4.

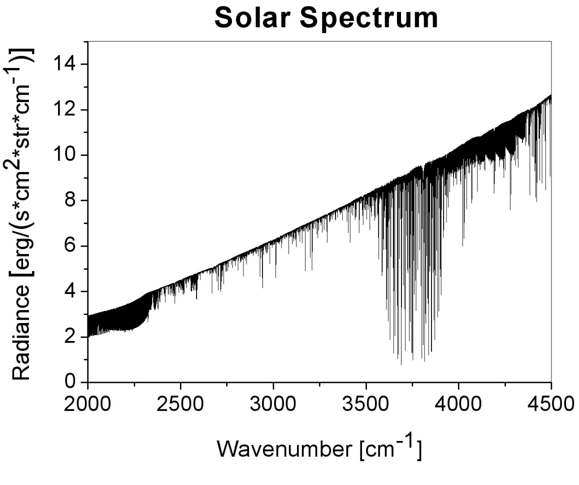

Figure 4.4: Solar spectrum from [78] used to calculate the synthetic spectrum.

The final step of the algorithm involves the convolution with the instrumental function $\Phi$:

$$I(\nu) = \int I_{\nu'} \Phi(\nu - \nu') d\nu'. \tag{4.15}$$

The same operation is done with the monochromatic transmittance and reflectance to calculate the convolved transmittance and reflectance.

The spectrum is calculated considering a specific gas ($H_2O$ or CO) mixing ratio, which is the tuning parameter in the retrieval algorithm. Variations of the $CO_2$ abundance in the atmosphere are considered as surface pressure variations (taken from the MCD model or from PFS measurements) rather than mixing ratio variations, which is assumed to be 0.9532

A typical apodized synthetic spectrum thus generated in the entire spectral range of interest (2000-4400 cm$^{-1}$) is shown in Figure 4.5.

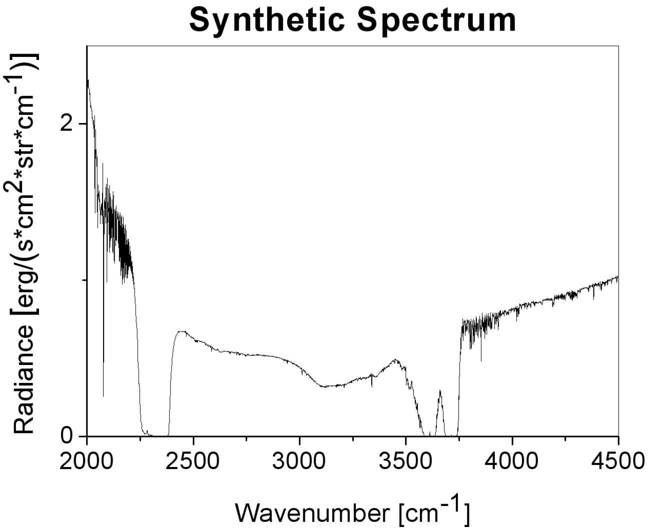

Figure 4.5: Typical apodized synthetic spectrum generated in the spectral range of interest (2000-4400 cm$^{-1}$).

### 4.2.4 Spectra Normalization

In order to use the relative band depths, it is necessary to normalize the spectrum to its continuum in the spectral region where the absorption bands of interest are present. This purpose is achieved using the approach suggested by Tschimmel et al. [112]. In this way we obtain a normalized synthetic spectrum $N_{syn}(\nu)$ and a normalized measured spectrum $N_{PFS}(\nu)$ in the spectral ranges from 3780 to 3950 cm$^{-1}$ and from 4160 to 4300 cm$^{-1}$ for analysis of water vapour and carbon monoxide concentration, respectively.

The spectral continuum, both for the measured and the synthetic spectrum, is defined as a piecewise function $C(\nu)$, linear between two local maxima. The $C(\nu)$ function is chosen in order to take account of the possible variations of the instrumental behaviour and the different spectral characteristics of the albedo in the two spectral ranges considered for the $H_2O$ and CO analysis (fig. 4.6). . A local maximum is defined as the spectral point $\nu_M$ which has an higher radiance than its five adjacent spectral points, for the $H_2O$ analysis, and higher than its three adjacent spectral points, for the CO analysis. The choice of the best number of such spectral points for the continuum definition represents the most reliable result obtained from several tests performed using a different number of spectral point steps. For each step, the best fit ($\chi^2$) between the observed and the synthetic spectrum gives us the best estimate of the number of spectral points to be considered in order to have the best continuum definition.

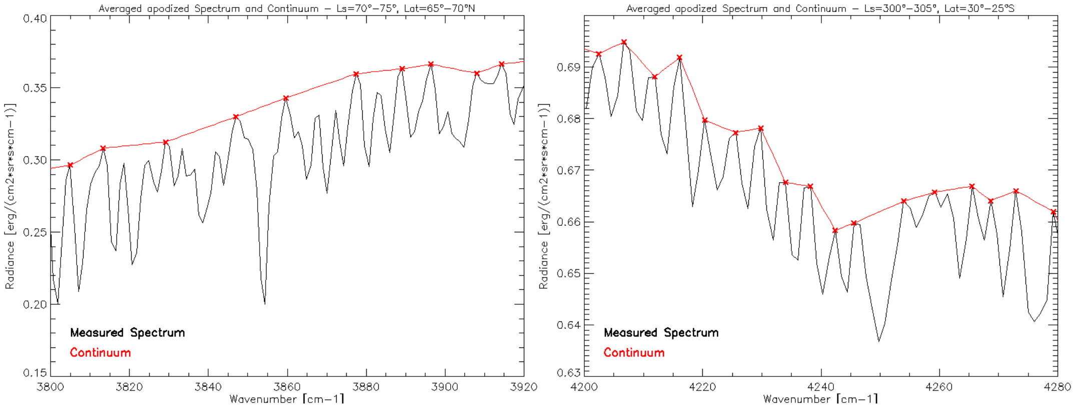

Figure 4.6: Typical examples of the continuum definition for PFS averaged measured spectra in the spectral ranges containing the absorption band of $H_2O$ (left) and of CO (right). We marked the selected points for the continuum definition with crosses.

Mathematically, the normalized spectrum is generated by

$$N(\nu) = \frac{I(\nu)}{C(\nu)},$$

where $N(\nu)$ is the normalized spectrum, $I(\nu)$ is the radiance spectrum and $C(\nu)$ is the continuum.

### 4.2.5 Best Fit Procedure

In the best fit procedure for measured and synthetic spectra the mixing ratio of the atmospheric component ($H_2O$ or CO) is the resulting variable parameter. In the case of water vapour band, the mixing ratio is considered constant at altitudes below the condensation level and equal to the saturation mixing ratio above it, whereas for the CO analysis a constant distributed vertical profile is considered. Therefore, the synthetic spectrum has to be calculated in each step of the fitting loop in order to keep into account the changing of the saturation level due to the variable $H_2O$ content. The fit criterion is the minimization of the $\chi^2$ parameter, weighed by the instrumental noise and defined as

$$\chi^2 = \frac{\sum_{i=1}^{np} \left(N_{PFS}(\nu_i) - N_{syn}(\nu_i)\right)^2}{np \cdot \left(\frac{NER/l_{cont}}{\sqrt{nm}}\right)^2}, \qquad (4.16)$$

where the sum is extended on all the points of the normalized spectra in the considered spectral range, $np$ is the number of these points, the $NER$ (Noise Equivalent Radiance) [93] is assumed to have its mean value in the considered range (0.023 and 0.035 $erg \cdot sec^{-1} \cdot cm^{-2} \cdot sr^{-1} \cdot cm$ , for the $H_2O$ and the CO, respectively), $l_{cont}$ is the mean continuum radiance in the spectral range and $nm$ is the number of the measured averaged spectra. We applied this procedure to a spectral range where the absorption band is stronger and the influence of the solar spectrum is not too strong, i.e, the 3785-3925 cm$^{-1}$ range for the H2O band and the 4200-4245 cm$^{-1}$ for the CO band.

The synthetic spectrum calculation and its normalization are iterated in a cycle that use a $\chi^2$ minimization method. The minimum $\chi^2$ provides the fit quality. The method consists in generating, as a first step, a synthetic spectrum with a mixing ratio arbitrarily chosen[5], together with other two synthetic spectra having a mixing ratio which differs from the first one for the ±10%. For each of these three synthetic spectra the $\chi^2$ are calculated and the resulting spectrum with the minimum $\chi^2$ takes the place of the first spectrum generated in the fit cycle. For example, if the minimum $\chi^2$ minimum results to be the synthetic spectrum with a mixing ratio +10%, this one is regarded as a temporary possible candidate to be the best fit of the average measured spectrum, then another synthetic spectrum having a +10% in the mixing ratio with respect to the latter is then generated. The $\chi^2$ is again recalculated and the minimum is detected, and the cycle continues, until the temporary candidate for the best fit appears to be the one having the lowest $\chi^2$ between the three compared synthetic spectra (with +0% and ±10% in mixing ratio). At this point the step of variation of the mixing ratio between compared synthetic spectra is decreased from ±10% to ±5% and the cycle begins again starting with the best candidate synthetic spectrum previously found. Similarly, when the candidate synthetic spectrum has the lowest $\chi^2$ between the three compared synthetic spectra (with +0% and ±5% in mixing ratio), the loop stops providing the synthetic spectrum representing the best fit of the PFS average measured spectrum with an accuracy of 5% in the mixing ratio of analyzed atmospheric component. The corresponding minimum $\chi^2$ represents the value providing the quality of the fit, which is a measure of the disturbance of the average measured spectrum due to instrumental behavior. In Figure 4.7 the flowchart representing the retrieval algorithm based on the $\chi^2$ minimization is shown.

Figure 4.8 shows an example of good quality spectral fit of the $H_2O$ absorption band for an averaged spectrum, corresponding to 200 single spectra selected within the bin Ls=70°-75°, Lat=65°-70° N. The vertical atmospheric profiles have been calculated for a latitude of 68.2° N and a longitude of 21.4°

---

[5] Usually the mixing ratio for the first synthetic spectrum of the fit cycle is chosen taking as reference the Martian atmospheric modeling currently available (MCD, vers. 4.2).

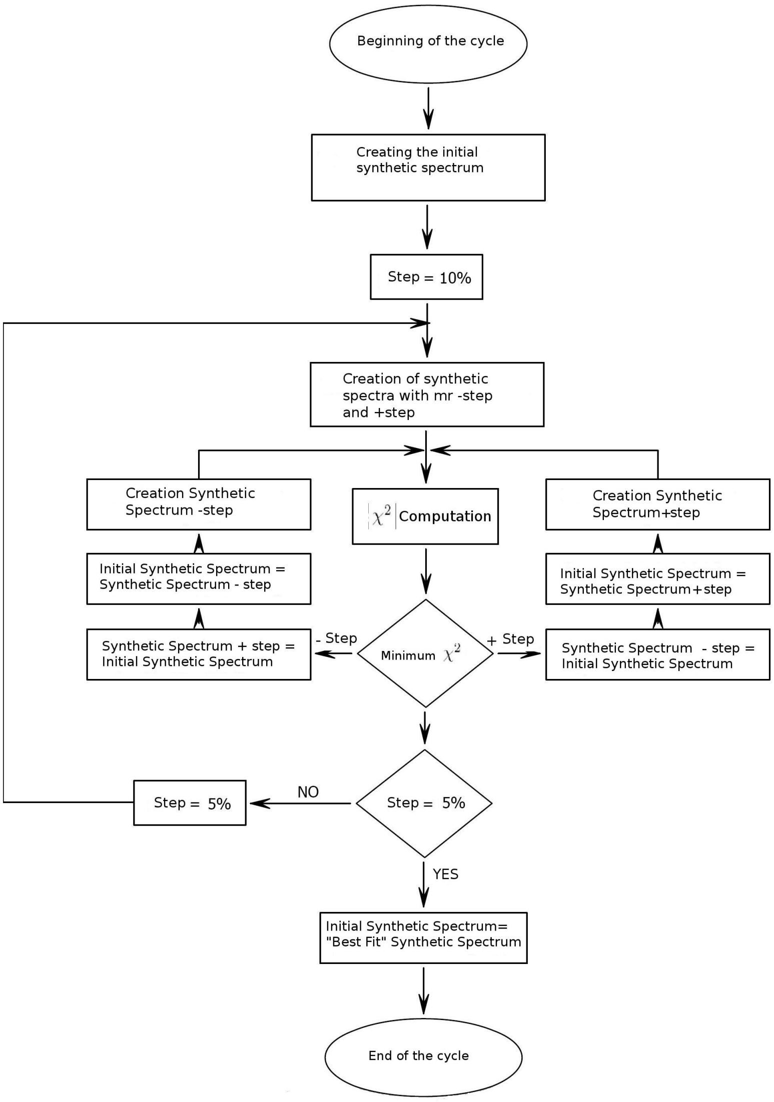

Figure 4.7: Flowchart representing the $\chi^2$ minimization algorithm developed and implemented for the concentrations analysis of of Martian atmospheric components.

E, during Ls=72.9° and a solar local time (Lt) of 8.82. In this case the analysis algorithm gives us a mixing ratio of 297 ppm.

Figure 4.9 shows an example of good quality spectral fit of the CO absorption band for an averaged spectrum, corresponding to 243 single spectra selected within the bin Ls=300°-305°, Lat=25°-30° S. The vertical atmospheric profiles have been calculated for a latitude of 27.5° S and a longitude of 10.6° W, during Ls=301.9° and for a solar local time (Lt) of 10.63. In this case the analysis algorithm gives us a mixing ratio of 640 ppm.

However, in spite of the good quality fit, some features, as for example

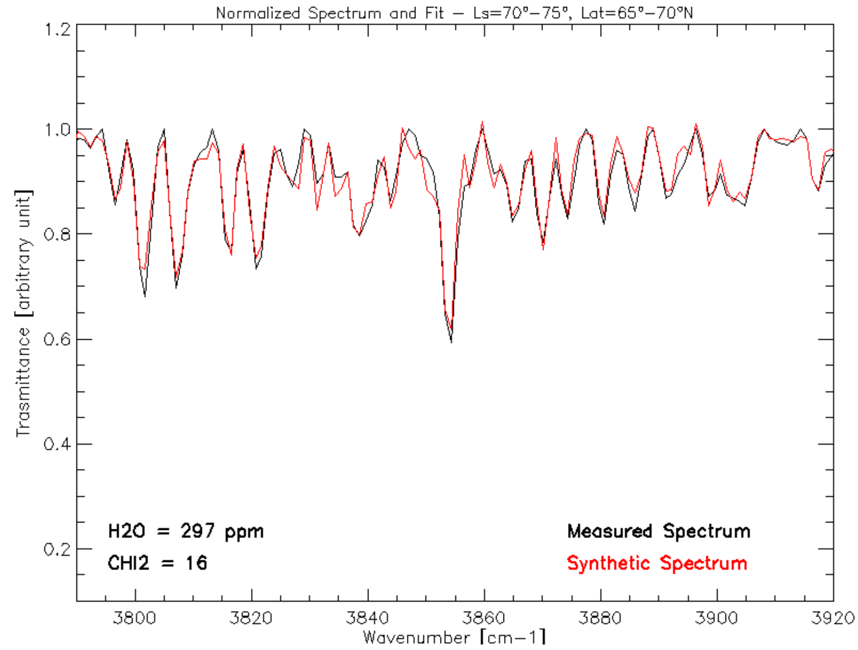

Figure 4.8: Spectral fit example of the water vapour absorption band for an averaged spectrum (normalized to its continuum), corresponding to 200 single spectra selected into the bin Ls=70°-75°, Lat=65°-70° N. The retrieved mixing ratio is 297 ppm with a minimum $\chi^2$ of 16 (over 130 sampling points).

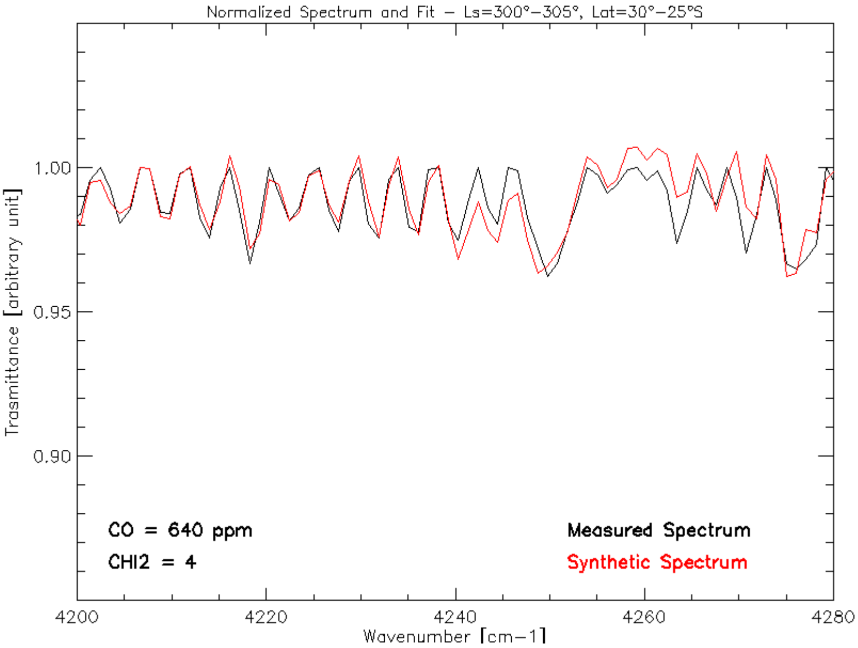

Figure 4.9: Spectral fit example of the carbon monoxide absorption band for an averaged spectrum (normalized to its continuum), corresponding to 243 single spectra selected into the bin Ls=300°-305°, Lat=25°-30° S. The retrieved mixing ratio is 640 ppm with a minimum $\chi^2$ of 4 (over 40 sampling points).

those around 3830 $cm^{-1}$ and 3850 $cm^{-1}$ in Figure 4.8, and those around 4245 $cm^{-1}$ and 4260 $cm^{-1}$ in Figure 4.9, remain not well fitted. These features are common to almost all the spectra and their origin has probably to be found in a wrong line broadening factor in the model, in systematic instrumental features or in an unknown contribution of other atmospheric components.

When the averaged measured spectrum radiance level is too low, resulting in a very low signal to noise ratio, or when particular albedo features do not allow a correct continuum definition, it is not possible to obtain a good fit. Therefore, results obtained with a poor fit quality will be excluded a posteriori using a selection method that takes into account the $\chi^2$ value.

The presence of another CO absorption band in the PFS/SWC spectrum, around 2150 $cm^{-1}$, allows sometimes the comparison between concentration values obtained from the two different band fits. The analysis of the this absorption band does not require the correction for the modulation centered around 5000 $cm^{-1}$ and, at the same time, being very intense, it is not affected significantly by the instrumental noise. Therefore, in its analysis we do not need to apply the spectrum normalization to its continuum before performing the best fit procedure. However, this band in the thermal region of the spectrum, although it is more intense than the other one, hides some analysis problems. The main problem is the calibration of the thermal region of the spectrum, because it is a very complex task when in the spectra there are one or more "thermal inversions", which depend on the relative temperature between Mars and the detector. Indeed, in the thermal radiation range (up to 2900 $cm^{-1}$), the PFS/SW channel is sensitive to the difference of temperature between the emitting source (Mars) and the detector temperature [93]. So, when Mars becomes hotter or cooler than the detector, one or more "phase jumps" occur and they prevent a good spectrum calibration. A typical fit example of an ill-calibrated spectrum is shown in Figure 4.10. Unfortunately, we have not still a stable algorithm able to perform this kind of phase correction, therefore spectra affected by thermal inversions cannot be used in the retrieval analysis.

Another significant problem in the CO band analysis in the termal region of the SWC spectrum arises in the generation of the synthetic spectrum having a correct surface temperature, which deeply affects both the slope of the continuum and the depth of the spectrum absorption lines in the this region. Since the slope of the spectrum continuum in the thermal region of the PFS/SWC reflects the tail of a theorical theorical Planckian function, the surface temperature has a great importance. Usually, the surface temperature corresponding to an average spectrum of PFS is derived from the averages of surface temperatures corresponding to each spectrum involved. The surface temperatures are extracted by means of a software package based on the algorithm developed by D. Grassi et al. [96]. However, the surface temperature thus obtained does not always turn out to be correct, as we can see in the comparison between synthetic and measured spectra, where the slope is not the same. Figure 4.11 is a typical example of a no correct fit because of the difficulty in determining the correct surface temperature, where this effect is reflected on the depth of

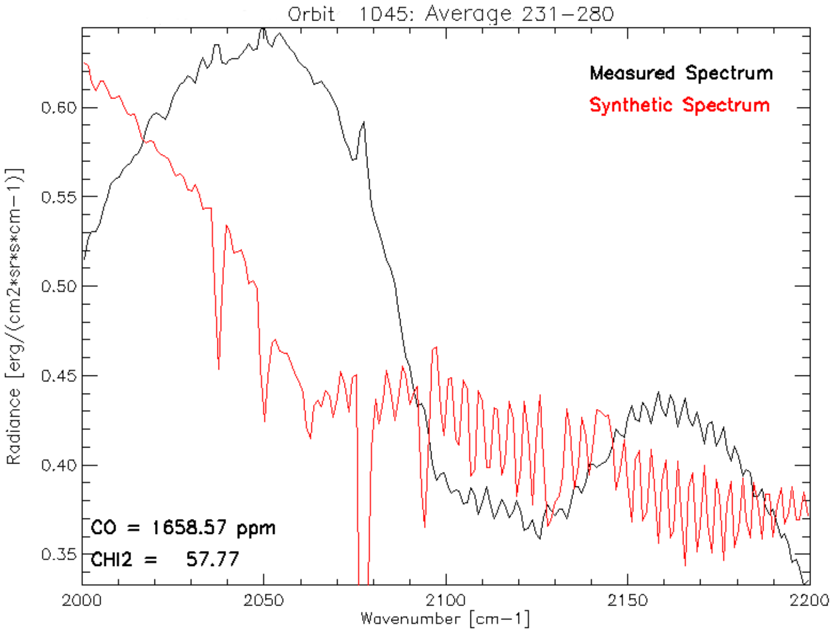

Figure 4.10: Example of a spectral fit (measurements 231-280 of orbit 1045) with calibration problems in the thermal region. The values given for the CO mixing ratio and for the $\chi^2$ are obviously meaningless.

the absorption lines.

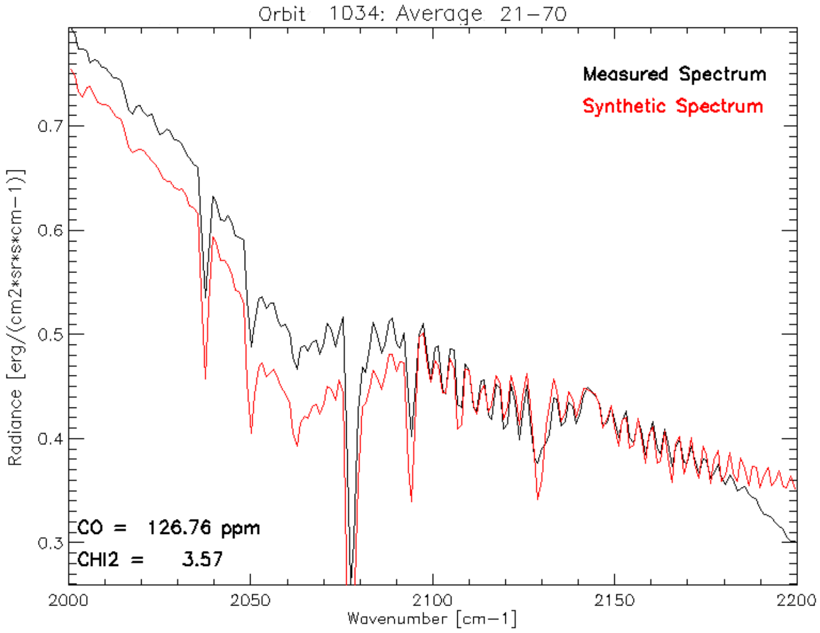

Figure 4.11: Example of a spectral fit (measurements 21-70 of orbit 1034) with problems in determining the correct surface temperature used to generate synthetic spectra. The values given for the mixing CO ratio and for the $\chi^2$ are obviously meaningless.

In some cases, in which it was possible to apply the same analysis procedure described above (without spectrum normalization), in the spectral range 2100-2180 cm$^{-1}$, we have compared results from the two bands (an example is shown in Figure 4.12). The retrievals obtained from the two bands, analysing the same spectra, differ by about 6%. The result of this comparison validates the method used for the 4200-4245 cm-1 band.

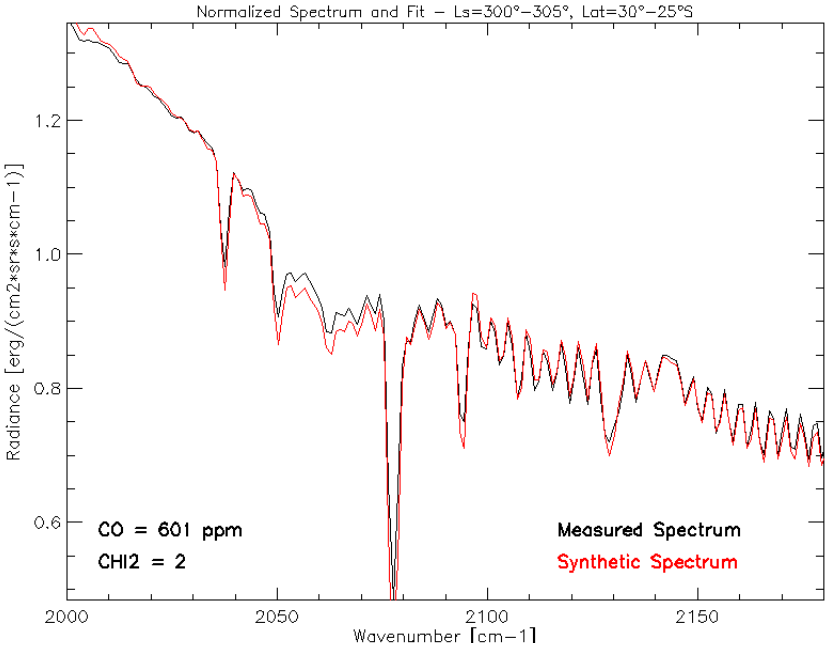

Figure 4.12: Spectral fit example of the carbon monoxide absorption band in the range 2000-2180 cm$^{-1}$ for an averaged spectrum, corresponding to 243 single spectra selected into the bin Ls=300°-305°, Lat=25°-30° S. The retrieved mixing ratio is 601 ppm with a minimum $\chi^2$ of 2. We compare this result with the one obtained in Figure 4.9, referring to the same spectrum. We note that the difference in the retrieved concentration is about 6%.

### 4.2.6 Corrections of CO values a Posteriori

The PFS/SWC spectrum has a spectral modulation, due to instrumental problems, centred at about 2 $\mu$m (5000 cm$^{-1}$) which starts from about 4000 cm$^{-1}$, and therefore it affects the CO absorption band (4235 cm$^{-1}$). Comolli and Saggin [56] suggested that the modulation affects only the spectral continuum level without changing the relative depth of the spectral features. Therefore the normalization procedure should correct this effect and the mixing ratio values should be independent on the spectral continuum slope. In order to test a possible effect of the 2 $\mu$m spectral modulation on the CO band depth we considered the 36174 good quality spectral fits ($\chi^2 < 25$) and we studied the mixing ratio values as a function of the slope of the spectral continuum in the CO band spectral range. Figure 4.13 shows the retrieved values for the CO mixing ratio (each point is the average of CO values for slope bins of $5 \cdot 10^{-5}$) as a function of the slope. It is clear from the figure that there is a linear

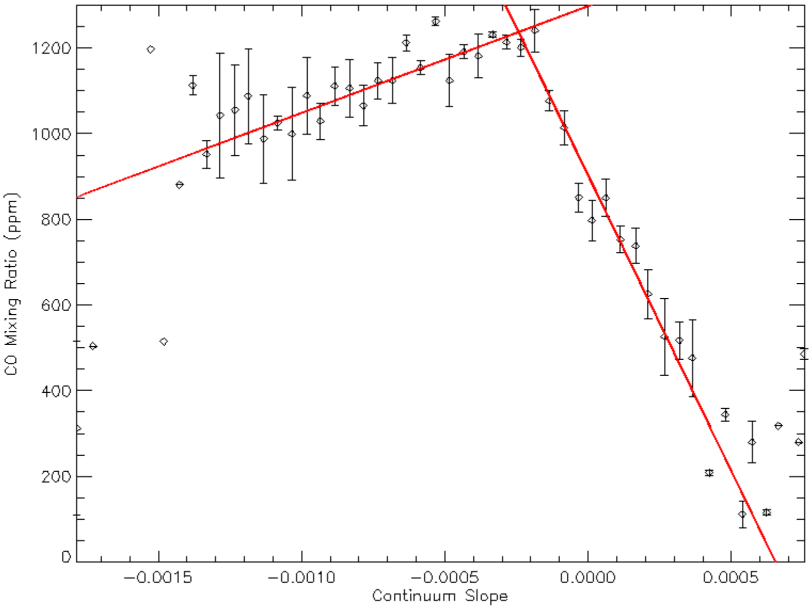

Figure 4.13: Trend of retrieved CO mixing ratio values on 36174 averaged spectra as a function of the continuum slope (bins of $5 \cdot 10^{-5}$). Two linear fits are used to find this dependence: $y_1(m) = 1297.75 + 249272.00 \cdot m$ for $m < -2.42 \cdot 10^{-4}$ and $y_1(m) = 903.285 - 1.38009 \cdot 10^6 \cdot m$ for $m > -2.42 \cdot 10^{-4}$. The error bars are calculated as the data standard deviations.

relationship between the two quantities described by two linear fits defined as:

$$y(m) = \begin{cases} 1297.75 + 249272.00 \cdot m & for \;\; m < -2.42 \cdot 10^{-4} \\ 903.28 - 1.38 \cdot 10^6 \cdot m & for \;\; m > -2.42 \cdot 10^{-4} \end{cases}$$

We have demonstrated that the 2 $\mu$m modulation affects the band depth and therefore our result is not in agreement with the suggestion by Comolli and Saggin [56]. Thus, we have to correct this modulation using the “calibration function” $y(m)$. The corrected mixing ratio value ($cmr$) can be calculated for each data-point as follows:

$$cmr = omr \cdot \frac{y(m_{synt})}{y(m)},$$

where $omr$ is the retrieved mixing ratio value, $y(m_{synt})$ is the reference mixing ratio (903 ppm) and $y(m)$ is the mixing ratio value of the calibration function at a considered angular coefficient $m$.

The reference mixing ratio $y(m_{synt})$, considered as the expected mean value of the whole dataset, has been obtained applying the calibration function to the slope of the continuum of a synthetic spectrum (without modulation) in the CO band.

## 4.3 Saturation of the Absorption Bands

If the abundance of the studied atmospheric component is sufficiently high and the intensity of the spectral lines of the corresponding band is very high, these lines will not increase in depth beyond a certain mixing ratio limit. Indeed, by increasing the abundance of the component which generates the absorption beyond a certain limit, called *band saturation limit*, a corresponding increase of the spectral lines depth is not observed in the spectrum, but we can notice only a slight broadening of the lines themselves, and at the same time a progressive growth of the importance of their wings, which tend to take on the “damping profile” trend. Obviously, this observed effect is not sufficient to represent the correct value assumed by the mixing ratio for the atmospheric component whose bandwidth is saturated. Therefore, we need to study what is the saturation limit for the $H_2O$ and CO bands we want to analyze, so that we can exclude a posteriori, if needed, any data obtained for abundances beyond this limit.

The saturation level is obtained from a study carried out exclusively on synthetic spectra and it consists in generating identical spectra in the spectral range where there is the band to be investigated by varying a single parameter: the mixing ratio of the component present in this spectral range. In particular, we generated 10 synthetic spectra, each with 0, 10, 100, 1000, 2000, 3000, 5000, 10000, 20000, 100000 ppm. In order to study the relative depth of only the gaseous band we are interested in, each synthetic spectrum having a mixing ratio of non-zero has been divided by the one having 0 ppm. This normalization eliminates any spectral contribution due to other components, leaving only the lines whose saturation we want to study (Fig. 4.14). From the spectrum so normalized we choose the three most intense absorption lines (Fig. 4.14) and on them we obtain, from time to time, the relative depth. By plotting, in logarithmic scales, the percentage of relative depth of the three selected lines as a function of the concentration of investigated atmospheric component, we note that the deviation from the law (*growth curve*), which describes the relationship between abundance and line depth generated by it, is obtained only for abundance values much greater than 1000 ppm for the $H_2O$ band and than 2000 ppm for the CO band at 2100-2180 $cm^{-1}$, while it is negligible at all in the case of the CO band at 4200-4245 $cm^{-1}$ (Fig. 4.15). Since, customarily the values conceivably assumed by the abundances of these two studied elements do not exceed the limits in which the relative band has a significant saturation, we can consider all the data obtained from the fit procedure not influenced by this effect.

## 4.4 Evaluation of Uncertainties

There are many sources of uncertainties in the procedure described above. First of all, in the synthetic spectra calculation the main error source is the broadening line factor in a $CO_2$ dominated atmosphere. Although it is an important parameter, there is little experimental information about its correct

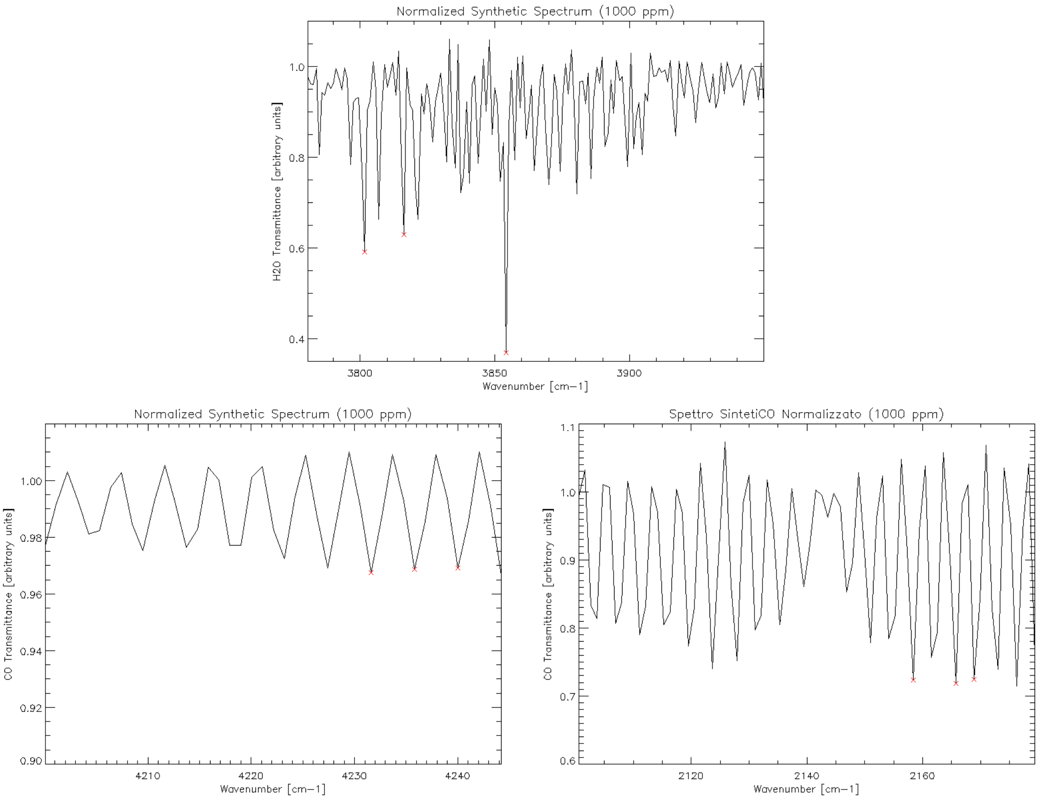

Figure 4.14: Normalized synthetic spectra with 1000 ppm of $H_2O$ (top), CO (bottom), in the spectral ranges 3780-3950 $cm^{-1}$ , 4200-4245 $cm^{-1}$ (left) and 2100-2180 $cm^{-1}$ (right), respectively. The crosses indicate the choice of the three deeper absorption lines in the spectral ranges of interest.

value in the considered spectral ranges. The error coming from this factor was evaluated changing its value between 1.3 [76] and 1.7 [87]. In this way we obtained a variation in the retrieved abundance values of about 15% for the $H_2O$ and of about 10% for the CO. Another source of error has to be found in the used climatic model: the uncertainty derived from the MCD pressure is less than 2%, and the one derived from the MCD temperature is about 5%. For the water vapour analysis, the uncertainty coming from the MCD temperature affects the saturation profile producing an error of about 5% in its abundance. In order to estimate the uncertainty derived if we will want to neglect the aerosols effect, we have generated a synthetic spectra set, using different dust and ice opacities. The range of variability for the dust optical depth (at 1075 $cm^{-1}$) was chosen between 0.05 and 0.4, which represents the Martian mean conditions out of the global dust storm [186, 190]. Processing each spectrum of this set with the analysis procedure used for actual Martian data, we obtained an error (standard deviation of retrieved results) of 7% and of 9% in the retrieved concentration for the water vapour and for the carbon monoxide, respectively. For the variability of the water ice content in the Martian atmosphere, we considered an optical depth range between 0.05 and 0.12 at 825 $cm^{-1}$ [186]. The ice particle content in the atmosphere results to be to-

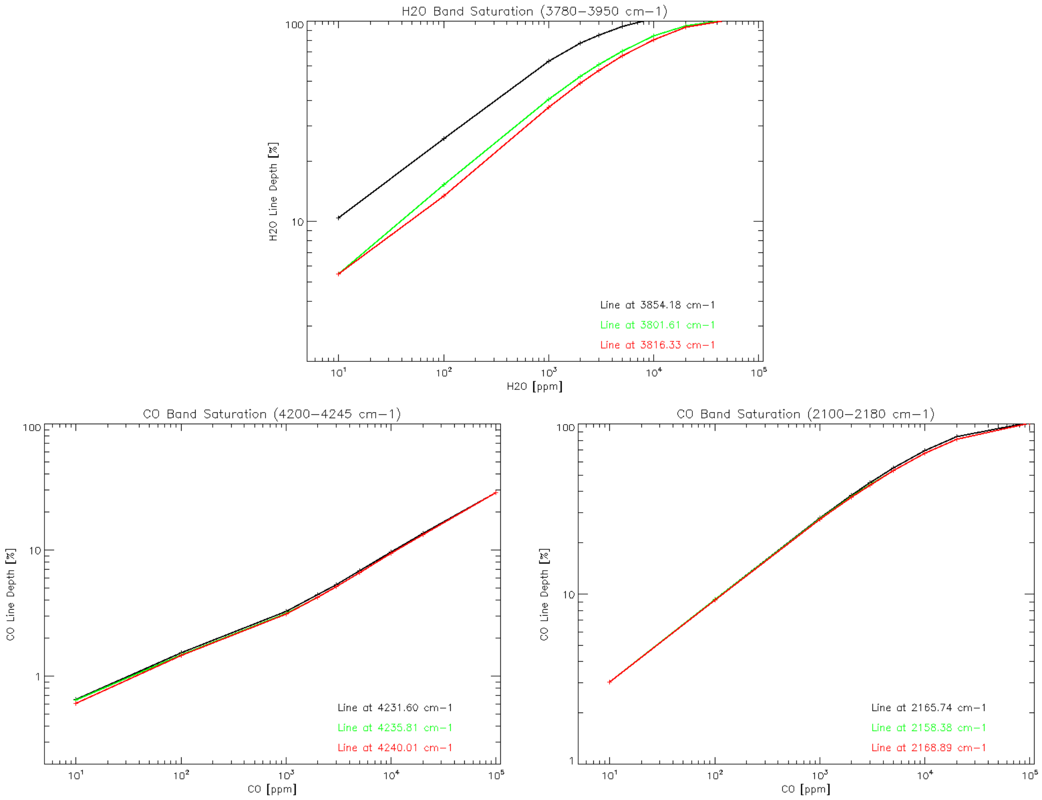

Figure 4.15: Trends of the percentage relative depth for the three most intense lines of the $H_2O$ (top) and CO (bottom) bands, respectively, in the spectral range 3780-3950 $cm^{-1}$, 4200-4245 $cm^{-1}$ (Left), 2100-2180 $cm^{-1}$ (Right), as a function of the mixing ratio. Saturation occurs when the deviation from linearity in the graph with logarithmic scales becomes important.

tally negligible for the two absorption bands considered in our study. Another important contribution to the error evaluation derives from the continuum definition: a little variation in its definition and the presence of the instrumental noise can result in errors up to about 5% and 15% in the $H_2O$ and CO concentration, respectively. In addition, only for the CO concentration retrieval, we have to consider the uncertainty due to the “a posteriori correction” for the 2 $\mu$m modulation 4.2.6: the error (standard deviation) is evaluated to be about 5%. Finally, there is also an intrinsic error in the fit cycle. Since the synthetic spectra are calculated with a minimum step of 5% (Section 4.2.5) in the mixing ratio, this value also represents the accuracy of the best fit procedure. Moreover, the fit quality given by the $\chi^2$ value provides an estimation of the error on concentration of the considered atmospheric component. Therefore, we can conclude that the broadening line factor and the continuum definition (only for the CO retrieval) represent the main sources of error in the whole procedure. Considering all the contributions, the total error (square sum) for each retrieved concentration value is estimated to be about 19% for the water vapour and about 22% for the carbon monoxide.

# Chapter 5

# Atmospheric $H_2O$ and CO variability Mapping

In this chapter we will investigate the seasonal and geographical distribution of water vapor and carbon monoxide, as well as their connections, in the Martian atmosphere [183] using the data analysis method described in Chapter 4. The lack of many simultaneous measurements of these two gaseous species makes their comparison a topic of great interest for the understanding of photochemical and dynamical processes involved in the Mars planetary atmosphere.

## 5.1 Dataset

### 5.1.1 Observations

The PFS/SW dataset used in this work covers more than two and a half Martian years from Ls = 62° of MY 27 (orbit 634) to Ls = 203° of MY 29 (orbit 6537). For the creation of a single mean spectrum several measurements have to be averaged. This purpose is achieved by averaging spectra in two different ways, making two kinds of datasets. The first, called in this work "orbital dataset", is obtained by choosing the ideal number of measurements to average in order to represent the best compromise between the increase of the signal to noise ratio and the maintenance of a good spatial resolution: for the $H_2O$ analysis 15 individual measurements have been averaged, whereas for the CO, the relative band being much weaker (see Chapter 4), it was necessary to average 50 single measurements. For a single orbit, the first mean spectrum was built by averaging 15 (or 50) individual measurements between the index[1] 1 and 15 (or 1 and 50); the following mean spectra were built by averaging the same number of measurements, but increasing the starting index by 10 respect to the previous average: i.e., 1-15, 11-25, 21-35, . . . , (for the $H_2O$), or 1-50, 11-60, 21-70, . . . , (for the CO) and so on. In this way 42935 mean spectra have been generated for the water vapour analysis and 36174 mean spectra for the carbon monoxide analysis. The second kind of dataset, called in this work "bin dataset", is obtained by averaging spectra in square bins

---

[1] The PFS acquisitions of one orbit are counted by an increasing index.

of 5° Solar Longitude (Ls) x 5° Latitude for seasonal behaviour studies and in square bins of 10° Longitude x 10° Latitude for geographic distribution studies. The Latitude vs Longitude bin averages are calculated separately for each of the four seasons: northern Spring (Ls=0-90°), Summer (Ls=90-180°), Fall (Ls=180-270°) and Winter (Ls=305-360°). Since the aim of our work is the study of the average behaviour of $H_2O$ and CO, data from Ls=270° to Ls=305° were excluded, because they are affected by the global-encircling dust storm occurred during the MY 28. In this way we have 2592 mean spectra for the Latitude vs Ls studies and 648 mean spectra for each season of the Latitude vs Longitude studies. Obviously, the number of averaged spectra in a single bin is not constant and varies from a minimum of 1 to a maximum of 1277 with a mean value of about 213 for the seasonal study bin dataset (Figure 5.1) and of 208 (Spring), 256 (Summer), 74 (Fall) and 159 (Winter) for the geographical study dataset (Figure 5.2). It is necessary to make two different kinds of dataset to optimize the S/N ratio according to the study aim. The best S/N ratio is obtained in the bin dataset, but this averaging method causes the loss of important information linked to the mean spectrum, such as temporal or orbital information. Therefore, the bin dataset is used when we have to investigate only the seasonal and geographical mean trends of the gaseous concentrations, while the orbital dataset, keeping the orbital information, allow us to investigate variations on relatively small scales, although with a poorer S/N ratio.

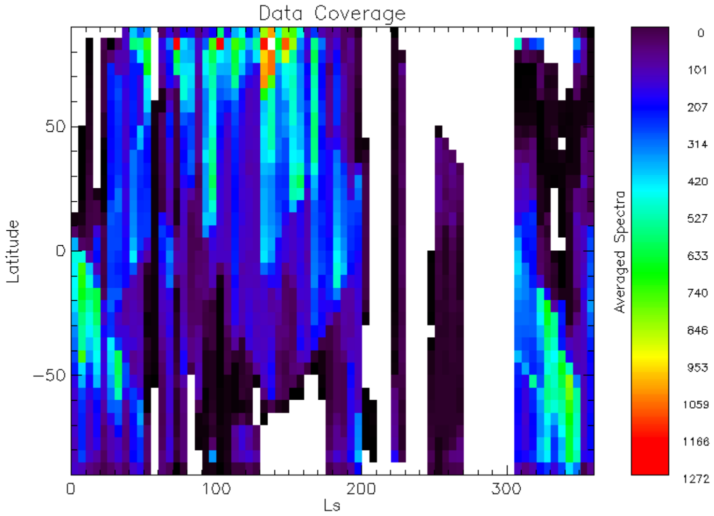

Figure 5.1: Data coverage for the 5° Ls vs 5° Latitude dataset. Data affected by the global-encircling dust storm of MY 28 (Ls=270°-305°) were excluded. The mean number of averaged spectra in a single bin is 213. White bins indicate no data.

### 5.1.2 Data Selection

When the averaged measured spectrum radiance level is too low, resulting in a very low signal to noise ratio, or when particular albedo features do not allow a

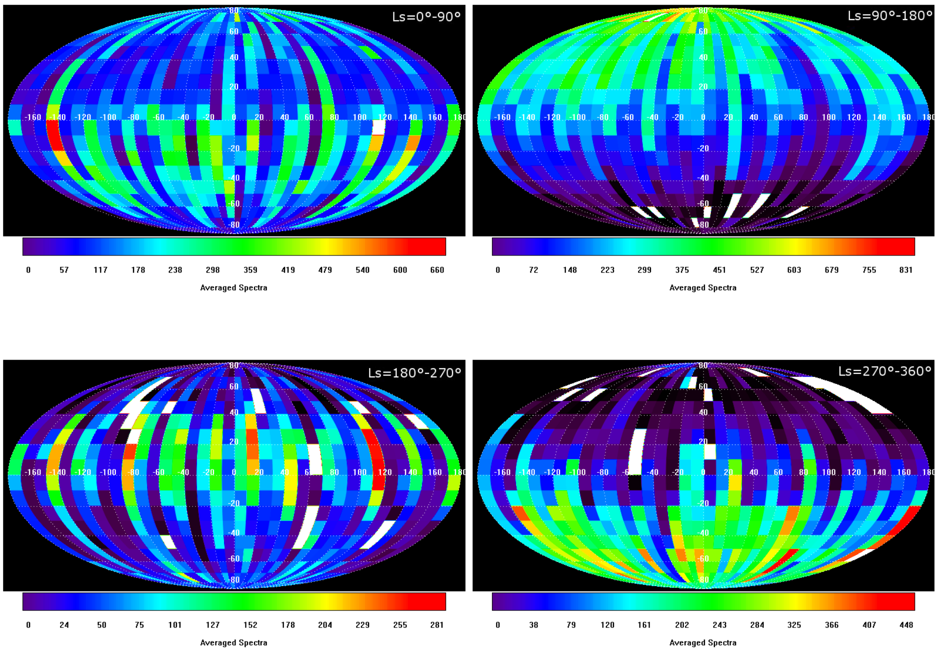

Figure 5.2: Data coverage for the 10° Longitude vs 10° Latitude dataset for the four seasons: northern Spring (Ls=0-90°), Summer (Ls=90-180°), Fall (Ls=180-270°) and Winter (Ls=305°-360°). Data affected by the global-encircling dust storm of MY 28 (Ls=270°-305°) were excluded. The mean number of averaged spectra in a single bin is 208 for Ls=0°-90°, 256 for Ls=90°-180°, 74 for Ls=180°-270° and 159 for Ls=270°-360°. White bins indicate no data.

correct continuum definition, it is not possible to obtain a good fit. Therefore, results obtained with a poor fit quality will be excluded a posteriori using a selection method that takes into account the $\chi^2$ value. The $\chi^2$ histogram distribution reveals a peak in correspondence of a value of 1.5 for the $H_2O$ retrieval and of 2.5 for the CO retrieval, but with a less broad distribution for the last one. The $\chi^2$ threshold (50 and 25 for the $H_2O$ and the CO band fit, respectively) was chosen in order to strike a balance between the maintenance of a relevant data coverage and a sufficiently good fit quality (Figure 5.3). In this way we discarded about 25% of the water vapour data and about 20% of the carbon monoxide data, mostly relating to the night (winter) polar regions, which have a very low signal to noise ratio.

## 5.2 Water Vapour: Seasonal and Geographical Behaviour

The water vapour behaviour we retrieve reproduces the well known *seasonal water cycle* in the Mars atmosphere.

In order to come out $H_2O$ results more comparable with other datasets, we converted them in pr.$\mu$m, taking into account the saturation and pressure

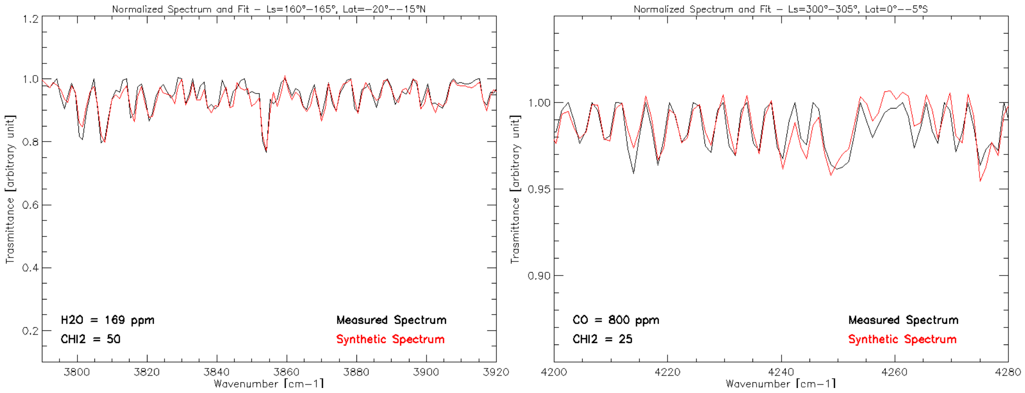

Figure 5.3: Spectral fit examples of the water vapour (left) and carbon monoxide (right) absorption bands for averaged spectra (normalized to their continuum) having a minimum $\chi^2$ of 50 and 25, respectively, which represent the limit values of the selection criterion.

profiles. Moreover, since the real vertical distribution of water vapour is still unknown, we applied the topographic correction usually used on the $H_2O$ retrieved values to rule out the topographic effect on the absorption band depth: this effect must be taken into account because the vertical distribution of the water vapour on the Mars atmosphere is non-uniform [202]. Therefore, this topographic correction is obtained normalizing each column density value to the mean superficial pressure value of 6.1 mbar, i.e., each column density value is multiplied by a 6.1/ps factor, where ps [mbar] is the superficial pressure corresponding to the considered spectrum. This normalization, which seems to give reasonable results, should remove the first-order influence of topography on the retrieved abundances of water vapour.

The retrieved $H_2O$ abundances as a function of Solar Longitude (Ls) and latitude, as observed by PFS/SWC, from orbit 634 to orbit 6537, allow us to study its seasonal cycle. The map obtained, using spectra averaged in 5° Ls x 5° Latitude bins, is shown in Figure 5.4.

The mean abundance for the whole dataset results to be about 9.6 pr.$\mu$m with a maximum of 59.0 pr.$\mu$m in correspondence of the summer northern polar cap (Ls=105°-125°, Latitude=70°-80°N). The standard deviation over the mean value is about 9.0 pr.$\mu$m. Since the error in estimating the mean water vapour abundance is about 1.8 pr.$\mu$m ($\ll$9.0 pr.$\mu$m), the large value of the standard deviation indicates the very large spread in the water vapour abundance values and therefore its variability in the Marian atmosphere. The map shows the expected water vapour cycle in the Mars atmosphere. The atmospheric content of the water vapour before Ls=70° begins to increase at middle-high latitudes, between 40°N and 70°N, because of the start of the northern polar cap sublimation; then the latitudinal distribution is characterized by a gradient between Ls=80° and about Ls=140° (northern summer). During the period Ls=130°-150° the amount of water vapour at high northern latitudes begins to decrease rapidly. At the same time, a region with relatively high $H_2O$ abundance (about 15.9 pr.$\mu$m) develops at about 45°N. It moves with

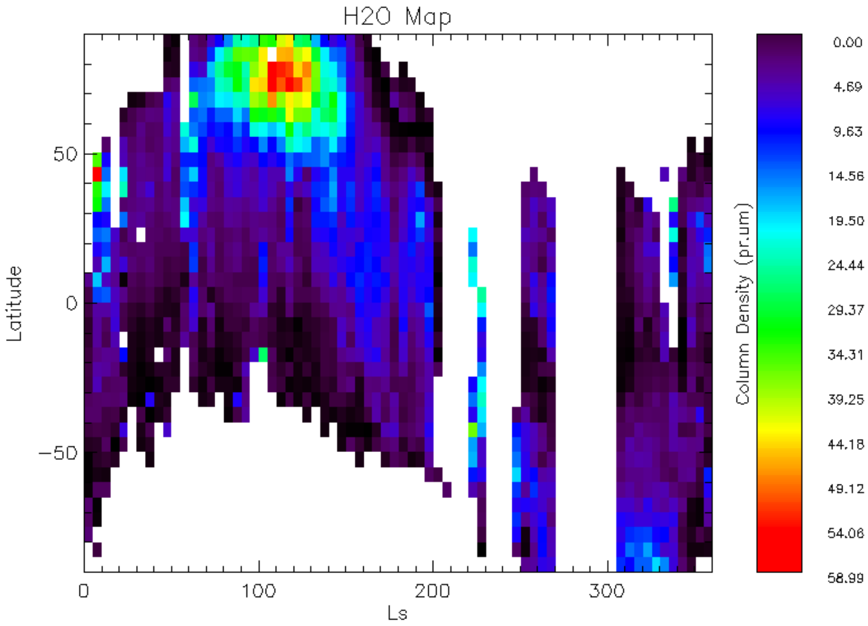

Figure 5.4: Map of retrieved abundance of water vapor as a function of Solar Longitude (Ls) and Latitude as observed by PFS/SWC, from orbit 634 to orbit 6537, obtained using spectra averaged in 5° Ls x 5° Latitude bins.

season toward the equator reaching it at about Ls=190° and then it continues to move toward south having a mean value of about 9.5 pr.$\mu$m from Ls=190° to Ls=270° (northern fall). During the northern winter (southern summer) for Ls=305°-340° we can see the increase of the $H_2O$ amount due to the sublimation of the south polar cap (70°-90° S), with a maximum value of about 22.8 pr.$\mu$m. Finally, from Ls=340° the water vapour moves toward north joining at Ls=360° with the already discussed spring season, starting from Ls=0°.

In order to study the water vapour distribution in the Martian atmosphere, we used the averaged spectra in square bins of 10° Longitude x 10° Latitude for each season. The results obtained for Ls=0°-90° (northern Spring), Ls=90°-180° (northern Summer), Ls=180°-270° (northern Fall) and Ls=305°-360° (northern Winter) are shown in Figure 5.5.

We note a peculiarity in almost all the seasons (Spring, Fall and Winter): an increase of the water vapour abundance over two particular regions, Arabia Terra (30°E, 0°N) and Tharsis (100°W, 0°N). Both these maxima have been also observed by many instruments and two explanations have been given for them: interaction soil-atmosphere [185] and atmospheric circulation influence with the presence of stationary waves causing a water vapour build-up over certain regions [86].

It is now interesting to comment on the maximum in the water vapour abundance during the north summer (Figure 5.5). Clearly, the biggest $H_2O$ densities are at latitudes between 60°N and 85°N, centred around 75°N. Therefore, the centre of the water distribution is localized out of the permanent polar cap border, which spreads to a latitude of about 80°N, whereas the seasonal

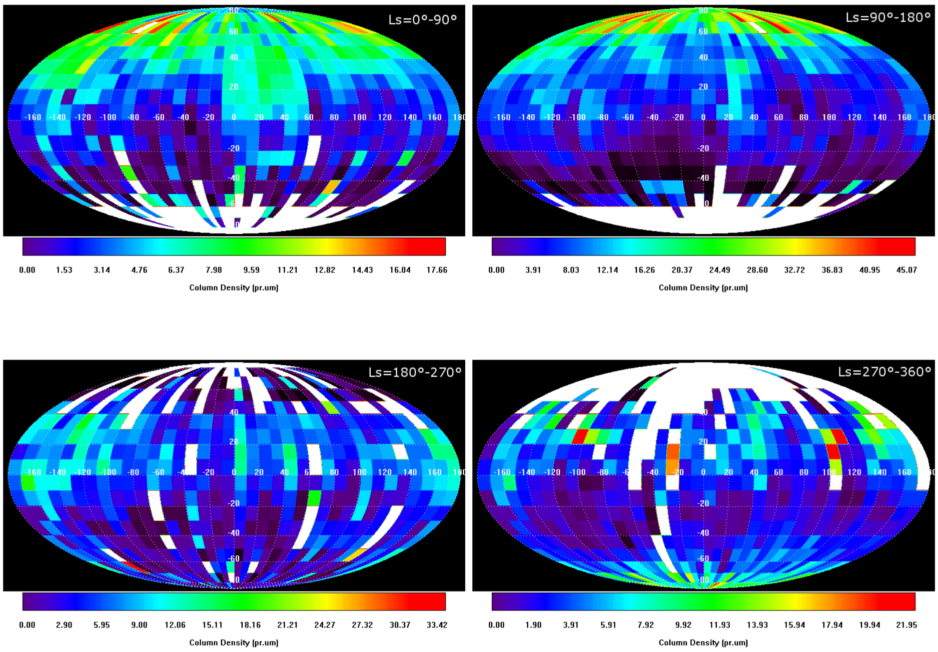

Figure 5.5: Map of retrieved abundance of water vapour as a function of Longitude and Latitude as observed by PFS/SWC, from orbit 634 to orbit 6537, obtained using averaged spectra in square bins of 10° Longitude x 10° Latitude for each season: Ls=0°-90° (northern Spring), Ls=90°-180° (northern Summer), Ls=180°-270° (northern Fall) and Ls=305°-360° (northern Winter).

polar cap is already completely withdrawn at Ls=90°.

### 5.2.1 Comparison with the MCD Model

The MCD (Mars Climate Database) [80], developed by the LMD (Paris), AOPP (Oxford), Department of Physics and Astronomy (The Open University) and IAA (Granada), with the support of the European Space Agency (ESA) and the French National Center of Space Studies (CNES), is a database of atmospheric statistics compiled by numerical simulations of the Global Circulation Model (GCM) for the Martian atmosphere. The database extends up to approximately 250 km in altitude and provides, in addition to temperature, pressure, wind and radiative fluxes values, also data on the atmospheric composition, which include content of dust, water vapor and water ice. A linear time interpolation of the data is used to reconstruct the variables under certain specified conditions, such as the day-time and the solar longitude. Moreover, various types of vertical coordinates can be specified as input.

In order to make a comparison between the $H_2O$ concentrations values extracted by the model and results obtained from our analysis of experimental data, we used as input for the MCD all the geometry information (latitude, longitude, solar longitude, altitude and local time) of our measurements. Both measured and the data by the model were averaged in bins of 5° in latitude, either on the whole Martian year (Ls = 0°-360°) and for four different periods: Ls = 330°-60°, Ls = 60°-150°, Ls = 150°-240° and Ls = 240°-330°. The comparison of the data so treated is shown in Figure 5.6.

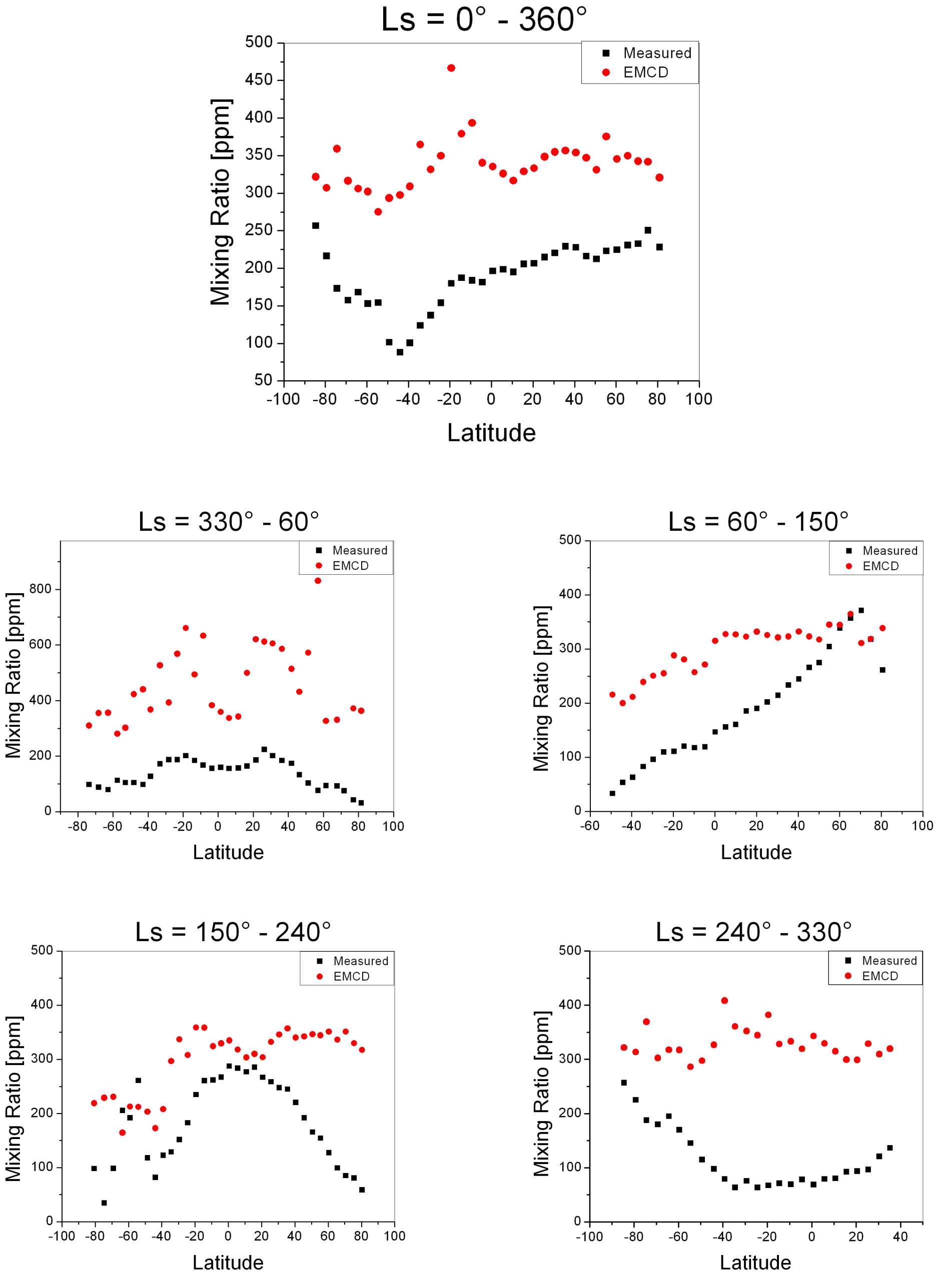

Figure 5.6: Latitudinal trends of the atmospheric water vapor concentration on data averaged into 5° bins in latitude both for all the Martian year (Ls = 0°-360°, top) and for four different periods: Ls = 330°-60°, Ls = 60°-150° (center), Ls = 150°-240° and Ls = 240°-330° (bottom). Black dots represent the measured data, while red dots represent data extracted from the MCD model.

The latitudinal trend is not always coincident, in fact we have a correspondence only in the panel representing the annual average and for the one showing the period Ls = 330°-60° (northern winter-spring), while other periods seem to have not any correspondence. Furthermore, it is important to stress that in all the studied cases, the MCD model provides values greater than about 150-200 ppm with respect to measured data. The reason for this overestimation lies in the fact that thte MCD determination of the atmospheric water vapor abundance has been calibrated with the original TES database, which should be corrected, as already noted by Fouchet et al. [86] and Tschimmel et al. [204].

Using data extracted from the MCD model, it is also possible to study the relation between the abundance of atmospheric water vapor and the surface pressure. The Figure 5.7 shows the mixing ratio trends as a function of surface pressure averaged in bins of 0.05 mbar for both the normalized (to 6.1 mbar pressure) measured data and those extracted from the MCD model. The

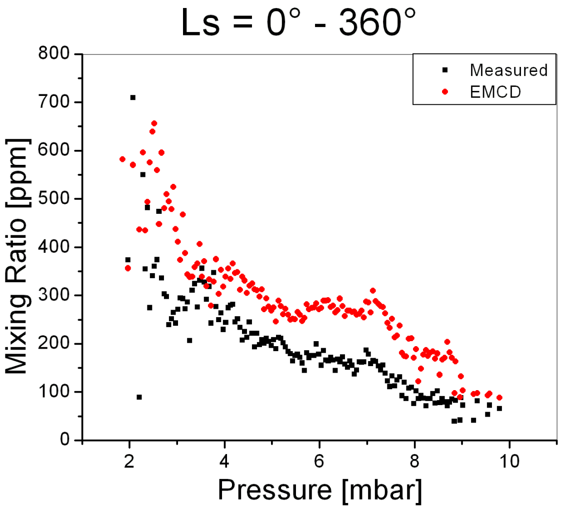

Figure 5.7: Normalized (to 6.1 mbar pressure)concentrations retrieved from measured data (in black) and extracted from the MCD model (in red) as a function of surface pressure for the whole Martian year. The measurements, selected in latitude between 30° S and 30° N, were averaged in pressure bins of 0.05 mbar.

expected anticorrelation in the measured data is perfectly reproduced by the model[2], which uses the MCD database (version 4.2), in contrast to what has been obtained by Fouchet et al. [86] using the previous version of the model itself. In fact, version 4.2 of MCD, used for this work, in addition to taking account of dynamic and saturation processes, which may lead to a $H_2O$ mixing ratio or saturation height dependence by the surface properties (such as the previous version), also includes processes that may involve a subsurface source.

---

[2] We have to note that, despite the $H_2O$ concentration trend as a function of surface pressure retrieved from the measured data is in agreement withe the one extracted from the MCD model, there is a model overestimation of about 150-200 ppm (as already discussed above).

## 5.3 Carbon Monoxide: Seasonal and Geographical Behaviour

Since the carbon monoxide is assumed to be uniformly distributed in the Mars atmosphere, so being independent on the topography [190], we do not need to apply the topographic correction to its concentration values.

The retrieved concentration of carbon monoxide as a function of Solar Longitude (Ls) and latitude, as observed by PFS/SWC, from orbit 634 to orbit 6537, allows us to study its seasonal cycle. The map obtained, using spectra averaged in 5° Ls x 5° Latitude bins, is shown in Figure 5.8.

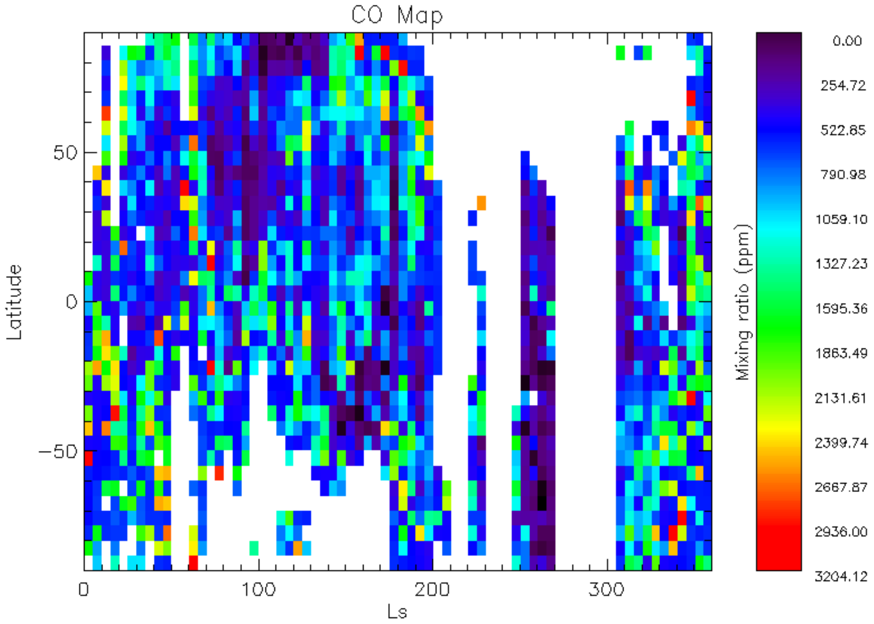

Figure 5.8: Map of retrieved concentration of carbon monoxide as a function of Solar Longitude (Ls) and Latitude as observed by PFS/SWC, from orbit 634 to orbit 6537, obtained using spectra averaged in 5° Ls x 5° Latitude bins.

The mean concentration for the whole dataset results to be 990 ppm with a maximum of 3217 ppm. The standard deviation over the mean value is about 580 ppm. Since the error in estimating the mean carbon monoxide concentration is about 220 ppm ($\ll$ 580 ppm), the big value of the standard deviation indicates, also in this case, the large spread (even if less strong than for the $H_2O$) in the carbon monoxide concentration values and therefore its variability in the Marian atmosphere. The retrieved CO mixing ratio is noisy because of the weakness of the CO absorption band and the relatively weak dependence of the absorption on CO mixing ratio. For the same reason we have sometimes a bad data coverage, due to the impossibility of having a good fit quality. Despite that, from the map we can see a general seasonal behaviour. Before Ls=70° there is a CO concentration of about 900 ppm with a definite increase in the middle latitudes of the southern hemisphere and over the north polar cap. From Ls=70° to Ls=100° the CO mixing ratio decreases over the north polar cap (less than 600 ppm) and its maximum value moves southward. The minimum mean quantity of revealed CO (about 400 ppm or less) is measured between Ls=100° and Ls=130° over the north polar cap (Latitude=75°-90° N). In this period it is evident that there is a CO concentration gradient that extends from lower values in the north to higher values (about 980 ppm) in the south. From Ls=130° to Ls=190° we can observe a new CO maximum zone in the middle-high latitude (50°-90° N): here the mixing ratio values are around 1120 ppm. In the period Ls=250°-270° the south polar cap sublimation causes a CO and non-condensable gases depletion (down to values less than 400 ppm), in an analogous way to what happens in the summer north pole. Finally, from Ls=305° the CO maximum zone moves toward the equator and at the same time a high CO concentration is evident in the northern hemisphere.

In order to study the carbon monoxide distribution in the Martian atmosphere, we used the averaged spectra in square bin of 10° Longitude x 10° Latitude for each season. The results obtained for Ls=0°-90° (Spring), Ls=90°-180° (Summer), Ls=180°-270° (Fall) and Ls=305°-360° (Winter) are shown in Figure 5.9. The CO geographical variability is characterized by a quite uniform longitudinal distribution, even if it is clear an asymmetry between the

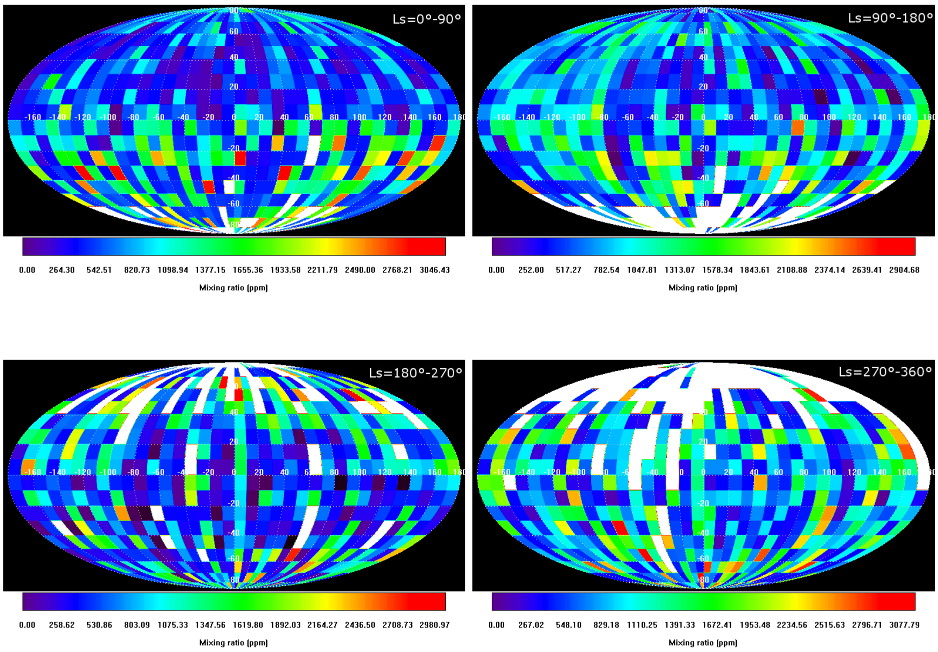

Figure 5.9: Map of retrieved concentration of carbon monoxide as a function of Longitude and Latitude as observed by PFS/SWC, from orbit 634 to orbit 6537, obtained using averaged spectra in square bins of 10° Longitude x 10° Latitude for each season: Ls=0°-90° (northern Spring), Ls=90°-180° (northern Summer), Ls=180°-270° (northern Fall) and Ls=305-360° (northern Winter).

two hemispheres: during northern spring and summer the carbon monoxide is mainly distributed in the southern hemisphere, while during the northern fall and winter it is has an higher mean concentration in the northern hemisphere. Moreover, no important features seem to indicate an increase over particular geographical regions.

## 5.4 Comparing $H_2O$ and CO results

In order to find correlations/anticorrelations in the latitudinal distribution between water vapour and carbon monoxide, we compared the orbital latitudinal trend for a few orbits of each season. For this purpose we used the "orbital dataset" and we expressed both gaseous concentrations in mixing ratios. The orbits selected as examples of the general seasonal latitudinal trend are: 3218 (Ls=78.4°) and 3234 (Ls=80.3°) for northern Spring, 1012 (Ls=109.2°) and 1219 (Ls=136.5°) for northern Summer, 1545 (Ls=184.9°) and 4456 (Ls=263.7°) for northern Fall, and 4777 (Ls=318.2°) and 4803 (Ls=322.3°) for northern Winter. The latitudinal trend of $H_2O$ and CO concentrations for these orbits is shown in Figure 5.10. Choosing individual orbits instead of mean orbital profiles for this kind of study is useful to demonstrate that we are able to maintain a good temporal and spatial resolution in retrieving the gaseous concentrations. The single orbit trends are representative of their own seasonal trends and this is clear comparing them with the averaged ones: in Figure 5.11 we show, as examples, the mean latitudinal trends retrieved between Ls = 90° and Ls = 120° (early northern summer) and between Ls = 240° and Ls = 270° (late northern fall).

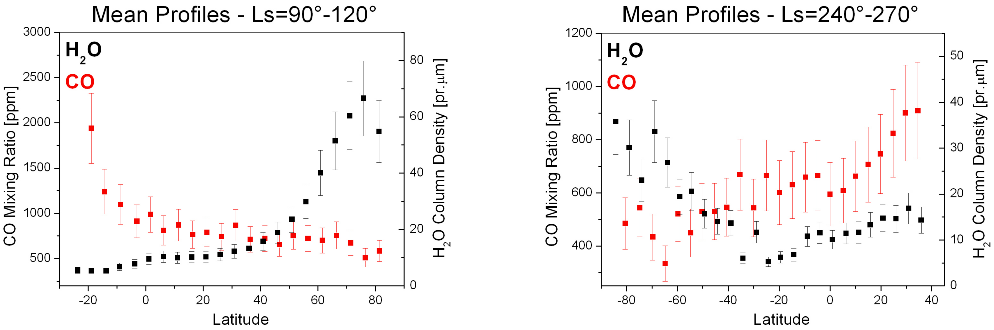

Figure 5.11: Examples of mean latitudinal trends retrieved between Ls = 90° and Ls = 120° (early northern summer) (left) and between Ls = 240° and Ls = 270° (late northern fall) (right).

We can start from the first two orbits, 3218 and 3234, examples of the late Spring latitudinal trend. We see the $H_2O$ enhancement over the northern polar cap region due to the seasonal polar cap sublimation and a corresponding relatively weak depletion of CO in the same region. We find an opposite behaviour in the southern hemisphere, where the coming of the southern polar

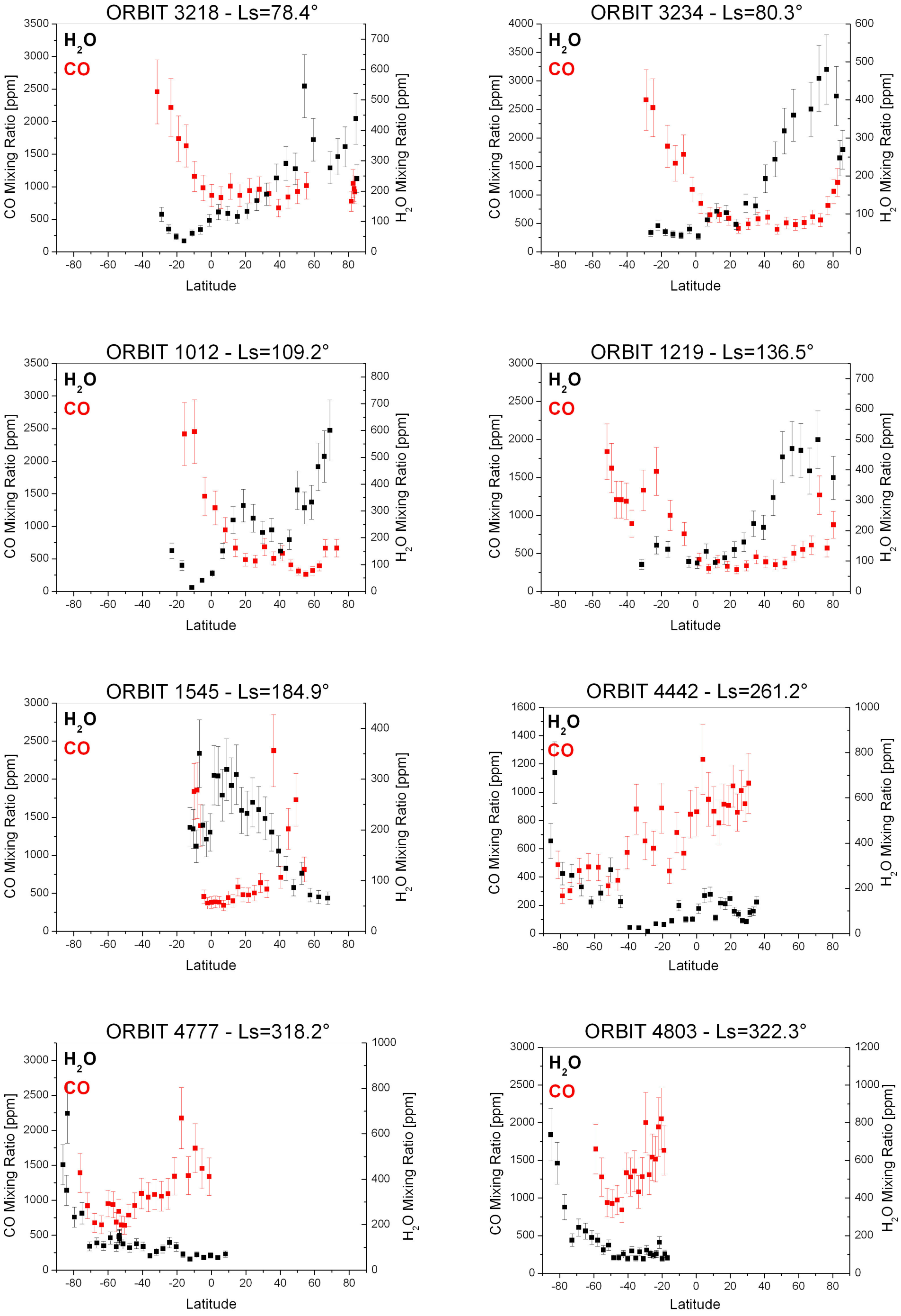

Figure 5.10: Latitudinal trend of the $H_2O$ (black) and CO (red) abundances for two orbits of each season: Spring (Orbits 3218, 3234), Summer (Orbits 1012, 1219), Fall (Orbits 1545, 4442) and Winter (Orbits 4777, 4803).

cap condensation causes an enhancement, as we have already said, of non-condensable gases, including CO, and an $H_2O$ values of less than 100 ppm in the same region with its maximum centred around 75° N, in agreement with our data obtained analyzing the “bin dataset” (Section 5.2).

Following the annual evolution we have the Summer season. For this period we have selected the orbits 1012 and 1219. During the Summer, the latitudinal trend already noticed in the Spring becomes now stronger, as an effect of the more intense north polar cap sublimation and south polar cap condensation processes. For Ls=109.2° (orbit 1012), over the northern polar cap, we find a water vapour maximum of about 600 ppm and lower values of CO mixing ratio (about 550 ppm), while, in the southern hemisphere around 20° S, the CO enhancement and the $H_2O$ depletion do not seem to be very different than during the Spring season. For Ls=136.5° (orbit 1219) the latitudinal trend becomes weaker again because the water vapour amount begins to move southward, even if the sublimation/condensation processes remain quite evident.

During the Fall season, orbit 1545 shows a relative flattening of the latitudinal distribution of the two gaseous species, even though we can note a weak increase of the CO mixing ratio toward the north pole and of the $H_2O$ toward the south pole. This trend becomes clearer in the latitudinal distribution of water vapour and carbon monoxide during the late Fall (orbit 4442) and the Winter (orbits 4777 and 4803), when the sublimation of the southern polar cap causes an increase of water vapour (maximum of about 700 ppm at 83° S), while the CO concentration grows northward.

Therefore, from latitudinal orbital study it is possible to confirm the $H_2O$ and CO seasonal behaviour already shown in the Sections 5.2 and 5.3: their tendency is generally anticorrelated.

## 5.5 Correlations between Gaseous Concentrations and Surface Pressure

In order to investigate the correlation between the atmospheric water vapor and carbon monoxide concentrations and the surface pressure, which is closely related to the topography of the planet, we selected all data, from the “orbital dataset”, at latitudes between 30° S and 30° N, so as to avoid relevant seasonal effects and, in particular, the particular abundances typical of the northern summer at high latitudes.

We averaged data for all the seasons (annual behaviour) and for two different seasons, one around the northern spring equinox (Ls = 330°-60°), and the other around the northern summer-early fall (Ls = 90°-200°), respectively.

### 5.5.1 Water Vapor

The Figure 5.12 shows the trends of absolute and normalized (to a pressure of 6.1 mbar) mixing ratio as a function of surface pressure, averaged in bins of 0.05 mbar pressure. This figure shows that, as expected for a generally well mixed distribution of water wapor in the atmosphere, the absolute abundance is positively correlated with pressure. We may note that the absolute concentration of water vapor increases more slowly than expected in the case of a

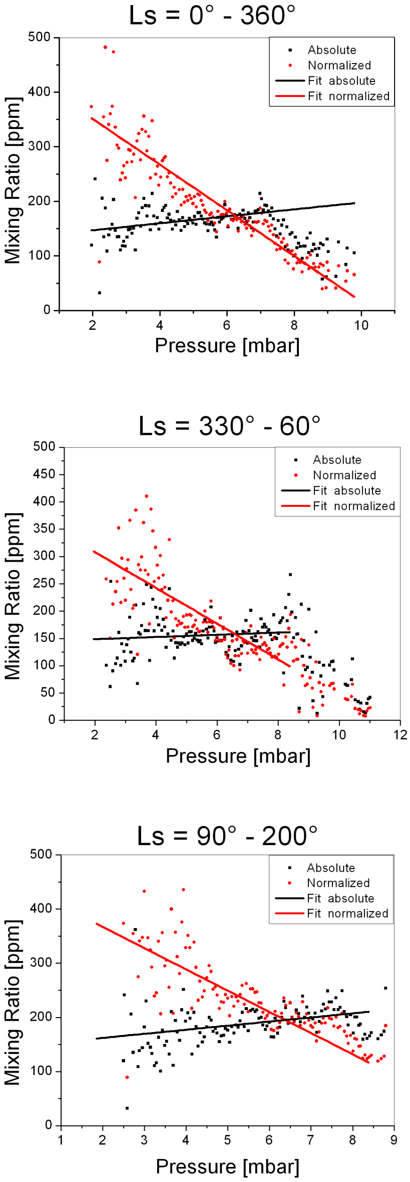

Figure 5.12: Absolute (black) and normalized to 6.1 mbar pressure (red) $H_2O$ concentratons as a function of the surface pressure averaged for the whole Matian year (upper panel), for Ls = 330°-60° (center panel) and for Ls = 90°-200° (lower panel). Measurements, selected at latitudes between 30° S and 30° N, are averaged in bins of 0.05 mbar pressure. Le lines represents the linear fit ($H_2O = a + b \cdot p_s$) of data.

linear pressure dependence, so that the normalized concentration results to be anticorrelated with the pressure itself. Table 5.1 shows the parameters of the linear fit performed on the statistical sample examined.

| Selected Data | a | b |
|---|---|---|
| Ls = 0°-360°: absolute concentrations | 134.59 | 6.37 |
| Ls = 330°-60°: absolute concentrations | 144.25 | 2.05 |
| Ls = 90°-200°: absolute concentrations | 146.92 | 7.55 |
| Ls = 0°-360°: normalized concentrations | 434.67 | -41.85 |
| Ls = 330°-60°: normalized concentrations | 373.59 | -32.79 |
| Ls = 90°-200°: normalized concentrations | 463.06 | -39.24 |

Table 5.1: Correlation between the atmospheric water vapor and the surface pressure. The a and b parameters represent the linear best fit ($H_2O$ = a + b · $p_s$) of data.

These results indicate that the water is not completely well mixed in the atmosphere and the normalization to a pressure of 6.1 mbar overcompensates the topographic effects. The values of the parameter b in the linear best fit ($H_2O$ = a + b · $p_s$) of data indicate a situation in which the water vapor is only partially mixed in the atmosphere and in which a substantial part of it is confined in a near-surface layer. This behavior is not consistent with a $H_2O$ distribution profile defined by a uniform mixing and a saturation level independent by the surface pressure: this situation should lead to a decrease of the mixing ratio with the decrease of the average surface pressure, i.e. to a positive correlation between the normalized water vapor concentration and the surface pressure itself.

Unfortunately, direct measurements of the vertical distribution of atmospheric water vapor are very limited. Since we have not data by adequate instrumentation aboard the descending probes on Mars, the only investigation methods are: occultations or limb measurements and absorption measurements with multiple paths in a given atmospheric column [86]. From the solar occultation measurements obtained by Phobos 2/Auguste for Ls = 2°-18°, Rodin et al. [175] observed an approximately uniform mixing ratio around about 10-25 km, and a sharp decrease above. Davies key-83[61] used observations at multiple angles of the Viking 1 lander with the Viking 1/MAWD instruments to deduce a $H_2O$ uniform distribution below 10 km above the lander site and at Ls = 102°. By a similar technique, but looking at the Sun from the Martian surface, Titov et al. [202] found, on the contrary, that the water vapor is confined in the first 1-3 km for Ls = 150°. The altitude variations of the residence condensation level of water vapor with the seasons were fully established by Clancy et al. [50] using the millimeter spectroscopy. They found that the water vapor is confined at altitudes lower than 10 km near the aphelion (Ls = 71°), but invades the entire atmosphere up to 50-70 km near the perihelion (Ls = 251°). Additional observations of Encrenaz et al. [63, 64], Gurwell et al. [99] and Biver et al. [39] support this scenario, as well as numerical simulations by Richardson and Wilson [173], and Montmessin et al. [151]. Titov [203], reviewing all these observations, concluded that the seasonal variation of the layer in which the water vapor is well mixed is from about 5 km for Ls = 90°-150° to about 20-25 km for Ls = 330°-30°. Moreover, Fedorova et al. [77] reported $H_2O$ results from SPICAM measurements by 24 MEX orbits acquired in solar occultation during MY28 at Ls 130°–160°, and in the latitude range of 40°–55° N. They detected an higher and strongly decreasing concentration of water vapor from about 15 Km ($\sim$ 115 ppm) to 30 Km ($\sim$ 10 ppm) in the atmosphere, whereas above 30 Km it is almost stable around 10-15 ppm. Recently, also Maltagliati et al. [138] retrieved the vertical distribution of water vapor using SPICAM data and they found evidence of the frequent presence of water vapor in excess of saturation, by an amount far surpassing that encountered in Earth's atmosphere.

The results obtained in this work for the correlation between the water vapor concentrations and the surface pressure are in agreement both with those obtained by Fouchet et al. [86] and with those by Smith [185] with TES data. He suggested that linearly rescaling the atmospheric water vapor abundance to the surface pressure results in a overcompensation for the topography effects. He also found that the anti-correlation between the abundance and the normalized surface pressure is stronger in the northern hemisphere than in the south, i.e on annual averages, the water vapor is more mixed in the south than the north.

In addition, the anti-correlation observed between the normalized abundances and the surface pressure is indicative of the fact that a small amount of "background" water (130-140 ppm, as indicated by the coefficient a in Table 5.1) may be present regardless of the altitude (except on the tops of volcanoes), presumably due to soil-atmosphere exchanges.

### 5.5.2 Carbon Monoxide

The Figure 5.13 shows the trends of absolute and normalized (to a pressure of 6.1 mbar) mixing ratio as a function of surface pressure, averaged in bins of 0.05 mbar pressure. While Table 5.2 shows the parameters of the linear fit performed on the statistical sample examined. From the figure 5.13 and Table 5.2 we can immediately notice that a slight anticorrelation of absolute concentrations with pressure seems to exist, which becomes more noticeable when we refer to the normalized concentrations. This is perfectly consistent with what we concluded in Section 5.5.1, which shows that water vapor tends

| Selected Data | a | b |
|---|---|---|
| Ls = 0°-360°: absolute concentrations | 1345.12 | -28.59 |
| Ls = 330°-60°: absolute concentrations | 2397.69 | -62.60 |
| Ls = 90°-200°: absolute concentrations | 1134.72 | -8.04 |
| Ls = 0°-360°: normalized concentrations | 2199.06 | -164.55 |
| Ls = 330°-60°: normalized concentrations | 3814.60 | -292.33 |
| Ls = 90°-200°: normalized concentrations | 1903.76 | -131.46 |

Table 5.2: Correlation between the atmospheric carbon monoxide and the surface pressure. The a and b parameters represent the linear best fit (CO = a + b $\cdot$ $p_s$) of data, in which we excluded the low pressures, indicating large elevations such as volcanoes.

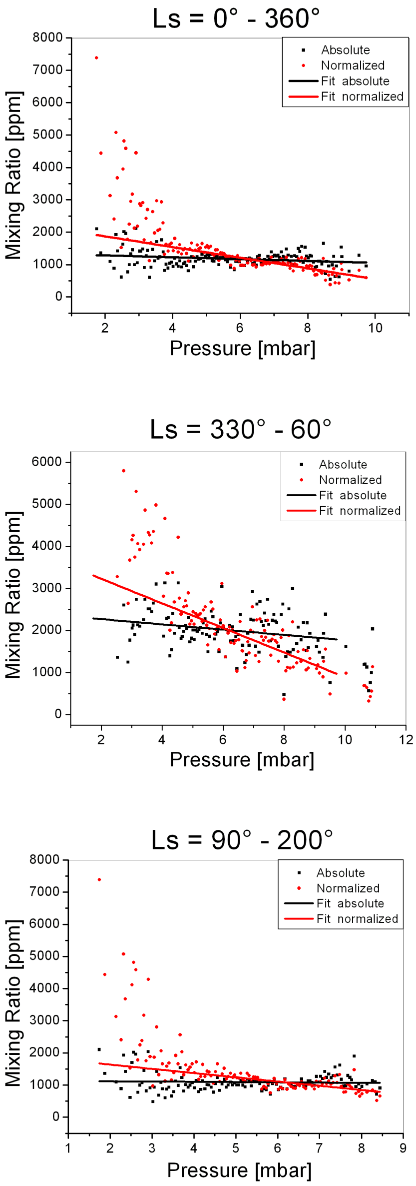

Figure 5.13: Absolute (black) and normalized to 6.1 mbar pressure (red) CO concentrations as a function of the surface pressure averaged for the whole Martian year (upper panel), for Ls = 330°-60° (center panel) and for Ls = 90°-200° (lower panel). Measurements, selected at latitudes between 30° S and 30° N, are averaged in bins of 0.05 mbar pressure. Le lines represents the linear fit ($H_2O = a + b \cdot p_s$) of data, in which we excluded the low pressures, indicating large elevations such as volcanoes.

to partially confined in the atmospheric surface layer. Taking into account that the statistical analysis of the CO concentration dependence from the surface pressure was only carried out in the equatorial zone (for the reasons mentioned above), we can note that the greater anticorrelation occurs just when in this geographical region a greater amount of $H_2O$ is present. Indeed, for Ls = 330°-60° the water vapor is transported by atmospheric dynamics

(Section 5.2), while when the water vapor is concentrated at high latitudes due to the sublimation of the north polar cap (Ls = 90°-200°), we observe the slightest anticorrelation. Then, when the pressure is high, the column of the atmosphere on which is integrated the CO abundance extends up to the regions in which the amount of $H_2O$ becomes important, thus producing the relative disappearance of the carbon monoxide in that region and leaving it almost unaltered in the rest of the atmospheric column. In fact, without factors such as the presence of water vapor, it is expected that CO is uniformly distributed in the atmosphere up to at least about 40 km. This is due to the fact that the vertical mixing time of the CO is $H^2/K \approx 2$ weeks, where $H$ is the *scale height* and $K \approx 10^6$ cm$^2$s$^{-1}$ [125] is the *turbulent diffusion coefficient.*

Unfortunately, direct measurements on the vertical distribution of atmospheric carbon monoxide are very limited. The observations made by Phobos orbiter using the low-resolution spectroscopy of the CO band at 2.35 $\mu$m [176] showed a decrease in the carbon monoxide abundance by a factor of 5-8 over the great volcanoes, but this result is completely inconsistent with the photochemical predictions [124]. Whereas, Krasnopolsky [122] did not reveal any significant variation in the CO mixing ratio with the altitude in the range from -6 to 3 km using data acquired by the IRTF/CSHELL telescope. The analysis performed in this work is in good agreement with the results obtained by Krasnopolsky [122], in fact we can see in Figure 5.14, that there is no significant variation in the CO abundance with altitude until at least 5 km in height, while there is a significant increase which reaches its maximum for an altitude of about 6.75 km before returning to fall for higher altitudes. The not

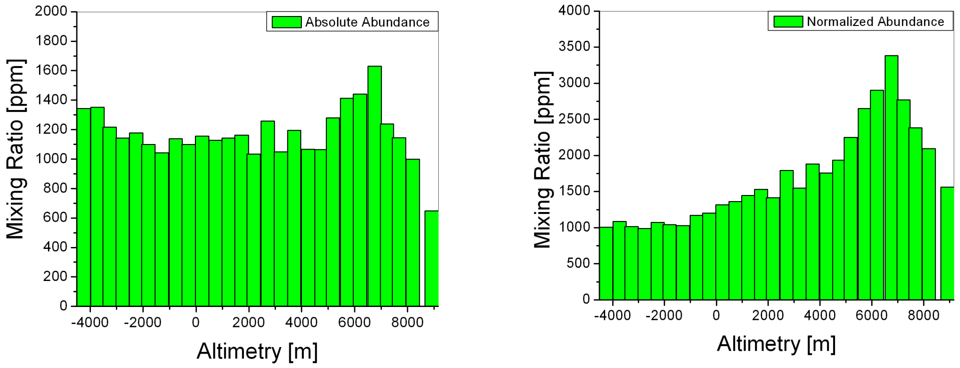

Figure 5.14: Distribution of absolute (left) and normalized (to the pressure of 6.1 mbar) (right) CO concentrations in the atmosphere of Mars as a function of the altimetry. The measurement, selected in latitude between 30° S and 30° N, are averaged in bins of 500 m in height.

expected trend by Rosenqvist et al. [176] has been justified by Hunten [111], who states that small changes in the continuum definition of the CO band could remove the mixing ratio variations in the Phobos observations.

## 5.6 Discussion

The seasonal cycle of water vapour obtained from this analysis was observed also by other instruments, as MAWD [113, 122], TES [186], SPICAM [76], and CRISM [190], and by PFS/LWC [86] and PFS/SWC [204]. Tschimmel et al. [204] studied the water vapour distribution during the period between Ls=331° of MY 26 and Ls=196° of MY 27, analyzing its 2.6 $\mu$m absorption band. Despite their dataset does not overlap in time with ours, it is possible to compare the mean $H_2O$ behaviour. They observed the maximum value of water vapour abundance of about 60 pr.$\mu$m over the sublimating northern polar cap and the typical seasonal cycle, just in agreement with our results. Also their geographical distribution shows the water vapour behaviour we observed, but the local maxima over Arabia Terra and Tharsis are about one and a half time higher than in our maps, while the maxima values, centred around the latitude of 75°N, over the northern polar cap during its summer are in good agreement with our measurements. Since results by Tschimmel et al. [204] are referred to a period in which the sublimation of the northern polar cap dominates, their average column density of 16.2 pr.$\mu$m is higher than our mean value (9.6 pr.$\mu$m).

Unfortunately, at the time of this writing only CRISM data can be compared with our data because these are the only data corresponding in time (MY 28-29) to our observations. CRISM measures a water vapour maximum during the northern hemisphere summer at high latitude. Its value is about 50 pr.$\mu$m and it is in agreement with our maximum value of 59 pr.$\mu$m. The location of the centre of the water vapour distribution out of the permanent polar cap border during the northern summer (Section 5.2) is explained by Montmessin et al. [151] suggestion: the water vapour produced by the seasonal polar cap sublimation is partly carried by the circulation toward the pole and redeposited on the permanent polar cap, whereas the remaining $H_2O$ is carried by the atmospheric dynamics toward the equatorial regions, where it forms the "Equatorial Cloud Belt". After that, in the centre of the summer (about Ls=110°), even the ice created by the $H_2O$ redeposited in the permanent polar cap sublimates, producing the peak that we observe in the maps.

In the southern summer, instead, CRISM data show a reduced water vapour abundance if compared to observations from previous years. These low values are due to the fact that Smith et al. [190] studied only the MY 28 southern summer: in this year, between Ls=270° and Ls=305° there was a planet-encircling dust storm, which is known to produce significant changes of the atmospheric state [185] and of the surface albedo [186], resulting in the absence of the southern summer maximum. A similar effect was already noticed by TES data during the MY 25 dust storm [185] and by Viking Orbiter MAWD during the MY 12 dust storm [75]. The normal water vapour trend in the southern hemisphere summer was shown for MY 24-25-26 by TES [185] and for MY 27 by Mars Express SPICAM [76] and OMEGA [137]. Our data, out of the global dust storm, show between Ls=305° and Ls=340° a maximum value of 22.8 pr.$\mu$m over the south polar cap: this lower value compared to the northern summer one is explained by the shorter summer in the southern hemisphere, so the water vapour sublimation is hindered by the presence of a layer of $CO_2$ ice for most of the cap. Moreover, also the apparent partial $H_2O$ geographical confinement in the northern hemisphere, probably due to the global circulation, could have a role in this evidence.

The CO seasonal trend as retrieved by our PFS data shows the same latitudinal gradient in the northern hemisphere summer observed by Smith et al. [190] with CRISM and Krasnopolsky [122] with the IRTF/CSHELL spectrograph. At Ls=112° Krasnopolsky measured a CO gradient increasing from north of 23° N latitude (about 830 ppm) to south (about 1250 ppm at 45°S latitude), while Smith et al. [190] revealed a CO mixing ratio gradient from about 450 ppm poleward of 30°N to 700 ppm at 30°S. Our measurement provides for the same period a gradient varying from about 270 ppm in the 75°-90° N latitude to about 1250 ppm in the 30°-45° S latitude. This hemispheric asymmetry is due to the condensation of the $CO_2$ gas in the south polar cap, which would lead to an enhancement in non-condensable gases, such as carbon monoxide, in the southern polar atmosphere. At the same time, the sublimation of the northern polar cap leads to a non-condensable gas depletion causing the strong reduction of the CO mixing ratio. In the same way, but in the opposite hemisphere, during the northern winter we see an enhancement in the CO mixing ratio, while over the south pole we observe a CO depletion due to the ice sublimation. This CO behaviour during the northern winter has also been observed by Billebaud et al. [38], but they show results for only 90 PFS/MEX orbits, between Ls=331.17° and Ls=51.61°, measuring 1110 ppm for the CO mixing ratio averaged over their entire data sample. This mean value is slightly higher than the values determined in our and previous works, probably because it refers to a limited dataset. Comparing their CO mixing ratio trends as a function of latitude for three Ls ranges (Ls=331°-360°, Ls=0°-30° and Ls=30°-52°) with our mean latitudinal trends for the same periods, we find an agreement for the first two trends, although with a 40% higher mean concentration in our data, but an opposite behaviour for the range Ls=30°-60°. In this period we measure a gradual decrease of the CO concentration between 40°S and 0° in latitude and a quite constant value of about 1000 ppm going northward up to 80°N, while Billebaud et al. [38] reveal a gradual increase up to 0° and a quite constant concentration value around 1000 ppm in the northern hemisphere. These differences could be due to the different dataset analyzed and so to the interannual variations in the Mars atmosphere. Billebaud et al. [38] studied also the trends of the CO mixing ratio as a function of geographical longitude for three latitudinal ranges (90°S-30°S, 30°S-30°N and 30°N-90°N). Comparing these results with our mean trends, we find a very good agreement both in the trends themselves and in the mean concentrations values. Moreover, we observe in the exact same positions the local CO maxima (around 125°W, 50°E and 150°E), probably due to planetary waves.

The LMD/GMC model expects that the mixing ratio of non-condensable gases over Hellas basin should reach two times higher values than the mean ones during the summer and a minimum concentration during the winter [68].

This effect should be due to the isolation of this zone with respect to local vortex. This CO enhancement over Hellas basin has been confirmed by OMEGA/MEX data [68] and CRISM/MRO [190], but not by the ground-based IRTF/CSHELL data analyzed by Krasnopolsky [122, 124], which do not show significant variations between the atmosphere in and out the basin. So our observations of the Hellas basin agree with Krasnopolsky's. Moreover, Krasnopolsky [122] revealed an asymmetry between the northern and southern hemisphere, measuring a CO increasing up to 50% from 23°N (830 ppm) to 50°S (1240 ppm). This effect is interpreted as a consequence of the $CO_2$ condensation during the polar winter, which leads to an atmospheric enhancement of non-condensable gases. This enhancement effect has also been observed by the Mars Odyssey GRS instrument through the study of argon distribution in the Mars atmosphere [195, 197]. We measure a depletion of about 70% over the summer northern polar cap, while over the summer southern polar cap we find a depletion of about 50% with respect to the planetary mean value. The different weight of the depletion should be due to the different duration of the summer season in the two hemispheres (178 days in the north and 154 days in the south).

The models [79, 81, 156, 130] also confirmed that the $CO_2$ condensation on the winter polar cap causes an increase of the non-condensable gases mixing ratio, and in a similar way, the sublimation from the summer polar cap produces a depletion of non-condensable gases. But, the NASA GCM (General Circulation Model) [156] seems to underestimate the strength and the duration of the depletion, while the LMD model [81, 130] seems to underestimate only the duration of the depletion, when these previsions are compared with our data and with CRISM data.

Finally, comparing $H_2O$ and CO results we can conclude that these two gaseous species are generally anticorrelated. The main cause of this anticorrelation is the following: the water vapour being a condensable species and the carbon monoxide a non-condensable one, they are strongly influenced in an opposite way by the processes of condensation and sublimation in the polar caps.

# Chapter 6

# Planetary Waves and Dynamics by $H_2O$ and CO Retrievals

The study of the geographic distribution of water vapor and carbon monoxide in the atmosphere of Mars using PFS data (Chapter 5 and [183]) has revealed a periodic longitudinal localization of minor gaseous species (Fig. 5.5 and 5.9).

In this chapter we will examine this periodic phenomenon and we will look for correlations between the longitudinal distributions of retrieved concentrations of the studied minor species from quasi-nadir measurements and the dynamic processes of the atmosphere, which depend on the altitude they occur.

## 6.1 Dataset

The PFS/SWC dataset used for this work covers about three Martian years, from Ls = 62° of MY 27 (orbit 634) to Ls = 340° of MY 29 (orbit 7327).

The dataset was obtained by averaging dayside spectra, acquired in quasi-nadir geometries, in square bins of 10° in longitude x 10° in latitude. The three Martian years (MY 27-28-29) were divided in order to be independent of particular bias due to the orbit of MEX, and every Martian year has been divided, in turn, in twelve seasonal ranges of 30° of solar longitude. Latitude vs longitude averages were calculated separately for each of the twelve seasonal ranges of each Martian year, giving particular attention to the local time of acquisitions. Indeed, since the wave phenomena in the Martian atmosphere can be strongly affected by the thermal conditions, we decided to average only spectra having a maximum local time span of ± 1.5 hours around its average value for each latitudinal strip. In this way we have a total of 7798 mean spectra and the number of averaged spectra in each bin ranges from 1 to 414. The data coverage of the planet is shown in Figure 6.1.

To retrieve the water vapor and carbon monoxide concentrations we applied the analysis algorithm described in Chapter 5, using, as input, the vertical profiles of temperature and pressure extracted by the MCD model, first, and then the ones retrieved following the approach by Grassi et al.[96], which here we call “BDM”. The latter provides atmospheric vertical profiles as measured

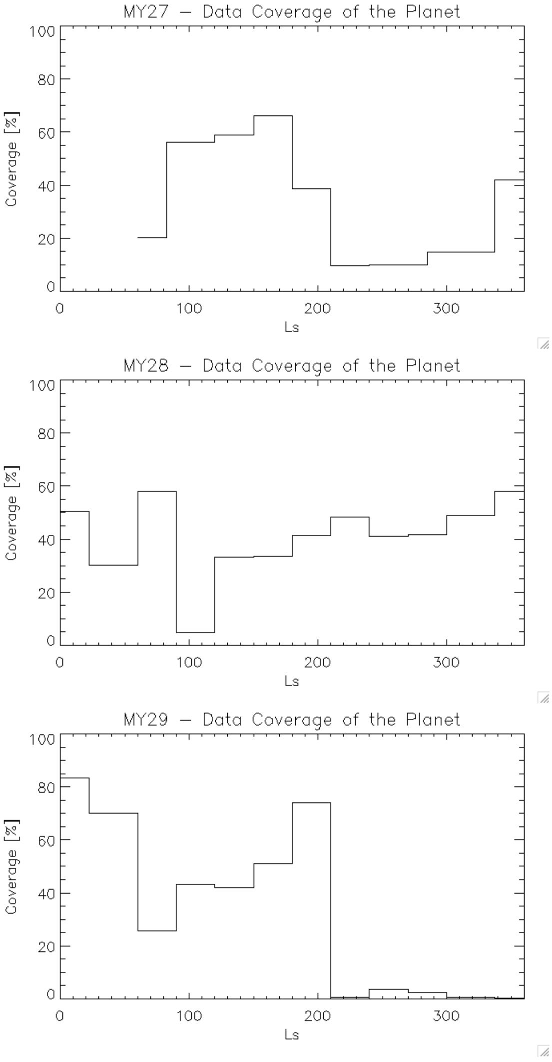

Figure 6.1: Data coverage of the planet in percentage for the three Martian years (27, 28 and 29).

by the LWC of PFS. Since the limit of reliability of the BDM profiles is an altitude of about 45 Km above the surface [96] and there the pressure is almost negligible for our purpose, we decided to cut the vertical profiles at this value. Moreover, we considered the actual dust and water ice opacity (extracted by the MCD model or retrieved by PFS/LWC measurements) in the computation of synthetic spectra. We decided to retrieve the water vapor and carbon monoxide concentration two times, according to the two different approaches (i.e. using the MCD or the BDM input), for the same mean spectrum because we want to exclude or stress possible dynamical effects of the Martian atmosphere which are not included in the MCD model.

The analysis method, naturally determines a criterion to select good data. As we have already done in Chapter 5, we decided to discard the results obtained by a best fit having a $\chi^2$ higher than 50 and 25 for the $H_2O$ and the CO band, respectively. In this way we discarded about 3% of the water vapour data, with a maximum of about 27% in the seasonal bin between Ls 270° and 300° of the MY 28 because of the global-encircling dust storm 5, and about 33% of the carbon monoxide data, with a maximum of about 70% in the seasonal bin between Ls 120° and 150° of the MY 29.

## 6.2 Observation of Wave Phenomena

In order to study wave phenomena in a quasi-stationary form, we divided the planet into 18 latitudinal strips of equal size (10°). For each strip of each sub-seasonal range we consider, we averaged the relative concentration results, keeping a longitudinal width of about 20°, and again excluding the values corresponding to a mean local time higher (or lower) than + (or −) 1.5 respect to the mean local time of the entire strip. In this way, each latitudinal strip contains only values retrieved for a stable thermal condition. Then we excluded the latitudinal strips having an insufficient number of retrieved values to define a clear trend. We chose a threshold of 5 values for each latitudinal strip and in this way we obtained 113 and 130 latitudinal strips, for $H_2O$ and CO, respectively, on which we can search for wave trends.

We recognize a wave pattern in a latitudinal strip when the concentrations values oscillate along longitudes around a mean value. So we applied to each strip a (least squares) best fit procedure using a sinusoidal curve: if the related $\chi^2$ variable is inside the 60% confidence interval and the percentage amplitude of the sine curve is more than 30% therefore the wave trend is observed. In our criterion we chose a threshold of 30% for the percentage amplitude of the sine curve fitting the longitudinal trend of $H_2O$ and CO concentrations because it is quite higher than the uncertainties (around 20%) of the retrieved values (Section 4.4). A typical example for the water vapor and carbon monoxide is shown in Fig. 6.2. The figure represents two very different atmospheric conditions: the near-equatorial region (10°-30° N) during northern spring (Ls = 0°-30°) and the near-polar region (50°-70° S) during southern spring (Ls = 180°-210°) of the Martian Year 29. The difference between the two cases is clear: during the first period, both the water vapor and the carbon monoxide show a double peak around a longitude of 120°W and 50°E, even if the (order 2) wave trend is more marked and less broad for the $H_2O$ than for the CO. In the second period, the water vapor seems to have an order 1 wave trend with a single minimum around 20°W and a single maximum around 180°E. The carbon monoxide has a different behaviour: it shows an order 3 wave trend with a double peak around 100°W and 0°E and another minor peak around 100°E. Moreover, the differences between the values retrieved using the two different approaches for the atmospheric modelling (MCD and BDM) are on average less than 5%.

### 6.2.1 Comparison with Vertical Thermal Profiles

In order to correlate the trends observed in the longitudinal distributions of minor species with atmospheric dynamics phenomena, we studied the tem-

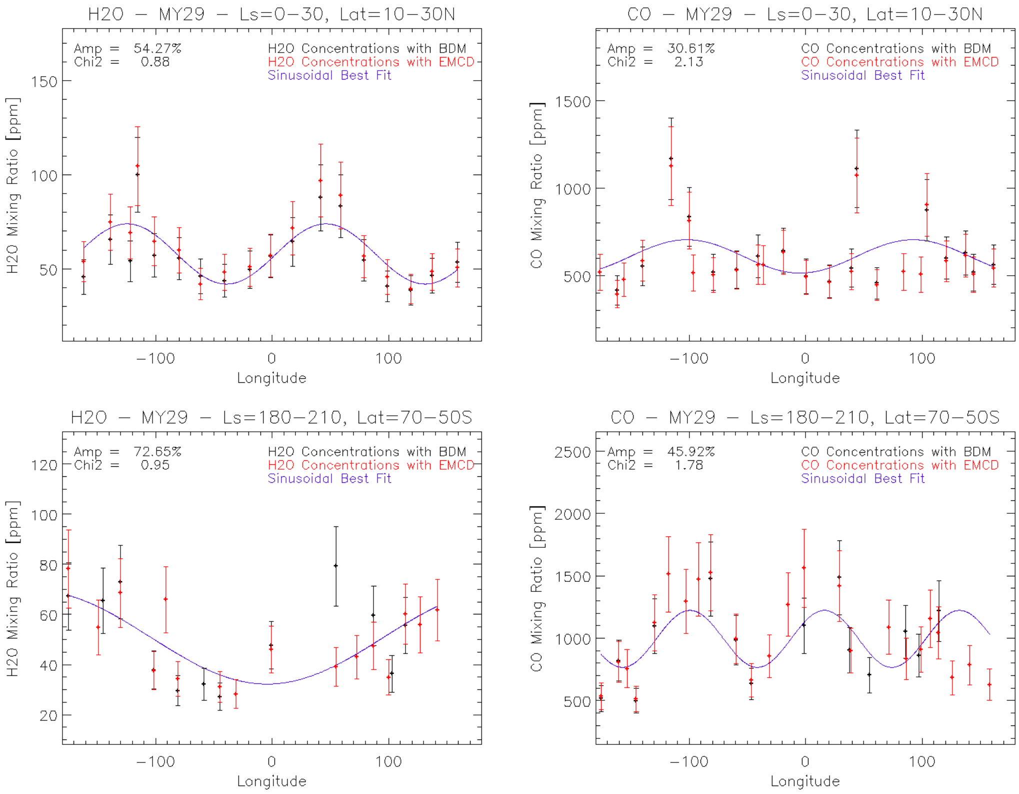

Figure 6.2: Typical examples of wave longitudinal trends of water vapor (left) and carbon monoxide (right) concentrations. The top panel refers to the near-equatorial region (10°-30° N) during northern spring (Ls = 0°-30°), whereas the bottom panels refers to the near-polar region (50°-70° S) during southern spring (Ls = 180°-210°) of the Martian Year 29. The black values are obtained using the vertical atmospheric profiles retrieved by PFS/LWC, whereas the red values are retrieved using the MCD ones. The blue line represents the sinusoidal best fit having the amplitude and the reduced $\chi^2$ indicated in the panel.

perature profiles, retrieved both by PFS measurements and MCD, and then averaged exactly as the relative spectra. Figure 6.3 shows examples of the vertical temperature cross-sections as retrieved by the BDM method: they refer to the two case examined in Figure 6.2. As we can clearly notice, the bottom of the vertical temperature maps represents the mean topography of Mars in the considered regions.

During northern spring (Ls = 0°-30°) over the near-equatorial region (10°-30° N) temperatures do not have strong changes along longitudes and they range between about 227 K near the surface and 134 K at 48 Km. We find a different condition during southern spring (Ls = 180°-210°) over the near-polar region (50°-70° S), where temperatures strongly change along longitudes and in different way at different altitudes, having a maximum of about 223 K near the surface at 150°-160° W and a minimum of about 140 K at high altitude above the region located at 120°-130° E. Moreover, we can recognize the border of the Hellas basin between 70° E and 80° E.

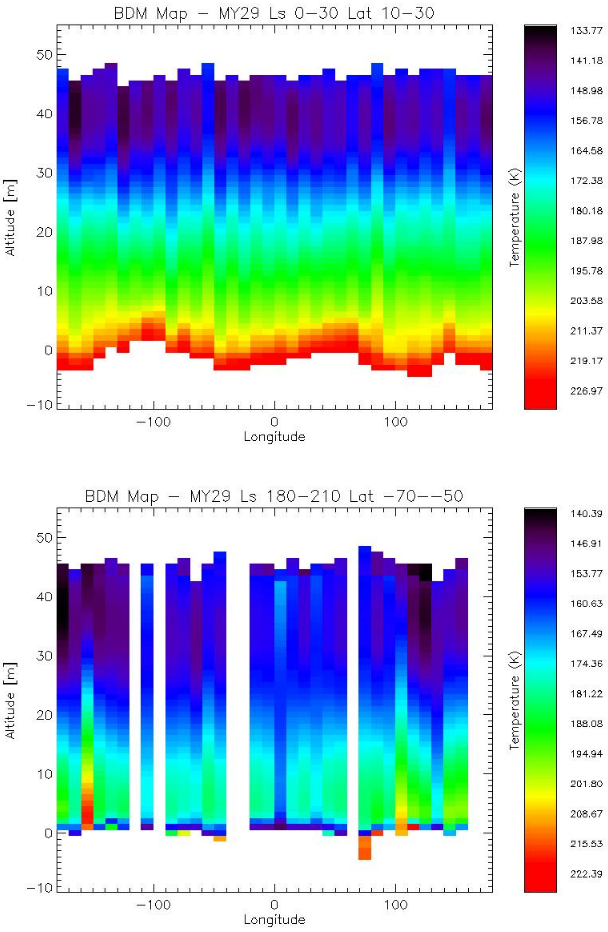

Figure 6.3: Typical examples of vertical temperature cross-sections: on the top panel for the near-equatorial region (10°-30° N) during northern spring (Ls = 0°-30°) and on the bottom panel for the near-polar region (50°-70° S) during southern spring (Ls = 180°-210°) of the Martian Year 29, as retrieved using the PFS/LWC spectra and the approach by Grassi et al. [96].

Since we want to compare the longitudinal trends of temperatures and gaseous concentrations, we divided the atmosphere above the region of interest in bins of 10 Km in altitude. In this way we obtained 6 temperature trends for both the cases previously taken as examples (Figure 6.4).

As we have already noticed showing the temperature cross-sections, for the first case we considered (Ls = 0°-30°, 10°-30° N), the longitudinal thermal trend is almost flat above 10 Km, while temperatures clearly reproduce the Martian topography, and the water vapor trend (Fig. 6.2), for 0-10 Km: in fact, at this altitude bin, temperatures have maxima around 120°W and 50°E. This correlation between the water vapor distribution, temperature trends and topography suggests an interaction soil-lower atmosphere. The carbon monoxide has the same two maxima in its longitudinal distribution, but with an overall flatter trend than the water vapor one. Furthermore, the MCD temperatures are in very good agreement with the measured (BDM) ones: the

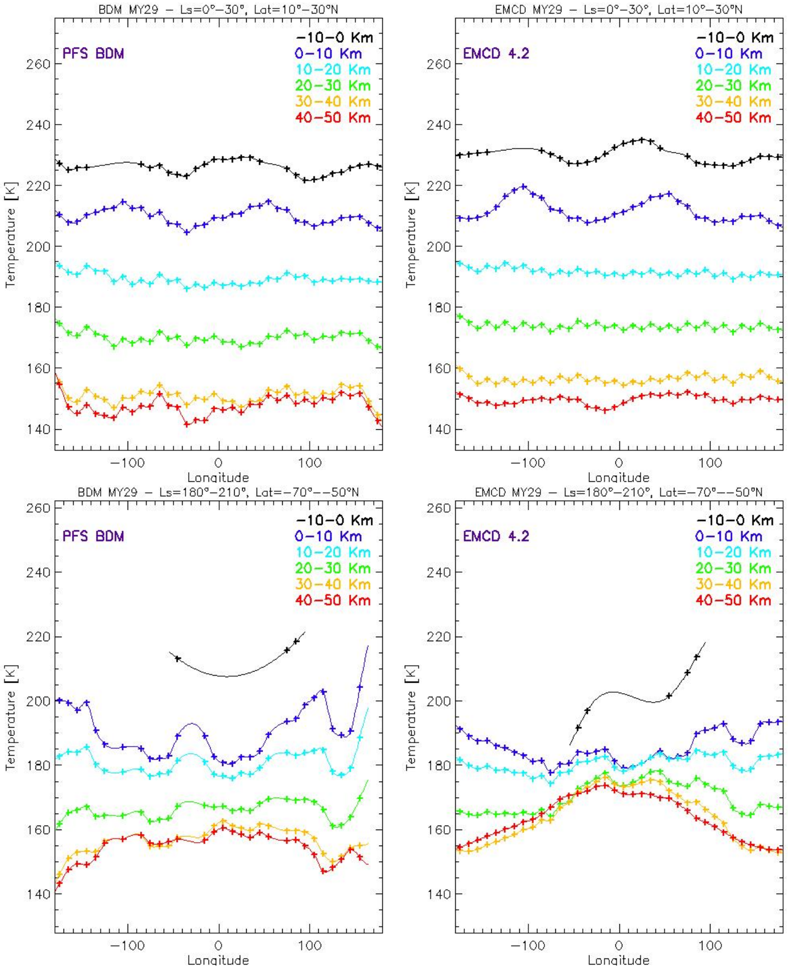

Figure 6.4: Typical examples of longitudinal trends of temperatures (BDM on the left and MCD on the right) at different altitudes (bins of 10 Km). The top panels refer to the near-equatorial region (10°-30° N) during northern spring (Ls = 0°-30°), whereas the bottom panels refer to the near-polar region (50°-70° S) during southern spring (Ls = 180°-210°) of the Martian Year 29.

differences between them are less than about 2.5% for all the altitudes.

The second case we considered (Ls = 180°-210°, 50°-70° S) represents a much more different condition (Fig. 6.4): the latitudinal thermal trend shows an order one wave having its maximum around 180° E and its minimum around 0° E, for the near-surface atmosphere. Then, going upward, the temperatures show a decrease in the wave amplitude, up to about 25 Km, where the trend is almost flat. Coming on upward in the atmosphere, the wave amplitude grows again, but in phase opposition with the wave trend in the lower atmosphere. At an altitude of 40-50 Km, the temperature has its maximum around 0° E and its minimum around 180° E. The maximum amplitude (about 20 K) of the thermal wave trend is reached for both the lower (0-10 Km) and higher (40-50 Km) atmosphere. In this case, we do not recognize any direct correlation with the topography, therefore the wave pattern genesis should be related to dynamical effect of the Martian atmosphere above the southern near-polar region during the fall season. Although the temperatures extracted by the MCD model and the measured ones (BDM) have a good agreement in their longitudinal trends, they show differences of about 5% in the lower atmosphere and of about 9% at the higher altitudes.

Comparing the gaseous concentrations trends with the thermal ones in these conditions (Ls = 180°-210°, 50°-70° S), we can identify a clear correlation between the water vapor trend with the lower atmosphere dynamics: both $H_2O$ concentrations and temperatures show a minimum around 0° E for altitudes of 0-10 Km, while they are almost perfectly anti-correlated at altitudes of 40-50 Km. Regarding the carbon monoxide distribution, we observe a general opposite behaviour: it shows a triple peak trend, with a small peak-to-peak distance, and a clear minimum around 180° E. This longitudinal distribution recall the thermal trend at high altitudes (40-50 Km) and it is in almost completely anti-correlation with the near-surface atmosphere.

#### 6.2.1.1 Observation of the Polar Warming

Strong meridional winds above 50 km lead to a horizontal convergence of mass and downward motion above the northern polar region, resulting in adiabatic warming down to about 30 km. This warming is expected to be most pronounced during perihelion conditions, when maximum solar insolation and strong dust heating prevail, but we can observe it since the early northern fall. As example, Figure 6.5 shows the thermal cross-section of the Martian atmosphere near the polar region (50°-70° N) during the seasonal bin Ls=180°-210° of the MY 27 and the relative longitudinal trends at different altitudes. First of all, we can notice that the MCD model does not foresee the presence of a strong polar warming in these conditions, whereas the PFS/LWC temperature retrievals (BDM) can observe it. The polar warming is represented by an increase of temperatures at high altitudes, which reach its maximum around 42 Km and at a longitude of 10°-20° E. At this longitude and altitude the temperature is about 185 K, against the temperature of about 175 K of the near surface atmosphere. Also in this case, the temperatures show an order 1 wave trend, having an opposite phase between the lower and the higher atmosphere.

We can study the effect of the polar warming on the gaseous distributions by comparing the longitudinal trends of temperatures with the gas ones. In Figure 6.6 are shown the water vapor and carbon monoxide longitudinal trends for the case we have already discussed, in which we can observe a clear polar warming. Both gaseous species show an order 1 wave trend, even if it is clearer for water vapor than for carbon monoxide. The $H_2O$ concentration has a maximum (50 ppm) around 100° W and a minimum (20 ppm) around 20° E. This trend is in phase with temperature trend at lower altitudes, whereas the CO concentration has a weakly clear wave trend with a maximum (2200 ppm) around 20° E and a minimum (about 1000 ppm) around 180° E, just in phase with the temperatures at high altitudes. Finally, the conditions observed during the polar warming reflect the typical case of the near-polar region during southern spring that we discussed above.

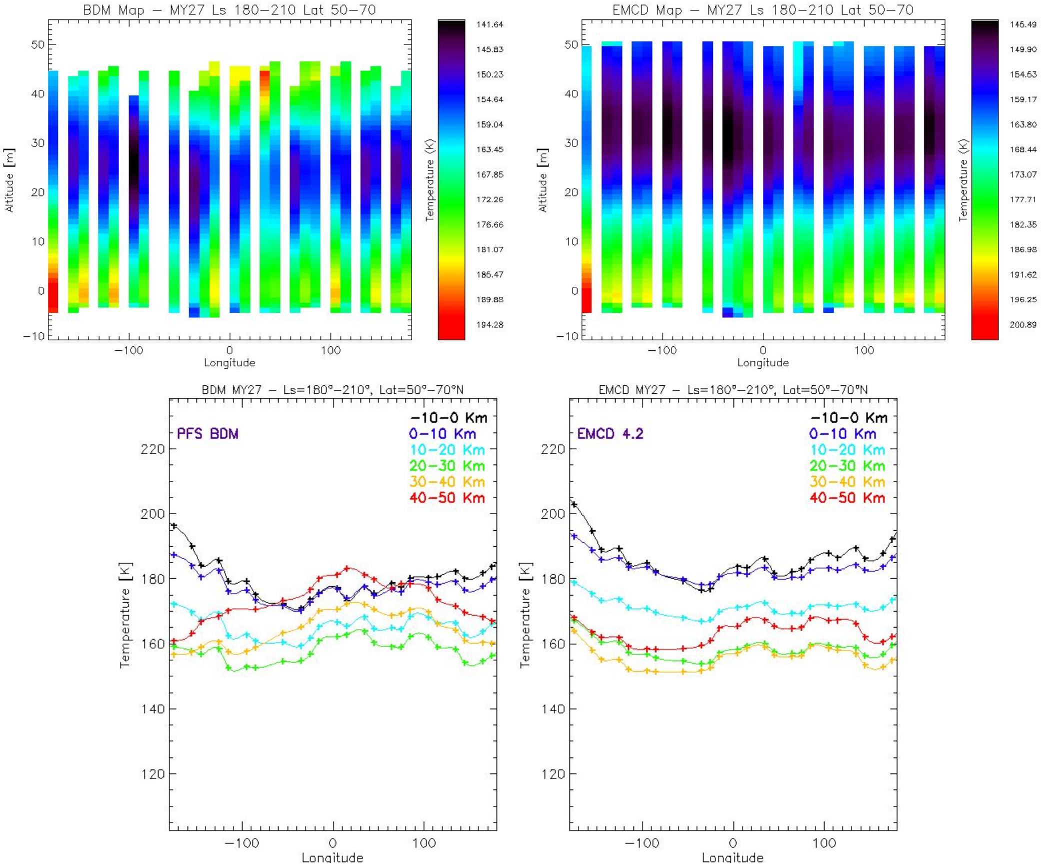

Figure 6.5: Thermal cross-section (top) and longitudinal trends of temperatures (bottom) at different altitudes (bins of 10 Km) for the near polar region (50°-70 N) during the early northern fall (Ls=180°-210°) of the MY 27, as retrieved by PFS/LWC (left) and extracted by MCD (right). The polar warming is visible down to about 35 km.

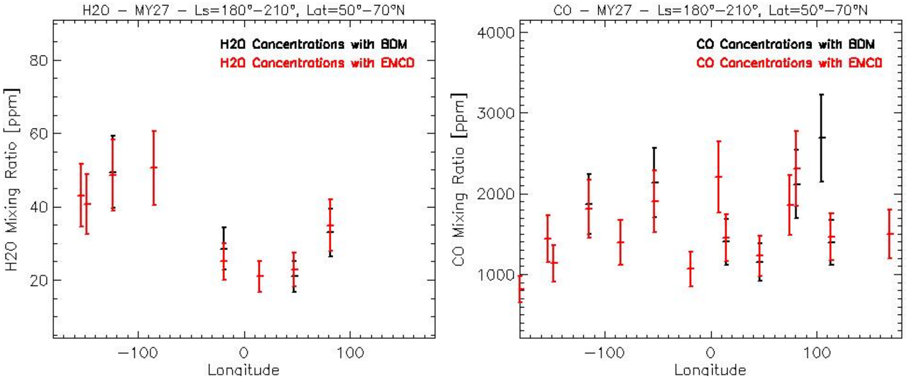

Figure 6.6: Longitudinal trends of water vapor (left) and carbon monoxide (right) concentrations for the near polar region (50°-70° N) during the early northern fall (Ls=180°-210°) of the MY 27.

### 6.2.2 Statistics on Wave Distributions of $H_2O$ and CO

We studied the trend of the gaseous abundances as a function of longitude for 20° latitude strips and for 30° solar longitude intervals. We obtained 113 and 130 latitudinal strips, for $H_2O$ and CO, respectively, having a sufficient number of points to define a longitudinal trend, but only 31 of them (in both cases) show a clear wave pattern, according to the criterion described in Section 6.2. The different significance of the two polulations (latitudinal strips with or without wave patterns) was evaluated using the *Student's T-statistic*. The T-statistic for two sample populations $x$ and $y$, having average values $\overline{x}$ and $\overline{y}$ is defined as

$$T = \frac{\overline{x} - \overline{y}}{\sqrt{\frac{\sum_{i=1}^{N}(x_i - \overline{x})^2 + \sum_{j=1}^{M}(y_j - \overline{y})^2}{(N+M-2)} \left(\frac{1}{N} + \frac{1}{M}\right)}} \tag{6.1}$$

where $N$ and $M$ are the numbers of the elements of the $x$ and $y$ populations, respectively. In our case each population is composed by the mean relative differences between all the two adjacent points of each latitudinal strip. In a clear wave trend the difference between two adjacent points is relatively small, whereas we observe an opposite behaviour when the longitudinal trend is pattern free. The water vapor T-statistic gives a value of 2.477 with a significance value of 0.015, whereas the carbon monoxide T-statistics gives a value of 1.202 with a significance value of 0.232. These results indicate that the wave trends in the water vapor distribution are extremely evident since there is not correlation between the two population (very little significance value of the T-statistic), whereas we find a less strong, even if important, evidence in the wave trends of carbon monoxide distribution. In other words, the water vapor is more sensitive to planetary waves with respect to carbon monoxide since they occur with greater force in the $H_2O$ distributions.

Figure 6.7 shows the histogram distribution of the latitudinal frequency of wave phenomena observed in the longitudinal trends of the water vapor and carbon monoxide concentrations. The $H_2O$ statistics suggest that wave distributions can be observed mostly (30-40%) in the near equatorial regions (30°S-30°N), whereas the measurements acquired on the equatorial and near equatorial regions are interested by wave trends only for about the 20% of the

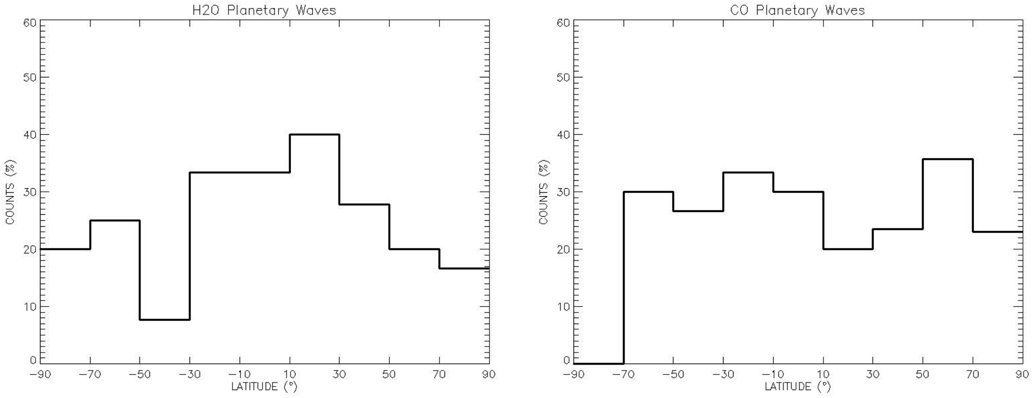

Figure 6.7: Latitudinal frequency of the wave phenomenon observed in the longitudinal trends of the water vapor (left) and carbon monoxide (right) concentrations for the whole dataset.

total cases. The CO statistics suggest a general flat latitudinal distribution of the wave occurrences, which represents about the 30% of the observed cases between 70°S-10°N, a minimum of 20% between 10°-30°N and a maximum of about 35% between 50°-70°N.

To study the order of the observed wave phenomena we decided to divide the histrogram distributions of their latitudinal frequency in order 1 (s=1) and order 2 (s=2) occurrences (Figure 6.8). Since the order 3 occurrences are rare and the third peak is usually less strong than the others, we considered them as order 2 occurrences in this statistical study. The water vapor distributions suggest that the equatorial region (30°S-30°N) is almost equally dominated by order 1 and order 2 with a little predominance of the latter (about the 20% of cases), but in the latitudinal strip between 10° and 30° N the order 2 shows the maximum number of cases (25%). The north polar region is dominated by order 1 regions and the south polar region is dominated by order 2 wave. The carbon monoxide distributions have a different behavior: only the equatorial and near equatorial regions (30°S-30°N) show order 2 wave phenomena, with the maximum number of cases (25%) in the latitudinal strip between 30°S and 10°S, while moving towards poles we find only order 1 wave trends (for about 30% of cases).

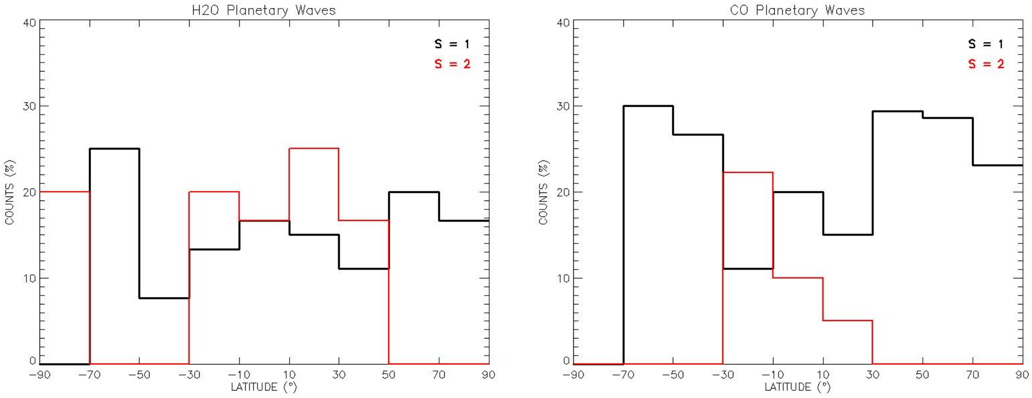

Figure 6.8: Latitudinal frequency of the wave phenomenon observed in the longitudinal trends of the water vapor (left) and carbon monoxide (right) concentrations for the whole dataset. We divided the order of the wave trend: in black the order 1 and in red the order 2.

Statistics on gaseous wave trends was performed also to investigate the seasonal dependence of the phenomenon. Figure 6.9 represents the seasonal frequency of the wave occurrences for the longitudinal distributions of water vapor and carbon monoxide in the whole dataset. The wave trends occur mostly (about the 55%) before the aphelion (Ls=30°-60°) for both gasses. $H_2O$ has large number of occurrences (about 50%) also during the early northern fall (Ls=180°-210°), whereas the CO distributions show many wave patterns (60%) during Ls = 270°-300°.

Also for the study of the seasonal frequency of the wave phenomena we divided the histogram distributions into order 1 and order 2 occurrences (Figure 6.10). The water vapor histograms shows that order 1 and order 2 are almost

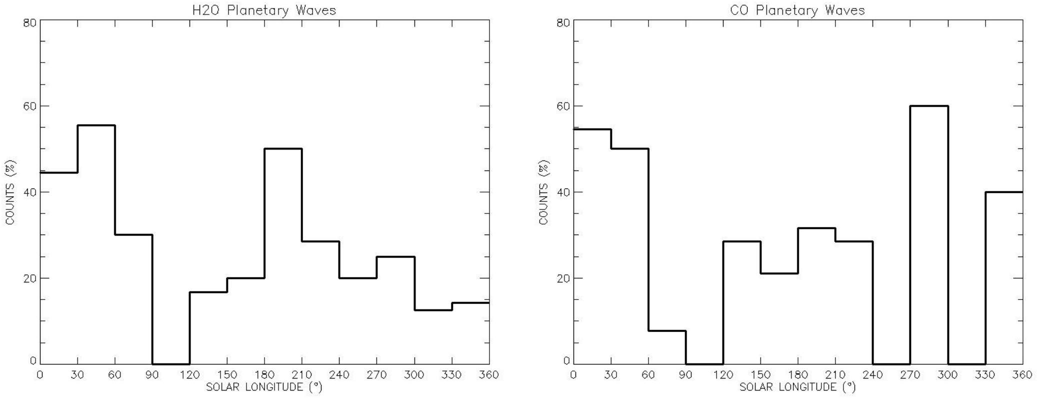

Figure 6.9: Seasonal frequency of the wave phenomenon observed in the longitudinal trends of the water vapor (left) and carbon monoxide (right) concentrations for the whole dataset.

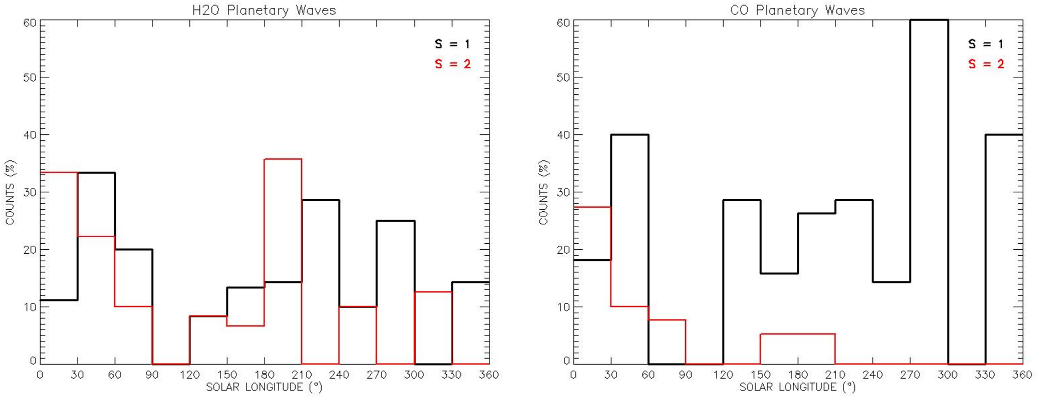

Figure 6.10: Seasonal frequency of the wave phenomenon observed in the longitudinal trends of the water vapor (left) and carbon monoxide (right) concentrations for the whole dataset. We divided the order of the wave trend: in black the order 1 and in red the order 2.

equally dominant along all the year, but we can clearly identify an order 2 predominance during the early northern fall (Ls = 180°-210°), whereas for the carbon monoxide the order 1 is mostly dominant along all the year and order 2 is important (about 28% of cases) only between Ls = 0° and Ls = 30°.

## 6.3 Discussion

We observed mainly two types of wave phenomena in the atmosphere of Mars: the first in the equatorial areas during the spring and the second in the polar regions during the respective fall. The comparison between gaseous distributions with the thermal profiles has provided clear indications both on the causes of the phenomenon and on the stratification of gasses in different layers of the atmosphere.

### 6.3.1 Equatorial and Near-Equatorial Regions

The wave trends observed in the $H_2O$ and CO longitudinal distributions on the equatorial regions have not relations with the temperatures at middle-high altitudes. Indeed, water vapor concentrations have a strong correlation with the temperatures of the near-surface atmosphere: this correlation suggests a direct relationship with the topography of Mars in those regions. Moreover, the enhancement of $H_2O$ abundance over these two particular regions, Arabia Terra (30°E, 0°N) and Tharsis (100°W, 0°N) was observed by many intruments.

We have to notice that around the equatorial area (10°S-40°N) there is roughly 50% more water vapor than out of it (Chapter 5 and [183]). The annually averaged water vapor abundance is high in this latitude band because water vapor is maintained at these latitudes by the global circulation [185]. This peculiarity allows us to perform a better characterization of this region.

In the two areas where we observe the maxima of the water vapor content, there is a strong positive correlation with albedo, which was noticed by Smith et al. [185] from TES visible bolometric observations, Jakosky and Farmer [113] using MAWD results and by Rosenqvist et al. [176] using results from the ISM instrument on the Phobos spacecraft. Moreover, at these latitudes the water vapor is also anti-correlated with the surface pressure [184] and with the thermal inertia [146]. Albedo, thermal inertia, and surface pressure (topography) have direct relations to the average and diurnal variation of surface and subsurface temperatures, the pore space size and grain size of the regolith, and to the circulation patterns of the atmosphere [185]. These can in turn influence the transport of water vapor and its adsorption and desorption into the regolith. On the contrary, coming toward the poles, the correlation between water vapor and surface albedo, pressure and thermal inertia abruptly vanishes. Fouchet et al. [86] suggest that the observed spatial variations can be explained by the modulation (stationary wave) of the atmospheric flow induced by the surface properties (topography and/or albedo of the surface) and a convergence of air in the near regions.

Moreover, we computed the saturation altitude above the surface of the water vapor by using the Marti and Mauersberger formula [140] and the PFS/LWC temperature profiles for each seasonal period we considered. Figure 6.11 shows the saturation altitude for Ls=0°-30° of the MY 29. If we compare the saturation map with the water vapor trend shown in Figure 6.2 for the same period, we observe a clear anticorrelation between the $H_2O$ concentration and the saturation altitude for the latitudinal strip 10°-30° N. Therefore, the water vapor is not equally distribuited along the vertical direction of the atmosphere and, at a certain latitude, clouds of ice particles can be generated at different altitudes for different longitudes.

All these clues and the strong positive correlation between the longitudinal distribution of water vapor and the topography suggest that the $H_2O$ is generally located in the boundary layer (near-surface atmosphere), as also suggested by Tschimmel et al. [204]. However, in accordance with Fouchet et al. [86] an intermediate way between confinement and uniform mixing seems reasonable, and the importance of a gas exchange between the atmosphere and the surface

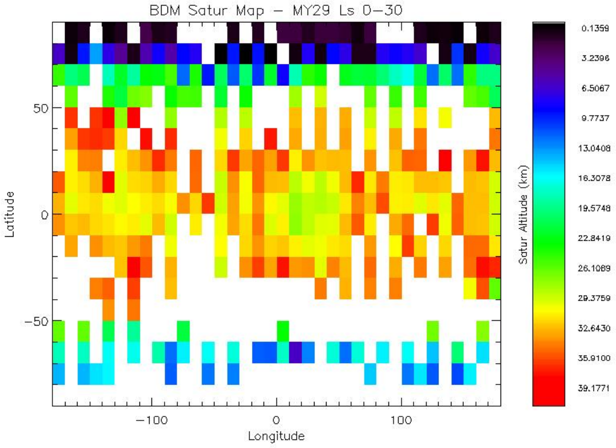

Figure 6.11: Geographical map of the $H_2O$ saturation altitude above the surface for Ls=0°-30° of the MY 29.

is emphasized.

Regarding the carbon monoxide behavior, we can conclude that it is generally well mixed in the atmosphere of Mars, as we expected since it is a non condensable gas and its longitudinal trend is almost flat as the corresponding temperatures at middle-high altitudes. Indeed, we observe a very weak correlation with the topography, and this is probably due to the presence of water ice clouds at low altitudes at those longitudes. These clouds can “hide” the atmosphere under them because of their opacity in the analyzed spectral range, and therefore they can affect the retrieved gaseous concentrations, which are integrated on the entire vertical column.

### 6.3.2 Near-Polar Regions

The general circulation of Mars is characterized by strong eastward winds in the fall-winter hemisphere. The interaction of this flow with zonally varying topography excites quasi-stationary waves, which take the form of planetary waves for forcing at the largest horizontal scales [105]. The stationary waves can influence the stability of the atmosphere, enhancing the formation of disturbances at certain longitudes and impeding their formation at others [28]. Our results suggest that these effects can affect the distribution of minor gasses, especially in the near polar regions.

Our thermal cross sections are in agreement with results by Banfield et al. [28], who have characterized the global structure of stationary waves and their seasonal evolution through analysis of nadir observations by the MGS Thermal Emission Spectrometer (TES). They isolated the diurnal Kelvin wave, with results roughly consistent with models. The $s = 1$ and $s = 2$ stationary waves were found to have significant amplitude coming toward the winter polar jets. Moreover, they found that $s = 1$ stationary wave has a little phase tilt with height during northern winter (at 60° N), but a significant westward phase tilt with height in the southern winter (at 60° S), over 4 scale heights. We observe the same tilt (Figure 6.4) on the southern near polar atmosphere (50°-70° S), where the maximum temperature is around 180° E near the surface and around 0° E at an altitude of about 45 Km ($\sim$ 4 scale heights). Barnes et al. [32] note that the $s = 1$ stationary wave poleward they found is the dominant component of eddy poleward heat transport in the south, but not in the north (where transient waves dominate their eddy poleward heat transport). Moreover, Banfield et al. [28] suggest that the most significant contributor to meridional heat flux from the stationary waves is the $s = 1$ stationary wave during southern winter, with heat fluxes reaching as large as $\sim$ 40 K m/s in the southern winter polar vortex, while those in the northern winter polar vortex are no larger than $\sim$ 12 K m/s. They found that for Ls=195°–225°, the $s = 1$ stationary wave carries heat equatorward in the southern hemisphere on the poleward edge of the polar jet, with an amplitude almost as large as the maximum fluxes in the north, $\sim$ 5 K m/s; whereas, generally the contributions of the $s = 2$ stationary waves to meridional heat flux are relatively small respect to the $s = 1$ stationary waves[28].

The relationships between temperatures and gaseous concentrations suggest that in these conditions water vapor is confined near the surface, while the carbon monoxide is located mainly in the middle-high atmosphere. This scenario is compatible with the beginning of the $H_2O$ sublimation from the southern polar cap, and the transport of the CO toward the equator, since it is a non condensable gas.

Regarding the gaseous distributions during all the year (Fig. 6.10), both water vapor and carbon monoxide show a decreasing number of order 2 trends from Ls=0° to Ls=90° and an increasing number of order 1 trends for Ls=0°-60°. Then, from Ls=120° to Ls=240° the order 1 wave trend increases, becoming predominant. These results are in agreement with the seasonal variation of zonal mean temperature as a function of longitude observed by Banfield et al. [28].

# Chapter 7

# Development of a Code for Minor Species Retrieval by Limb Data

In Chapter 6 we showed how we can indirectly draw indications about the vertical distribution of gaseous species in the Martian atmosphere using nadir (and quasi-nadir) measurements acquired by PFS. We tried to relate the temperature profiles, which are the best tracers of dynamical processes occurring in the atmosphere, to the spatial distribution of water vapor and carbon monoxide. We retrieved the gaseous concentrations (integrated along the line of sight from the surface to the detector) using the stable algorithm described in Chapter 4.

Although many PFS limb measurements are currently available and several radiative transfer codes able to simulate limb observations were developed, or are currently under development, unfortunately, there is not, at present, a stable algorithm for the retrieval of minor species concentrations by analyzing PFS spectra acquired in limb geometries. Therefore, the aim of this Chapter is to describe the development of an algorithm for the retrieval of minor species concentrations by limb measurements. This work is currently in progress.

## 7.1 The importance of the Multiple Scattering

The reason for the lack of a stable method for the retrieval of minor species concentrations by limb infrared measurements lies in the difficulty to model the radiative transfer of photons in the atmosphere taking into account the multiple scattering by molecules (Rayleigh) or by particles (Mie).

Stamnes et al. [199] developed a stable algorithm taking into account the multiple scattering in radiative transfer problems using the plane-parallel approximation: they called it DISORT (Discrete Ordinates Radiative Transfer Program for a Multi-Layered Plane-Parallel Medium) [200]. The the numerical implementation of this method was written in FORTRAN. It considers a scattering, absorbing, and emitting atmosphere in local thermodynamic equilibrium and provides general discrete ordinates as well as specific two-stream solutions to the radiative transfer equation pertaining to inhomogeneous, nonisothermal, plane parallel media. These computer codes can be used to compute fluxes and mean intensities as well as the complete azimuthal dependence of the intensity at arbitrary (user specified) polar and azimuthal angles and atmospheric optical depths [198]. However, this method has some limitations: one of them is that its solutions only apply to plane parallel atmospheres, thus there are a number of interesting twilight phenomena that cannot be adequately modelled unless spherical geometry is adopted. In particular, the plane parallel approximation does not allow the modelling of limb observations, whereas it is very suitable for nadir (or quasi-nadir) measurements. The Ignatiev et al. [112] approach we used for the retrieval of minor species concentrations (Chapter 4) by nadir measurements is based on the DISORT algorithm, and thus on the plane parallel approximation.

A way to simulate limb measurements taking into account the multiple scattering by atmospheric particles is to use the Monte Carlo approach, which is totally different from the DISORT one and it easily deals with spherical shells atmospheres. We decided to use this approach for our study and the following paragraphs will describe it and its application to the Martian atmosphere.

## 7.2 The Monte Carlo Radiative Transfer (MCRT) Technique

The Monte Carlo Radiative Transfer (MCRT) technique “mimics” reality by tracking the passage of individual photons through a density field to their eventual end (either absorption or escape from the medium). Although a process that originally was regarded as CPU-intensive, systems can now be envisaged using Monte Carlo Techniques on a desktop CPU within reasonable accuracy on timescales of a few hours.

### 7.2.1 Scattering and Phase Functions

When a photon interacts with the medium, it can be scattered or it can be absorbed. This eventuality occurs depending on the *single scattering albedo* $\omega$, which is simply the probability that a photon is scattered (and not absorbed):

$$\omega = \frac{n_s \cdot \sigma_s}{n_s \cdot \sigma_s + n_a \cdot \sigma_a} \tag{7.1}$$

where $n$ is the number density, and $\sigma$ is the cross section (subscripts indicate scatterers and absorbers, respectively).

Scattering is governed by the angular phase function $P(cos\Theta)$ of the scattering particle. This is simply the probability that the photon will be scattered from its initial direction through an angle $\Theta$.

In order to find the location of interaction, we need a completely probabilistic formalism for tracking the progress of an individual photon through a medium. If we want to construct the probability that a photon can traverse a distance $x$ without interaction, first we have to define the mean free path

$$l = \frac{1}{\rho \cdot \kappa} \tag{7.2}$$

which is the mean distance between photon interactions and where $\rho$ and $\kappa$ are, respectively, the density and the opacity of the medium. Thus, we can deduce the probability that a photon interacts within an infinitesimal length $dx$:

$$\frac{dx}{dl} = \rho \cdot \kappa \cdot dx \tag{7.3}$$

Hence, the probability of no interaction within $dx$ is

$$1 - \frac{dx}{dl} = 1 - \rho \cdot \kappa \cdot dx \tag{7.4}$$

If we then define a distance $x = N \cdot dx$, where $N$ sufficiently large, the probability of transmission of the photon $P(x)$ along $x$ can be written as

$$P(x) = 1 - \rho \cdot \kappa \cdot x = e^{-\tau} \tag{7.5}$$

where we have utilised the Taylor expansion for the exponential function, and substituted the expression for optical depth $\tau$. Therefore, the probablity that an interaction does occur is the complementary probability

$$P(\tau) = 1 - e^{-\tau} \tag{7.6}$$

### 7.2.2 The Monte Carlo Approach

As we have seen, it is difficult to know how a single photon will behave in a medium. Therefore, it is easier to constrain how an ensemble of N photons behave in terms of their statistical properties: this is ideally suited for Monte Carlo methods. The basic procedure is based on the following steps:

1. Emit a *packet of N photons.*

2. Track the progress of each photon, one-by-one, through the medium. The locations of interaction are found by sampling the optical depth from the distribution described in equation 7.6. The scattering and absorption of the photons are determined by sampling from the albedo and phase function.

3. As photons exit from the medium, capture them on a detector.

#### 7.2.2.1 Sampling Random Variables from a Probability Distribution

A key feature of MCRT is the sampling of parameters from probability distribution functions (PDFs). There are two main methods of sampling parameters from probability distribution functions (PDFs):

**The Cumulative Distribution Method** The simplest way of sampling from the cumulative distribution $\psi(x_0)$ uses the fundamental principle:

$$\int_a^{x_0} P(x)dx = \psi(x_0) \tag{7.7}$$

where $a$ here is the lower limit of the distribution function, and $x_0$ is the parameter we want to obtain. Thus, we need to generate a a random number $\zeta$, such that

$$\zeta = \psi(x_0) \tag{7.8}$$

and inverting this equation we can determine $x_0$. In the case of optical depth, equation 7.6 is already a cumulative distribution function (as we have integrated over the distance $x$), so sampling optical depths from this distribution uses the equation

$$\tau = -log(1 - \zeta) \tag{7.9}$$

**The Accept/Reject Method** If an analytic solution for $x_0$ is not possible, then the accept-reject method is an available alternative. If the peak of the PDF is known, then we can use the following algorithm:

1. Sample $x_0$ from a uniform distribution within the range of the PDF.
2. Sample $y$ from a uniform distribution between zero and the peak value of the PDF $y_{max}$.
3. Calculate $y_0 = P(x_0)$.
4. If $y > y_0$ , then reject this $x_0$ and return to 1, otherwise, accept this $x_0$.

#### 7.2.2.2 Finding the Scattering Location

Inside each atmospheric cell we consider, the value of the density is constant. Therefore, the optical depth through the cell is

$$\tau_{cell} = \rho_{cell} \cdot \kappa \cdot s \tag{7.10}$$

where $s$ is the distance travelled inside the cell along the photon's trajectory. Moreover, the optical depth along a given line of sight $\tau_{run}$ is simply the sum of the optical depths in each cell the photon intersects.

In order to deduce the scattering location, firstly we have to determine the scattering optical depth $\tau_{scatter}$, using the equation 7.9. The photon is then allowed to travel along its trajectory: the optical depth from each cell is calculated and logged, until $\tau_{run} > \tau_{scatter}$. Once this criterion is satisfied, the scattering location is found by travelling a distance $ds$ into the last cell traversed (Fig. 7.1):

$$ds = \frac{\tau_{scatter} - \tau_{run}}{\rho_{cell} \cdot \kappa} \tag{7.11}$$

Systems with isotropic scattering are the simplest to model: when a scattering event occurs, the photon's direction must be resampled using the same prescription as at emission.

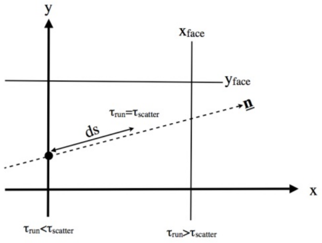

Figure 7.1: Schematic representation of the considered atmospheric cell for the determination of the scattering location. For simplicity we reported it only on a the cartesian grid.

#### 7.2.2.3 Errors

MCRT is by definition a stochastic process: the used random numbers introduce random sampling errors. Fortunately, these errors are simple to quantify: the emission (and capture) of photons is essentially a Poisson process, so the errors obtained must obey Poisson statistics. Therefore, the final error $\sigma_{err}$ is simply:

$$\sigma_{err}(\nu) = \frac{E(\nu)}{\sqrt{N(\nu)}} \tag{7.12}$$

where $E(\nu)$ is the energy collected by the detector for a certain frequency $\nu$ and $N$ is the total number of emitted photons. Thus, if we want to achieve a low error, a large number of photons must be emitted and captured.

#### 7.2.2.4 Computational Constraints

The timescale $T$ for an MCRT code to complete can be simply parametrised:

$$T \sim N_\gamma N_{steps} \tag{7.13}$$

where $N_\gamma$ is the total number of photons coming from the source and $N_{step}$ describes the (average) number of calculation steps required to simulate a photon's entire journey in the medium until its eventual exit. The latter can be estimated as

$$N_{steps} = \frac{d\gamma}{dx} \tag{7.14}$$

where $d\gamma$ is the typical path length of a photon, and $dx$ is the resolution of the grids used. This will be sensitive to the amount of scattering the photon receives:

$$d\gamma = N_{scatt} \cdot l \tag{7.15}$$

Where $l$ is the mean free path (eq. 7.2). For a simple sphere, $N_{scatt}$ can be approximated. Assuming that the photon is free to scatter in 3 dimensions, and the sphere has radius $R$, then the photon must travel approximately $\sqrt{N_{scatt}/3}$ mean free paths to escape:

$$R = \sqrt{\frac{N_{scatt}}{3}} l \tag{7.16}$$

thus

$$d_\gamma \sim \frac{R^2}{l} \tag{7.17}$$

and hence

$$T \sim N_\gamma \cdot \frac{R^2}{l \cdot dx} \sim N_\gamma \cdot < \tau > \cdot \frac{R}{dx} \tag{7.18}$$

where $< \tau >$ is the typical optical depth of the system.

## 7.3 The MCRT on a Planetary Atmosphere

Our final purpose is to apply the Monte Carlo Radiative Transfer technique on a planetary atmosphere. In this section we will describe the algorithm we developed and its application to the Martian atmosphere to obtain synthetic spectra in limb geometry. However, we have to stress that this code is suitable for the application on all the planetary atmospheres, it takes into account the multiple scattering and it is optimized for the near infrared spectral range.

The code is written in IDL and it is based on the SCATRD_OFOS routine, which was developed in FORTRAN by Mayorov et al. [143]. The subroutine SCATRD-OFOS calculates spectral monochromatic intensity for optically spherically-symmetric parametrically-defined atmosphere. Calculations are mainly based on the method of statistical Monte-Carlo modeling realized in the code SCATRD 06.10 [205], and modified for spacecraft applications (OFOS - observations from orbital spacecraft spectrometer). Unfortunately, the current version does not implement thermal radiation, non-LTE emission, refraction and polarization processes. The IDL code computes and gets ready all input variables as requested by SCATRD_OFOS and it can call this FORTRAN subroutine, providing, as a final result, the monochromatic radiance spectrum in the selected spectral range. Finally, another IDL code computes the convoluted spectrum for the instrumental function of the instruments of which we want to simulate measurements.

### 7.3.1 Input Parameters

#### 7.3.1.1 Geometric Description

Figure 7.2 shows the geometrical description of the input variables, where C is the center of the planet, D is the point (position) of the detector, I is the point on the planet surface (intersection line of sight with the planet surface for planetary surface observations or point under tangent point T for limb observations), and R is the radius of the planet solid body.

Two ways to describe a geometry of observations are present in the code:

- SCATRD's (internal default) geometrical parameters (red color in Fig. 7.2):
  - $h_d > 0$: altitude of observation (detector) above the surface;
  - $z_s \in [0, 180°]$: solar zenith angle (SZA);

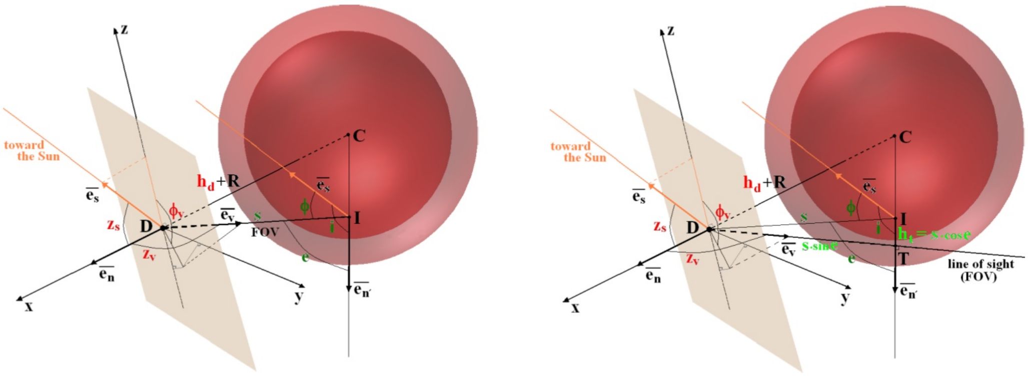

Figure 7.2: Geometrical description of the input variables of SCATRD_OFOS for observations pointing the surface (left) and for limb observations (right). The meaning of all the variables is described in the text.

  - $z_v \in [0, 90°]$: zenith angle for the line of sight;
  - $\varphi_v \in [0, 180°]$: azimuth angle for the line of sight;

- Conventional geometric parameters (green color in Fig. 7.2):
  - $i \in [0, 180°]$: incidence angle;
  - $e \in [0, 180°]$: emergence angle;
  - $\varphi \in [0, 180°]$: phase angle;
  - $s > 0$: distance of the detector;
  - $h_t \geq 0$: tangent altitude[1] of the target.

#### 7.3.1.2 Optical Properties of the Atmosphere

For a given model of atmosphere, we have the vertical profiles of the following quantities:

- temperature
- pressure
- volume mixing ratios of gaseous species
- number density of the aerosols

and the optical properties of the aerosol particles (size distribution and refraction index).

The knowledge of these quantities allow us to compute the absorption and scattering coefficient for every layer of the considered vertical grid. The computation of the gaseous absorption coefficients $k^R_{abs}$ is performed using the approach already described in Chapter 4.2.3, using the actual mixing ratio of the

---

[1] The *tangent altitude* is defined as the minimum distance between the line of sight and the planetary surface.

species. The scattering coefficients ($k^R_{sca} = \sigma_R \cdot n_d$) of the gasses are provided by the Rayleigh theory:

$$\sigma_R = \frac{32\pi^3}{3\lambda^4}\frac{(m-1)^2}{n_d^2} f_{anisotropic} \tag{7.19}$$

where $\sigma_R$ is the Rayleigh cross-section, $\lambda$ is the wavelength of the radiation, $m$ is the refraction index, $n_d$ is the number density and $f_{anisotropic}$ is the anisotropic factor, defined as

$$f_{anisotropic} = \frac{3 \cdot (2+\Delta)}{(6-7\Delta)} \tag{7.20}$$

with $\Delta$ depolarization factor. The values of $m = 1 + A(1 + B/\lambda^2)$ and of $\Delta$ at STP (Standard Temperature and Pressure) conditions for a large number of molecules can be extracted from tables by Allen (1976) [20]. Taking into account the actual temperature and pressure conditions, the refraction index must be rescaled as follow

$$m = 1 + A(1 + B/\lambda^2) \cdot \frac{n_d}{n_{STP}} \tag{7.21}$$

where $n_{STP}$ is the number density of the considered molecular species at STP conditions. Thus, the relation 7.19 can be rewritten as

$$\sigma_R = \frac{32\pi^3}{3\lambda^4}\frac{(m-1)^2}{n_d^2} f_{anisotropic} \cdot \frac{n_d^2}{n_{STP}^2} = \sigma_R = \frac{32\pi^3}{3\lambda^4}\frac{(m-1)^2}{n_{STP}^2} f_{anisotropic} \tag{7.22}$$

The Rayleigh phase function is simply defined as

$$P_R(\theta) = \frac{3}{16\pi}(1 + \cos^2\theta) \tag{7.23}$$

and it is indipendent from the waveleigth. However, it is clear that the contribution by the Rayleigh scattering becomes important for small wavelengths (large wavenumbers) and a great number of scattering molecules.

The interaction between the radiation and the aerosol particles is modelled using the approach by Wiscombe [213] for the application of the Mie theory. This algorithm computes the extinction cross-section $\sigma_M$, the single-scattering albedo $\omega_0$, and all the moments of the scattering phase function $g_l$, for a given particles size distribution. Therefore, for each wavenumber, we have

$$k^{Mie}_{abs} = n_d \cdot \sigma_M \cdot (1 - \omega_0) \tag{7.24}$$

$$k^{Mie}_{sca} = n_d \cdot \sigma_M \cdot \omega_0 \tag{7.25}$$

where $k^{Mie}_{abs}$ and $k^{Mie}_{sca}$ are, respectively, the absorption and scattering coefficients and $n_d$ is the number density of the aerosol particles. We assumes that the scattering phase function depends only on the angle $\Theta$ between the incident and scattered beams and we express it as the expansion of a series of $2M$ Legendre polynomials $P_l$:

$$P_M(\tau, \cos\Theta) = \sum_{l=0}^{2M-1} (2l+1) g_l(\tau) P_l(\cos\Theta) \tag{7.26}$$

where $\tau$ is the optical depth and, by virtue of the orthogonality of Legendre polynomials, the expansion coefficients $g_l(\tau)$ are given by

$$g_l(\tau) = \frac{1}{2}\int_{-1}^{+1} P_l(\cos\Theta)P(\tau,\cos\Theta)d(\cos\Theta) \tag{7.27}$$

The coefficient $g_0$ is equal to 1 because the phase function, being a probability distribution, is normalized to unity. $g_1$ is called the "asymmetry factor", and ranges from 0.7 to 0.9 for aerosols and clouds in the solar spectrum.

Finally, the optical depth $\tau$ of an atmospheric layer is

$$\tau = \left(\sum_{i=1}^{N}\left(k_{abs,i}^{R} + K_{sca,i}^{R}\right) + \sum_{j=1}^{L}\left(n_{d,j}^{aero}\cdot\sigma_{M,j}\right)\right)\cdot h \tag{7.28}$$

where $N$ and $L$ are, respectively, the number of gaseous and aerosol species in the layer and $h$ is the thickness of the layer.

### 7.3.2 Stability of the Algorithm

In order to study the sensitivity of our MCRT code, we considered an ideal atmosphere observed in nadir geometry and composed by only one layer of dust particles. We increased progressively its optical depth and we computed the radiance at the TOA[2] for a fixed wavenumber (3775 cm$^{-1}$), where there is not any narrow spectral feature. We compared results with the ones obtained performing the same simulation with the DISORT algorithm, which is widely validated and considered stable [199, 200]. In Figure 7.3 the comparison between the radiance computed with DISORT and the one computed with MCRT is shown. The DISORT code is stable for an optical depth lower than about 18 and then it saturates in order to avoid numerical errors and to limit

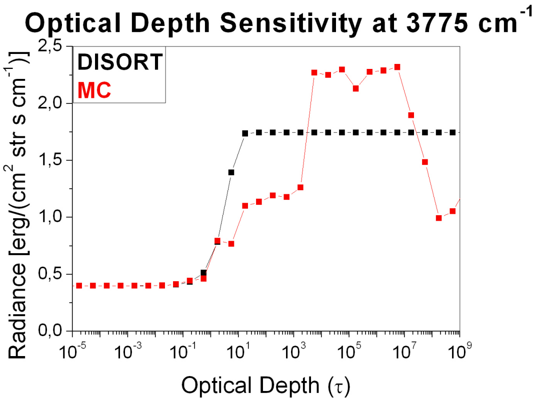

Figure 7.3: Radiance at 3775 cm$^{-1}$ as a function of the optical depth computed using the DISORT (black) and the MCRT (red) algorithms.

---

[2] TOA: *Top Of the Atmosphere.*

the computational time. The MCRT code is in agreement with the DISORT code up to an optical depth of about 2 and then it becomes unstable.

The MCRT codes are more sensitive to the optical depth than the DISORT ones, since the Monte Carlo approach is based on the probability of transmission of the photon through the atmosphere. Indeed, if a photon tries to go beyond an atmospheric layer having an optical depth higher than 2, then it has only two possibilities: it can be scattered and, if the geometrical conditions are appropriate, it can be collected by the detector, or it can be absorbed and be completely lost. To avoid the loss of photons in the crossing of the atmosphere, and in this way to increase the probability that a photon can reach the detector, we split each atmospheric layer in several sub-layers, such as each sub-layer has an optical depth lower than a preselected threshold and the total optical depth of the original layer is kept. Since increasing the number of layers in which the atmosphere is modelled causes an increase of the computational time, we developed this algorithm dynamically: the optical depth of each single layer is checked for each wavenumber of the monochromatic spectral grid, thus the total number of atmospheric layers changes for different grid points and the computational time is optimized. Applying this method to the simulation we showed before, we obtain the Figure 7.4. The splitting of the layers with a high optical depth causes an improvement of the stability of the code. Using a $\tau$ threshold of 5, the code can be considered stable up to an optical depth of about 6, whereas using a $\tau$ threshold of 1 the code can be considered stable up to optical depth of about 18, and even much more. The difference between the latter results and the reference values obtained by the DISORT code are under the 4.5% for $\tau < 18$. Since the DISORT radiance saturates for $\tau > 18$ in our simulation, it is difficult to put a limit for the stability of our MCRT code, but Martian (and most of the planetary) conditions cannot allow to have an

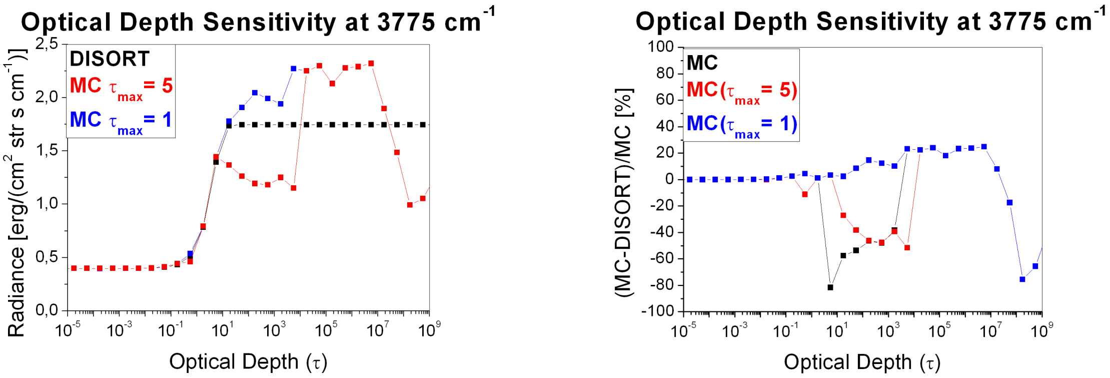

Figure 7.4: Left: Radiance at 3775 cm$^{-1}$ as a function of the optical depth computed using the DISORT (black) and the MCRT (red and blue) algorithms. In the MCRT code the optical depth control method (see text) was implemented using as thresholds $\tau = 5$ (red) and $\tau = 1$ (blue). Right: Percentage differences between the MCRT and DISORT codes, using no optical depth threshold (black) and optical depth threshold of 5 (red) and 1 (blue).

optical depth higher than about ten for each layer. Therefore, we can consider the MCRT code we developed stable for the use required by our purposes.

### 7.3.3 Validation of the Code

The validation of our MCRT code was performed by the comparison between radiances obtained with it and the ones obtained using two DISORT-based codes: ARS, which uses the Ignatiev et al. [112] approach in simulating nadir measurements, and SARTre [147, 148], which is developed for limb applications. We selected the spectral range between 3500 and 4500 cm$^{-1}$ because of the presence of the carbon dioxide, carbon monoxide and water vapor spectral features, as also of aerosols (dust and water ice) ones.

We considered a typical Martian atmosphere composed by $CO_2$, $H_2O$ and CO, and by dust and water ice aerosol particles. The vertical profiles of temperature and pressure are shown in Figure 7.5, whereas we used uniform vertical distribution of gasses and aerosols. $CO_2$, $H_2O$ and CO have mixing ratios of 0.9532, $3.0 \cdot 10^{-4}$ and $8.0 \cdot 10^{-4}$, respectively. The dust and ice aerosol particles have an exponential vertical distribution (Fig. 7.5) and the properties of dust as a function of wavenumber are those proposed by Kleinböhl et al. [158, 115], whereas for water ice we used the ones published by Warren and Brandt [207]. The grain size distribution used for the aerosols is that described in the model by Clancy et al. [54]. These quantities determine the optical depth of the dust and water ice in the atmosphere, which varies between 0.36 and 0.41, with a mean value of 0.38, for dust and between 0.031 and 0.15, with a mean value of 0.09, for water ice (Fig. 7.6). The surface albedo we used is constant in all the considered spectral range and its value is 0.1.

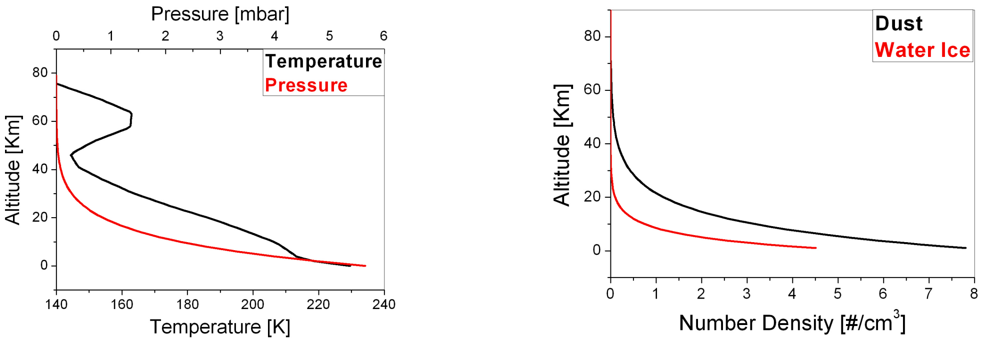

Figure 7.5: Left: Vertical profiles of temperature (black) and pressure (red). Right: Vertical profiles of dust (black) and water ice (red) number densities. These profiles represent the typical Martian conditions.

Regarding the MCRT code, we set the 32000 as the maximum number of interaction that a photon can have in its path through the atmosphere. This value is the almost the maximum allowable value for the SCATRD-OFOS routine and we chose to use it to improve the efficiency of the simulations, despite it causes an important increase of the computational time. Moreover, we set

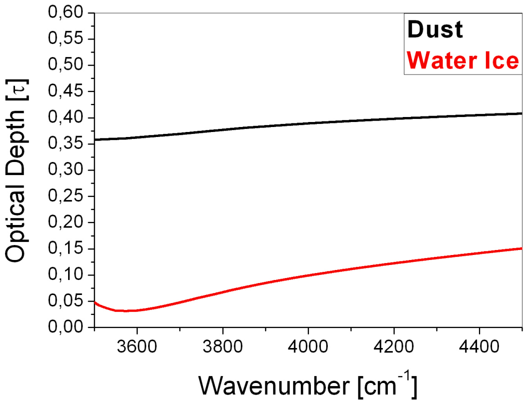

Figure 7.6: Total optical depth of dust (black) and water ice (red) between 3500 and 4500 cm$^{-1}$ for the model of atmosphere that we considered.

the accuracy of the MCRT code to 5% because this is the best compromise between the computational time and a good result.

#### 7.3.3.1 Nadir Geometry

The ARS code was widely used in this work (Chapter 4) and it is suitable for the use of the DISORT algorithm in nadir geometries (plane-parallel approximation).

In Figure 7.7 we report results obtained in computing spectra with the two approaches (MCRT and DISORT), for clear sky and aerosol conditions, in nadir geometry and for SZA=0°. It is useful to compare also results in clear sky conditions, in order to validate the treatment of the pure gaseous absorption, since in the considered spectral range and for the low Martian pressure the Rayleigh scattering by molecules can be neglected.

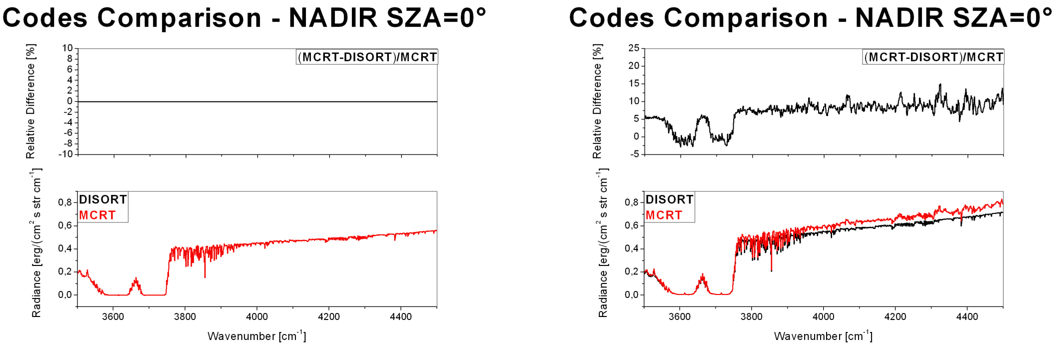

Figure 7.7: Spectra computed by the MCRT (red) and DISORT (black) codes for clear sky (left) and aerosol (right) conditions and for SZA=0°. The upper panels represent the relative difference of the radiances.

The right panel of Figure 7.7 demonstrates that the absorption by atmospheric components is well processed and it validates the use of our MCRT code in clear sky conditions, since the spectra computed with the two codes are exactly alike each other.

The difference between the radiances computed with the two codes for an atmosphere with aerosol particles has an average of 6.91%, with the minima around the wings of the strong saturated bands of $CO_2$ (3500-3750 $cm^{-1}$) and little fluctuations having an amplitude of about 3% around the mean value in the spectral range covering the $H_2O$ and CO absorption bands (3750-4500 $cm^{-1}$). Moreover, the difference between the MCRT and the DISORT codes is negative (-2.5%) only in the bottom of the $CO_2$ saturated bands.

We performed the same simulation (with aerosol particles) also for SZA=30° and SZA=60° (Fig. 7.8), in order to avoid the pure backscattering case, which is very sensitive to numerical uncertainties and so it can produce an increase of errors in radiative transfer codes. As we expect, in these cases, the differences between the MCRT and DISORT codes are less than for SZA=0° and it has an almost constant mean value along the whole spectral range we considered. The mean difference for SZA=30° is about -1.32%, i.e. on average the MCRT code has a lower radiance than the DISORT code, whereas the fluctuations around the mean value have an amplitude of about 4%. The simulation for SZA=60° shows a mean difference of about -0.91%, but the amplitude of the fluctuations around this value are increasing with the wavenumber: around the saturated $CO_2$ band (3500-3750 $cm^{-1}$) it is about of 3%, around the $H_2O$ band (3780-3920 $cm^{-1}$) it is about of 5% and around the CO band (4200-4300 $cm^{-1}$) it is about of 12%.

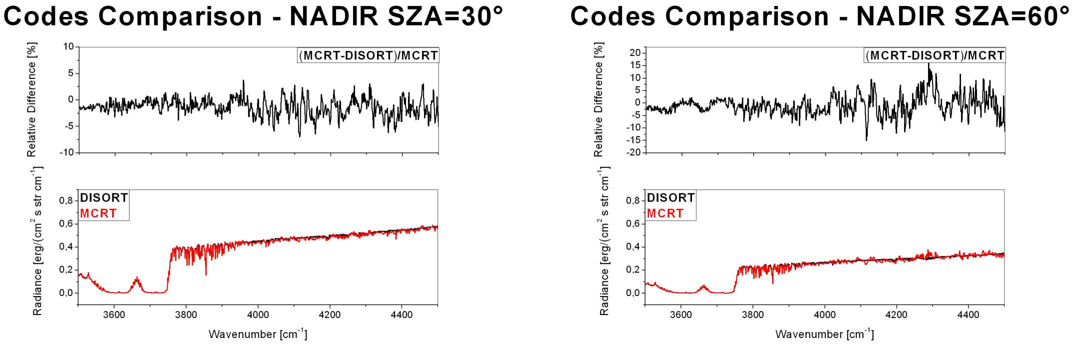

Figure 7.8: Spectra computed by the MCRT (red) and DISORT (black) codes in aerosol conditions for SZA=30° (left) and SZA=60° (right). The upper panels represent the relative difference of the radiances.

### 7.3.3.2 The Curti-Godson Approximation

Since we want to use the DISORT-based approach, which is suitable only for nadir (or pseudo-nadir) simulations, in a limb geometry, we can apply the *Curtis-Godson approximation* [60, 95]. This approximation replaces an inhomogeneous path with a homogeneous one by using average values for the various band-model parameters. The Curtis-Godson approximation is very accurate for paths where the temperature and concentration gradients are not particularly steep. In formulas we can express it as:

$$\overline{U_{m,l}} = \int_{z_{l-1},\varphi_{l-1}}^{z_l,\varphi_l} U_m(z,\varphi) \cdot \eta\left(P(z,\varphi),T(z,\varphi)\right) \cdot ds(z,\varphi) \tag{7.29}$$

$$\overline{P_{m,l}} = \frac{\int_{z_{l-1},\varphi_{l-1}}^{z_l,\varphi_l} P(z,\varphi) \cdot U_m(z,\varphi) \cdot \eta\left(P(z,\varphi),T(z,\varphi)\right) \cdot ds(z,\varphi)}{\int_{z_{l-1},\varphi_{l-1}}^{z_l,\varphi_l} U_m(z,\varphi) \cdot \eta\left(P(z,\varphi),T(z,\varphi)\right) \cdot ds(z,\varphi)} \tag{7.30}$$

$$\overline{T_{m,l}} = \frac{\int_{z_{l-1},\varphi_{l-1}}^{z_l,\varphi_l} T(z,\varphi) \cdot U_m(z,\varphi) \cdot \eta\left(P(z,\varphi),T(z,\varphi)\right) \cdot ds(z,\varphi)}{\int_{z_{l-1},\varphi_{l-1}}^{z_l,\varphi_l} U_m(z,\varphi) \cdot \eta\left(P(z,\varphi),T(z,\varphi)\right) \cdot ds(z,\varphi)} \tag{7.31}$$

where $z$ is the altitude, $z_l$ and $z_{l-1}$ are the altitudes of the boundaries of the layer, $\varphi_l$ and $\varphi_{l-1}$are the angles corresponding to the intersection of the optical path with the extremes of the layer, $U_m(z,\varphi)$ is the Volume Mixing Ratio of the $m^{th}$ gas, $ds$ is the line of sight dependent on the geometry, $P(z,\varphi)$ and $T(z,\varphi)$ are the pressure and temperature for the layer, $\eta\left(P(z,\varphi),T(z,\varphi)\right)$ is the air number density and $\overline{U_{m,l}}$, $\overline{P_{m,l}}$ and $\overline{T_{m,l}}$ are the equivalent corresponding values for the gas $m$ and the layer $l$.

Obviously, this approximation can take into account the multiple scattering only along the line of sight, where the atmosphere is considered locally plane parallel, whereas the multiple scattered radiation coming from the upper and lower layers is neglected. Therefore, we can use it only to compare spectra in single scattering conditions.

Figure 7.10 shows spectra computed with our MCRT and DISORT (ARS) approaches, applying the Curtis-Godson approximation, in single scattering conditions. We considered SZA=90°, phase angle of 0°, a tangent altitude of 20 Km and an observer altitude of 79 Km. In Figure 7.9 the equivalent profiles

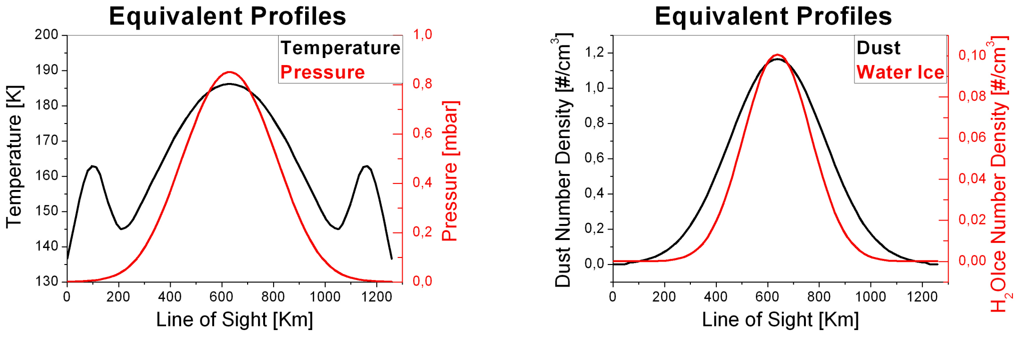

Figure 7.9: Left: Curtis-Godson equivalent profiles of temperature (black) and pressure (red). Right: Curtis-Godson equivalent profiles of dust (black) and water ice (red) number densities. These profiles represent the typical Martian conditions in observing the atmosphere in limb geometry (see text for parameters).

of temperature, pressure, dust and water ice are shown. They are computed applying the Curtis-Godson formulas to the vertical profiles shown in Figure 7.5. We divided the line of sight into 80 steps, each identifying an atmospheric cell.

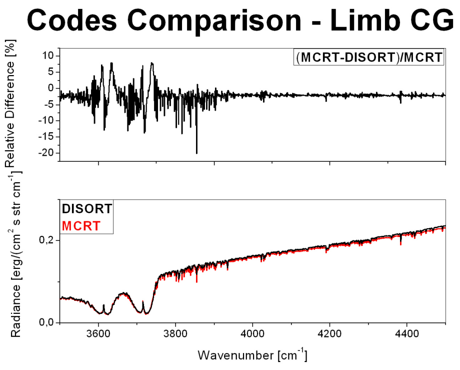

Figure 7.10: Single scattering spectra computed by the MCRT (red) and ARS with Curtis-Godson approximation (black) codes for SZA=90°, phase angle of 0°, a tangent altitude of 20 Km and an observer altitude of 79 Km for SZA=90°, phase angle of 0°, a tangent altitude of 20 Km and an observer altitude of 79 Km.

The comparison between the two spectra reveals a mean difference of -2.24%, with maxima values (up to about 20%) around the $CO_2$ band and the water vapor band. The spectral range covered by the carbon monoxide band is less affected by large differences and so it shows discrepancies of some percent. The Curtis-Godson approximation causes an understimation of the absorbed light by molecules: we can clearly recognize the absorption features of the water vapor in the percentage difference. The reason of these discrepancies can be the difficulty of modelling a spherical shell atmosphere using vertical parallel flat layers. Therefore, this approximation results to be not suitable for retrieving minor species concentrations by simulating limb measurements, even in single scattering conditions.

#### 7.3.3.3 Limb Geometry

Since we want to compare results by our code and a different one in modelling limb observations and taking into account the multiple scattering, we need to use a specifically designed code. The SARTre code was designed for monochromatic high resolution RT modeling in the infrared spectral range and beyond for arbitrary viewing geometries in spherical atmospheres, taking emission and scattering into account as sources [148]. It is based on DISORT algorithm and it approximates spherical shell atmospheres [147]. The SARTre code was applied to the Martian atmosphere by Aoki et al. [22].

In our simulation we considered a limb geometry having a tangent altitude of 20 Km, an observer altitude of 300 Km above the surface, SZA=0° and phase angle of 90°. The comparison between our MCRT code and SARTre both in single scattering approximation and in multiple scattering is shown in

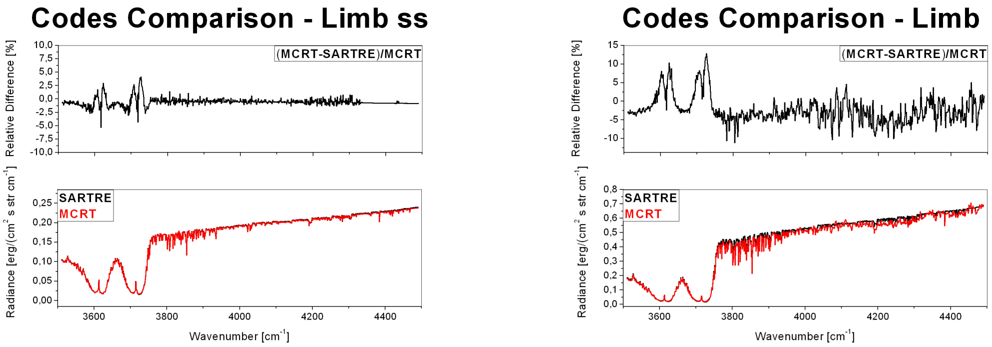

Figure 7.11: Spectra computed by the MCRT (red) and SARTre (black) codes in aerosol conditions for SZA=0°, tangent altitude of 20 Km and observer altitude of 300 Km in single scattering approximation (left) and in multiple scattering (right). The upper panels represent the relative difference of the radiances.

Figure 7.11. It is useful to compare also spectra compute in single scattering approximation to check the geometrical parameters description.

The comparison between our MCRT code and the SARTre one in single scattering approximation shows a good agreement, with a mean difference of -0.5% and fluctuations around this value of amplitude of about 4% in the range which covers the bottom of the strong $CO_2$ band and of about 0.5% in the range covering the $H_2O$ and CO absorption bands. Since the differences between the two spectra are always under the 5% (the accuracy of our MCRT code), and mostly under the 0.5%, this result demonstrates that the geometrical parameters are described in the correct way.

The comparison between the two codes taking into account the multiple scattering shows a mean difference of -2.23% with fluctuations around this value of amplitude up to 15% in the strong $CO_2$ band and about 7% in the $H_2O$ and CO spectral range.

## 7.4 Retrieval of Water Vapor by Limb PFS measurements

The final aim of our work is the development of an algorithm able to retrieve the vertical distribution of minor species in the Martian atmosphere by spacecraft limb measurements. In Chapter 4 we described the algorithm we developed to retrieve the integrated concentrations of water vapor and carbon monoxide by nadir measurements. We applied our MCRT code to that algorithm only by replacing the Ignatiev et al. approach [112] with ours in the synthetic spectrum computation. However, since at the moment our MCRT code does not take into account the thermal radiation, the algorithm can be used only in the solar region of the spectrum, where the thermal emission is almost totally negligible. Moreover, we cannot take into account the Field Of View (FOV) of the instrument, therefore we can compute the radiation only along the line of sight. Despite all these limits, we are able to perform a qualitative analysis of the data and it is enough to give a strong suggestion about the vertical distribution of minor species.

We selected PFS limb measurements acquired in almost the same conditions on which we focused on in Chapter 6 for the indirect study of the vertical distribution of water vapor and carbon monoxide: 1) northern spring (Ls = 0°-30°) over the near-equatorial region (10°-30° N) and 2) southern spring (Ls = 180°-210°) over the near-polar region (50°-70° S). Unfortunately, the PFS measurements acquired in limb geometry are pretty limited in number, therefore it is difficult to average many spectra and to have a good signal to noise ratio in the selected observing conditions. For this reason we decided to apply our algorithm, as first attempt, only to the water vapor band at 2.6 $\mu$m (3845 cm-1), which is much more stronger than the carbon monoxide one at 2.36 $\mu$m (4235 cm-1).

For each case we considered, we averaged spectra in tangent altitude bins of 30 Km, from the surface to 80 Km, and by shifting by 10 Km in the tangent altitude of limb measurements from an average to the next one: for example, 0-30 Km, 10-40 Km, 20-50 Km, . . . , and so on. Moreover, we excluded spectra having their FOV partially on the surface and we discarded best fit values having a $\chi^2 > 50$, as we have already described in Chapter 5. In this way we obtained 6 and 4 mean spectra for the case 1) and the case 2), respectively. The number of averaged spectra for each altitude bin varies between 1 and 34 (Table 7.1).

|  | **Mean Tang Alt [Km]** | **# of Averaged Spectra** |
|---|---|---|
| 1) | 29.10 | 1 |
|  | 32.93 | 3 |
|  | 40.86 | 5 |
|  | 49.10 | 5 |
|  | 59.83 | 4 |
|  | 70.62 | 5 |

|  | **Mean Tang Alt [Km]** | **# of Averaged Spectra** |
|---|---|---|
| 2) | 38.20 | 1 |
|  | 57.76 | 7 |
|  | 64.16 | 23 |
|  | 67.52 | 34 |

Table 7.1: Coverage of PFS limb data 1) for the northern spring (Ls = 0°-30°) over the near-equatorial region (10°-30° N) and 2) for the southern spring (Ls = 180°-210°) over the near-polar region (50°-70° S).

In Figure 7.12 a typical example of the good fit between the synthetic spectrum, computed with our MCRT code, and the measured PFS limb spectrum is shown. This spectrum corresponds to a single spectrum selected into the bin Ls=0°-30°, Lat=10°-30° and acquired pointing a tangent altitude of 29.1 Km. The limb spectra have the advantage of having a very high radiance when

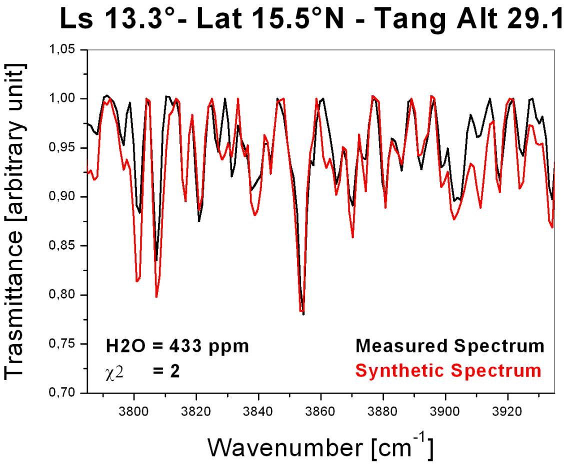

Figure 7.12: Spectral fit example of the water vapor absorption band for an averaged spectrum (normalized to its continuum), corresponding to a single spectrum selected into the bin Ls=0°-30°, Lat=10°-30°N and acquired pointing a tangent altitude of 29.1 Km. The retrieved mixing ratio is 433 ppm with a minimum $\chi^2$ of 2 (over 130 sampling points).

pointing the lower atmosphere, because of the absence of the surface absorption. This advantage allow us to obtain a good fit even on a single spectrum. The uncertainty on the retrieved values of concentrations is 24%, because 19% is the uncertainty we estimated for the retrieval of water vapor using our algorithm (Section 4.4) on which we have to add the accuracy we set for the Monte Carlo computations (5%).

Applying the procedure we developed to all the mean spectra we selected, we obtain the vertical profiles of water vapor (Figure 7.13).

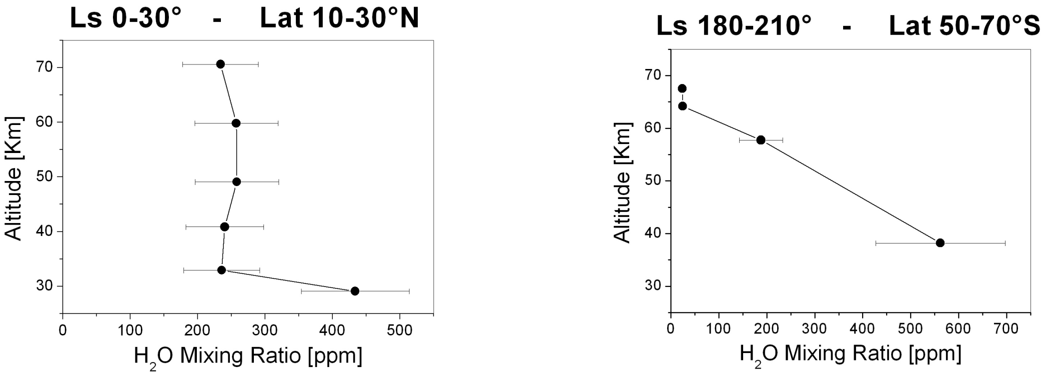

Figure 7.13: $H_2O$ vertical profiles for the northern spring (Ls = 0°-30°) over the near-equatorial region (10°-30° N) (left) and for the southern spring (Ls = 180°-210°) over the near-polar region (50°-70° S) (right).

During the northern spring over the near-equatorial region (Ls = 0°-30°, Lat = 10°-30° N) we observe a mean water vapor concentration of 276.36 ppm, with a maximum of 433 ppm at 29 Km. From 32 Km to 70 Km the $H_2O$ amount has a lower value almost constant around 240 ppm, with a little increase (about 260 ppm) between 50 and 60 Km.

During the southern spring over the near-polar region (Ls = 180°-210°, Lat = 50°-70° S), we detect a mean water vapor concentration of about 200 ppm, with a strongly decreasing amount of water vapor between 38 Km and 64 Km. The lower atmosphere has the maximum amount of water vapor, with 562 ppm at 38 Km, whereas higher than 64 Km the atmosphere appears to be extremely dry (about 25 ppm of $H_2O$).

## 7.5 Conclusions and Future Developments

We developed a method to retrieve the minor species concentration by limb measurements using a code based on the Monte Carlo approach. We validated this radiative transfer code by comparing its results with the ones obtained using DISORT based codes (ARS for Nadir and SARTre for Limb). For all the different cases we examined we measured fluctuations of amplitude generally less then the 5% and 10% around the mean difference of the continua, respectively, in the spectral range covering the $H_2O$ and CO absorption band we used for our analysis. Since our retrieval method works on the normalized spectra, we can neglect the differences on the continuum. Moreover, we set the Monte Carlo accuracy to 5% because this represents the best compromise between a good accuracy and its computational time. Therefore, in the water vapor range (3780-3920 $cm^{-1}$), in which the comparisons between the different codes give a difference of 5%, equal to the accuracy we set, our MCRT code is validated.

We applied the new algorithm for the retrieval of the water vapor in the two particular cases we examined in details in Chapter 6. Although our method has still to be improved, since at the moment it can simulate the radiation coming along the line of sight, whereas it is not able to simulate the radiation collected by a real instrument having a certain FOV and to take into account the air refraction, its application to PFS limb data gave us some very interesting information about the vertical distribution of water vapor in the Martian atmosphere. In both cases that we examined the $H_2O$ results to be confined mainly in the first 30 Km. This direct result confirms the indirect suggestions that we got by nadir measurements for the study of the correlation between the surface pressure and the integrated water vapor concentration (Section 5.5.1) and for the study of dynamics, as the presence of planetary waves (Section 6.3). Moreover, the water vapor confinement in the atmosphere of Mars was also suggested by observations of other instruments and models, that we have already discussed in Section 5.5.1. But, because of the large PFS field of view and the MEX orbit, we cannot acquire measurements with a tangent altitude lower than about 25 Km, therefore it is difficult to make assumption about the very low atmosphere (boundary layer), as done by the studies we mentioned. However, we can infer that this confinement of the water vapor in the lower layers is probably due to soil-atmosphere interactions.

The $H_2O$ vertical trends we studied revealed another important information: during the northern spring on the near equatorial regions, the atmosphere above 35 Km is relatively wet, having a water vapor concentration ($\sim$ 240 ppm) higher than its mean global and annual average value ($\sim$ 150 ppm). During this period, the $H_2O$ is kept around the equator by the global circulation (Chapter 5) and since it is seasonally and geographically far from its sources, the summer polar caps, the atmosphere has enough time to mix it vertically. On the contrary, during the southern spring the atmosphere near the south polar region becomes extremely dry above 60 Km ($\sim$ 25 ppm), reaching almost the minimum quantity we detected in the Martian atmosphere. This is due to the beginning of the sublimation of the water ice by the southern polar cap (Chapter 5), which increases the water vapor amount in the atmosphere near the surface, whereas the atmospheric circulation has not had enough time yet to mix it vertically.

However, the MCRD code is not still complete and we plan to make it more stable and suitable for several applications in planetary atmosphere. The first step in the improvement of the code is the implementation of the thermal radiation and the performing of a deeper validation in a wider spectral range. A more precise treatment of the scattering by aerosols could allow to apply our code to the study of clouds. Moreover, we plan to add further improvements, as to take into account the air refraction of the line of sight (*Ray Tracing*) and the polarization effects. Finally, we plan also to add the modelling of the non-LTE emission.

As these improvements will be applied, it will be possible to perform a wide mapping of the vertical distribution of minor species (especially $H_2O$ and CO) in order to study deeper their behaviour and their connection with the atmospheric dynamics.

# Conclusions

In this thesis work we have studied the concentration trends of two very important minor species in the Mars atmosphere: water vapor and carbon monoxide. We used observations acquired for more than two and a half Martian years (MY 27–28–29) with Mars Express PFS instrument. Although there are several $H_2O$ and CO absorption bands in the spectral range covered by PFS, we decided to focus on the band at 2.6 $\mu$m (3846 cm$^{-1}$) for the water vapor and on that at 2.36 $\mu$m (4235 cm$^{-1}$) for the carbon monoxide. However, although there is a CO absorption band, which is much more intense, at 4.65 $\mu$m (2150 cm$^{-1}$), in the thermal region of the SW channel of PFS, we decided to perform the analysis of this atmospheric minor species using the weaker band at 2.36 $\mu$m (4235 cm$^{-1}$), because the study of the thermal region of the spectrum has, at the time of this writing, different problems, and their resolution would require further study. Nevertheless, it was possible to validate the CO analysis for comparison between the results obtained in the two bands for only a few cases in which it was allowed by the analysis conditions of the thermal region.

In order to correct the possible instrumental effects, causing the modulation of the spectral continuum at wavenumbers around 5000 cm$^{-1}$, we developed an analysis method (described in Chapter 4), which involves the use of the relative bands depth rather than the absolute ones, in order to be independent from the absolute calibration.

## $H_2O$ and CO Variability

The water vapor retrieval revealed the same seasonal behaviour already observed by TES and other instruments, as PFS by indipendent studies and CRISM. The mean global value is 9.6 pr.mm and we measure a maximum water vapor concentration of about 59 pr.mm during the northern summer in the atmosphere over the north polar cap, in agreement with CRISM and all other observational data. After the sublimation of the northern polar cap we observe the water vapor migration toward tropical regions. A similar behaviour is evident in the southern hemisphere: the polar cap sublimation during its summer causes an enhancement of the atmospheric content of water vapor.

The geographical distribution of water vapor is characterized by a peculiarity in almost all the seasons (Spring, Fall and Winter): an increase of the water vapor abundance over two particular regions, Arabia Terra (30°E, 0°N) and Tharsis (100°W, 0°N). Both these maxima have been also observed by many instruments and two explanations have been given for them: interaction soil-atmosphere and atmospheric circulation influence with the presence of stationary waves causing a water vapor build-up over certain region.

Studying the correlation of the water vapor concentrations with the pressure, we found that the absolute concentrations are positively correlated with the pressure, as expected, whereas the abundances normalized to a fixed pressure (6.1 mbar) appear to be anticorrelated with it. This effect may be due to a scenario in which the water vapor is only partially mixed in the atmosphere and a large part of it is confined to a near-surface layer (*boundary layer*).

Finally, we made a comparison between the values provided by the MCD model (*Mars Climate Database*) with the results obtained by the analysis of experimental PFS data: we observe that the latitudinal trend is not always coincident.

Our study of the CO concentrations in the Mars atmosphere led us to observe large variations strictly bound by the condensing and subliming processes in the polar caps. We measured a mean CO mixing ratio of about 990 ppm, but when the summer polar cap sublimes, releasing $CO_2$ in the atmosphere, we can see a very strong CO depletion (down to values less than 400 ppm). An opposite behaviour is expected over the winter polar cap, when the $CO_2$ condenses causing an atmospheric enrichment of non-condensable gases such as carbon monoxide. This trend is indicated by our data, but unfortunately the PFS/SWC can study carbon monoxide only during daytime, thus we have poor information about the atmosphere over the winter polar cap.

## Planetary Waves

The geographical mapping of water vapor and carbon monoxide for different seasonal periods revealed the presence of mainly two types of wave phenomena in the atmosphere of Mars: the first one in the equatorial areas during the spring and the second one in the polar regions during the respective fall. The comparison between gaseous distributions and the thermal profiles has provided clear indications both on the causes of the phenomenon and on the stratification of gasses in different layers of the atmosphere.

The wave trends observed in the $H_2O$ and CO longitudinal distributions on the equatorial regions have not relations with the temperatures at middle-high altitudes. Indeed, water vapor concentrations have a strong correlation with the temperatures of the near-surface atmosphere: this correlation suggests a direct relationship with the topography of Mars in those regions. Moreover, other intruments observed the enhancement of $H_2O$ abundance over these two particular regions, Arabia Terra (30°E, 0°N) and Tharsis (100°W, 0°N).

The strong positive correlation between the longitudinal distribution of water vapor and the topography suggests that the $H_2O$ is generally located in the boundary layer (near-surface atmosphere), whereas the carbon monoxide behavior suggests that it is generally well mixed in the atmosphere of Mars, since it is a non condensable gas and its longitudinal trend is almost flat as the corresponding temperatures at middle-high altitudes.

During the southern spring in the near polar atmosphere, the relationships between temperatures and gaseous concentrations suggest that in these conditions water vapor is confined near the surface, while the carbon monoxide is located mainly in the middle-high atmosphere. This scenario is compatible with the beginning of the $H_2O$ sublimation from the southern polar cap, and the transport of the CO toward the equator, since it is a non condensable gas.

## Limb Retrieval Algorithm and $H_2O$ Vertical Distribution

All the clues about the vertical distribution of minor species, which we discovered by studying the integrated abundance of water vapor and carbon monoxide retrieved by nadir PFS measurements, required a direct confirmation. The lack of stable radiative transfer codes able to simulate limb measurements, at the moment of this writing, led us to develop a new own algorithm. So we developed a method to retrieve the minor species concentration by limb measurements using a code based on the Monte Carlo approach. We validated this radiative transfer code by comparing its results with the ones obtained using DISORT based codes (ARS for Nadir and SARTre for Limb). This validation in the water vapor absorption band at (3780-3920 $cm^{-1}$), under a certain uncertainty equal to the Monte Carlo accuracy that we set (5%), allowed us to implement it in the algorithm we developed for nadir retrievals, making it able to retrieve the concentrations of minor species by limb measurements.

We selected PFS measured spectra acquired in limb geometries and in the observing conditions we focus on for the planetary waves study: 1) northern spring ($Ls = 0°$-$30°$) over the near-equatorial region (10°-30° N) and 2) southern spring ($Ls = 180°$-$210°$) over the near-polar region (50°-70° S). Unfortunately, the PFS measurements acquired in limb geometry are pretty limited in number, therefore it is difficult to average many spectra and to have a good signal to noise ratio in the selected observing conditions. For this reason we decided to apply our algorithm, as first attempt, only to the water vapor band at 2.6 $\mu$m (3845 cm-1), which is much more stronger than the carbon monoxide one at 2.36 $\mu$m (4235 cm-1).

The water vapor retrieval gave us important results: in both cases we examined the $H_2O$ results to be confined mainly in the first 30 Km, as suggested by our indirect indications (surface pressure correlation and planetary waves), and other previous studies. This confinement is probably due to soil-atmosphere interactions.

The $H_2O$ vertical trends we studied revealed another important information: during the northern spring on the near equatorial regions, the atmosphere above 35 Km is relatively wet, having a water vapor concentration ($\sim$ 240 ppm) higher than its mean global and annual average value ($\sim$ 150 ppm), whereas during the southern spring the atmosphere near the south polar region becomes extremely dry above 60 Km ($\sim$ 25 ppm), reaching almost the minimum quantity we detected in the Martian atmosphere. The explanation of this behaviour lies in the dynamical processes that occur in the Martian atmosphere: in the first case the global circulation keeps the water vapor vertically mixed in the equatorial latitudes; in the second case the beginning of the sublimation of the southern polar cap increases the water vapor amount in the atmosphere near the surface, leaving the higher layers relatively dry.

Finally, the improvement of our algorithm will allow to widely map the vertical distribution of minor species (especially $H_2O$ and CO) and so to study deeper their behaviour and their connection with the atmospheric dynamics.

This thesis work will be useful in future data processing of both PFS and other instruments on board future missions, as NOMAD aboard the ExoMars spacecraft. The *Nadir and Occultation for MArs Discovery*, or NOMAD, will be part of the ExoMars Trace Gas Orbiter payload, to be launched in 2016. It is a spectrometer suite that can measure the spectrum of sunlight across a wide range of wavelengths (infrared, ultraviolet and visible). This broad coverage of the instrument enables the detection of the components of the Martian atmosphere, even in low concentrations. In addition to identifying the constituents of the Martian atmosphere, NOMAD will also map their locations. Therefore, our study, providing important information about the Martian atmosphere, will be also useful for the science planning of future observations.

# Appendix

## Dissemination of the Scientific Activity

- V. Formisano, **G. Sindoni**, 2009. *Study of Carbon monoxide in martian atmosphere.* EGU General Assembly 2009, held 19-24 April, 2009 in Vienna, Austria, p.4310.

- **G. Sindoni**, V. Formisano, 2010. *Study of H2O and CO in Martian atmosphere with PFS/MEX data.* EGU General Assembly 2010, held 2-7 May, 2010 in Vienna, Austria, p.3368.

- **G. Sindoni**, V. Formisano, 2010. *Study of H2O and CO in Martian atmosphere with PFS/MEX data.* EPSC Abstracts Vol. 5, EPSC2010-486, 2010 European Planetary Science Congress 2010, Vol. 5, EPSC2010-486, 2010.

- A. Geminale, V. Formisano, **G. Sindoni**, 2010. *Mapping Methane in Martian Atmosphere with PFS-MEX Data.* Planetary and Space Science, Volume 59, Issue 2-3, p. 137-148, doi:10.1016/j.pss.2010.07.011.

- **G. Sindoni**, V. Formisano, A. Geminale, 2011a. *Observations of water vapour and carbon monoxide in the Martian atmosphere with the SWC of PFS/MEX.* Planetary and Space Science, Volume 59, Issue 2-3, p. 149-162, doi:10.1016/j.pss.2010.12.006.

- **G. Sindoni**, M. Giuranna, A. Geminale, D. Grassi, 2011b. *Planetary Waves in the Martian Atmosphere Observed with PFS/MEX Data.* Fourth International Congress on the Mars Atmosphere: Modelling and Observation, February 8 - 11 2011, Paris, France.

- P. Wolkenberg, M. D. Smith, V. Formisano, **G. Sindoni**, 2011. *Variability of the Martian atmosphere from PFS and TES observations during 1999 - 2009.* Icarus 215, 628–638, doi:10.1016/j.icarus.2011.07.032.

- A. Geminale, V. Formisano, A. García Muñoz, **G. Sindoni**, M. Giuranna, D. Grassi, 2011. *Study of the oxygen day glow in the Martian atmosphere with nadir data of PFS-MEX.* Fourth International Congress on the Mars Atmosphere: Modelling and Observation, February 8 - 11 2011, Paris, France.

- **G. Sindoni**, M. Giuranna, D. Grassi, V. Formisano, 2011c. *Planetary Waves, Dynamics, and Minor Species Distribution in the Martian Atmosphere observed with PFS/MEX data.* EPSC-DPS Joint Meeting 2011, Vol. 6, EPSC-DPS2011-768, 2011.

- M. I. Błęcka, T. Encrenaz, P. Hartogh, C. Jarchow, E. Lellouch, **G. Sindoni**, M. Rengel, 2011. *Observations of Carbon Monoxide in the Martian Atmosphere-the comparison of the measurements done by PFS MEX, OMEGA MEX and HIFI on Herschel.* EPSC-DPS Joint Meeting 2011, held 2-7 October 2011 in Nantes, France. http://meetings.copernicus.org/epsc-dps2011, p.1321.

- S. Aoki, Y. Kasaba, M. Giuranna, A. Geminale, **G. Sindoni**, H. Nakagawa, Y. Kasai, I. Murata, D. Grassi, V. Formisano, 2011. *Detection of hydrogen peroxide (H2O2) in the Martian atmosphere with MEX / PFS.* EPSC-DPS Joint Meeting 2011, held 2-7 October 2011 in Nantes, France. http://meetings.copernicus.org/epsc-dps2011, p.622.

- A. Geminale, D. Grassi, V. Formisano, A. García Muñoz, **G. Sindoni**, M. Giuranna, 2012. *Interannual study and vertical profiles of the oxygen day-glow in the Martian atmosphere with data of PFS-MeX.* EGU General Assembly 2012, held 22-27 April, 2012 in Vienna, Austria., p.12565.

# Acknowledgements

The research work which is the subject of this PhD thesis was carried out at the "Istituto di Astrofisica e Planetologia Spaziali" (IAPS) of the "Istituto Nazionale di Astrofisica" (INAF) in Rome, in the context of the Italian participation to the ESA Mars Express mission. The computational resources used in this research have been supplied by INAF-IAPS through the project *HPP - High Performance Planetology.*

Foremost, I would like to express my sincere gratitude to my advisor in IAPS, Dr. Davide Grassi, for the continuous support of my PhD study and research, for his patience and motivation. His guidance helped me in my research and writing of this thesis.

I extend my thanks also to the tutor of my thesis in Sapienza (University of Rome), Prof. Roberto Seu, for allowing me to undertake this research thesis journey.

I would like to express my thanks to Dr. Vittorio Formisano for having initiated me into scientific research with great enthusiasm and to Dr. Alberto Adriani for having supported me in the last year of my PhD course.

I cannot let me off to thank all the directors of IAPS (ex-IFSI) of Rome who have come and gone in these PhD years, particularly Dr. Angioletta Corradini, for their hospitality.

I express feelings of gratitude to Dr. Anna Geminale, Dr. Marco Giuranna, Dr. Shohei Aoki and Dr. Giovanna Rinaldi for suggestions and constant concrete support, and for the encouragement during the preparation of my thesis.

Moreover, I must give my thanks to Dr. Francesca Altieri, Dr. Alessandro Aronica, Dr. Giacomo Carrozzo, Dr. Emiliano D'Aversa, Dr. Marco Giardino, Dr. Andrea Longobardo, Dr. Fabrizio Oliva and Dr. Ernesto Palomba, for supporting me in my research journey.

I thank all my family for giving me for its tender feelings, which I consider very important in my life, and in particular I thank my partner Alessia Di Felice for coming with me in this research journey and for sweetly suffering all my related anxieties.

Finally, I thank all my friends and in particular Sergio Fabiani and Katia Cramerotti for our long dinners spent in scientific and non discussions.

# Bibliography

[1] *"NASA Images Suggest Water Still Flows in Brief Spurts on Mars"*. NASA/JPL (December 6, 2006). Retrieved on 2007-01-04.

[2] *"Other Mars Missions"*. Journey through the galaxy. Retrieved on 2006-06-13.

[3] *"Mars Global Surveyor"*. CNN- Destination Mars. Retrieved on 2006-06-13.

[4] *"Mars Exploration Rovers- Science"*. NASA MER website. Retrieved on 2006-06-13.

[5] *"Photo shows avalanche on Mars"*. CNN. Retrieved on 2008-03-04.

[6] *"Mars Pulls Phoenix In"*. University of Arizona Phoenix mission Website. Retrieved on 2008-05-25.

[7] *"Phoenix: The Search for Water"*. NASA website. Retrieved on 2007-03-03.

[8] *"Mars Science Laboratory"*. NASA's MSL website. Retrieved on 2007-03-03.

[9] *"ExoMars"*. ESA website. Retrieved on 2007-03-03.

[10] *"Water at Martian south pole"* . March 17, 2004 ESA Press release. URL accessed March 17, 2006.

[11] *"Orbiter's Long Life Helps Scientists Track Changes on Mars"*. Sept. 20, 2005 NASA Press release. URL accessed March 17, 2006.

[12] *"Mars' South Pole Ice Deep and Wide"*. NASA (March 15, 2007). Retrieved on 2007-03-16.

[13] *"Martian soil could support life"*. BBC News (June 27, 2008). Retrieved on 2008-08-07.

[14] *"NASA Spacecraft Analyzing Martian Soil Data"*. JPL. Retrieved on 2008-08-05.

[15] *"Mars Meteorites"*. NASA. Retrieved on 2008-08-15.

[16] *"Allan Hills 84001"*. The Meteorolitical Society (April 2008). Retrieved on 2008-08-21.

[17] *"Rotating image of a Nakhla meteorite fragment"*. London Natural History Museum (2008). Retrieved on 2008-08-17.

[18] *"Mars Rovers Spot Water-Clue Mineral, Frost, Clouds"*, NASA (Dec. 13, 2004). Retrieved on 2006-03-17.

[19] *"Mars Express confirms methane in the Martian atmosphere"*, ESA (March 30, 2004). Retrieved on 2006-03-17.

[20] Allen, C.W., (1976). *"Astrophysical quantities"*. Athelone Press (London and Atlantic Highlands N.J.), 3rd 1973, Repr. with corrections 1976 edition.

[21] Altieri, F.; Zasova, L.; D'Aversa, E.; Bellucci, G.; Carrozzo, F. G.; Gondet, B.; Bibring, J.-P., (2009). *"$O_2$ 1.27 $\mu$m emission maps as derived from OMEGA/MEx data"*. Icarus, Volume 204, Issue 2, p. 499-511, doi: 10.1016/j.icarus.2009.07.022.

[22] Aoki, S., Nakagawa, H., Kasaba, Y., Giuranna, M., Geminale, A., Sindoni, G., Sagawa, H., Mendrok, J., Kasai, Y., Formisano, V., (2012). *"Study of trace gases in the Martian atmosphere: Ground-based observation using SUBARU/IRCS and development of radiative transfer model for MEX/PFS limb observation"*. EPSC Abstracts Vol. 7EPSC2012-207-12012.

[23] Atreya, S.K., Blamont, J.E., (1990). *"Stability of the Martian atmosphere: Possible role of heterogeneous chemistry"*, Geophys. Res. Left., 17,287.

[24] Atreya, S.K., and Gu, Z.G., (1994). *"Stability of the Martian Atmosphere – Is Heterogeneous Catalysis Essential?"*. J. Geophys. Res., 99, 13133.

[25] Atreya, S.K., Gu, Z.G., (1995). *"Photochemistry and stability of the atmosphere of Mars"*. Adv. Space Res. 16,57-68.

[26] Baalke, Ron (1995). *"The Nakhla Meteorite"*. Jet Propulsion Lab. NASA. Retrieved on 2008-08-17.

[27] Banfield, D., Conrath, B., Pearl, J.C., Smith, M.D., Christensen, P., (2000). *"Thermal tides and stationary waves on Mars as revealed by Mars Global Surveyor thermal emission spectrometer"*. J. Geophys. Res. 105, 9521–9537.

[28] Banfield, D., Conrarh, B. J., Smith, M. D., Christensen, P. R., Wilson R. J., (2003). *“Forced waves in the Martian atmosphere from MGS TES nadir data”*. Icarus, 161, 319-345.

[29] Banfield D, Conrath BJ, Gierasch PJ, Wilson RJ, Smith MD. (2004). *“Traveling waves in the Martian atmosphere from MGS TES nadir data”*. Icarus 170:365403.

[30] Banin, A. , Clark, B. C., Wanke, H., (1992). *“Surface chemistry and mineralogy”*. Mars, p. 594 - 625.

[31] Barker, E. S., (1976). “Martian atmospheric water vapor observations: 1972–1974 apparition”. Icarus 28, 247-268.

[32] Barnes, J.R., Haberle, R.M., Pollack, J.B., Lee, H., Schaeffer, J., (1996). *“Mars atmospheric dynamics as simulated by the NASA Ames general circulation model. 3. Winter quasi-stationary eddies”*. J. Geophys. Res. 101, 12753–12776.

[33] Barth, CA., (1974). *“The atmosphere of Mars”*. Ann. Rev. Earth Planet. Sci., 2, 333.

[34] Basilevsky, A. T., Rodin, A. V., Raitala, J., Neukum, G.,Werner, S., Kozyrev, A. S., Sanin, A. B., Mitrofanov, I. G., Head, J. W., Boynton, W., Saunders, R. S., (2006). *“Search for causes of the low epithermal neutron flux anomaly in the Arabia Terra region (Mars)”*. Solar System Research 40, 355374.

[35] Baucom, Martin (2006). *"Life on Mars?"*. American Scientist 94 (2). Retrieved on 2007-02-26.

[36] Bertaux et al., Jean-Loup (June 9, 2005). *"Discovery of an aurora on Mars"*. Nature Magazine. Retrieved on 2006-06-13.

[37] Bibring, Jean-Pierre (2006). *"Global Mineralogical and Aqueous Mars History Derived from OMEGA/Mars Express Data"*. Science 312 (5772): 400404. doi:10.1126/science.1122659. PMID 16627738.

[38] Billebaud, F., Brillet, J., Lellouch, E., Fouchet, T., Encrenaz, T., Cottini, V., Ignatiev, N., Formisano, V., Giuranna, M., Maturilli, A., Forget, F. (2009). *“Observations of CO in the atmosphere of Mars with PFS onboard Mars Express”*. Planetary and Space Science, Volume 57, Issue 12, p. 1446-1457, doi:10.1016/j.pss.2009.07.004.

[39] Biver, N., and 10 colleagues, (2005). *“Wide-band observations of the 557 GHz water line in Mars with Odin”*. Astron. Astrophys. 435, 765-772.

[40] Blamont, J.E. and Chassefiere, E., (1993). *"First detection of ozone in the middle atmosphere of Mars from solar occultation measurements"*. Icarus (ISSN 0019-1035), vol. 104, no. 2, p. 324-336, doi: 10.1006/icar.1993.1104.

[41] Boisson, J. , Heggy, E., Clifford, S. M., Yoshikawa, K., Anglade, A., Lognonné, P., (2011). *"Radar sounding of temperate permafrost in Alaska: Analogy to the Martian midlatitude to high-latitude ice-rich terrains"*. Journal of Geophysical Research, vol. 116, E11003, doi:10.1029/2010JE003768.

[42] Bottger, H. M., Lewis, S. R., Read, P. L., Forget, F., (2004). *"The effect of a global dust storm on simulations of the Martian water cycle"*. Geophys. Res. Letters 31, 22.

[43] Boynton, W.V., et al., (2002). *"Distribution of hydrogen in the near surface of Mars: Evidence for subsurface ice deposits"*. Science 297: 81-85.

[44] Britt, Robert (March 14, 2003). *"Odyssey Spacecraft Generates New Mars Mysteries"*. Space.com. Retrieved on 2006-06-13.

[45] Caplinger, Mike. *"Determining the age of surfaces on Mars"*. Retrieved on 2007-03-02.

[46] Chang, Alicia. *"Scientists: Salt in Mars soil not bad for life"*. AP. Retrieved on 2008-08-07.

[47] Chicarro, A.F., (1999). *"MARS EXPRESS MISSION: Overview and Scientific Observations"*. 5th International Conference on Mars, Pasadena, CA.

[48] Chicarro A., Martin P., Traunter R. (2004). *"Mars Express: A European Mission to the Red Planet"*. SP-1240, pp. 3-16, European Space Agency Publication Division, Noordwijk, Netherlands.

[49] Clancey, R.T. , Lee, S.W., James, P.B., Martin, L., Singer, R., Kahn, R., Zurek, R., (1992). *"Hubble Space Telescope ultraviolet imaging and spectroscopy of Mars: Monitoring ozone and dust in the Mars atmosphere"*. BAAS, 24, #3, 1007.

[50] Clancy RT, Grossman AW,Wolff MJ, James PB, Rudy DJ, et al. (1996).*"Water vapor saturation at low altitudes around aphelion: a key to Mars climate?"*. Icarus 122, 3662.

[51] Clancy, R.T., Nair, H., (1996). *"Annual (perihelion-aphelion) cycles in the photochemical behavior of the global Mars atmosphere"*. J. Geophys. Res. 101, 1278512790.

[52] Clancy, R.T., Wolff, M.J., James, P.B., Smith, E., Billawala, Y.N., Lee, S.W., Callan, M., (1996). *"Mars ozone measurements near the 1995 aphelion: Hubble Space Telescope ultraviolet spectroscopy with the faint object spectrograph"*. J. Geophys. Res. 101, 12777-12783.

[53] Clancy, R. T., Sandor, B. J., Wolff, M. J., Christensen, P. R., Smith, M. D., Pearl, J. C., Conrath, B. J., Wilson, R. J., (2000). *"An intercomparison of ground-based millimeter, MGS TES, and Viking atmospheric temperature measurements: Seasonal and interannual variability of temperatures and dust loading in the global Mars atmosphere"*. Journal of Geophysical Research, Volume 105, Issue E4, p. 9553-9572, doi:10.1029/1999JE001089.

[54] Clancy, R. T., Wolff, M. J., Christensen, P. R., (2003). *"Mars aerosol studies with the MGS TES emission phase function observations: Optical depths, particle sizes, and ice cloud types versus latitude and solar longitude"*. J. Geophys. Res. 108 (E9).

[55] Clancy, R.T., Sandor, B.J., Moriarty-Schieven, G.H., (2004). *"A measurement of the 362 GHz absorption line of Mars atmospheric* $H_2O_2$*"*. Icarus 168, 116-121.

[56] Comolli, L., Saggin, B., (2005). *"Evaluation of the sensitivity to mechanical vibrations of an IR Fourier spectrometer"*. Review of Scientific Instruments 76 (12), 123112.

[57] Conrath BJ. (1972). *"Vertical resolution of temperature profiles obtained from remote radiation measurements"*. J. Atmos. Sci. 29:126271.

[58] Conrath BJ, Curran R, Hanel R, Kunde V, Maguire WC, et al. (1973). *"Atmospheric and surface properties of Mars obtained by infrared spectroscopy on Mariner 9"*. J. Geophys. Res. 78:426778.

[59] Conrath BJ, Pearl JC, Smith MD, Maguire WC, Christensen PR, et al. (2000). *"Mars Global Surveyor Thermal Emission Spectrometer (TES) observations: atmospheric temperatures during aerobraking and science phasing"*. J. Geophys. Res. 105:950919.

[60] Curtis, A. R. (1952). *"Discussion of a statistical model for water vapour absorption"*. Q. J. R. Meteorol. Soc., 78, 638 – 640.

[61] Davies, D.W., (1979). *"The relative humidity of Mars atmosphere"*. J. Geophys. Res. 84, 83358340.

[62] Ehlmann B.; Mustard, JF; Murchie, SL; Poulet, F; Bishop, JL; Brown, AJ; Calvin, WM; Clark, RN et al. (2008). *"Orbital identification of carbonate-bearing rocks on Mars"*. Science 322 (5909): 1828–1832. Bibcode 2008Sci...322.1828E. doi:10.1126/science.1164759. PMID 19095939.

[63] Encrenaz, T., Lellouch, E., Rosenqvist, J., Drossart, P., Combes, M., Billebaud, F., de Pater, I., Gulkis, S., Maillard, J.P., Paubert, G., (1991). *"The atmospheric composition of Mars-ISM and ground-based observational data"*. Ann. Geophys. 9, 797803.

[64] Encrenaz, T., Lellouch, E., Cernicharo, J., Paubert, G., Gulkis, S., (1995). *"A tentative detection of the 183-GHz water vapor line in the martian atmosphere: Constraints upon the $H_2O$ abundance and vertical distribution"*. Icarus 113, 110118.

[65] Encrenaz T. (2001). *"The atmosphere of Mars as constrained by remote sensing"*. Space Sci. Rev. 96:41124.

[66] Encrenaz, T., Bezard, B., Greathouse, T.K., Richter, M.J., Lacy, J.H., Atreya, S.K., Wong, A.S., Lebonnois, S., Lefevre, F., Forget, F., (2004). *"Hydrogen peroxide on Mars: Evidence for spatial and seasonal variations"*. Icarus 170, 424-429.

[67] Encrenaz, T., Melchiorri, R., Fouchet, T., Drossart, P., Lellouch, E., Gondet, B., Bibring, J.-P., Langevin, Y., Titov, D., Ignatiev, N., Forget, F., (2005). *"A mapping of martian water sublimation during early northern summer using OMEGA/Mars Express"* . Astron. Astrophys.441, L9L12.

[68] Encrenaz, T., Fouchet, T. Melchiorri, R., Drossart, P., Gondet, B., Langevin, Y., Bibring J.-P., Forget, F. Bézard, B., (2006). *"Seasonal variation of the martian CO over Hellas as observed by OMEGA/Mars Express"*. Astron. Astrophys. 459, 265-270.

[69] Encrenaz, T., Greathouse, T. K., Richter, M. J., Bézard, B., Fouchet, T., Lefèvre, F., Montmessin, F., Forget, F., Lebonnois, S. and Atreya, S. K. (2008), *"Simultaneous mapping of $H_2O$ and $H_2O_2$ on Mars from infrared high-resolution imaging spectroscopy"*. Icarus, 195, 547-556.

[70] ESA - MarsExpress - The spacecraft, http://www.esa.int/SPECIALS/Mars_Express/SEMC785V9ED_0.html.

[71] Espenak, F., Mumma, M.J., Kostiuk, T., Zipoy, D., (1991). *"Ground-based infrared measurements of the global distribution of ozone in the atmosphere of Mars"*. Icarus 92, 252262.

[72] Farmer, C.B., Davis, D.W., Holland, A.L., LaPorte, D.D., Docus, P.E., (1977). *"Water vapor observations from the Viking Orbiters"*. J. Geophys. Res., 82,4225.

[73] Fast, K.E., (2005). *"Mars Ozone Abundances from Infrared Heterodyne Spectra and Their Application to the Study of the Stability of the Martian Atmosphere"*. Thesis, University of Maryland, College Park.

[74] Fast, K. E., Kostiuk, T., Lefèvre, F., Hewagama, T., Livengood, T. A., Delgado, J. D., Annen, J., Sonnabend, G., (2009). *"Comparison of HIPWAC and Mars Express SPICAM observations of ozone on Mars 2006–2008 and variation from 1993 IRHS observations"*. Icarus, 203, 20-27.

[75] Fedorova, A. A., Rodin, A. V., Baklanova, I. V., (2004). *"MAWD observations revisited: seasonal behavior of water vapor in the martian atmosphere"*. Icarus 171, 5467.

[76] Fedorova, A. A., Korablev, O., Bertaux, J.-L., Rodin, A., Kiselev, A., Perrier, S., (2006). *"Mars water vapor abundance from SPICAM IR spectrometer: Seasonal and geographic distributions"*. J. Geophys. Res., 111, E09S08, doi:10.1029/2006JE002695.

[77] Fedorova, A. A.; Korablev, O. I.; Bertaux, J.-L.; Rodin, A. V.; Montmessin, F.; Belyaev, D. A.; Reberac, A., (2009). *"Solar infrared occultation observations by SPICAM experiment on Mars-Express: Simultaneous measurements of the vertical distributions of $H_2O$, $CO_2$ and aerosol"*. Icarus, Volume 200, Issue 1, p. 96-117, doi: 10.1016/j.icarus.2008.11.006.

[78] Fiorenza, C., Formisano, V., (2005). *"A solar spectrum for PFS data analysis"*. Planet. Space Sci. 53, 1009-1016.

[79] Forget, F., Montabone, L., Lebonnois, S., (2006). *"Non-condensable gas enrichment and depletion in the martian polar regions"*, Proc. of the Second Workshop on Mars Modeling and Observations, Granada, Spain.

[80] Forget, F.; Millour, E.; González-Galindo, F.; Spiga, A.; Lewis, S. R.; Montabone, L.; Read, P. L.; López-Valverde, M. A.; Gilli, G.; Desjean, M.-C.; Huot, J.-P.; McD/Gcm Development Team, (2007). *"The New (Version 4.2) Mars Climate Database"*. Seventh International Conference on Mars, held July 9-13, 2007 in Pasadena, California, LPI Contribution No. 1353, p.3098.

[81] Forget, F., Millour, E., Montabone, L., Lefèvre, F., (2008). *"Noncondensable gas enrichment and depletion in the martian polar regions"*, Proc. of the Third Workshop on Mars Modeling and Observations, Williamsburg, Virginia.

[82] Formisano, V., Grassi, D., Ignatiev, N. I., Zasova, L., (2001). *"IRIS Mariner 9 data revisited: water and dust daily cycles"*. Planetary and Space Science. 49, 1331-1346.

[83] Formisano, V., Atreya, S., Encrenaz, T., Ignatiev, N. ., Giuranna, M., (2004). *"Detection of Methane in the Atmosphere of Mars"*. Science 306: 17581761. doi:10.1126/science.1101732. PMID 15514118.

[84] Formisano, V., Angrilli, F., Arnold, G., Atreya, S., Bianchini, G., Biondi, D., Blanco, A., Blecka, M.I., Coradini, A., Colangeli, L., Ekonomov, A., Esposito, F., Fonti, S., Giuranna, M., Grassi, D., Gnedykh, V., Grigoriev, A., Hansen, G., Hirsh, H., Khatuntsev, I., Kiselev, A., Ignatiev, N., Jurewicz, A., Lellouch, E., Lopez Moreno, J., Marten, A., Mattana, A., Maturilli, A., Mencarelli, E., Michalska, M., Moroz, V., Moshkin, B., Nespoli, F., Nikolsky, Y., Orfei, R., Orleanski, P., Orofino, V., Palomba, E., Patsaev, D., Piccioni, G., Rataj, M., Rodrigo, R., Rodriguez, J., Rossi, M., Saggin, B., Titov, D., Zasova, L., (2005). *"The Planetary Fourier Spectrometer (PFS) onboard the European Mars Express mission"*. Planet. Space Sci. 53, 963–974, doi: 10.1016/j.pss.2004.12.006.

[85] Formisano, V., et al. (2005) *"A Martian PFS average spectrum: comparison with ISO SWS"*. Planet. Space Sci., 53:975-991, doi:10.1016/j.pss.2005.03.009.

[86] Fouchet, T., Lellouch, E., Ignatiev, N. I., Titov, D., Tschimmel, M., Formisano, V., Giuranna, M., Maturilli, A., Encrenaz, T., (2007). *"Martian water vapor: Mars Express PFS/LW observations"*. Icarus, 190, 32-49.

[87] Gamache, R. R., Neshyba, S. P., Plateaux, J. J., Barbe, A., Régalia, L., Pollack, J. B., (1995). *"CO2-broadening of water-vapor lines"*. J. Mol. Spectrosc. 170, 131-151.

[88] Geminale, A., Formisano, V., Sindoni, G. (2011). *"Mapping methane in Martian atmosphere with PFS-MEX data"*. Planetary and Space Science, Volume 59, Issue 2-3, p. 137-148, doi:10.1016/j.pss.2010.07.011.

[89] Geminale, A.; Grassi, D.; Formisano, V.; García Muñoz, A.; Sindoni, G.; Giuranna, M., (2012). *"Interannual study and vertical profiles of the oxygen day-glow in the Martian atmosphere*

*with data of PFS-MeX"*. EGU General Assembly 2012, held 22-27 April, 2012 in Vienna, Austria., p.12565.

[90] Goddard Space Flight Center. *"New Map Provides More Evidence Mars Once Like Earth"*. Retrieved on 2006-03-17.

[91] Giuranna, M.; Roush, T. L.; Duxbury, T.; Hogan, R. C.; Carli, C.; Geminale, A.; Formisano, V. (2011). *"Compositional interpretation of PFS/MEx and TES/MGS thermal infrared spectra of Phobos"*. Planetary and Space Science, Volume 59, Issue 13, p. 1308-1325.

[92] Giuranna, M., et al. (2004). *"Calibration of the planetary Fourier spectrometer long wavelength channel"*. Planet. Space Sci., 53:975-991, doi:10.1016/j.pss.2005.02.007.

[93] Giuranna, M., et al. (2004). *"Calibration of the planetary Fourier spectrometer short wavelength channel"*. Planet. Space Sci., 53:975-991, doi:10.1016/j.pss.2004.12.007.

[94] Giuranna, M., Hansen, G., Maturilli, A., Zasova, L., Formisano, V., Grassi, D., Ignatiev, N., (2007). *"Spatial variability, composition and thickness of the seasonal north polar cap of Mars in mid-spring"*. Planet. Space Sci., in press.

[95] Godson, W. L. (1953). *"The evaluation of infrared-radiative fluxes due to atmospheric water vapour"*. Q. J. R. Meteorol. Soc., 79, 367–379.

[96] Grassi, D., Ignatiev, N., Zasova, L., Maturilli, A., Formisano, V., Bianchini, G., Giuranna, M., (2005). *"Methods for the analysis of data from the Planetary Fourier Spectrometer on the Mars Express Mission"*. Planet. Space Sci. 53, 1017-1034.

[97] Gurnett D. A.and Bhattacharjee A. (2005). *"Introduction to Plasma Physics with Space and Laboratory Applications"*. Cambridge University Press, Cambridge, 91.

[98] Gurnett D. A., et al. (2005). *"Radar Soundings of the Ionosphere of Mars"*. Science 310, 1929, DOI: 10.1126/science.1121868.

[99] Gurwell, M.A., and 20 colleagues, (2000). *"Submillimeter wave astronomy satellite observations of the martian atmosphere: Temperature and vertical distribution of water vapor"*. Astrophys. J. 539, L143L146.

[100] Haberle, R. M., Jacosky, B. M., (1990). *"Sublimation and transport of water from the north residual polar cap on Mars"*. J. Geophys. Res. 95, 1423-1437.

[101] Hansen, G. B., (1999). *"Control of the radiative properties of the martian polar caps by surface CO2 ice: Evidence from Mars Global Surveyor measurements"*. J. Geophys. Res. 104, 16471–16486.

[102] Hess, SL, Henry, RM, Leovy, CB, Ryan, JA, Tillman, JE. (1977). *"Meteorological results from the surface of Mars: Viking 1 and 2"*. J. Geophys. Res. 82:455974.

[103] Hinson DP, Simpson RA, Twicken JD, Tyler GL, Flasar FM. (1999). *"Initial results from radio occultation measurements with Mars Global Surveyor"*. J. Geophys. Res. 104:269977012.

[104] Hinson, D.P., Tyler, G.L., Hollingsworth, J.L., Wilson, R.J., (2001). "Radio occultation measurements of forced atmospheric waves on Mars". J. Geophys. Res. 106, 1463–1480.

[105] Hinson, D. P., Wilson, R. J., Smith, M. D., Conrath, B. J., (2003). *"Stationary planetary waves in the atmosphere of Mars during southern winter"*. Jour. Geoph. Resear., 108, 5004.

[106] Hinson DP, Smith MD, Conrath BJ. (2004). *"Comparison of atmospheric temperatures obtained through infrared sounding and radio occultation by Mars Global Surveyor"*. J. Geophys. Res. 109:doi:10.1029/2004JE002344.

[107] Hinson DP, Wilson RJ. (2004). *"Temperature inversions, thermal tides, and water ice clouds in the Martian tropics"*. J. Geophys. Res. 109:doi:10.1029/2003JE002129.

[108] Hirsch, H., Arnold, G., (1993). *"Fourier transform spectroscopy in remote sensing of solid planetary surfaces"*. Vib. Spectrosc. 5, 119123.

[109] Hourdin, F., Forget, F., Talagrand, O., (1995). *"The sensitivity of the martian surface pressure and atmospheric mass budget to various parameters: A comparison between numerical simulations and Viking observations"*. J. Geophys. Res. 100, 55015523.

[110] Humlicek, J. (1982). *"Optimized computation of the Voight and complex probability functions"*. J. Quant. Spectrosc. Rad. Transfer, v. 27, no. 4, p. 437.

[111] Hunten, D.M., (1993). *"CO on Mars: Comment on paper by Rosenqvist et al."*. Icarus 101, 4244.

[112] Ignatiev, N. I., Grassi, D., Zasova, L. V., (2005). *"Planetary Fourier spectrometer data analysis: Fast radiative transfer models"*. Planet. Space Sci., 53:1035-1042, doi:10.1016/j.pss.2004.12.009.

[113] Jakosky, B. M., and C. B. Farmer, (1982). *"The seasonal and global behavior of water vapor in the Mars atmosphere: Complete global results of the Viking Atmospheric Water Detector Experiment"*, J. Geophys. Res., 87, 2999 – 3019.

[114] Jacqué, Dave (2003-09-26). *"APS X-rays reveal secrets of Mars' core"* (in English), Argonne National Laboratory. Retrieved on 2006-07-01.

[115] Kleinböhl, Armin; Schofield, John T.; Kass, David M.; Abdou, Wedad A.; Backus, Charles R.; Sen, Bhaswar; Shirley, James H.; Lawson, W. Gregory; Richardson, Mark I.; Taylor, Fredric W.; Teanby, Nicholas A.; McCleese, Daniel J. (2009). *"Mars Climate Sounder limb profile retrieval of atmospheric temperature, pressure, and dust and water ice opacity"*. Journal of Geophysical Research, Volume 114, Issue E10, CiteID E10006.

[116] Kostama, V.-P., Kreslavsky, M. A. & Head, J. W. (June 3, 2006), *"Recent high-latitude icy mantle in the northern plains of Mars: Characteristics and ages of emplacement"*, Geophysical Research Letters 33: L11201, doi:10.1029/2006GL025946. Retrieved on 1 August 2008.

[117] Krasnopolskii, V. A., Korablev, O. I., Moroz, V. I., Krysko, A. A., Blamont, J. E., Chassefiere, E., (1991). *"Infrared solar occultation sounding of the Martian atmosphere by the Phobos spacecraft"*. Icarus 94, 32-44.

[118] Krasnopolsky, V.A., (1995). *"Uniqueness of a solution of a steady-state photochemical problem: Applications to Mars"*. J. Geophys. Res. 100, 3263-3276.

[119] Krasnopolsky, V.A., (1997). *"Photochemical mapping of Mars"*. J. Geophys. Res. 102, 1311313320.

[120] Krasnopolsky, V.A., Bjoraker, G.L., (2000). *"Mapping of Mars $O_2(^1\Delta)$ dayglow"*. J. Geophys. Res. 105, 2017920188.

[121] Krasnopolsky, V.A., (2003). *"Mapping of Mars $O_2$ 1.27 $\mu$m dayglow at four seasonal points"*. Icarus 165, 315325.

[122] Krasnopolsky, V.A., (2003). *"Spectroscopic mapping of Mars CO mixing ratio: Detection of northsouth asymmetry"*. J. Geophys. Res. 108 (E2). 5010.

[123] Krasnopolsky, VA, Maillard, JP, Owen, TC. (2004). *"Detection of methane in the Martian atmosphere: evidence for life?"*. Icarus 172:53747.

[124] Krasnopolsky, V.A., (2006). *"Long-term spectroscopic observations of latitudinal and seasonal variations of O2 dayglow and CO on Mars"*. Icarus 190, 93-102.

[125] Korablev, O.I., Krasnopolsky, V.A., Rodin, A.V., Chassefiere, E., (1993). *"Vertical structure of martian dust measured by solar infrared occultations from the Phobos spacecraft"*. Icarus 102, 7687.

[126] Langevin, Y.; Poulet, F.; Bibring, J.-P.; Schmitt, B.; Douté, S.; Gondet, B. (2005). *"Summer Evolution of the North Polar Cap of Mars as Observed by OMEGA/Mars Express"*. Science, Volume 307, Issue 5715, pp. 1581-1584, doi: 10.1126/science.1109438.

[127] Langevin Y., et al. (2005). *"Sulfates in the North Polar Region of Mars Detected by OMEGA/Mars Express"*. Science 307, 1584, DOI: 10.1126/science.1109091.

[128] Lebonnois, S.; Quémerais, E.; Montmessin, F.; Lefèvre, F.; Perrier, S.; Bertaux, J.; Forget, F., (2006). *"Vertical distribution of ozone on Mars as measured by SPICAM/Mars Express using stellar occultations"*. Journal of Geophysical Research, Volume 111, Issue E9, doi: 10.1029/2005JE002643.

[129] Lefevre, F., Lebonnois, S., Montmessin, F., Forget, F., (2004). *"Threedimensional model of ozone on Mars"*. J. Geophys. Res. 109, doi:10.1029/ 2004JE002268. E07004.

[130] Lefèvre, F., and F. Forget, (2009). *"Observed variations of methane on Mars unexplained by known atmospheric chemistry and physics"*. Nature, Volume 460, pp. 720-723, doi:10.1038/nature08228.

[131] Leovy CB. 1979. *"Martian meteorology"*. Annu. Rev. Astron. Astrophys. 17:387413.

[132] Liu J, Richardson MI, Wilson RJ. 2003. *"An assessment of the global, seasonal, and interannual spacecraft record of Martian climate in the thermal infrared"*. J. Geophys. Res. 108:doi:10.1029/2002JE001921.

[133] Lundin, R., et al. (2004). *"Solar Wind-Induced Atmospheric Erosion at Mars: First Results from ASPERA-3 on Mars Express"*. Science 305: 19331936. doi:10.1126/science.1101860. PMID 15448263. Retrieved on 2007-02-26.

[134] Lundin R., et al. (2006). *"Ionospheric plasma acceleration at Mars: ASPERA-3 resoult"*. Icarus, 182:308-319.

[135] Magalhaes JA, Schofield JT, Seiff A. (1999). *"Results of the Mars Pathfinder atmospheric structure investigation"*. J. Geophys. Res. 104:894356.

[136] Maguire WC. (1977). *"Martian isotope ratios and upper limits for possible minor constituents as derived from Mariner 9 infrared spectrometer data"*. Icarus 32:85-97.

[137] Maltagliati, L. , Titov, D. V., Encrenaz, T., Melchiorri, R., Forget, F., Garcia-Comas, M., Keller, H. U., Langevin, Y., Bibring, J.-P., (2008). *"Observations of atmospheric water vapor above the Tharsis volcanoes on Mars with the OMEGA/MEx imaging spectrometer"*. Icarus, 194, 53–64.

[138] Maltagliati, L.; Montmessin, F.; Fedorova, A.; Korablev, O.; Forget, F.; Bertaux, J.-L., (2011). *"Evidence of Water Vapor in Excess of Saturation in the Atmosphere of Mars"*. Science, Volume 333, Issue 6051, pp. 1868- (2011), doi: 10.1126/science.1207957.

[139] Martel, Linda M.V. *"Pretty Green Mineral – Pretty Dry Mars?"*. psrd.hawaii.edu. Retrieved on 2007-02-23.

[140] Marti, J., Mauersberger, K., (1993). *"A survey and new mwsurements of ice vapor pressure at temperature between 170 and 250 K"*. GRL, 20, 363-366.

[141] Masson, P., (1982).*"The geologic evolution of the planet Mars"*. Formation of planetary systems. (A83-19451 06-91) Toulouse, Cepadues-Editions, 1982, p. 797, 799-816.

[142] Matveev, V. S. (1972). *"Approximate presentation of the absorption coefficient and equivalent width of spectral lines with Voight contour"*. Zhurnal prikladnoi spectroskopii (Applied spectroscopy journal), v. 16, no. 2, p. 228-233 (in Russian).

[143] Mayorov, B., http://spectrum.iki.rssi.ru/optics/SCATRD-OFOS.files/Code.htm

[144] McElroy, M.B., Donahue, T.M., (1972). *"Stability of the Martian atmosphere"*. Science", 177,986.

[145] Melchiorri R, Encrenaz T, Fouchet T, Drossart P, Lellouch E, et al. (2007). *"Water vapor mapping on Mars using OMEGA/Mars Express"*. Planet. Space Sci. 55:33342.

[146] Mellon, M. T., B. M. Jakosky, H. H. Kieffer, and P. R. Christensen, (2000). *"High-resolution thermal inertia mapping from the Mars Global Surveyor Thermal Emission Spectrometer"*, Icarus, 148, 437 – 455, 2000.

[147] Mendrok, J. (2006). *"The SARTre model for radiative transfer in spherical atmospheres and its application to the derivation of cirrus cloud properties"*. Ph.D. thesis, Freie Univ., Berlin.

[148] Mendrok, J., Schreier, F., Höpfner, M., (2007). *"Estimating cirrus cloud properties from MIPAS data"*. Geophysical Research Letters, Vol. 34, L08807, doi:10.1029/2006GL028246.

[149] Meyer, C. (2004). *"Mars Meteorite Compendium"* (PDF). NASA. Retrieved on 2008-08-21.

[150] Mohlmann, D. T. F., (2004). *"Water in the upper martian surface at midand low-latitudes: presence, state, and consequences"*. Icarus 168, 318323.

[151] Montmessin, F., Forget, F., Rannou, P., Cabane, M., Haberle, R. M., (2004). *"Origin and role of water ice clouds in the Martian water cycle as inferred from a general circulation model"*. J. Geophys. Res.109, 10004.

[152] Mouginot, J., Kofman, W., Safaeinili, A., Herique, A., Plaut, J., Picardi, G., Grima, C., (2008). *"Thickness of south polar residual cap of mars by MARSIS"*. 37th COSPAR Scientific Assembly. Held 13-20 July 2008, in Montréal, Canada., p.2117.

[153] Mumma MJ, Novak RE, DiSanti MA, Bonev BP, Dello Russo N. 2004. *"Detection and mapping of methane and water on Mars"*. Bull. Am. Astron. Soc. 36:1127216.

[154] Mustard, J. F.; Poulet, F.; Gendrin, A.; Bibring, J.-P.; Langevin, Y.; Gondet, B.; Mangold, N.; Bellucci, G.; Altieri, F. (2005). *"Olivine and Pyroxene Diversity in the Crust of Mars"*. Science, Volume 307, Issue 5715, pp. 1594-1597, doi: 10.1126/science.1109098

[155] Nair, H., Allen, M., Anbar, A.D., Yung, Y.L., Clancy, R.T., (1994). *"A photochemical model of the martian atmosphere"*. Icarus 111, 124150.

[156] Nelli, S. M., J. R. Murphy, A. L. Sprague, W. V. Boynton, K. E. Kerry, D. M. Janes, and A. E. Metzger, (2007). *"Dissecting the polar dichotomy of the noncondensable gas enhancement on Mars using the NASA Ames Mars General Circulation Model"*, J. Geophys. Res., 112, E08S91, doi:10.1029/2006JE002849.

[157] Novak, R.E., Mumma, M.J., Di Santi, M.A., Dello Russo, N., Magee-Sauer, K., (2002). *"Mapping of ozone and water in the atmosphere of Mars near the 1997 aphelion"*. Icarus 158, 1423.

[158] Ockert, M. E., Bell, J. F., Pollack, J. B., McKay, C. P., Forget, F., (1997). “Absorption and scattering properties of the martian dust in the solar wavelengths”. J. Geophys. Res. 102 (E4), 9039–9050.

[159] Orofino, V., Blanco, A., Blecka, M.I., Fonti, S., Jurewicz, A., (2000). *“Search for carbonates on the surface of Mars by means of the PFS”*. Planet. Space Sci. 48, 1341.

[160] Owen, T. (1992). *“The composition and early history of the atmoshere of Mars”*. Mars, p. 818 - 834.

[161] Owen T, Biemann K, Rushneck DR, Biller JE, Howarth DW, et al. 1977. *“The composition of the atmosphere at the surface of Mars”*. J. Geophys. Res. 82:463539.

[162] Palomba, E., Colangeli, L., Formisano, V., Piccioni, G., Cafaro, N., Moroz, V., (1997). *“The spectroscopic performances of the Planetary Fourier Spectrometer for the Mars 96 mission”*. Planet. Space Sci. 45 (4), 409418.

[163] Palomba, E., Zinzi, A., Cloutis, E. A., D’Amore, M., Grassi, D., Maturilli, A., (2009). *"Evidence for Mg-rich carbonates on Mars from a 3.9 $\mu m$ absorption feature"*. Icarus, volume 203, issue 1, p. 58–65.

[164] Parkinson, T.D., Hunten, D.M., (1972). *“Spectroscopy and Aeronomy of $C0_2$ on Mars”*. J. Atmos. Sci., 29,1380.

[165] Pätzold, M.; Neubauer, F. M.; Carone, L.; Hagermann, A.; Stanzel, C.; Häusler, B.; Remus, S.; Selle, J.; Hagl, D.; Hinson, D. P.; Simpson, R. A.; Tyler, G. L.; Asmar, S. W.; Axford, W. I.; Hagfors, T.; Barriot, J.-P.; Cerisier, J.-C.; Imamura, T.; Oyama, K.-I.; Janle, P.; Kirchengast, G.; Dehant, V. (2004). *“MaRS: Mars Express Orbiter Radio Science”*. In: Mars Express: the scientific payload. Ed. by Andrew Wilson, scientific coordination: Agustin Chicarro. ESA SP-1240, Noordwijk, Netherlands: ESA Publications Division, ISBN 92-9092-556-6, 2004, p. 141 - 163.

[166] Patzold M., et al. (2005). *“A Sporadic Third Layer in the Ionosphere of Mars”*. Science 310, 837, DOI: 10.1126/science.1117755.

[167] Perrier S, Bertaux J-L, Lefèvre F, Lebonnois S, Korablev O, et al. 2006. *“Global distribution of total ozone on Mars from SPICAM/MEX UV measurements”*. J. Geophys. Res. 111:doi:10.1029/2006JE002681.

[168] Philips, Tony (2001). *"The Solar Wind at Mars"*. Science@NASA. Retrieved on 2006-10-08.

[169] Picardi G., Biccari D., Seu R., Plaut J., Johnson W. T. K., Jordan R. L., Safaeinili A., Gurnett D. A., Huff R., Orosei R., Bombaci O., Calabrese D., and Zampolini E. (2004). *"Mars Express: A European Mission to The Red Planet"*. SP- 1240, pp.51- 70, European Space Agency Publication Division, Noordwijk, Netherlands.

[170] Piccioni, G., Formisano, V., Moroz, V., (1997). *"Extra sampling and thermal behaviour of diode laser used as reference source in a FT-IR"*. Appl. Optics. 36 (27).

[171] Pollack, J.B., Haberle, R.M., Murthy, J.R., Schaeffer, J., Lee, H., (1993). *"Simulations of the general circulation of the martian atmosphere. 2. Seasonal pressure variations"*. J. Geophys. Res. 98, 3149-3181.

[172] Quémerais E, Bertaux J-L, Korablev O, Dimarellis E, Cot C, et al. 2006. *"Stellar occultations observed by SPICAM on Mars Express"*. J. Geophys. Res. 111:doi:10.1029/2005JE002604.

[173] Richardson, M.I.,Wilson, R.J., (2002). *"Investigation of the nature and stability of the martian seasonal water cycle with a general circulation model"*. J. Geophys. Res. 107, doi:10.1029/2001JE001536. 5031.

[174] Rincon, Paul (8 February 2006). *"Space rock re-opens Mars debate"*, BBC News. Retrieved on 2008-08-17.

[175] Rodin, A.V., Korablev, O.I., Moroz, V.I., (1997). *"Vertical distribution of water in the near-equatorial troposphere of Mars: Water vapor and clouds"*. Icarus 125, 212-229.

[176] Rosenqvist, J., Drossart, P., Combes, M., Encrenaz, T., Lellouch, E., Bibring, J.P., Erard, S., Langevin, Y., Chassefiere, E., (1992). *"Minor constituents in the martian atmosphere from the ISM/Phobos experiment"*. Icarus 98, 254270.

[177] Rothman, L. S., et al. (1996). *"The HITRAN molecular spectroscopic database and HAWKS (HITRAN atmospheric workstation): 1996 edition"*. (PDF document supplied with HITRAN).

[178] Rothman, et al., (2005). *"The HITRAN 2004 molecular spectroscopic database"*. J. Quant. Spectrosc. Rad. Transfer 96, 139-204.

[179] Schofield JT, Barnes JR, Crisp D, Haberle RM, Larsen S, et al. (1997). *"The Mars Pathfinder Atmospheric Structure Investigation/Meteorology"*. Science 278:175-257.

[180] Sharma, Oze, M. (2005). *"Have olivine, will gas: Serpentinization and the abiogenic production of methane on Mars"*. Geophys. Res. Lett. 32: L10203. doi:10.1029/2005GL022691. Retrieved on 2006-04-18.

[181] Seiff A, Kirk DB. (1977). *"Structure of the atmosphere of Mars in summer at midlatitudes"*. J. Geophys. Res. 82:436478.

[182] Seiff, A., (1982). *"Post-Viking models for the structure of the summer atmosphere of Mars"*. Adv. Space Res., 2,#2,3.

[183] Sindoni, G., Formisano, V., Geminale, A. (2011). *"Observations of water vapour and carbon monoxide in the Martian atmosphere with the SWC of PFS/MEX"*. Planetary and Space Science, Volume 59, Issue 2-3, p. 149-162, doi:10.1016/j.pss.2010.12.006.

[184] Smith, D. E., et al., (1999). *"The global topography of Mars and implications for surface evolution"*, Science, 284, 1495 – 1503, 1999.

[185] Smith, M. D., (2002). *"The annual cycle of water vapor on Mars as observed by the Thermal Emission Spectrometer"*. J. Geophys. Res.107, 251.

[186] Smith, M. D., (2004). *"Interannual variability in TES atmospheric observations of Mars during 1999-2003"* . Icarus 167, 148-165.

[187] Smith MD, Wolff MJ, Spanovich N, Ghosh A, Banfield D, et al. (2006). *"One Martian year of atmospheric observations using MER Mini-TES"*. J. Geophys. Res. 111:doi:10.1029/2006JE002770.

[188] Smith, M. D., (2006). *"TES atmospheric temperature, aerosol optical depth, and water vapor observations 1999-2004"*. In: Forget, F., Lopez-Valverde, M. A., Desjean, M. C., Huot, J. P., Lefevre, F., Lebonnois, S., Lewis, S. R., Millour, E., Read, P. L., Wilson, R. J. (Eds.), *"Mars Atmosphere Modelling and Observations"*. pp. 211.

[189] Smith, M. D., (2008). "*Mars water vapor climatology from MGS/TES*". Mars Water Cycle Workshop, April 2008, Paris, France (abstract).

[190] Smith, M. D., Wolff, M. J., Clancy, R., T., Murchie, S. L., (2009). *"Compact Reconnaissance Imaging Spectrometer observations of water vapor and carbon monoxide"*. Journal of Geophysical Research, Volume 114, Issue E9, E00D03, doi:10.1029/2008JE003288.

[191] Spanovich N, Smith MD, Smith PH,Wolff MJ, Christensen PR, Squyres SW. (2006). *"Surface and near-surface atmospheric temperatures from the Mars Exploration Rover landing sites"*. Icarus 180:31420.

[192] Spiga, A.; Forget, F.; Dolla, B.; Vinatier, S.; Melchiorri, R.; Drossart, P.; Gendrin, A.; Bibring, J.; Langevin, Y.; Gondet, B., (2007). *"Remote sensing of surface pressure on Mars with the Mars Express/OMEGA spectrometer: 2. Meteorological maps"*. Journal of Geophysical Research, Volume 112, Issue E8, doi: 10.1029/2006JE002870.

[193] Spinrad, H., Munch, G., Kaplan, L. D., (1963). *"Letter to the Editor: the Detection of Water Vapor on Mars"*. Astrophys. J.137, 13-19.

[194] Sprague, A. L., Hunten, D. M., Doose, L. R., Hill, R. E., (2003). *"Mars atmospheric water vapor abundance: 1996-1997"*. Icarus 163, 88-101.

[195] Sprague, A. L. , Boynton, W. V., Kerry, K. E., Janes, D. M., Hunten, D. M., Kim, K. J., Reedy, R. C., Metzger, A. E., (2004). *"Mars' south polar Ar enhancement: A tracer for south polar seasonal meridional mixing"*. Science, 306, 1364–1367.

[196] Sprague, A. L., Hunten, D. M., Doose, L. R., Hill, R. E., Boynton, W. V., Smith, M. D., Pearl, J. C., (2006). *"Mars atmospheric water vapor abundance: 1991-1999, emphasis 1998-1999"*. Icarus 184, 372-400.

[197] Sprague, A. L., W. V. Boynton, K. E. Kerry, D. M. Janes, N. J. Kelly, M. K. Crombie, S. M. Nelli, J. R. Murphy, R. C. Reedy, and A. E. Metzger, (2007). *"Mars' atmospheric argon: Tracer for understanding Martian atmospheric circulation and dynamics"*. J. Geophys. Res., 112, E03S02, doi:10.1029/2005JE002597.

[198] Stamnes, K., (1986). *"The Theory of Multiple Scattering of Radiation in Plane Parallel Atmosphere"*. Reviews of Geophysics, vol. 24, no. 2, p. 299-310.

[199] Stamnes, K., S.-C. Tsay, W. Wiscombe and K. Jayaweera, (1988). *"Numerically stable algorithm for discrete-ordinate-method radiative transfer in multiple scattering and emitting layered media"*. Appl. Opt. 27, 2502-2509.

[200] Stamnes, K., S. C. Tsay, W. J. Wiscombe, and I. Laszlo, (2000). *"DISORT: A general-purpose Fortran program for discrete ordinate-method radiative transfer in scattering and emitting*

*layered media: documentation of methodology"*, NASA Report. ftp://climate1.gsfc.nasa.gov/wiscombe/Multiple_Scatt /DISORTReport1.1.pdf.

[201] Tillman JE, Johnson NC, Guttorp P, Percival DB. (1993). *"The Martian annual atmospheric pressure cycleyears without great dust storms"*. J. Geophys. Res. 98:1096371.

[202] Titov, D.V., Markiewicz, W.J., Thomas, N., Keller, H.U., Sablotny, R.M., Tomasko, M.G., Lemmon, M.T., Smith, P.H., (1999). *"Measurements of the atmospheric water vapor on Mars by the Imager for Mars Pathfinder"*. J. Geophys. Res. 104, 9019-9026.

[203] Titov, D.V., 2002. *"Water vapor in the atmosphere of Mars"*. Adv. Space Res. 29, 183-191.

[204] Tschimmel, M., Ignatiev, N. I., Titov, D., Lellouch, E., Fouchet, T., Giuranna, M., Formisano, V., (2008). *"Investigation of the water vapour on Mars with PFS/SW of Mars Express"*. Icarus, 195, 557-575.

[205] Vasilyev A. V., Mayorov B. S., Zasova L. V., Jean-Pierre Bibring, Formisano V., Fedorova A. A., (2006). *"'SCATRD' code for calculation of multiple scattering solar radiation in the spherical atmosphere. First application to Omega MEX limb aerosol profiles"*. Conference consecrate to forty years French-Russian cooperation in space science, session "Planetary studies and future missions" devoted to 75-anniversary of V. I. Moroz; 19 October 2006, IKI.

[206] Wardell, Jane (January 26, 2004). *"Europe's Beagle 2 Mars Probe Stays Ominously Silent"*. Space.com. Retrieved on 2006-06-13.

[207] Warren, B., Richard, E. (2008). *"Optical constants of ice from the ultraviolet to the microwave: A revised compilation"*. Journal of Geophysical Research, Volume 113, Issue D14, CiteID D14220.

[208] Westall, E. K. Jr. F.D., McKay, S., Thomas-Keprta, K., Wentworth, S., Romanek, C. S., (1998). *"Evidence for ancient Martian life"*. NASA Johnson Space Center.

[209] Whitehouse, David (August 27, 1999). *"Life on Mars - new claims"*, BBC News. Retrieved on 2008-08-20.

[210] Williams, Chris. *"Probe reveals three ages of Mars"*. Retrieved on 2007-03-02.

[211] Williams, David R., (September 1, 2004). *"Mars Fact Sheet"*. National Space Science Data Center. NASA. Retrieved on 2006-06-24.

[212] Wilson, R.J., (2000). *“Evidence for diurnal period Kelvin waves in the Martian atmosphere from Mars Global Surveyor TES data”*. Geophys. Res. Lett. 27, 3889–3892.

[213] Wiscombe, W. J., (1980). *“Improved Mie scattering algorithms”*. Applied Optics, Vol. 19, Issue 9, pp. 1505-1509.

[214] Withers P, Smith MD. 2006. *“Atmospheric entry profiles from the Mars Exploration Rovers Spirit and Opportunity”*. Icarus 185:13342.

[215] Zent, A. P., Haberle, R. M., Houben, H. C., Jacosky, B. M., (1993). *“A coupled subsurface-boundary layer model of water on Mars”*. J. Geophys. Res. 98, 3319-3337.

[216] Zurek RW. 1981. *“Inference of dust opacities for the 1977 Martian great dust storms from Viking Lander 1 pressure data”*. Icarus 45:20215.

Planetary and Space Science 59 (2011) 149–162

Contents lists available at ScienceDirect

Planetary and Space Science

journal homepage: www.elsevier.com/locate/pss

# Observations of water vapour and carbon monoxide in the Martian atmosphere with the SWC of PFS/MEX

G. Sindoni*, V. Formisano, A. Geminale

*Istituto di Fisica dello Spazio Interplanetario (IFSI)—INAF, Via del Fosso del Cavaliere, 100, 00133 Roma, Italy*

ARTICLE INFO

*Article history:*
Received 3 March 2010
Received in revised form
6 December 2010
Accepted 8 December 2010
Available online 28 December 2010

*Keywords:*
Mars
Atmosphere
Carbon monoxide
Water vapour
Spectroscopy

ABSTRACT

In the history of Mars exploration its atmosphere and planetary climatology aroused particular interest. In the study of the minor gases abundance in the Martian atmosphere, water vapour became especially important, both because it is the most variable trace gas, and because it is involved in several processes characterizing the planetary atmosphere. The water vapour photolysis regulates the Martian atmosphere photochemistry, and so it is strictly related to carbon monoxide. The CO study is very important for the so-called "atmosphere stability problem", solved by the theoretical modelling involving photochemical reactions in which the $H_2O$ and the CO gases are main characters.

The Planetary Fourier Spectrometer (PFS) on board the ESA Mars Express (MEX) mission can probe the Mars atmosphere in the infrared spectral range between 200 and 2000 $cm^{-1}$ (5–50 μm) with the Long Wavelength Channel (LWC) and between 1700 and 8000 $cm^{-1}$ (1.2–5.8 μm) with the Short Wavelength Channel (SWC). Although there are several $H_2O$ and CO absorption bands in the spectral range covered by PFS, we used the 3845 $cm^{-1}$ (2.6 μm) and the 4235 $cm^{-1}$ (2.36 μm) bands for the analysis of water vapour and carbon monoxide, respectively, because these ranges are less affected by instrumental problems than the other ones. The gaseous concentrations are retrieved by using an algorithm developed for this purpose.

The PFS/SW dataset used in this work covers more than two and a half Martian years from $Ls = 62^\circ$ of MY 27 (orbit 634) to $Ls = 203^\circ$ of MY 29 (orbit 6537). We measured a mean column density of water vapour of about 9.6 pr. μm and a mean mixing ratio of carbon monoxide of about 990 ppm, but with strong seasonal variations at high latitudes. The seasonal water vapour map reproduces very well the known seasonal water cycle. In the northern summer, water vapour and CO show a good anticorrelation most of the time. This behaviour is due to the carbon dioxide and water sublimation from the north polar ice cap, which dilutes non-condensable species including carbon monoxide. An analogous process takes place during the winter polar cap, but in this case the condensation of carbon dioxide and water vapour causes an increase of the concentration of non-condensable species. Finally, the results show the seasonal variation of the carbon monoxide mixing ratio with the surface pressure.

## 1. Introduction

In the study of the constituent gases of the Martian atmosphere, water vapour arouses particular interest, both because it is the most variable minor gas and because it is involved in many processes characterizing the planetary atmosphere. In fact, the water vapour photolysis controls the Mars atmosphere photochemistry, producing odd hydrogen species, such as H, OH, $HO_2$ and $H_2O_2$. The latest mean global models of Mars photochemistry were calculated by Nair et al. (1994) and Krasnopolsky (1995).

The carbon monoxide (CO), produced by the $CO_2$ photodissociation, is strictly related to water vapour not only by photochemical causes, such as the $CO_2$ catalysed recombination ($CO + OH \rightarrow CO_2 + H$), but also by dynamical effects. The water vapour is a condensable species, while the carbon monoxide is a non-condensable one, so they respond differently to atmospheric processes.

The first observations of Mars atmosphere composition were made using ground-based instruments in the first 1960s (Spinrad et al., 1963). About the seasonal evolution of water vapour, the first dataset was provided by the Echelle-Coudé scanner at McDonald Observatory during the period between 1972 and 1974 (Barker, 1976) and later by the MAWD spectrometer on board the *Viking* 1 lander using the 1.38 μm absorption band. The main result obtained from this experiment was the coverage of the complete seasonal cycle on Mars, showing a variability of water vapour abundance from a few up to about 100 pr. μm (precipitable microns). These results suggested a water vapour exchange between the atmosphere and the superficial reserves, as permanent and seasonal polar caps and regolith, and a clear transport from north to south caused by the global circulation (Jakosky and Farmer, 1982).

---

* Corresponding author. Tel.: +39 0645488511.
*E-mail address:* giuseppe.sindoni@ifsi-roma.inaf.it (G. Sindoni).

0032-0633/$ - see front matter © 2010 Elsevier Ltd. All rights reserved.
doi:10.1016/j.pss.2010.12.006

At the end of the 1980s and in the 1990s data acquired by new spacecrafts were available. The ISM spectrometer on board the *Phobos* 2 measured a mean column density of 9 ± 3 pr. μm in the south and of 12 ± 3 pr. μm in the north (Rosenqvist et al., 1992). In 1997 the photocamera on board the lander *Pathfinder* measured photometrically a column density of 6 ± 4 pr. μm in the Ares Vallis region at Ls = 150° and a water vapour confinement in the boundary layer (1–3 km upon the surface) (Titov et al., 1999).

In the period between 1999 and August 2004 the "Thermal Emission Spectrometer" (TES) on board the Mars Global Surveyor acquired spectra covering the spectral band 20–45 μm. These data cover more than three Martian years always at 14:00 local time (Smith, 2004). A reanalysis of TES acquired spectra has lowered the water vapour results by 30% (Smith, 2008). The whole seasonal coverage includes three summers of the northern hemisphere and shows a maximum water vapour column density from 55 to 80 pr. μm varying in the three different years. Recently, Smith et al. (2009) published also the water vapour results obtained from MRO/CRISM data.

Since January 2004 Europe has been contributing to the Mars exploration with *Mars Express*. Water vapour in the atmosphere has been studied by the three spectrometers on board: OMEGA (Encrenaz et al., 2005; Melchiorri et al., 2007), SPICAM (Fedorova et al., 2006) and PFS (Fouchet et al., 2007; Tschimmel et al., 2008).

Although water vapour and a few atmospheric species involved in Mars photochemistry, such as $O_3$ (Fast et al., 2009), $H_2O_2$ (Encrenaz et al., 2008) and the $O_2$ (Altieri et al., 2009; Krasnopolsky, 2006), were observed and studied with a close examination, we do not know much about the carbon monoxide. Regarding the CO study in the Mars atmosphere, Krasnopolsky (2006) published a paper in which the CO mixing ratio variations are shown as observed from Earth with the IRTF/CSHELL instrument using the 1.57 μm band spectroscopy. Another paper was published by Encrenaz et al. (2006) about the study of the CO concentration variations over Hellas region as observed by OMEGA instrument on board the Mars Express, but the first description of the seasonal dependence of the carbon monoxide mixing ratio over a wide latitude range was given by Smith et al. (2009) from CRISM data. Recently also a first paper on the CO observations from PFS-MEX data was published by Billebaud et al. (2009), but the dataset was rather limited.

The study of carbon monoxide is of primary importance for the so-called "stability problem" of the Mars atmosphere. In fact the $CO_2$ dissociation in CO and O by photolysis should destroy the whole atmosphere in 6000 years. Then, the CO is recombined forming again $CO_2$ thanks to the catalysis of $H_2O$ photolysis products.

The lack of many simultaneous measurements of water vapour and carbon monoxide makes their comparison an issue of great interest for the understanding of photochemical and dynamical processes involved in the Mars planetary atmosphere. So the aim of this work is to investigate these two atmospheric species and their connections.

In this paper we present the results of water vapour and carbon monoxide concentration in the Mars atmosphere using spectra acquired by the PFS SW channel for more than two Martian years. In Section 2 we present a brief instrument and dataset description. In Section 3 we discuss the retrieval algorithm, and finally in Section 4 we show the experimental results, discussing them in Section 5.

## 2. Dataset

### 2.1. The PFS instrument

The Planetary Fourier Spectrometer (PFS) is an instrument optimized for atmospheric studies and it is described in detail by Formisano et al. (2004, 2005). It covers the IR spectral range from 1.2 to 45 μm and it consists of two different channels: the Short Wavelength Channel (SW), which measures the reflected light from the planet, and the Long Wavelength Channel (LW), which is sensitive to the emitted light from the planet surface. The spatial resolution is about 8 and 13 km for the SW and LW channel, respectively, from an altitude of 300 km. The SW channel uses a PbSe detector passively cooled to 200–220 K, whereas the LW channel detector is a pyroelectric device ($LiTaO_3$), which works at room temperature. The interferogram is sampled using a reference laser diode signal.

Apodized spectra were used for this work because of their noise reduction and the decrease of the overshooting effect in the red wing that is typical for the PFS instrumental function. The spectral response function of the instrument has a FWHM of 2.04 $cm^{-1}$ with Hamming apodization and a sampling step of 1.05 $cm^{-1}$. The loss of spectral resolution caused by the use of apodized spectra is not a problem, because the abundance analysis is done on absorption bands and not on single lines.

Regarding the in-flight performance, there are three causes for instrumental uncertainties that have to be taken into account: problems with radiometric calibrations, random noise due to the detector and AD converter and the influence of spacecraft vibrations (Giuranna et al., 2005). These instrumental uncertainties may alter the effective depth of the absorption lines, leading to errors in the estimations of gas abundance. In order to reduce the noise and thus to improve the signal-to-noise ratio (S/N), we used average spectra and, to be independent on the absolute calibration, we analysed the relative band depths. As inferred by Comolli and Saggin (2005) and confirmed by Giuranna et al. (2007) the spacecraft vibrations affect only the level of the continuum leaving unaltered the relative depth of the atmospheric absorption lines.

### 2.2. Observations

The PFS/SW dataset used in this work covers more than two and a half Martian years from Ls = 62° of MY 27 (orbit 634) to Ls = 203° of MY 29 (orbit 6537). For the creation of a single mean spectrum several measurements have to be averaged. This purpose is achieved by averaging spectra in two different ways, making two kinds of datasets. The first, called in this paper "orbital dataset", is obtained by choosing the ideal number of measurements to average in order to represent the best compromise between the signal-to-noise ratio increase and the maintenance of a good spatial resolution: for the $H_2O$ analysis 15 individual measurements have been averaged, whereas for the CO, the relative band being much weaker (see Section 3), it was necessary to average 50 single measurements. For a single orbit, the mean spectra were built by shifting by 10 measurements from an average to the next one: for example, 1–15, 11–25, 21–35, …, (for the $H_2O$), or 1–50, 11–60, 21–70, …, (for the CO) and so on. In this way 42,935 mean spectra have been generated for the water vapour analysis and 36,174 mean spectra for the carbon monoxide analysis. The second kind of dataset, called in this paper "bin dataset", is obtained by averaging spectra in square bins of 5° Solar Longitude (Ls) × 5° Latitude for seasonal behaviour studies and in square bins of 10° Longitude × 10° Latitude for geographic distribution studies. The Latitude vs Longitude bin averages are calculated separately for each of the four seasons: northern Spring (Ls = 0–90°), Summer (Ls = 90–180°), Fall (Ls = 180–270°) and Winter (Ls = 305–360°). Since the aim of our work is the study of the average behaviour of $H_2O$ and CO, data from Ls = 270° to 305° were excluded, because they are affected by the global-encircling dust storm occurred during the MY 28. In this way we have 2592 mean spectra for the Latitude vs Ls studies and 648 mean spectra for each season of the Latitude vs Longitude studies.

Obviously, the number of averaged spectra in a single bin is not constant and varies from a minimum of 1 to a maximum of 1277 with a mean value of about 213 for the seasonal study bin dataset

(Fig. 1) and of 208 (Spring), 256 (Summer), 74 (Fall) and 159 (Winter) for the geographical study dataset (Fig. 2).

It is necessary to make two different kinds of dataset to optimize the S/N ratio according to the study aim. The best S/N ratio is obtained in the bin dataset, but this averaging method causes the loss of important information linked to the mean spectrum, such as temporal or orbital information. Therefore, the bin dataset is used when we have to investigate only the seasonal and geographical mean trends of the gaseous concentrations, while the orbital dataset, keeping the orbital information, allow us to investigate variations on relatively small scales, although with a poorer S/N ratio.

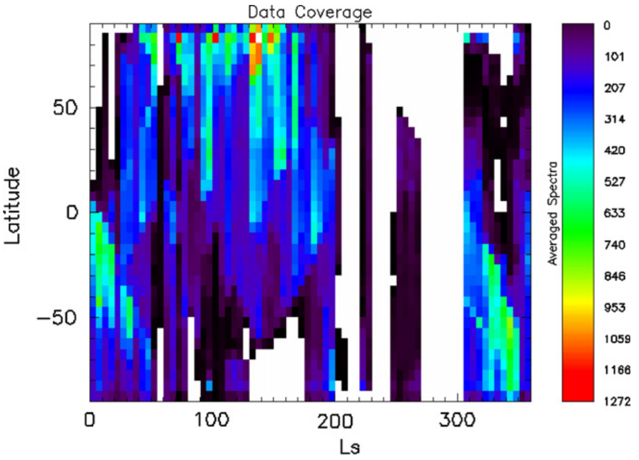

**Fig. 1.** Data coverage for the 5° Ls vs 5° Latitude dataset. Data affected by the global-encircling dust storm of MY 28 (Ls=270–305°) were excluded. The mean number of averaged spectra in a single bin is 213. White bins indicate no data.

## 3. Analysis procedure

Although there are several $H_2O$ and CO absorption bands in the spectral range covered by PFS, we used the 2.6 μm (3845 $cm^{-1}$) band for the water vapour and the 2.36 μm (4235 $cm^{-1}$) band for the CO analysis, because these ranges are less affected by instrumental problems respect to other ones, and are out of the thermal range limit, avoiding in this way calibration problems due to thermal inversions in the PFS/SWC spectrum (see Section 3.4).

In order to retrieve the $H_2O$ and CO concentration in the Mars atmosphere, we developed an analysis algorithm. The procedure carried out can be described in several points:

1. Reading of the averaged spectrum and its geometry data.
2. Wavelength grid correction.
3. Extraction of a vertical temperature and pressure profile from the Mars Climate Database (MCD, version 4.2).
4. Creation of synthetic spectrum by a line-by-line calculation of monochromatic opacities for $CO_2$, $H_2O$ (considering the saturation level of water, as defined in Section 3.2) and CO. The obtained transmittance spectrum is multiplied with the solar spectrum and convolved with the PFS instrumental function.
5. Division of the averaged PFS spectrum and of the synthetic spectrum by their own specific defined continuum (normalization).

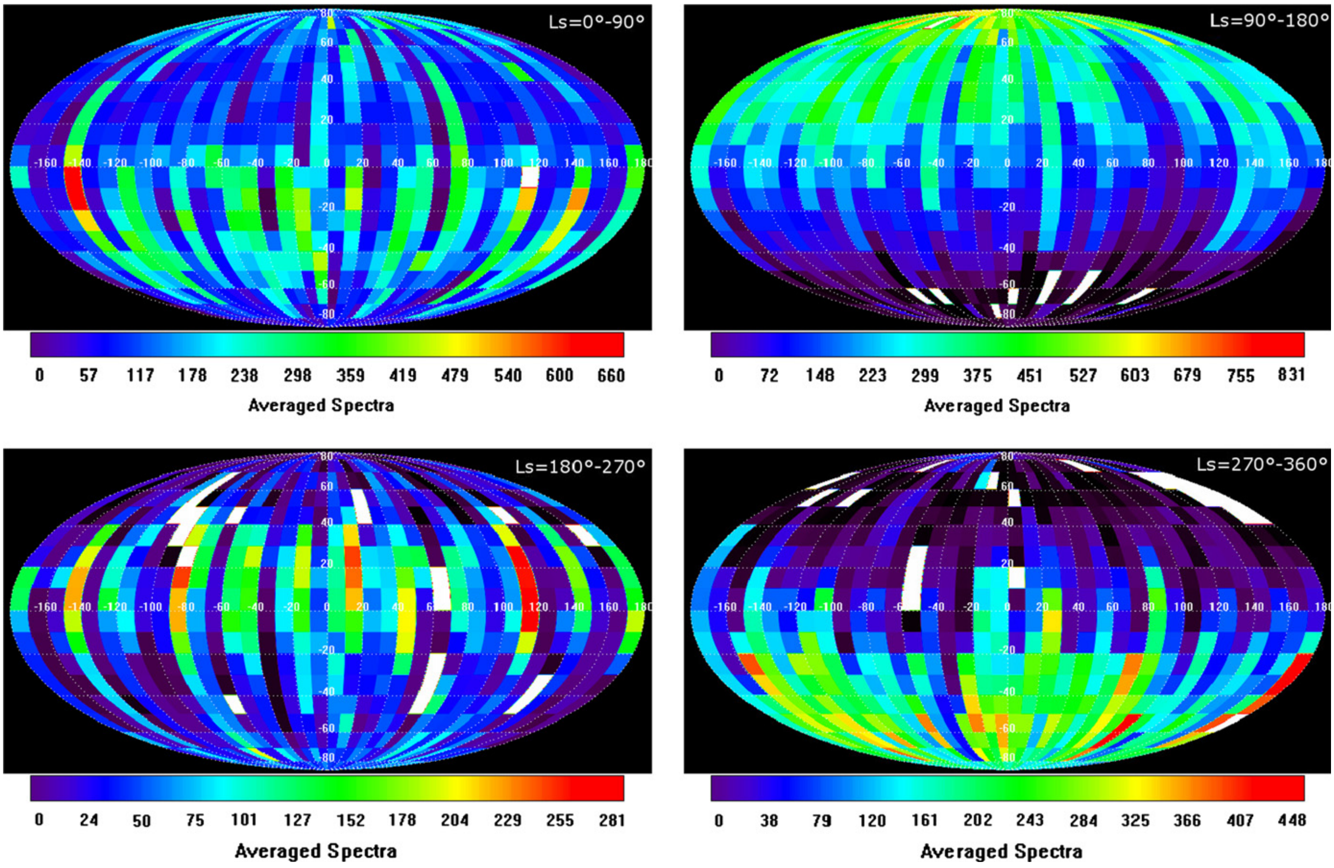

**Fig. 2.** Data coverage for the 10° Longitude vs 10° Latitude dataset for the four seasons: northern Spring (Ls=0–90°), Summer (Ls=90–180°), Fall (Ls=180–270°) and Winter (Ls=305–360°). Data affected by the global-encircling dust storm of MY 28 (Ls=270–305°) were excluded. The mean number of averaged spectra in a single bin is 208 for Ls=0–90°, 256 for Ls=90–180°, 74 for Ls=180–270° and 159 for Ls=270–360°. White bins indicate no data.

6. Finding the $H_2O$ and CO mixing ratio in a fitting loop using a $\chi^2$ minimization.

In the synthetic spectra we considered a fixed value of 0.10 for the dust and ice optical depth, respectively, at 1100 and 825 $cm^{-1}$, with an exponential vertical distribution of particles. This value of optical depths represents the typical Martian conditions out of the dust storm periods (Smith, 2004; Esposito et al., 2006). The properties of dust as a function of wavenumber are those proposed by Ockert-Bell et al. (1997), whereas for water ice we used infrared refractive indices published by Hansen (1999). The grain size distribution used for the aerosols is that described in the model by Clancy et al. (2003). The error related to having neglected variations in the aerosols opacity is evaluated in Section 3.6.

### 3.1. *Wavelength grid correction*

The wavelength sampling in the averaged measured spectra can be lightly shifted because of the small temporal variations in the laser diode temperature and in the pendulum motion. Then, it is necessary to follow a correction procedure for the spectrum grid. The correction is done for each individual spectrum using a reference synthetic spectrum, which contains 300 ppm of $H_2O$ and 800 ppm of CO: in this way the exact wavelength of each absorption line is well defined.

The procedure consists in the choice of three minima, representing the position in wavelength of three absorption lines in the observed and synthetic spectra in the spectral range in which the absorption band of interest is contained. The correction factor for the wavelength grid is the mean value of the ratio between the *wn* (wavenumber) positions in the measured spectrum (*wnm*) and the corresponding ones in the synthetic spectrum (*wns*), i.e.

$$corr = \frac{\sum_{i=1}^{3} wnm_i/wns_i}{3}$$

Averaging the three values is necessary because the correction factor can sometimes be slightly different over the whole spectral range considered. Therefore, in order to obtain the corrected spectrum it is sufficient to divide the old wavelength grid by the correction factor.

The correction factor ranges from 1.00000 to 1.00046, with a mean value of $1.00018 \pm 0.00008$ and a peak value of the histogram distribution of $1.00015 \pm 0.00015$.

### 3.2. *The synthetic spectrum*

To compute synthetic spectra, geometry data (Latitude, Longitude, Ls, Local Time and Altimetry) of the individual mean spectrum have been used as input for the MCD. From these coordinates, the Global Circulation Model (GCM) provides a vertical temperature and pressure profile with 65 layers. The vertical resolution of the model decreases with altitude, going from about 400 m close to the surface to 7 km at 115 km. Consequently the temperature profile determines the saturation water vapour pressure $p_s$ over ice (given in Pa), according to the formula by Marti and Mauersberger (1993)

$$\log p_s = -\frac{2663.5 \pm 0.8}{T} + (12.537 \pm 0.011)$$

The atmospheric modelling was performed using the approach of Ignatiev et al. (2005). Synthetic spectra are calculated line-by-line using the absorption coefficients extracted from precalculated gaseous opacities for the temperature and pressure profile of interest. The spectral lines are extracted from the molecular spectroscopic database HITRAN 2004 (Rothman et al., 2005). We have to keep in mind that since this database was created for the Earth's atmosphere, the correction for an atmosphere dominated by $CO_2$ (Mars case) is done using a broadening parameter varying between 0.9 and 1.9 from line to line (Gamache et al., 1995). In our case the broadening factor is set to 1.3, as done by Fedorova et al. (2006).

The transmittance spectrum is calculated considering a specific gas ($H_2O$ or CO) mixing ratio, which is the tuning parameter in the retrieval algorithm. Variations of the $CO_2$ abundance in the atmosphere are considered as surface pressure variations (taken from the MCD model) rather than mixing ratio variations, which is assumed to be 0.9532. Finally, the transmittance spectrum obtained in this way is multiplied by a high-resolution solar spectrum (Fiorenza and Formisano, 2005) and convolved with the apodized instrumental function.

### 3.3. *Spectra normalization*

In order to use the relative band depths, it is necessary to normalize the spectrum to its continuum in the spectral region where the absorption bands of interest are present. This purpose is achieved using the approach suggested by Tschimmel et al. (2008). In this way we obtain a normalized synthetic spectrum $N_{syn}(\lambda)$ and a normalized measured spectrum $N_{PFS}(\lambda)$ in the spectral ranges from 3780 to 3950 $cm^{-1}$ and 4160 to 4300 $cm^{-1}$ for analysis of water vapour and carbon monoxide concentration, respectively.

The spectral continuum, both for the measured and the synthetic spectrum, is defined as a piecewise function $C(\lambda)$, linear between two local maxima. The $C(\lambda)$ function is chosen in order to take account of the possible variations of the instrumental behaviour and the different spectral characteristics of the albedo in the two spectral ranges considered for the $H_2O$ and CO analysis (Fig. 3). A local maximum is defined as the spectral point $\lambda_M$ which has a higher radiance than its five adjacent spectral points, for the $H_2O$ analysis, and higher than its three adjacent spectral points, for the CO analysis. The choice of the best number of such spectral points for the continuum definition represents the most reliable result obtained from several tests performed using a different number of spectral point steps. For each step, the best fit ($\chi^2$) between the observed and the synthetic spectrum gives us the best estimate of the number of spectral points to be considered in order to have the best continuum definition.

Mathematically, the normalized spectrum is generated by

$$N(\lambda) = \frac{I(\lambda)}{C(\lambda)}$$

where $N(\lambda)$ is the normalized spectrum, $I(\lambda)$ is the radiance spectrum and $C(\lambda)$ is the continuum. Examples of normalized spectra are shown in Fig. 4 (black line), together with the best fit synthetic spectrum (red line).

### 3.4. *Best fit procedure*

In the best fit procedure for measured and synthetic spectra the mixing ratio of the atmospheric component ($H_2O$ or CO) is the resulting variable parameter. In the case of water vapour band, the mixing ratio is considered constant at altitudes below the condensation level and equal to the saturation mixing ratio above it, whereas for the CO analysis a constant distributed vertical profile is considered. Therefore, the synthetic spectrum has to be calculated in each step of the fitting loop in order to keep into account the changing of the saturation level due to the variable $H_2O$ content. The fit criterion is the minimization of the $\chi^2$ parameter, weighed by the instrumental noise and defined as

$$\chi^2 = \frac{\sum_{i=1}^{np} (N_{PFS}(\lambda_i) - N_{syn}(\lambda_i))^2}{np(NER/lcont/(\sqrt{nm}))^2}$$

where the sum is extended on all the points of the normalized spectra in the considered spectral range, *np* is the number of these

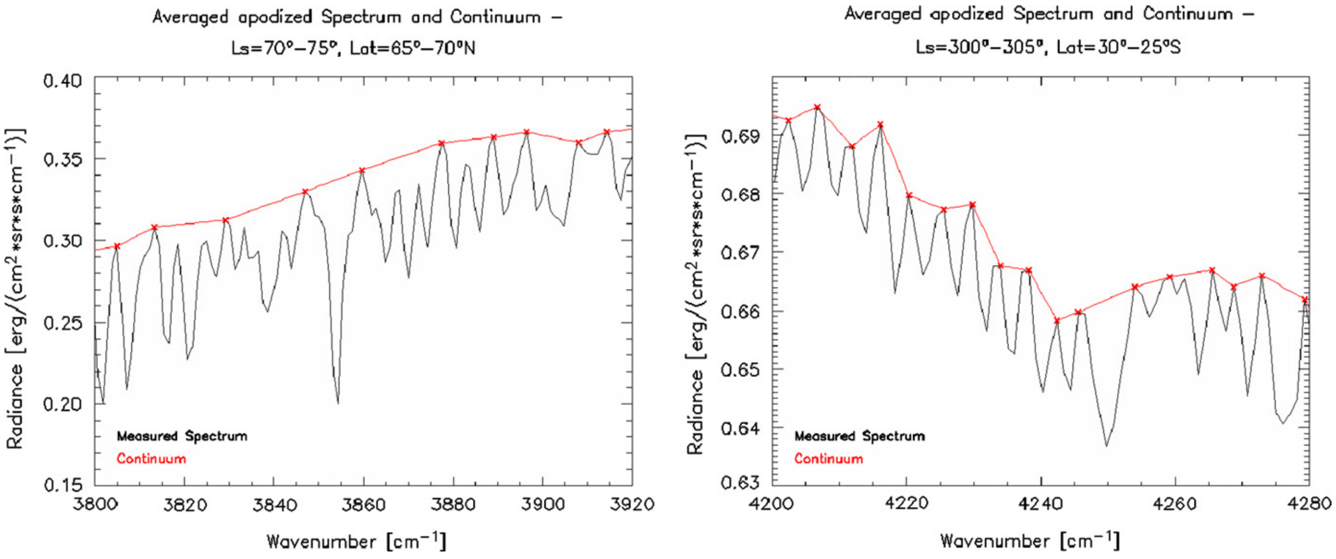

**Fig. 3.** Examples of continuum definition for PFS measured spectra in the absorption band spectral ranges for the $H_2O$ (left) and the CO (right). The black line is the measured spectrum and the red line is its continuum. The crosses are the spectral point used for the continuum definition. (For interpretation of the references to colour in this figure legend, the reader is referred to the web version of this article.)

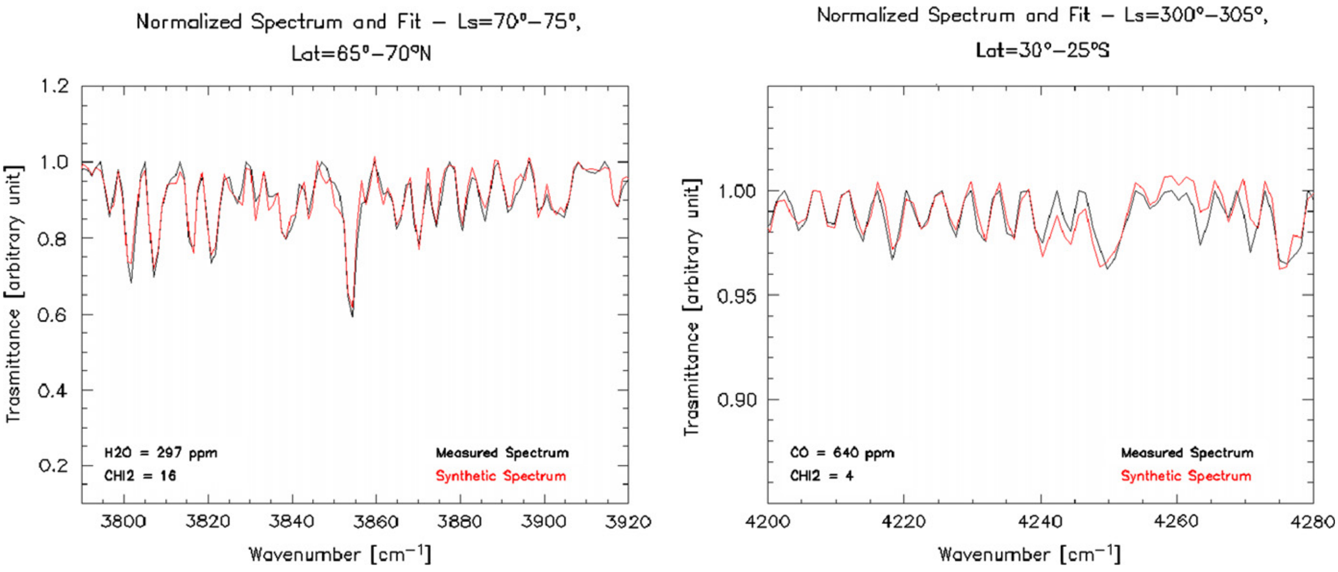

**Fig. 4.** Left-panel: Spectral fit example of the water vapour absorption band for an averaged spectrum (normalized to its continuum), corresponding to 200 single spectra selected into the bin Ls=70–75°, Lat=65–70°N. The retrieved mixing ratio is 297 ppm with a minimum $\chi^2$ of 16 (over 130 sampling points). Right-panel: Spectral fit example of the carbon monoxide absorption band for an averaged spectrum (normalized to its continuum), corresponding to 243 single spectra selected into the bin Ls=300–305°, Lat=25–30°S. The retrieved mixing ratio is 640 ppm with a minimum $\chi^2$ of 4 (over 40 sampling points).

points, the *NER* (Noise Equivalent Radiance) (Giuranna et al., 2005) is assumed to have its mean value in the considered range (0.023 and 0.035 erg $s^{-1}$ $cm^{-1}$ $sr^{-1}$ cm, for the $H_2O$ and the CO, respectively), *Icont* is the mean continuum radiance in the spectral range and *nm* is the number of the measured averaged spectra. We applied this procedure to a spectral range where the absorption band is stronger and the influence of the solar spectrum is not too strong, i.e. the 3785–3925 $cm^{-1}$ range for the $H_2O$ band and the 4200–4245 $cm^{-1}$ for the CO band.

The synthetic spectrum calculation and its normalization are iterated in a cycle that use a $\chi^2$ minimization method. The minimum $\chi^2$ provides the fit quality.

Fig. 4 (left-panel) shows an example of good quality spectral fit of the $H_2O$ absorption band for an averaged spectrum, corresponding to 200 single spectra selected within the bin Ls=70–75°, Lat=65–70°N. The vertical atmospheric profiles have been calculated for a latitude of 68.2°N and a longitude of 21.4°E, during Ls=72.9° and a solar local time (Lt) of 8.82. In this case the analysis algorithm gives us a mixing ratio of 297 ppm.

Fig. 4 (right-panel) shows an example of good quality spectral fit of the CO absorption band for an averaged spectrum, corresponding to 243 single spectra selected within the bin Ls=300–305°, Lat=25–30°S. The vertical atmospheric profiles have been calculated for a latitude of 27.5°S and a longitude of 10.6°W, during Ls=301.9° and a solar local time (Lt) of 10.63. In this case the analysis algorithm gives us a mixing ratio of 640 ppm.

However, in spite of the good quality fit, some features, as for example those around 3830 and 3850 $cm^{-1}$ in Fig. 4 (left-panel), and those around 4245 and 4260 cm$^{-1}$ in Fig. 4 (right-panel), remain not well fitted. These features are common to almost all the spectra and their origin has probably to be found in a wrong line broadening factor in the model, in systematic instrumental features or in an unknown contribution of other atmospheric components.

When the averaged measured spectrum radiance level is too low, resulting in a very low signal-to-noise ratio, or when particular albedo features do not allow a correct continuum definition, it is not possible to obtain a good fit. Therefore, results obtained with a poor fit quality will be excluded a posteriori using a selection method that takes into account the $\chi^2$ value. The $\chi^2$ histogram distribution reveals a peak in correspondence of a value of 1.5 for the $H_2O$ retrieval and of 2.5 for the CO retrieval, but with a less broad distribution for the last one. The $\chi^2$ threshold (50 and 25 for the $H_2O$ and the CO band fit, respectively) was chosen in order to strike a balance between the maintenance of a relevant data coverage and a sufficiently good fit quality (Fig. 5). In this way we discarded about 25% of the water vapour data and about 20% of the carbon monoxide data, mostly relating to the night (winter) polar regions, which have a very low signal-to-noise ratio.

The presence of another CO absorption band in the PFS/SWC spectrum, around 2150 cm$^{-1}$, allows sometimes the comparison between concentration values obtained from the two different band fits. However, this band in the thermal region of the spectrum, although it is more intense than the other one, hides some analysis problems. The main problem is the calibration of the thermal region of the spectrum, because it is a very complex task when in the spectra there are one or more "thermal inversions", which depend on the relative temperature between Mars and the detector. In fact, in the thermal radiation range (up to 2900 cm$^{-1}$), the PFS/SW channel is sensitive to the difference of temperature between the emitting source (Mars) and the detector temperature (Giuranna et al., 2005). So, when Mars becomes hotter or cooler than the detector, one or more "phase jumps" occur and they prevent a good spectrum calibration. Unfortunately, we have not still a stable algorithm able to perform this kind of phase correction, therefore spectra affected by thermal inversions can not be used in the retrieval analysis.

In some cases, in which it was possible to apply the same analysis procedure described above (without spectrum normalization), we have compared results from the two bands (an example is shown in Fig. 6). The retrievals obtained from the two bands, analysing the same spectra, differ by about 6%. The result of this comparison validates the method used for the 4200–4245 cm$^{-1}$ band.

### 3.5. Corrections of CO values a posteriori

The PFS/SWC spectrum has a spectral modulation, due to instrumental problems, centred at about 2 μm (5000 cm$^{-1}$) which starts from about 4000 cm$^{-1}$, and therefore it affects the CO absorption band (4235 cm$^{-1}$). Comolli and Saggin (2005) suggested that the modulation affects only the spectral continuum level without changing the relative depth of the spectral features. Therefore the normalization procedure should correct this effect and the mixing ratio values should be independent on the spectral continuum slope. In order to test a possible effect of the 2 μm spectral modulation on the CO band depth we considered the good quality spectral fit ($\chi^2 < 25$) of the "orbital dataset" and we studied the mixing ratio values as a function of the slope of the spectral continuum in the CO band spectral range. Fig. 7 shows the retrieved values for the CO mixing ratio (each point is the average of CO

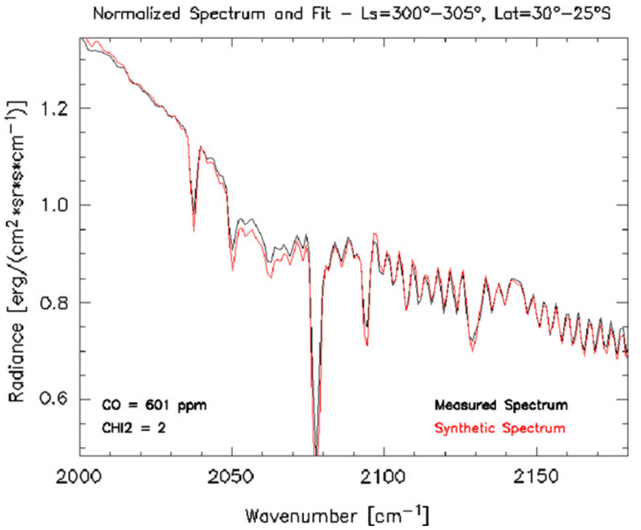

**Fig. 6.** Spectral fit example of the carbon monoxide absorption band in the range 2000–2180 cm$^{-1}$ for an averaged spectrum, corresponding to 243 single spectra selected into the bin Ls=300–305°, Lat=25–30°S. The retrieved mixing ratio is 601 ppm with a minimum $\chi^2$ of 2. We compare this result with the one obtained in Fig. 4, referring to the same spectrum. We note that the difference in the retrieved concentration is about 6%.

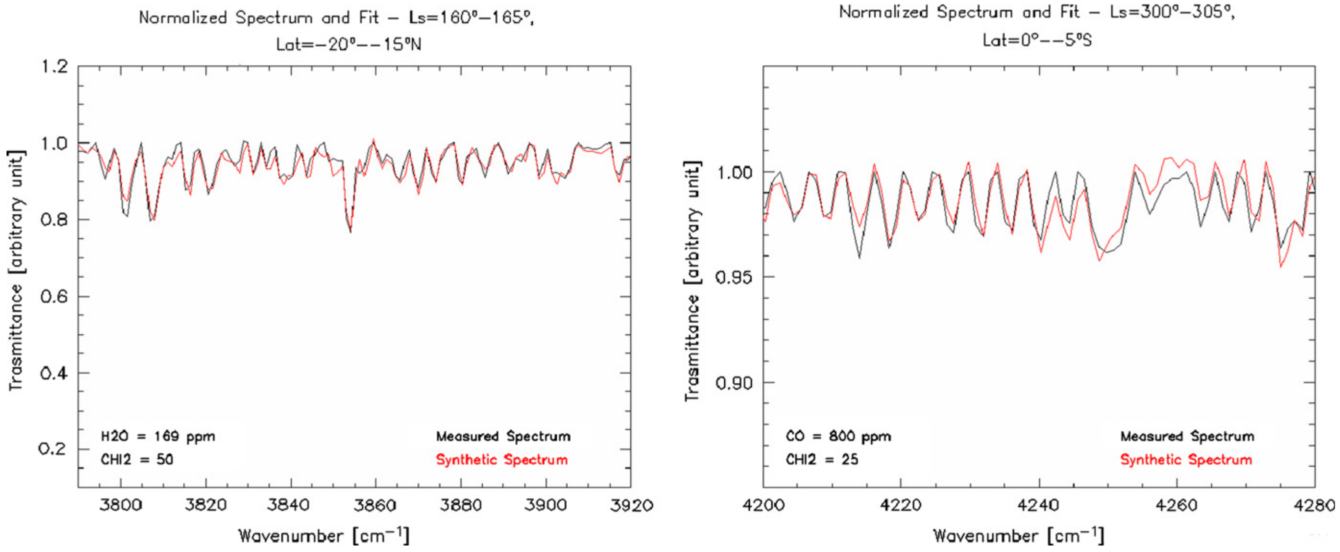

**Fig. 5.** Spectral fit examples of the water vapour (left) and carbon monoxide (right) absorption bands for averaged spectra (normalized to their continuum) having a minimum $\chi^2$ of 50 and 25, respectively, which represent the limit values of the selection criterion.

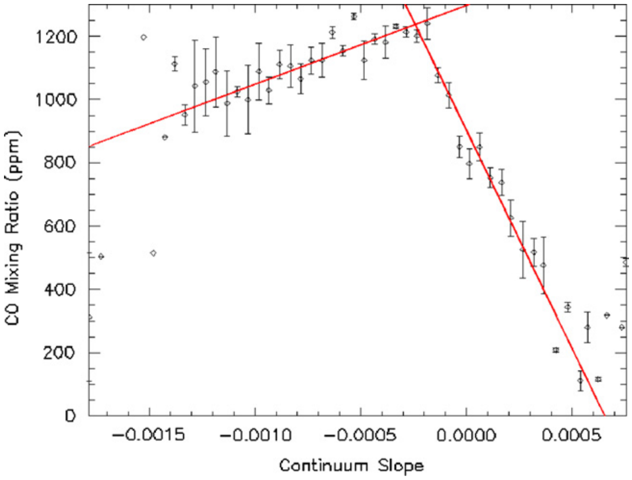

**Fig. 7.** Trend of retrieved CO mixing ratio values on 36174 averaged spectra as a function of the continuum slope (bins of $5\times10^{-5}$). Two linear fits are used to find this dependence: $y_1(m)=1297.75+249272.00m$ for $m<-2.42\times10^{-4}$ and $y_2(m)=903.285-1.38009e^6m$ for $m>-2.42\times10^{-4}$. The error bars are calculated as the data standard deviations.

values for slope bins of $5\times10^{-5}$) as a function of the slope. It is clear from the figure that there is a linear relationship between the two quantities described by two linear fits defined as:

$$y(m)=\begin{cases}1297.75+249{,}272.00\mathrm{m} & \text{for } m<-2.42\times10^{-4}\\ 903.28-1.38e^6m & \text{for } m>-2.42\times10^{-4}\end{cases}$$

We have demonstrated that the 2 μm modulation affects the band depth that therefore has to be corrected using the “calibration function” $y(m)$.

The corrected mixing ratio value ($cmr$) can be calculated for each data-point as follows:

$$cmr=omr\frac{y(m_{synt})}{y(m)}$$

where $omr$ is the retrieved mixing ratio value, $y(m_{synt})$ is the reference mixing ratio (903 ppm) and $y(m)$ is the mixing ratio value of the calibration function at a considered angular coefficient $m$.

The reference mixing ratio $y(m_{synt})$, considered as the expected mean value of the whole dataset, has been obtained applying the calibration function to the slope of the continuum of a synthetic spectrum (without modulation) in the CO band.

### 3.6. Evaluation of uncertainties

There are many sources of uncertainties in the procedure described above. First of all, in the synthetic spectra calculation the main error source is the broadening line factor in a $CO_2$ dominated atmosphere. Although it is an important parameter, there is little experimental information about its correct value in the considered spectral ranges. The error coming from this factor was evaluated changing its value between 1.3 (Fedorova et al., 2006) and 1.7 (Gamache et al., 1995). In this way we obtained a variation in the retrieved abundance values of about 15% for the $H_2O$ and of about 10% for the CO.

Another source of error has to be found in the used climatic model: the uncertainty derived from the MCD pressure is less than 2%, and the one derived from the MCD temperature is about 5%. For the water vapour analysis, the uncertainty coming from the MCD temperature affects the saturation profile producing an error of about 5% in its abundance.

In order to estimate the uncertainty derived by having neglected the aerosols effect, we have generated a synthetic spectra set, using different dust and ice opacities. The range of variability for the dust optical depth (at 1075 $cm^{-1}$) was chosen between 0.05 and 0.4, which represents the Martian mean conditions out of the global dust storm (Smith, 2004; Smith et al., 2009). Processing each spectrum of this set with the analysis procedure used for actual Martian data, we obtained an error (standard deviation of retrieved results) of 7% and 9% in the retrieved concentration for the water vapour and for the carbon monoxide, respectively.

For the variability of the water ice content in the Martian atmosphere, we considered an optical depth range between 0.05 and 0.12 at 825 $cm^{-1}$ (Smith, 2004). The ice particle content in the atmosphere results to be totally negligible for the two absorption bands considered in our study.

Another important contribution to the error evaluation derives from the continuum definition: a little variation in its definition and the presence of the instrumental noise can result in errors up to about 5% and 15% in the $H_2O$ and CO concentration, respectively. In addition, only for the CO concentration retrieval, we have to consider the uncertainty due to the “a posteriori correction” for the 2 μm modulation (Section 3.5): the error (standard deviation) is evaluated to be about 5%.

Finally, there is also an intrinsic error in the fit cycle. Since the synthetic spectra are calculated with a minimum step of 5% in the mixing ratio, this value also represents the accuracy of the best fit procedure. Moreover, the fit quality given by the $\chi^2$ value provides an estimation of the error on concentration of the considered atmospheric component.

Therefore, we can conclude that the broadening line factor and the continuum definition (only for the CO retrieval) represent the main sources of error in the whole procedure. Considering all the contributions, the total error (square sum) for each retrieved concentration value is estimated to be about 19% for the water vapour and about 22% for the carbon monoxide.

## 4. Results

### 4.1. Water vapour: seasonal and geographical behaviour

The water vapour behaviour we retrieve reproduces the well known *seasonal water cycle* in the Mars atmosphere.

In order to come out $H_2O$ results more comparable with other datasets, we converted them in pr. μm, taking into account the saturation and pressure profiles. Moreover, since the real vertical distribution of water vapour is still unknown, we applied the topographic correction usually used on the $H_2O$ retrieved values to rule out the topographic effect on the absorption band depth: this effect must be taken into account because the vertical distribution of the water vapour on the Mars atmosphere is non-uniform (Titov et al., 1999). Therefore, this topographic correction is obtained normalizing each column density value to the mean superficial pressure value of 6.1 mbar, i.e. each column density value is multiplied by a $6.1/p_s$ factor, where $p_s$ [mbar] is the superficial pressure corresponding to the considered spectrum. This normalization, which seems to give reasonable results, should remove the first-order influence of topography on the retrieved abundances of water vapour.

The retrieved $H_2O$ abundances as a function of Solar Longitude (Ls) and latitude, as observed by PFS/SWC, from orbit 634 to orbit 6537, allow us to study its seasonal cycle. The map obtained, using spectra averaged in 5° Ls × 5° Latitude bins, is shown in Fig. 8.

The mean abundance for the whole dataset results to be about 9.6 pr.μm with a maximum of 59.0 pr. μm in correspondence of the summer northern polar cap (Ls = 105–125°, Latitude = 70–80°N). The standard deviation over the mean value is about 9.0 pr. μm. Since the error in estimating the mean water vapour abundance is about 1.8 pr. μm ($\ll$ 9.0 pr. μm), the big value of the standard deviation indicates the very large spread in the water vapour abundance values and therefore its variability in the Marian atmosphere. The map shows the expected water vapour cycle in the Mars atmosphere. The atmospheric content of the water vapour before Ls = 70° begins to increase at middle-high latitudes, between 40°N and 70°N, because of the start of the northern polar cap sublimation; then the latitudinal distribution is characterized by a gradient between Ls = 80° and about Ls = 140° (northern summer). During the period Ls = 130–150° the amount of water vapour at high northern latitudes begins to decrease rapidly. At the same time, a region with relatively high $H_2O$ abundance (about 15.9 pr. µm) develops at about 45°N. It moves with season toward the equator reaching it at about Ls = 190° and then it continues to move toward south having a mean value of about 9.5 pr. µm from Ls = 190° to 270° (northern fall). During the northern winter (southern summer) for Ls = 305–340° we can see the increase of the $H_2O$ amount due to the sublimation of the south polar cap (70°–90°S), with a maximum value of about 22.8 pr. µm. Finally, from Ls = 340° the water vapour moves toward north joining at Ls = 360° with the already discussed spring season, starting from Ls = 0°.

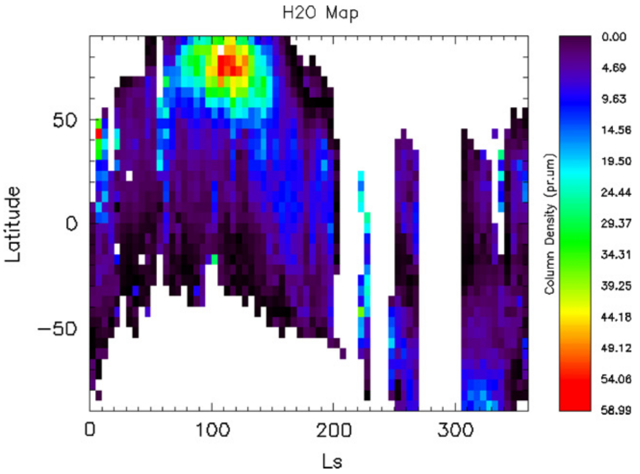

**Fig. 8.** Map of retrieved abundance of water vapour as a function of Solar Longitude (Ls) and Latitude as observed by PFS/SWC, from orbit 634 to orbit 6537, obtained using spectra averaged in 5° Ls × 5° Latitude bins.

In order to study the water vapour distribution in the Martian atmosphere, we used the averaged spectra in square bins of 10° Longitude × 10° Latitude for each season. The results obtained for Ls = 0–90° (northern Spring), Ls = 90–180° (northern Summer), Ls = 180–270° (northern Fall) and Ls = 305–360° (northern Winter) are shown in Fig. 9.

We note a peculiarity in almost all the seasons (Spring, Fall and Winter): an increase of the water vapour abundance over two particular regions, Arabia Terra (30°E, 0°N) and Tharsis (100°W, 0°N). Both these maxima have been also observed by many instruments and two explanations have been given for them: interaction soil–atmosphere (Smith, 2002) and atmospheric circulation influence with the presence of stationary waves causing a water vapour build-up over certain regions (Fouchet et al., 2007).

It is now interesting to comment on the maximum in the water vapour abundance during the north summer (Fig. 9). Clearly, the biggest $H_2O$ densities are at latitudes between 60°N and 85°N, centred around 75°N. Therefore, the centre of the water distribution is localized out of the permanent polar cap border, which spreads to a latitude of about 80°N, whereas the seasonal polar cap is already completely withdrawn at Ls = 90°.

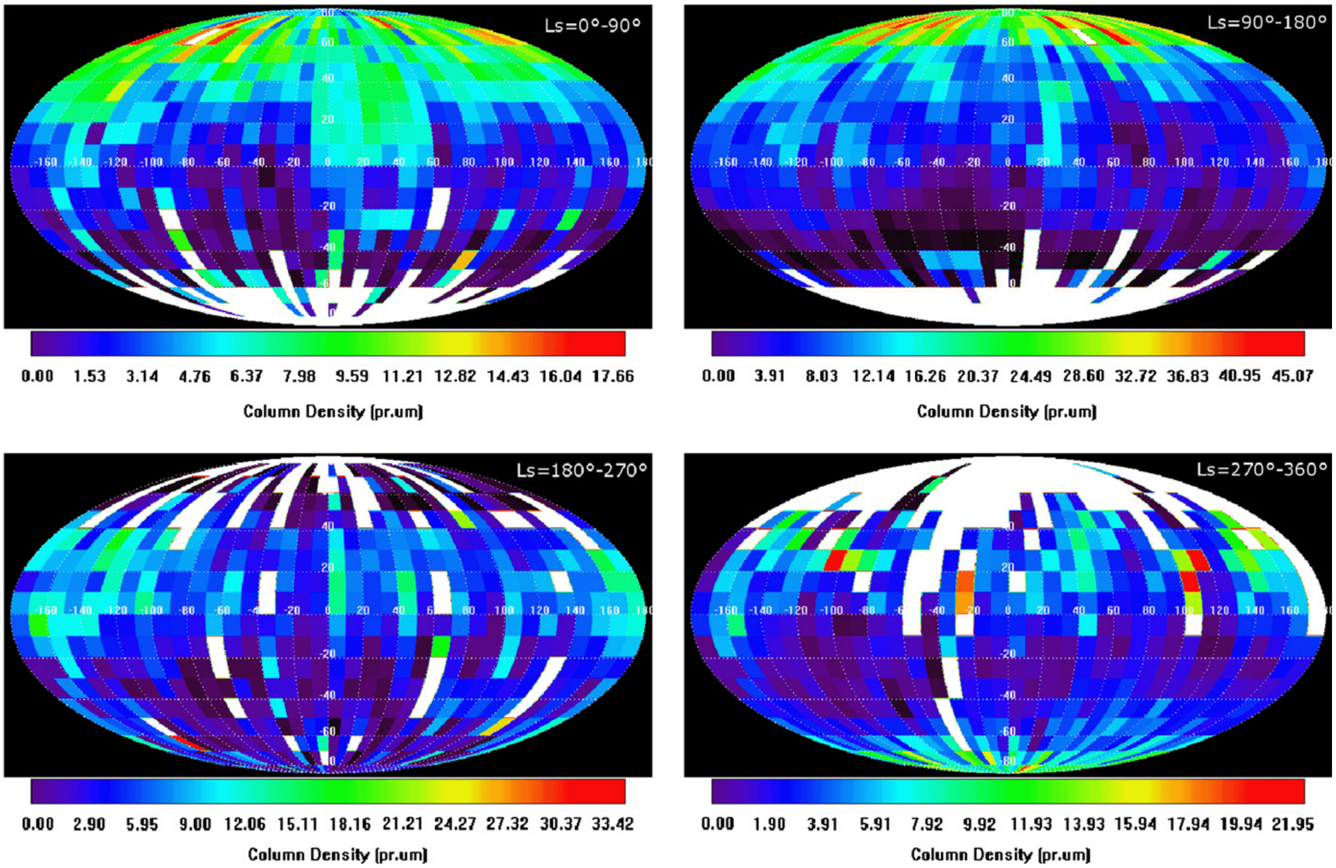

**Fig. 9.** Map of retrieved abundance of water vapour as a function of Longitude and Latitude as observed by PFS/SWC, from orbit 634 to orbit 6537, obtained using averaged spectra in square bins of 10° Longitude × 10° Latitude for each season: Ls = 0–90° (northern Spring), Ls = 90–180° (northern Summer), Ls = 180–270° (northern Fall) and Ls = 305–360° (northern Winter).

### 4.2. Carbon monoxide: seasonal and geographical behaviour

Since the carbon monoxide is assumed to be uniformly distributed in the Mars atmosphere, so being independent on the topography (Smith et al., 2009), we do not need to apply the topographic correction to its concentration values.

The retrieved concentration of carbon monoxide as a function of Solar Longitude (Ls) and latitude, as observed by PFS/SWC, from orbit 634 to orbit 6537, allows us to study its seasonal cycle. The map obtained, using spectra averaged in 5° Ls × 5° Latitude bins, is shown in Fig. 10.

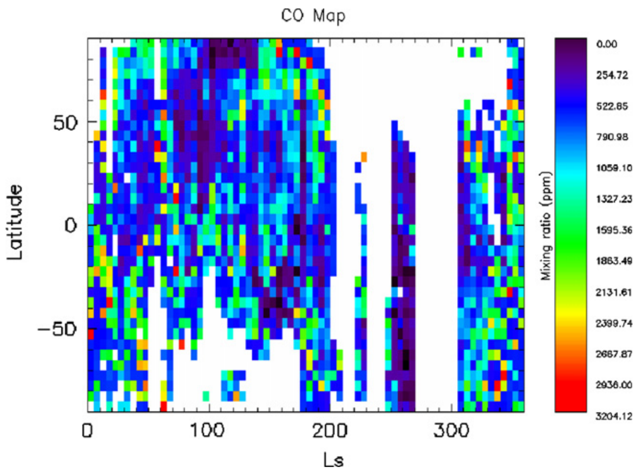

**Fig. 10.** Map of retrieved concentration of carbon monoxide as a function of Solar Longitude (Ls) and Latitude as observed by PFS/SWC, from orbit 634 to orbit 6537, obtained using spectra averaged in 5° Ls × 5° Latitude bins.

The mean concentration for the whole dataset results to be 990 ppm with a maximum of 3217 ppm. The standard deviation over the mean value is about 580 ppm. Since the error in estimating the mean carbon monoxide concentration is about 220 ppm ($\ll 580$ ppm), the big value of the standard deviation indicates, also in this case, the large spread (even if less strong than for the $H_2O$) in the carbon monoxide concentration values and therefore its variability in the Marian atmosphere. The retrieved CO mixing ratio is noisy because of the weakness of the CO absorption band and the relatively weak dependence of the absorption on CO mixing ratio. For the same reason we have sometimes a bad data coverage, due to the impossibility of having a good fit quality. Despite that, from the map we can see a general seasonal behaviour. Before Ls = 70° there is a CO concentration of about 900 ppm with a definite increase in the middle latitudes of the southern hemisphere and over the north polar cap. From Ls = 70° to 100° the CO mixing ratio decreases over the north polar cap (less than 600 ppm) and its maximum value moves southward. The minimum mean quantity of revealed CO (about 400 ppm or less) is measured between Ls = 100° and 130° over the north polar cap (Latitude = 75°–90°N). In this period it is evident that there is a CO concentration gradient that extends from lower values in the north to higher values (about 980 ppm) in the south. From Ls = 130° to 190° we can observe a new CO maximum zone in the middle-high latitude (50–90°N): here the mixing ratio values are around 1120 ppm. In the period Ls = 250–270° the south polar cap sublimation causes a CO and non-condensable gases depletion (down to values less than 400 ppm), in an analogous way to what happens in the summer north pole. Finally, from Ls = 305° the CO maximum zone moves toward the equator and at the same time a high CO concentration is evident in the northern hemisphere.

In order to study the carbon monoxide distribution in the Martian atmosphere, we used the averaged spectra in square bin of 10°

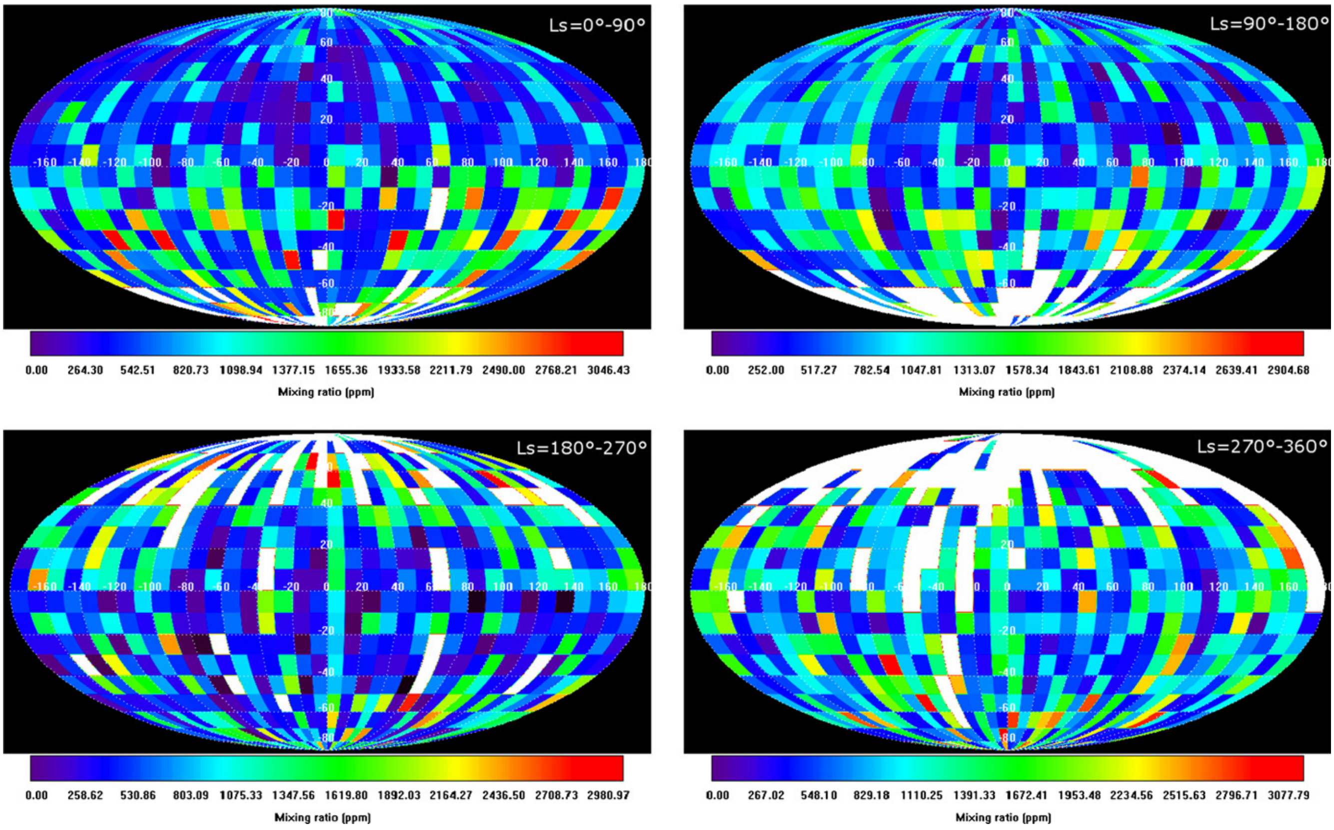

**Fig. 11.** Map of retrieved concentration of carbon monoxide as a function of Longitude and Latitude as observed by PFS/SWC, from orbit 634 to orbit 6537, obtained using averaged spectra in square bins of 10° Longitude × 10° Latitude for each season: Ls = 0–90° (northern Spring), Ls = 90 – 180° (northern Summer), Ls = 180 – 270° (northern Fall) and Ls = 305–360° (northern Winter).

Longitude x 10° Latitude for each season. The results obtained for Ls=0–90° (Spring), Ls=90–180° (Summer), Ls=180–270° (Fall) and Ls=305–360° (Winter) are shown in Fig. 11. The CO geographical variability is characterized by a quite uniform longitudinal distribution, even if it is clear an asymmetry between the two hemispheres: during northern spring and summer the carbon monoxide is mainly distributed in the southern hemisphere, while during northern fall and winter it has a higher mean concentration in the northern hemisphere. Moreover, no important features seem to indicate an increase over particular geographical regions.

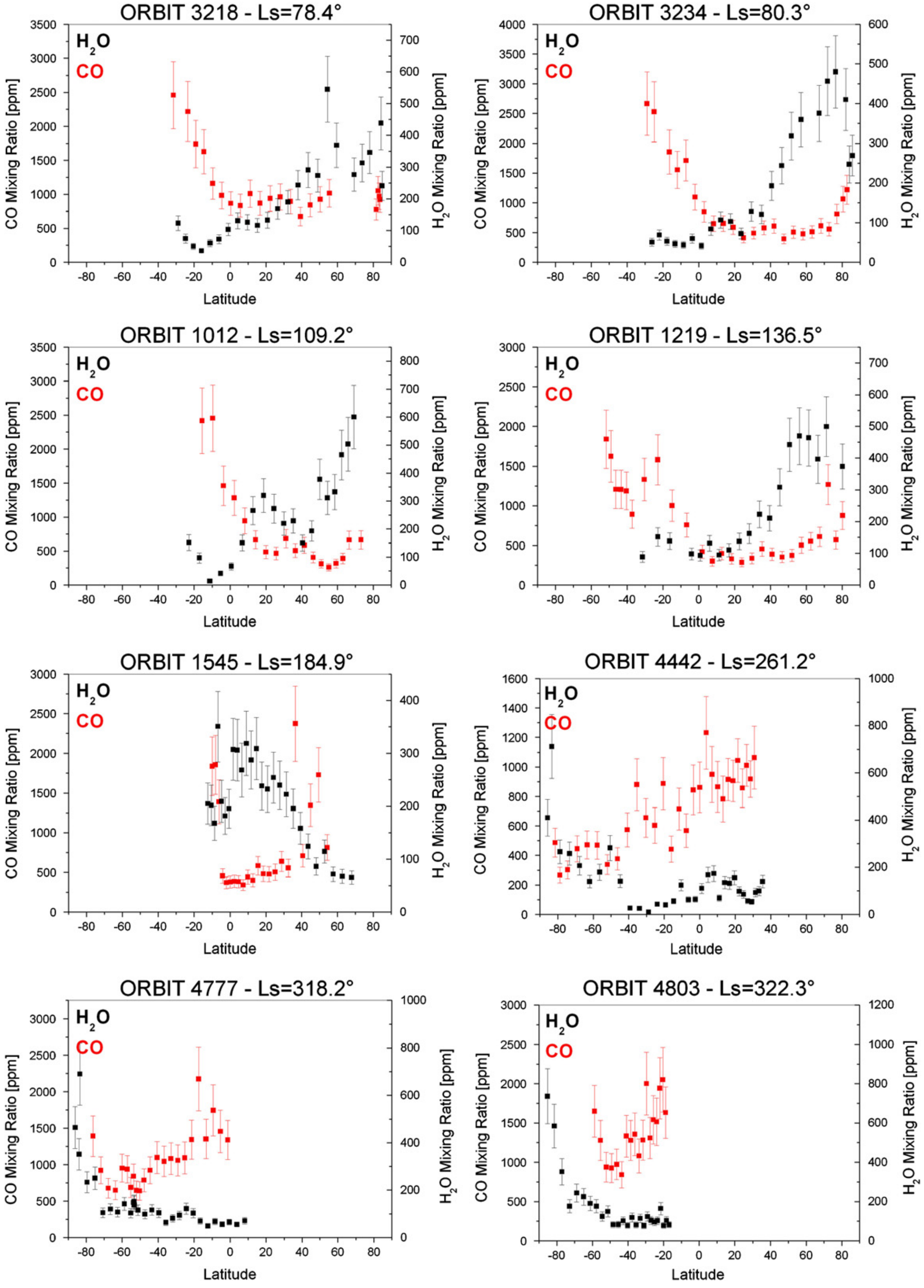

**Fig. 12.** Latitudinal trend of the $H_2O$ (black) and CO (red) abundances for two orbits of each season: Spring (Orbits 3218, 3234), Summer (Orbits 1012, 1219), Fall (Orbits 1545, 4442) and Winter (Orbits 4777, 4803). (For interpretation of the references to colour in this figure legend, the reader is referred to the web version of this article.)

### *4.3. Comparing $H_2O$ and CO results*

In order to find correlations/anticorrelations in the latitudinal distribution between water vapour and carbon monoxide, we compared the orbital latitudinal trend for a few orbits of each season. For this purpose we used the "orbital dataset" and we expressed both gaseous concentrations in mixing ratios. The orbits selected as examples of the general seasonal latitudinal trend are: 3218 (Ls = 78.4°) and 3234 (Ls = 80.3°) for northern Spring, 1012 (Ls = 109.2°) and 1219 (Ls = 136.5°) for northern Summer, 1545 (Ls = 184.9°) and 4442 (Ls = 261.2°) for northern Fall, and 4777 (Ls = 318.2°) and 4803 (Ls = 322.3°) for northern Winter. The latitudinal trend of $H_2O$ and CO concentrations for these orbits is shown in Fig. 12. Choosing individual orbits instead of mean orbital profiles for this kind of study is useful to demonstrate that we are able to maintain a good temporal and spatial resolution in retrieving the gaseous concentrations. The single orbit trends are representative of their own seasonal trends and this is clear comparing them with the averaged ones: in Fig. 13 we show, as examples, the mean latitudinal trends retrieved between Ls = 90° and 120° (early northern summer) and between Ls = 240° and 270° (late northern fall).

We can start from the first two orbits, 3218 and 3234, examples of the late Spring latitudinal trend. We see the $H_2O$ enhancement over the northern polar cap region due to the seasonal polar cap sublimation and a corresponding relatively weak depletion of CO in the same region. We find an opposite behaviour in the southern hemisphere, where the coming of the southern polar cap condensation causes an enhancement, as we have already said, of non-condensable gases, including CO, and an $H_2O$ values of less than 100 ppm in the same region with its maximum centred around 75°N, in agreement with our data obtained analysing the "bin dataset" (Section 4.1).

Following the annual evolution we have the Summer season. For this period we have selected the orbits 1012 and 1219. During the Summer, the latitudinal trend already noticed in the Spring becomes now stronger, as an effect of the more intense north polar cap sublimation and south polar cap condensation processes. For Ls = 109.2° (orbit 1012), over the northern polar cap, we find a water vapour maximum of about 600 ppm and lower values of CO mixing ratio (about 550 ppm), while, in the southern hemisphere around 20°S, the CO enhancement and the $H_2O$ depletion do not seem to be very different than during the Spring season. For Ls = 136.5° (orbit 1219) the latitudinal trend becomes weaker again because the water vapour amount begins to move southward, even if the sublimation/condensation processes remain quite evident.

During the Fall season, orbit 1545 shows a relative flattening of the latitudinal distribution of the two gaseous species, even though we can note a weak increase of the CO mixing ratio toward the north pole and of the $H_2O$ toward the south pole. This trend becomes more clear in the latitudinal distribution of water vapour and carbon monoxide during the late Fall (orbit 4442) and the Winter (orbits 4777 and 4803), when the sublimation of the southern polar cap causes an increase of water vapour (maximum of about 700 ppm at 83°S), while the CO concentration grows northward.

Therefore, from latitudinal orbital study it is possible to confirm the $H_2O$ and CO seasonal behaviour already shown in the : their tendency is to be generally anticorrelated.

The relationship between water vapour and carbon monoxide in the Mars atmosphere will have a dedicated paper with more details.

## 5. Discussion

The seasonal cycle of water vapour obtained from this analysis was observed also by other instruments, as MAWD (Jakosky and Farmer, 1982), TES (Smith, 2004), SPICAM (Fedorova et al., 2006), PFS/LWC (Fouchet et al., 2007) and PFS/SWC (Tschimmel et al., 2008), and CRISM (Smith et al., 2009). Tschimmel et al. (2008) studied the water vapour distribution during the period between Ls = 331° of MY 26 and Ls = 196° of MY 27, analysing its 2.6 μm absorption band. Despite their dataset does not overlap in time with ours, it is possible to compare the mean $H_2O$ behaviour. They observed the maximum value of water vapour abundance of about 60 pr. μm over the sublimating northern polar cap and the typical seasonal cycle, just in agreement with our results. Also their geographical distribution shows the water vapour behaviour we observed, but the local maxima over Arabia Terra and Tharsis are about one and a half time higher than in our maps, while the maxima values, centred around the latitude of 75°N, over the northern polar cap during its summer are in good agreement with our measurements. Since results by Tschimmel et al. (2008) are referred to a period in which the sublimation of the northern polar cap dominates, their average column density of 16.2 pr. μm is higher than our mean value (9.6 pr. μm).

Unfortunately, at the time of this writing only CRISM data can be compared with our data because these are the only data corresponding in time (MY 28–29) to our observations. CRISM measures a water vapour maximum during the northern hemisphere summer at high latitude. Its value is about 50 pr. μm and it is in

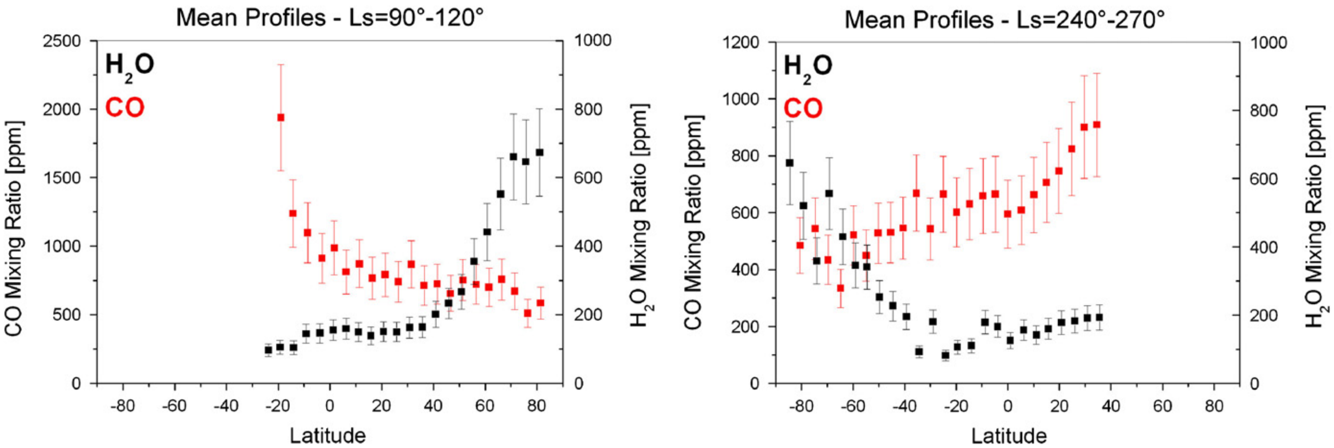

**Fig. 13.** Examples of mean latitudinal trends retrieved between Ls = 90° and 120° (early northern summer) (left) and between Ls = 240° and 270° (late northern fall) (right).

agreement with our maximum value of 59 pr. μm. The location of the centre of the water vapour distribution out of the permanent polar cap border during the northern summer (Section 4.1) is explained by Montmessin et al. (2004) suggestion: the water vapour produced by the seasonal polar cap sublimation is partly carried by the circulation toward the pole and redeposited on the permanent polar cap, whereas the remaining $H_2O$ is carried by the atmospheric dynamics toward the equatorial regions, where it forms the "Equatorial Cloud Belt". After that, in the centre of the summer (about $Ls=110^\circ$), even the ice created by the $H_2O$ redeposited in the permanent polar cap sublimates, producing the peak that we observe in the maps.

In the southern summer, instead, CRISM data show a reduced water vapour abundance if compared to observations from previous years. These low values are due to the fact that Smith et al. (2009) studied only the MY 28 southern summer: in this year, between $Ls=270^\circ$ and 305° there was a planet-encircling dust storm, which is known to produce significant changes of the atmospheric state (Smith, 2002) and of the surface albedo (Smith, 2004), resulting in the absence of the southern summer maximum. A similar effect was already noticed by TES data during the MY 25 dust storm (Smith, 2002) and by Viking Orbiter MAWD during the MY 12 dust storm (Fedorova et al., 2004). The normal water vapour trend in the southern hemisphere summer was shown for MY 24–25–26 by TES (Smith, 2002) and for MY 27 by Mars Express SPICAM (Fedorova et al., 2006) and OMEGA (Maltagliati et al., 2008). Our data, out of the global dust storm, show between $Ls=305^\circ$ and 340° a maximum value of 22.8 pr. μm over the south polar cap: this lower value compared to the northern summer one is explained by the shorter summer in the southern hemisphere, so the water vapour sublimation is hindered by the presence of a layer of $CO_2$ ice for most of the cap. Moreover, also the apparent partial $H_2O$ geographical confinement in the northern hemisphere, probably due to the global circulation, could have a role in this evidence.

The CO seasonal trend as retrieved by our PFS data shows the same latitudinal gradient in the northern hemisphere summer observed by Smith et al. (2009) with CRISM and Krasnopolsky (2003) with the IRTF/CSHELL spectrograph. At $Ls=112^\circ$ Krasnopolsky measured a CO gradient increasing from north of 23°N latitude (about 830 ppm) to south (about 1250 ppm at 45°S latitude), while Smith et al. (2009) revealed a CO mixing ratio gradient from about 450 ppm poleward of 30°N to 700 ppm at 30°S. Our measurement provides for the same period a gradient varying from about 270 ppm in the 75–90°N latitude to about 1250 ppm in the 30–45°S latitude. This hemispheric asymmetry is due to the condensation of the $CO_2$ gas in the south polar cap, which would lead to an enhancement in non-condensable gases, such as carbon monoxide, in the southern polar atmosphere. At the same time, the sublimation of the northern polar cap leads to a non-condensable gas depletion causing the strong reduction of the CO mixing ratio. In the same way, but in the opposite hemisphere, during the northern winter we see an enhancement in the CO mixing ratio, while over the south pole we observe a CO depletion due to the ice sublimation. This CO behaviour during the northern winter has also been observed by Billebaud et al. (2009), but they show results for only 90 PFS/MEX orbits, between $Ls=331.17^\circ$ and 51.61°, measuring 1110 ppm for the CO mixing ratio averaged over their entire data sample. This mean value is slightly higher than the values determined in our and previous works, probably because it refers to a limited dataset. Comparing their CO mixing ratio trends as a function of latitude for three Ls ranges ($Ls=331$–$360^\circ$, 0–30° and 30–52°) with our mean latitudinal trends for the same periods, we find an agreement for the first two trends, although with a 40% higher mean concentration in our data, but an opposite behaviour for the range $Ls=30$–$60^\circ$. In this period we measure a gradual decrease of the CO concentration between 40°S and 0°S in latitude and a quite constant value of about 1000 ppm going northward up to 80°N, while Billebaud et al. (2009) reveal a gradual increase up to 0° and a quite constant concentration value around 1000 ppm in the northern hemisphere. These differences could be due to the different dataset analysed and so to the interannual variations in the Mars atmosphere. Billebaud et al. (2009) studied also the trends of the CO mixing ratio as a function of geographical longitude for three latitudinal ranges (90°S–30°S, 30°S–30°N and 30°N–90°N). Comparing these results with our mean trends, we find a very good agreement both in the trends themselves and in the mean concentrations values. Moreover, we observe in the exact same positions the local CO maxima (around 125°W, 50°E and 150°E), probably due to planetary waves.

The LMD/GMC model expects that the mixing ratio of non-condensable gases over Hellas basin should reach two times higher values than the mean ones during the summer and a minimum concentration during the winter (Encrenaz et al., 2006). This effect should be due to the isolation of this zone with respect to local vortex. This CO enhancement over Hellas basin has been confirmed by OMEGA/MEX data (Encrenaz et al., 2006) and CRISM/MRO (Smith et al., 2009), but not by the ground-based IRTF/CSHELL data analysed by Krasnopolsky (2003, 2006), which do not show significant variations between the atmosphere in and out the basin. So our observations of the Hellas basin agree with Krasnopolsky's. Moreover, Krasnopolsky (2003) revealed an asymmetry between the northern and southern hemisphere, measuring a CO increasing up to 50% from 23°N (830 ppm) to 50°S (1240 ppm). This effect is interpreted as a consequence of the $CO_2$ condensation during the polar winter, which leads to an atmospheric enhancement of non-condensable gases. This enhancement effect has also been observed by the Mars Odyssey GRS instrument through the study of argon distribution in the Mars atmosphere (Sprague et al., 2004, 2007). We measure a depletion of about 70% over the summer northern polar cap, while over the summer southern polar cap we find a depletion of about 50% with respect to the planetary mean value. The different weight of the depletion should be due to the different duration of the summer season in the two hemispheres (178 days in the north and 154 days in the south).

The models (Forget et al., 2006; Nelli et al., 2007; Lefèvre and Forget, 2009) also confirmed that the $CO_2$ condensation on the winter polar cap causes an increase of the non-condensable gases mixing ratio, and in a similar way, the sublimation from the summer polar cap produces a depletion of non-condensable gases. But, the NASA GCM (General Circulation Model) (Nelli et al., 2007) seems to underestimate the strength and the duration of the depletion, while the LMD model (Forget et al., 2008; Lefèvre and Forget, 2009) seems to underestimate only the duration of the depletion, when these previsions are compared with our data and with CRISM data.

Finally, comparing $H_2O$ and CO results we can conclude that these two gaseous species are generally anticorrelated. The main cause of this anticorrelation is the following: the water vapour being a condensable species and the carbon monoxide a non-condensable one, they are strongly influenced in an opposite way by the processes of condensation and sublimation in the polar caps.

## 6. Conclusions

We have studied the concentration trend of two very important minor species in the Mars atmosphere: water vapour and carbon monoxide. We used observations acquired for more than two and a half Martian years (MY 27–28–29) with Mars Express PFS instrument.

The water vapour retrieval revealed the same seasonal behaviour already observed by TES and other instruments, as PFS and

CRISM. The mean global value is 9.6 pr. μm and we measure a maximum water vapour concentration of about 59 pr. μm during the northern summer in the atmosphere over the north polar cap, in agreement with CRISM and all other observational data. After the sublimation of the northern polar cap we observe the water vapour migration toward tropical regions. A similar behaviour is evident in the southern hemisphere: the polar cap sublimation during its summer causes an enhancement of the atmospheric content of water vapour.

Our study of the CO concentrations in the Mars atmosphere led us to observe large variations strictly bound by the condensing and subliming processes in the polar caps. We measured a mean CO mixing ratio of about 990 ppm, but when the summer polar cap sublimes, releasing $CO_2$ in the atmosphere, we can see a very strong CO depletion (down to values less than 400 ppm). An opposite behaviour is expected over the winter polar cap, when the $CO_2$ condenses causing an atmospheric enrichment of non-condensable gases such as carbon monoxide. This trend is indicated by our data, but unfortunately the PFS/SWC can study carbon monoxide only during daytime, thus we have poor information about the atmosphere over the winter polar cap.

Future observations will be useful for a better characterization of the Mars atmospheric composition and climatology. It also will be possible to search for possible new sources and sinks for these gases and their mutual interactions.

## Acknowledgements

The PFS experiment was built at the Istituto di Fisica dello Spazio Interplanetario (IFSI) of Istituto Nazionale di Astrofisica (INAF), and was funded by the Italian Space Agency (ASI) in the context of the Italian participation to the Mars Express mission of ESA. The authors are very grateful to A. Mattana for his data processing support, to N. Ignatiev for code development on synthetic spectra, to D. Grassi, M. Giuranna and M. Tschimmel for valuable discussions.

The authors are grateful to the referees for their very useful corrections and suggestions that improved the paper.

## References

Altieri, F., Zasova, L., D'Aversa, E., Bellucci, G., Carrozzo, F.G., Gondet, B., Bibring, J.-P., 2009. $O_2$ 1.27 μm emission maps as derived from OMEGA/MEx data. Icarus 204, 499–511.

Barker, E.S., 1976. Martian atmospheric water vapor observations: 1972–1974 apparition. Icarus 28, 247–268.

Billebaud, F., Brillet, J., Lellouch, E., Fouchet, T., Encrenaz, T., Cottini, V., Ignatiev, N., Formisano, V., Giuranna, M., Maturilli, A., Forget, F., 2009. Observations of CO in the atmosphere of Mars with PFS onboard Mars Express. Planet. Space Sci. 57, 1446–1457.

Clancy, R.T., Wolff, M.J., Christensen, P.R., 2003. Mars aerosol studies with the MGS TES emission phase function observations: optical depths, particle sizes, and ice cloud types versus latitude and solar longitude. J. Geophys. Res. 108 (E9).

Comolli, L., Saggin, B., 2005. Evaluation of the sensitivity to mechanical vibrations of an IR Fourier spectrometer. Rev. Sci. Instrum. 76 (12), 123112.

Encrenaz, T., Melchiorri, R., Fouchet, T., Drossart, P., Lellouch, E., Gondet, B., Bibring, J.-P., Langevin, Y., Titov, D., Ignatiev, N., Forget, F., 2005. A mapping of Martian water sublimation during early northern summer using OMEGA/Mars Express. Astron. Astrophys. 441, L9L12.

Encrenaz, T., Fouchet, T., Melchiorri, R., Drossart, P., Gondet, B., Langevin, Y., Bibring, J.-P., Forget, F., Bézard, B., 2006. Seasonal variation of the Martian CO over Hellas as observed by OMEGA/Mars Express. Astron. Astrophys. 459, 265–270.

Encrenaz, T., Greathouse, T.K., Richter, M.J., Bézard, B., Fouchet, T., Lefèvre, F., Montmessin, F., Forget, F., Lebonnois, S., Atreya, S.K., 2008. Simultaneous mapping of $H_2O$ and $H_2O_2$ on Mars from infrared high-resolution imaging spectroscopy. Icarus 195, 547–556.

Esposito, F., Giuranna, M., Maturilli, A., Palomba, E., Colangeli, L., Formisano, V., 2006. Albedo and photometric study of Mars with the Planetary Fourier Spectrometer on-board the Mars Express mission. Icarus 186, 527–546.

Fast, K.E., Kostiuk, T., Lefèvre, F., Hewagama, T., Livengood, T.A., Delgado, J.D., Annen, J., Sonnabend, G., 2009. Comparison of HIPWAC and Mars Express SPICAM observations of ozone on Mars 2006–2008 and variation from 1993 IRHS observations. Icarus 203, 20–27.

Fedorova, A.A., Rodin, A.V., Baklanova, I.V., 2004. MAWD observations revisited: seasonal behavior of water vapor in the Martian atmosphere. Icarus 171, 54–67.

Fedorova, A.A., Korablev, O., Bertaux, J.-L., Rodin, A., Kiselev, A., Perrier, S., 2006. Mars water vapor abundance from SPICAM IR spectrometer: seasonal and geographic distributions. J. Geophys. Res. 111, E09S08. doi:10.1029/2006JE002695.

Fiorenza, C., Formisano, V., 2005. A solar spectrum for PFS data analysis. Planet. Space Sci. 53, 1009–1016.

Forget, F., Montabone, L., Lebonnois, S., 2006. Non-condensable gas enrichment and depletion in the Martian polar regions. In: Proceedings of the Second Workshop on Mars Modeling and Observations, Granada, Spain.

Forget, F., Millour, E., Montabone, L., Lefèvre, F., 2008. Noncondensable gas enrichment and depletion in the Martian polar regions. In: Proceedings of the Third Workshop on Mars Modeling and Observations, Williamsburg, Virginia.

Formisano, V., Grassi, D., Orfei, R., Biondi, D., Mencarelli, E., Mattana, A., Nespoli, F., Maturilli, A., Giuranna, M., Rossi, M., Maggi, M., Baldetti, P., Chionchio, G., Saggin, B., Angrilli, F., Bianchini, G., Piccioni, G., di Lellis, A., Cerroni, P., Capaccioni, F., Capria, M.T., Coradini, A., Fonti, S., Orofino, V., Blanco, A., Colangeli, L., Palomba, E., Esposito, F., Patsaev, D., Moroz, V., Zasova, L., Ignatiev, N., Khatuntsev, I., Moshkin, B., Ekonomov, A., Grigoriev, A., Nechaev, V., Kiselev, A., Nikolsky, Y., Gnedykh, V., Titov, D., Orleanski, P., Rataj, M., Malgoska, M., Jurewicz, A., Blecka, M.I., Hirsh, H., Arnold, G., Lellouch, E., Marten, A., Encrenaz, T., Lopez Moreno, J., Atreya, S., Gobbi, P., 2004. PFS: the Planetary Fourier Spectrometer for Mars Express. In: Wilson, A., Chicarro, A. (Eds.), ESA Special Publication, vol. 1240. ESA Publications Division, Noordwijk, pp. 71–94.

Formisano, V., Angrilli, F., Arnold, G., Atreya, S., Bianchini, G., Biondi, D., Blanco, A., Blecka, M.I., Coradini, A., Colangeli, L., Ekonomov, A., Esposito, F., Fonti, S., Giuranna, M., Grassi, D., Gnedykh, V., Grigoriev, A., Hansen, G., Hirsh, H., Khatuntsev, I., Kiselev, A., Ignatiev, N., Jurewicz, A., Lellouch, E., Lopez Moreno, J., Marten, A., Mattana, A., Maturilli, A., Mencarelli, E., Michalska, M., Moroz, V., Moshkin, B., Nespoli, F., Nikolsky, Y., Orfei, R., Orleanski, P., Orofino, V., Palomba, E., Patsaev, D., Piccioni, G., Rataj, M., Rodrigo, R., Rodriguez, J., Rossi, M., Saggin, B., Titov, D., Zasova, L., 2005. The Planetary Fourier Spectrometer (PFS) onboard the European Mars Express mission. Planet. Space Sci. 53, 963–974.

Fouchet, T., Lellouch, E., Ignatiev, N.I., Titov, D., Tschimmel, M., Formisano, V., Giuranna, M., Maturilli, A., Encrenaz, T., 2007. Martian water vapor: Mars Express PFS/LW observations. Icarus 190, 32–49.

Gamache, R.R., Neshyba, S.P., Plateaux, J.J., Barbe, A., Régalia, L., Pollack, J.B., 1995. $CO_2$-broadening of water-vapor lines. J. Mol. Spectrosc. 170, 131–151.

Giuranna, M., Formisano, V., Biondi, D., Ekonomov, A., Fonti, S., Grassi, D., Hirsch, H., Khatuntsev, I., Ignatiev, N., Michalska, M., Mattana, A., Maturilli, A., Moshkin, B.E., Mencarelli, E., Nespoli, F., Orfei, R., Orleanski, P., Piccioni, G., Rataj, M., Saggin, B., Zasova, L., 2005. Calibration of the Planetary Fourier Spectrometer short wavelength channel. Planet. Space Sci. 53, 975–991. doi:10.1016/j.pss.2004.12.007.

Giuranna, M., Hansen, G., Maturilli, A., Zasova, L., Formisano, V., Grassi, D., Ignatiev, N., 2007. Spatial variability, composition and thickness of the seasonal north polar cap of Mars in mid-spring. Planet. Space Sci. 55, 1328–1345. doi:10.1016/j.pss.2007.03.006.

Hansen, G.B., 1999. Control of the radiative properties of the Martian polar caps by surface $CO_2$ ice: evidence from Mars Global Surveyor measurements. J. Geophys. Res. 104, 16471–16486.

Ignatiev, N.I., Grassi, D., Zasova, L.V., 2005. Planetary Fourier spectrometer data analysis: fast radiative transfer models. Planet. Space Sci. 53, 1035–1042. doi:10.1016/j.pss.2004.12.009.

Jakosky, B.M., Farmer, C.B., 1982. The seasonal and global behaviour of water vapor in the Mars atmosphere—complete global results of the Viking atmospheric water detector experiment. J. Geophys. Res. 87, 2999–3019.

Krasnopolsky, V.A., 1995. Uniqueness of a solution of a steady-state photochemical problem: applications to Mars. J. Geophys. Res. 100, 3263–3276.

Krasnopolsky, V.A., 2003. Spectroscopic mapping of Mars CO mixing ratio: detection of northsouth asymmetry. J. Geophys. Res. 108 (E2), 5010.

Krasnopolsky, V.A., 2006. Long-term spectroscopic observations of latitudinal and seasonal variations of $O_2$ dayglow and CO on Mars. Icarus 190, 93–102.

Lefèvre, F., Forget, F., 2009. Observed variations of methane on Mars unexplained by known atmospheric chemistry and physics. Nature 460, 720–723. doi:10.1038/nature08228.

Maltagliati, L., Titov, D.V., Encrenaz, T., Melchiorri, R., Forget, F., Garcia-Comas, M., Keller, H.U., Langevin, Y., Bibring, J.-P., 2008. Observations of atmospheric water vapor above the Tharsis volcanoes on Mars with the OMEGA/MEx imaging spectrometer. Icarus 194, 53–64.

Marti, J., Mauersberger, K., 1993. A survey and new measurements of ice vapor pressure at temperature between 170 and 250 K. Geophys. Res. Lett. 20, 363–366.

Melchiorri, R., Encrenaz, T., Fouchet, T., Drossart, P., Lellouch, E., Gondet, B., Bibring, J.-P., Langevin, Y., Schmitt, B., Titov, D., Ignatiev, N., 2007. Water vapor mapping on Mars using OMEGA/Mars Express. Planet. Space Sci. 55, 333–342.

Montmessin, F., Forget, F., Rannou, P., Cabane, M., Haberle, R.M., 2004. Origin and role of water ice clouds in the Martian water cycle as inferred from a general circulation model. J. Geophys. Res. 109, 10004.

Nair, H., Allen, M., Anbar, A.D., Yung, Y.L., Clancy, R.T., 1994. A photochemical model of the Martian atmosphere. Icarus 111, 124–150.

Nelli, S.M., Murphy, J.R., Sprague, A.L., Boynton, W.V., Kerry, K.E., Janes, D.M., Metzger, A.E., 2007. Dissecting the polar dichotomy of the noncondensable gas enhancement on Mars using the NASA Ames Mars General Circulation Model. J. Geophys. Res. 112, E08S91. doi:10.1029/2006JE002849.

Ockert-Bell, M.E., Bell, J.F., Pollack, J.B., McKay, C.P., Forget, F., 1997. Absorption and scattering properties of the Martian dust in the solar wavelengths. J. Geophys. Res. 102 (E4), 9039–9050.

Rosenqvist, J., Drossart, P., Combes, M., Encrenaz, T., Lellouch, E., Bibring, J.P., Erard, S., Langevin, Y., Chassefière, E., 1992. Minor constituents in the Martian atmosphere from the ISM/Phobos experiment. Icarus 98, 254–270.

Rothman, et al., 2005. The HITRAN 2004 molecular spectroscopic database. J. Quant. Spectrosc. Radiat. Transfer 96, 139–204.

Smith, M.D., 2002. The annual cycle of water vapor as observed by the Thermal Emission Spectrometer. J. Geophys. Res. 107. doi:10.1029/2001JE001522.

Smith, M.D., 2004. Interannual variability in TES atmospheric observations of Mars during 1999–2003. Icarus 167, 148–165.

Smith, M.D., 2008. Mars water vapor climatology from MGS/TES. Mars Water Cycle Workshop, April 2008, Paris, France (abstract).

Smith, M.D., Wolff, M.J., Clancy, R., T., Murchie, S.L., 2009. Compact Reconnaissance Imaging Spectrometer observations of water vapor and carbon monoxide. J. Geophys. Res. 114, E00D03. doi:10.1029/2008JE003288.

Spinrad, H., Munch, G., Kaplan, L.D., 1963. Letter to the Editor: the detection of water vapor on Mars. Astrophys. J. 137, 13–19.

Sprague, A.L., Boynton, W.V., Kerry, K.E., Janes, D.M., Hunten, D.M., Kim, K.J., Reedy, R.C., Metzger, A.E., 2004. Mars' south polar Ar enhancement: a tracer for south polar seasonal meridional mixing. Science 306, 1364–1367.

Sprague, A.L., Boynton, W.V., Kerry, K.E., Janes, D.M., Kelly, N.J., Crombie, M.K., Nelli, S.M., Murphy, J.R., Reedy, R.C., Metzger, A.E., 2007. Mars' atmospheric argon: tracer for understanding Martian atmospheric circulation and dynamics. J. Geophys. Res. 112, E03S02. doi:10.1029/2005JE002597.

Titov, D.V., Markiewicz, W.J., Thomas, N., Keller, H.U., Sablotny, R.M., Tomasko, M.G., Lemmon, M.T., Smith, P.H., 1999. Measurements of the atmospheric water vapor on Mars by the Imager for Mars Pathfinder. J. Geophys. Res. 104, 9019–9026.

Tschimmel, M., Ignatiev, N.I., Titov, D., Lellouch, E., Fouchet, T., Giuranna, M., Formisano, V., 2008. Investigation of the water vapour on Mars with PFS/SW of Mars Express. Icarus 195, 557–575.